Advanced characterisation of microstructural evolution and liquation mechanisms in RR1000 employing a novel semi-solid testing facility.

Sean Ethan John
(BEng *Hons.*)

Submitted to Swansea University in fulfilment of the requirements for the Degree of Doctor of Philosophy

Swansea University

2019

DECLARATION

This work has not previously been accepted in substance for any degree and is not being concurrently submitted in candidature for any degree.

.
Signed ..[redacted]..... (candidate)

Date .....08/02/2021.....

STATEMENT 1

This thesis is the result of my own investigations, except where otherwise stated. Where correction services have been used, the extent and nature of the correction is clearly marked in a footnote(s).

Other sources are acknowledged by footnotes giving explicit references. A bibliography is appended.

Signed ...[redacted]..... (candidate)

Date .....08/02/2021.....

STATEMENT 2

I hereby give consent for my thesis, if accepted, to be available for photocopying and for inter-library loans **after expiry of a bar on access approved by the Swansea University.**

Signed [redacted]..... (candidate)

Date .....08/02/2021.....

ABSTRACT

Inertia friction welding is a joining technique that is used in many industries as it can create high quality welds with narrow heat affected zones. The nickel superalloy RR1000 is routinely joined via inertia friction welding, during the manufacture of compressor components for gas turbine engines, at Rolls-Royce Plc. The conditions experienced at the weld interface of an inertia friction weld are extreme, with a combination of rapid heating rates to high temperatures and severe strain rates. These conditions are such that liquation of RR1000 is to be expected.

The liquation mechanisms of two variants of RR1000 have been investigated, building on previous research, to further understand the dynamic evolution of microstructure and mechanical properties during inertia friction welding of RR1000. This investigation was accomplished by the design and commissioning of a novel semi-solid testing facility. The facility underwent numerous modifications to allow representative replication of the conditions experienced during inertia friction welding.

To investigate the liquation mechanisms occurring in RR1000, fine grain and coarse grain compression specimens were heated to temperatures between 900°C and 1200°C at heating rates between $1°Cs^{-1}$ and $25°Cs^{-1}$. The fine grain and coarse grain variants were found to liquate via two mechanisms. The fine grain primarily experienced constitutional liquation of the primary γ' precipitates, while incipient melting of the γ phase was experienced by the coarse grain variant. The liquid propagation rate in both variants was characterised.

The knowledge and understanding gained via the use of this facility was then applied to analyse the microstructures from a series of interrupted RR1000 inertia friction welds. Inspection of these interrupted welds revealed evidence of liquation like that observed in the specimens tested in the semi-solid testing facility.

This research has given an insight into the role of liquation during inertia friction welding of RR1000.

TABLE OF CONTENTS

LIST OF FIGURES

LIST OF TABLES

ACKNOWLEDGEMENTS

A great thanks to my academic supervisor Dr. Helen Davies for the support, guidance and input throughout this project. Having an approachable, caring and passionate supervisor has been a huge help during this PhD.

I would also like to express my gratitude towards Rolls-Royce plc, and EPSRC for sponsoring me throughout this project and providing both the funding and the material needed. I'd like to thank my industrial supervisor Dr Simon Bray for his input and direction throughout this project. Your expertise was invaluable.

I would like to thank the entire staff at the Institute of Structural Materials at Swansea University. Professor Martin Bache, your passion for the department has made it a pleasure to work within the team. I'd like to thank the workshop staff who have helped with the development and maintenance of the test rig at all stages of the project. I'd also like to acknowledge the administration team who have been a great help throughout.

I could not have completed this work without the unwavering support of my family. Thank you for always believing in me.

To my friends, thank you for checking in with me and reminding me to look after myself.

To my partner Alys, thank you for your unconditional love, support and encouragement. I will be forever grateful.

NOMENCLATURE

SYMBOL	DESCRIPTION
IFW	Inertia friction welding
FG	Fine grain
CG	Coarse grain
γ’	Gamma prime
γ	Gamma
LP	Low pressure
IP	Intermediate pressure
HP	High pressure
FCC	Face centre cubic
TCP	Topologically close packed
HCP	Hexagonally close packed
HIP	Hot isostatic pressing
VIM	Vacuum induction melting
VAR	Vacuum arc re-melting
HAZ	Heat affected zone
TIG	Tungsten inert gas
EBM	Electron beam melting
LBW	Laser beam welding
CDFW	Continuous drive friction welding
WL	Weld line
TMAZ	Thermo-mechanically affected zone
HT-CLSM	High temperature confocal laser scanning microscopy
DSI	Dynamic Systems Inc.
DSC	Differential scanning calorimetry
FE	Finite element
PID	Proportional-integral-derivative
EDM	Electrical discharge machining
SEM	Scanning electron microscope
FEG	Field emission gun
MUD	Multiple of uniform density
KAM	Kernel average misorientation

ECD	Equivalent circle diameter
EDS	Energy-dispersive X-ray Spectroscopy
SIP	Strain induced porosity
VCP	Virtual control panel
R-R	Rolls-Royce
GPSN	Gas pressure sintered silicon nitride
RF	Radio Frequency
BSE	Back scattered electron
XRD	X-ray Diffraction

1 INTRODUCTION

Inertia friction welding (IFW) is a joining technique that is used in many industries due to its ability to produce high integrity welds with narrow heat affected zones in a very short amount of time. During friction welding the weld interface experiences extreme heating rates and temperatures combined with severe strain rates (~1000s^{-1}) [1]. Friction welding is usually considered to be a solid state bonding technique due to the lack of a weld pool like other welding techniques[2]. The thermal conditions at the weld interface during IFW are so extreme, that for certain alloys, some liquation must occur, especially if the alloys are susceptible to a sub-solidus liquation mechanism.

IFW is used to a great extent in the aerospace industry, particularly in the manufacturing of components for gas turbine engines via the joining of high temperature nickel superalloys. Some nickel super alloys have been reported to suffer from sub-solidus liquation mechanisms when exposed to rapid heating rates, especially if they are highly alloyed. This makes them a likely candidate to experience liquation during inertia friction welding[3].

Rolls-Royce Plc. routinely join disks of the powder processed polycrystalline nickel superalloy RR1000, via inertia friction welding, during the manufacture of high-pressure compressor components for civil large engines, e.g. the Trent 1000 and Trent XWB variants. RR1000 is only inertia friction welded in its fine grain (FG) variant while joining high pressure compressor rear stages, 5, 6 and cone, i.e. the hotter end of the compressor. The coarse grain variant of RR1000 has only been welded in scientific interest and is not welded in production. RR1000 is a nickel superalloy with a highly complex composition and is therefore, very likely to experience liquation during a rapid heating event, such as friction welding. The occurrence of hot tearing in the thermo-mechanically affected zone (TMAZ) of some FG and CG RR1000 inertia friction welds is further evidence that liquation is occurring during the IFW of these alloys. Previous studies have been conducted on the sub-solidus liquation mechanisms that occur in the FG variant, but no research has been conducted on the sub-solidus liquation mechanisms of the CG variant. For this reason, the purpose of this study is to characterise the microstructural changes caused by rapid heating rates and the associated liquation and liquid propagation in both RR1000 variants. Followed by an assessment of the consequences these changes have had on mechanical properties.

The two variants of RR1000 (FG & CG) have vastly different microstructures that differ, not only in grain size, but in the distribution of a second phase precipitate gamma prime (γ'). The details of these microstructural differences will be discussed in detail, in section 3.1 Materials. The difference in microstructure renders each variant of RR1000 susceptible to two different sub-solidus liquation mechanisms.

The first is constitutional liquation of the large primary γ' precipitates. Evidence of this phenomenon occurring in FG RR1000 was reported in a study conducted by M. Attallah et al [4], and is discussed in detail later.

The second mechanism is incipient melting of the γ matrix, due to a reduction in meting point of localised regions during the mass diffusion of the γ' precipitates into the γ matrix on heating. The possibility of this mechanism in nickel superalloys was reported by F. Tancret [5], and is also discussed later. The actual evidence for the occurrence of this mechanism in RR1000, had not been previously reported prior to the present research. Both sub-solidus liquation mechanisms rely on rapid heating rates for their occurrence, making the region around the weld interface of an IFW, the perfect location for them to occur. When the two variants of RR1000 are welded via IFW they behave very differently. The upset rates they experience are vastly different, as shown in Figure 1.

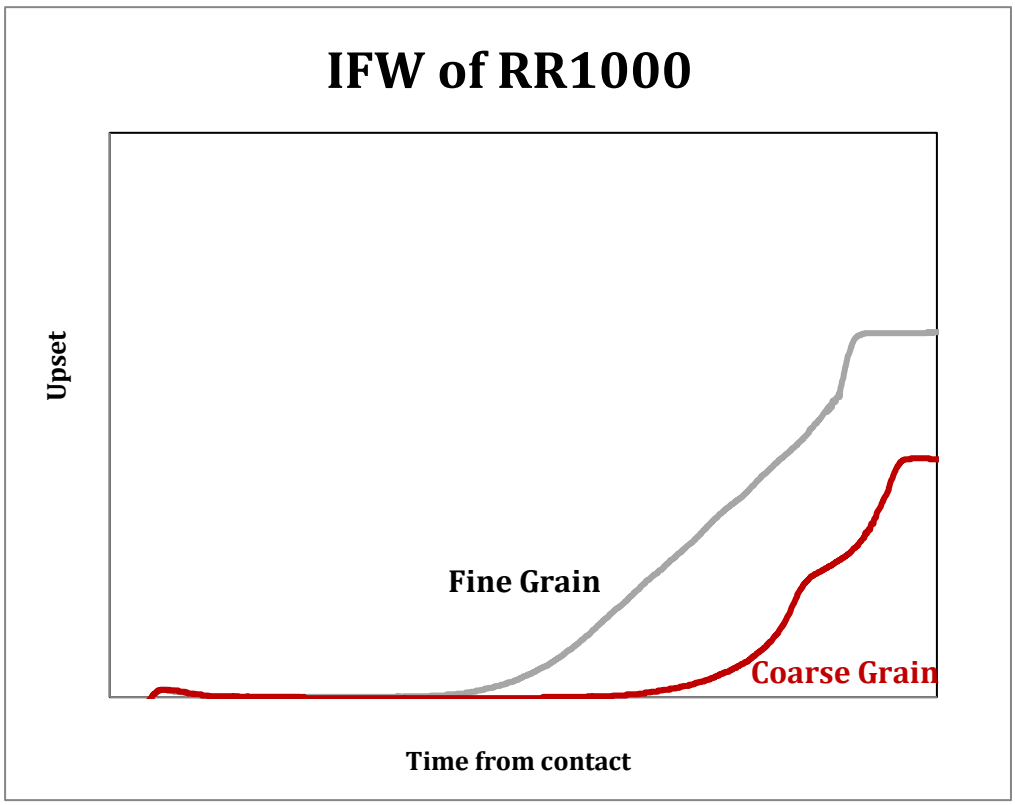

Figure 1 - Weld upset vs weld time plot for inertia friction welds of fine grain and coarse grain RR1000. Graph provided S. Bray - Rolls-Royce plc.

It is unlikely that the grain size alone would result in such vastly different upset behaviours during welding. It is probable, however, that the differences in microstructures and their inherent liquation mechanisms are a major contributor to their welding behaviours.

The resultant microstructures and mechanical properties of inertia friction welds of both RR1000 variants have been studied well in previous research and is detailed in section 2.4.2. However, the dynamic evolution of microstructure and the resultant mechanical properties are not fully understood, especially around the notion that liquation is a likely occurrence during welding.

This research project has been conducted with the aim of developing a greater understanding of weld line microstructural evolution during IFW of both RR1000 variants. A major part of the study has been design and development for the manufacture of a novel semi-solid testing facility capable of rapidly heating bulk RR1000 specimens to investigate liquation mechanisms.

The semi-solid testing facility has been designed around a servo-hydraulic compression machine with the idea that, after the liquation mechanisms of both RR1000 variants had been characterised, semi-solid compression tests could be conducted.

The semi-solid testing facility could then be used to quantify the effect that a semi-solid microstructure would have on the flow stress properties of the two RR1000 variants.

Unfortunately, due to the vast amount of time spent on the rig optimisation modifications coupled with unforeseen issues with the heating system, the planned semi-solid compression tests were not completed. Despite these problems, encountered during testing, a series of heat and quench only tests were performed. Microstructural characterisation of the specimens, used in these tests, has provided a wealth of knowledge on the microstructural evolution and liquation mechanisms occurring in both RR1000 variants when subject to rapid heating rates.

A series of heat, hold and quench tests were also conducted during this study, allowing the liquid propagation rate in each RR1000 variant to be investigated for the first time. This newfound understanding of RR1000's behaviour, under rapid heating, has been used to try and further understand the microstructural development during IFW.

The semi-solid specimens, created in this new facility, have been fully characterised and compared with a series of interrupted inertia friction welds that were conducted at

Rolls-Royce Plc by Simon Bray et al [6], [7]. Sections of these interrupted welds have been microstructurally characterised during this project to give an insight into the microstructure at key points in the welding cycles of both RR1000 variants. Knowledge gained from this research allowed the evolution of the structures, to be explained.

1.1 PROJECT OBJECTIVES

The microstructure of the parent RR1000 material and the final microstructure produced when RR1000 is inertia friction welded are understood well. The evolution however, of microstructure and mechanical properties, that occur between the two are not fully understood. This project aimed to provide an insight into this dynamic evolution.

The scope of this project was very optimistic, consisting of three substantial phases. Firstly, methods of semi-solid testing were reviewed to gain the knowledge and understanding required in order to be able to design and commission a new semi-solid testing facility. Even though a detailed statement of work was supplied to the external contractor, the rig, as-received required significant modifications before it was fully capable of replicating the conditions experienced at the weld interface of an inertia friction weld.

After many alterations and improvements, the semi-solid facility was ready for the second phase of the project, utilising the new testing facility to investigate the liquation mechanisms of both variants of RR1000 and characterising the liquid propagation rate. The final phase aimed to assess the effect liquation in RR1000 had on its mechanical properties. This new understanding could then be used to further comprehend the dynamic changes in microstructure and mechanical properties of RR1000 during an IFW.

The main objectives of the project are detailed on the next page:

1. Design, manufacture and optimise a novel semi-solid testing facility.
2. Investigate the sub-solidus liquation mechanisms of both RR1000 variants when rapidly heating bulk specimens, building on previous research in the literature.
3. Investigate the microstructural evolution that occurs leading up to these liquation mechanisms.
4. Characterise liquid propagation rate in both RR1000 variants.
5. Investigate the effect a semi-solid microstructure has on the flow stress properties of both RR1000 variants.
6. Characterise any re-solidification products produced on cooling.
7. Assess the effects of microstructural changes due to rapid heating on the mechanical properties of both RR1000 variants via hardness testing.
8. Assess the microstructures of interrupted RR1000 welds for evidence of liquation.
9. Use the new understanding of RR1000's microstructural evolution under rapid heating to decipher the microstructural evolution during IFW.

2 LITERATURE REVIEW

2.1 The gas turbine engine

2.1.1 Modern Gas Turbine Engines

All heat engines work on the same principle, extracting useful kinetic energy from the chemical energy stored in fuel. Most heat engines are based around the same working cycle of compressing and heating air, adding fuel and combusting it, then utilizing the resultant high temperature, high pressure gas to do work. The first pure turbo jets utilised this working cycle in a simple configuration of a single compressor driven by a single turbine. This configuration works well when propulsive efficiency is not paramount and manoeuvrability and the ability to perform rapid changes in power are more desirable. Most gas turbine engines used currently are in the commercial flight industry, where fuel efficiency and low noise levels are of upmost importance. Considering that in order to increase propulsive efficiency and therefore fuel efficiency, jet velocity must be minimised. Couple this with the fact that jet noise increases to the power of eight with jet velocity, it makes sense that commercial jet engines would benefit from reducing jet velocity as much as possible and retaining thrust, with bypass air flow. It is for this reason that many gas turbine engine manufacturers opt for multi-spool turbo fan jets with high bypass ratios. Examples include Rolls-Royce's Trent family of engines, GE's GE90 family of engines, Pratt & Whitney's PW4000 range of engines and the joint venture between the latter two, the GP7200. As this project was conducted in partnership with Rolls-Royce, a focus has been made on their Trent architecture [8]–[11].

Rolls-Royce have established triple-spool turbo fan engines with their three shaft design and continue to use it in their Trent family of engines. A simplified diagram of this three shaft design is shown in Figure 2 [12].

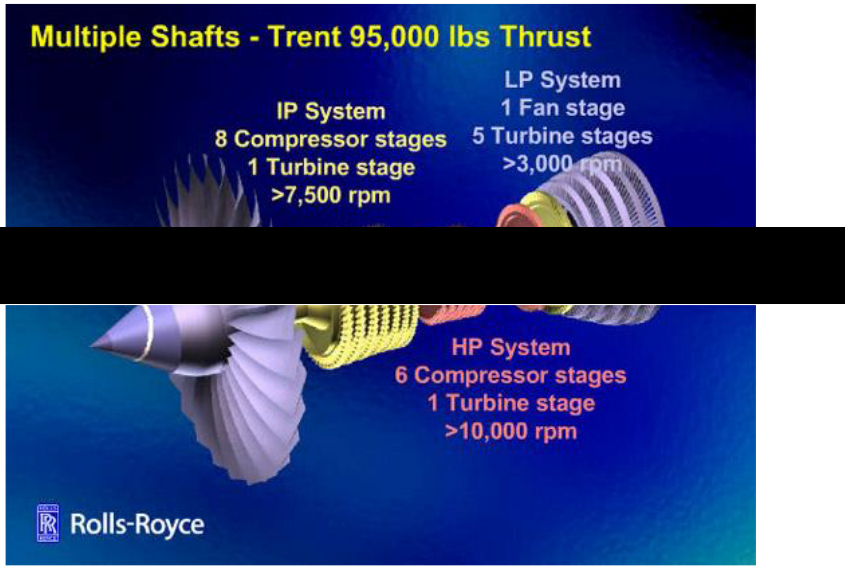

Figure 2 – Trent engines three shaft design [12].

The three shaft design maximises engine efficiency by splitting the engine into three sections: the high pressure system, intermediate pressure system and low pressure system. Doing this allows the three sections of the engine to rotate independently, therefore allowing each set of turbines to spin at their optimum RPM.

The air enters the engine via a large fan spinning at ~3,000 RPM, which is driven by the low pressure (LP) turbine at the back of the engine. This acts to further reduce the jet velocity, while increasing the mass air flow. The large fan blades only increase the speed of the air flow slightly more than the entry speed but make up for the required momentum change by the large mass of air being moved.

Most of the air passing through the fan will bypass the rest of the engine by flowing around it, in bypass ducts. Some of the air will be passed into the engine to be further compressed by the intermediate pressure (IP) system, which rotates at ~ 7,500 RPM. As the air passes through the IP system it is subject to 8 compressor stages. This increases the pressure and temperature of the of the air flowing through the engine, while maintaining axial velocity and increasing circumferential velocity via carefully designed rotating compressor blades and stators. As the air passes through the stages in the compressor the compressor blades gradually decrease in size. As a result, the smaller compressor blades must rotate faster in order to compress the air efficiently. This is the reason for the compressor being split in to two sections.

The air then passes through the high pressure (HP) system that rotates at ~ 10,000 RPM. At this stage the air is further compressed, and temperatures can reach up to 700°C. The fully pressurised air then flows into the combustion chamber. The fuel must be added to the pressurised air inside a flame tube in order to create a stoichiometric fuel mixture. The flame tube does this by allowing the temperamental flame to be shielded from the fast-flowing pressurised air, in the same fashion you would shield a candle from the wind when trying to light it. The burning fuel in the combustion chamber raises the temperature of the air to 2100°C. This temperature is too hot for the nozzle guide vanes and the first turbine rotors, so the temperature is reduced by diluting the combustion chamber air in a secondary dilution zone before entry into the turbine section. The reason for such a large increase in temperature is that at any given flow velocity at any given pressure, a hot gas has more flow area than a cold gas, therefore it requires less pressure drop to create the same amount of work. In applied terms the heated air flowing out of the combustion chamber can drive the IP and HP turbines with a smaller pressure change than the pressure increase of the compressors they are driving. This leaves spare pressure to be used to drive the fan via the LP turbines. In other cases the work harnessed from this spare pressure can be used to drive power generators or propellers on ships etc [9], [13].

2.1.2 Operating Conditions & Material Selection

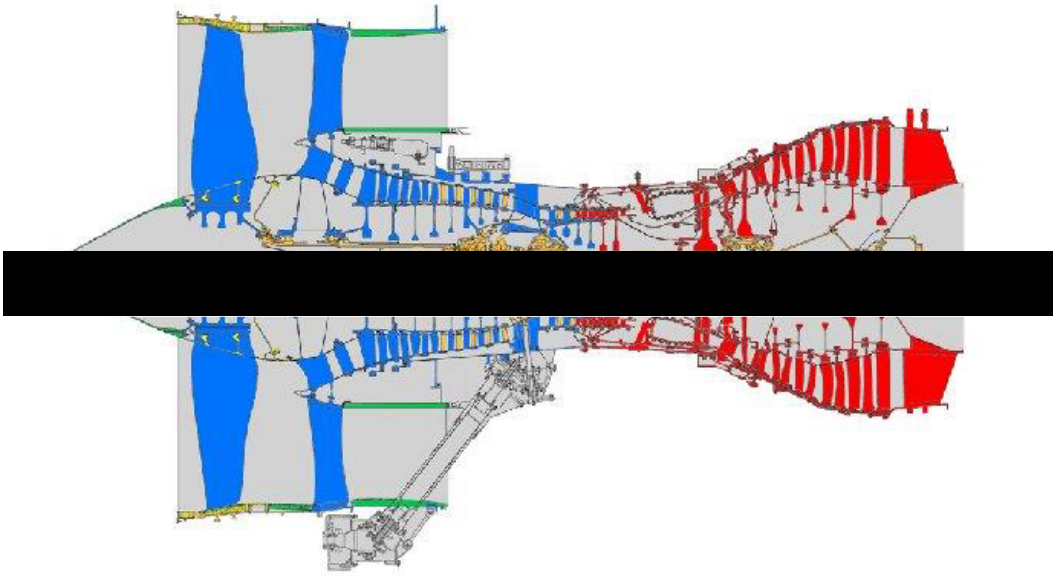

Figure 3 – Materials used in Rolls-Royce Trent Engines : Blue = Titanium alloys, Red = nickel-based superalloys and Orange = Steel Alloys. [14]

Figure 3 illustrates the materials selection throughout a typical three shaft design turbofan design, in this case the Rolls-Royce Trent family of engines (adapted from [14]). At the front of the engine the majority of the components are manufactured from titanium, utilising its high strength to weight ratio, as well as its unparalleled resistance to low and high cycle fatigue, produced by the rotation and vibration of the fan blades, respectively.

Some manufacturers have begun to replace the large titanium fan blades at the front of the engine with carbon fibre reinforced polymers in a bid to further reduce weight. This is possible as temperature is not a problem in this area of the engine and strength to weight ratio is more of a driving factor. Moving deeper into the engine the operating temperatures rise dramatically. This has resulted in the titanium alloys being replaced by Nickel based superalloys when operating temperatures exceed approximately 570°C, due to their great strength and corrosion resistance at elevated temperatures.

Powder processed polycrystalline nickel alloys are usually used for gas turbine disks due to their good ductility, toughness and defect tolerance. Nickel superalloy development for gas turbine blade applications has mainly focused around the removal of grain boundaries to aid creep resistance. This was first accomplished by the introduction of directionally solidified alloys, which removed grain boundaries

perpendicular to the loading axis. This technique then developed further, with the creation of single crystal alloys that contained no grain boundaries. The lack of grain boundaries meant that grain boundary strengthening elements such as boron and carbon could be removed, allowing better heat treatments to be applied to remove micro-segregation producing better fatigue life [13], [15].

2.1.3 High Temperature Disk Alloys

Disk components within a gas turbine engine are regarded as critical components. This is due to the high kinetic energy they possess while the engine is running. It is because of this kinetic energy, that if a disk were to fail then it would not be able to be contained and would exit the engine and potentially collide with the fuselage of the aircraft. Nickel superalloys have been the alloy of choice for disks running at temperatures up to 700°C for many reasons. Nickel superalloys can retain their strength at elevated temperatures, have good ductility, toughness and defect tolerance, as well as excellent resistance to fatigue crack initiation and growth. This makes nickel superalloys well suited to disk applications. But by far the best trait that makes them perfect for use as a disk material is their outstanding resistance to creep strain and stress rupture. This property helps prevent the catastrophic failure of a disk in flight [15], [16].

2.2 Nickel Superalloys & Development

The superalloys are a group of engineering materials consisting of iron-nickel, nickel and cobalt base, whose primary use is in conditions where strength is required above 540°C. Superalloys originally stemmed from stainless steel technology in attempt to increase the operating temperature of existing stainless steels. Of the three types, nickel superalloys have the ability to be used to a higher fraction of their melting point compared to almost any other commercially available material, with the exception of some refractory metals which do not possess the same mechanical properties limiting their use as a structural material. Nickel superalloys are utilised over a range of operating temperatures, with wrought and powder metallurgy nickel alloys being used to about 700°C and cast alloys being used at higher temperatures [15].

2.2.1 Alloying Elements

The base for all nickel-based superalloys is the gamma matrix phase consisting of nickel atoms arranged in a face centred cubic (FCC) crystal structure known as the gamma phase (γ). This FCC structure gives the gamma phase its toughness and ductility. The gamma matrix retains its FCC structure right through to its melting temperature, unlike iron and cobalt based alloy systems which undergo phase changes altering their crystal structure causing volumetric changes[17].

Alloying elements are added to the gamma matrix to enhance the mechanical properties and corrosion resistance. In chemical terms nickel superalloys are among the most complicated structural alloys in existence and can contain in the region of ten additional alloying elements, each adding a unique property to the alloy. A lot of elements added to nickel super alloys are from the d-block of transition metals such as Chromium (Cr), Cobalt (Co), Molybdenum (Mo) , Titanium (Ti), Hafnium (Hf), Iron (Fe), Ruthenium (Ru), Rhenium (Re), Tungsten (W), Niobium (Nb) and Tantalum (Ta) and Zirconium (Zr), although some p-block elements are also added such as Aluminium (Al), Boron (B) and Carbon (C). The location these alloying additions partition too is largely dictated by their position on the periodic table. Co, Fe, Cr, Ru, Mo, Re and W partition to the gamma nickel phase and act to stabilise and strengthen it through substitutional solid solution strengthening, whereas Al, Ti, Nb and Ta promote the formation of ordered phases such as γ’ due to their larger atomic radii. B,

C and Zr tend to segregate to the grain boundaries and can promote the formation of carbides and borides, as their atomic sizes are vastly different to that of nickel. Cr and Al also contribute to corrosion and oxidation resistance by forming protective oxides Cr_2O_3 and Al_2O_3, respectively, on the surface. These oxide layers help prevent further oxidative damage to the substrate material by forming a slow growing scale. Strong carbide formers include Cr, Mo, W, Nb, Ta and Ti due to their high affinity to carbon. These carbides are usually of the formation MC and are formed from the liquid on solidification, although solid state transitions can occur resulting in the formation of $M_{23}C_6$, M_6C and M_7C_3 carbides. Cr and Mo also advocate the formation of borides[18]–[20].

2.2.2 Nickel Superalloy Phases

The bulk of a nickel superalloy is made up of the γ phase which consists of mostly nickel atoms arranged in an FCC A1 crystal structure (Figure 4 adapted from [16]). Any alloying elements added will either be distributed in solid solution or will result in the precipitation of second phases with the most common being γ'.

γ' is a precipitate phase with an ordered $L1_2$ FCC crystal structure. The most prevalent γ' composition is Ni_3Al (Figure 4), here the nickel atoms at each corner of the FCC unit cell are substituted for aluminium atoms, this cell is then repeated thought the γ' phase in an ordered fashion.

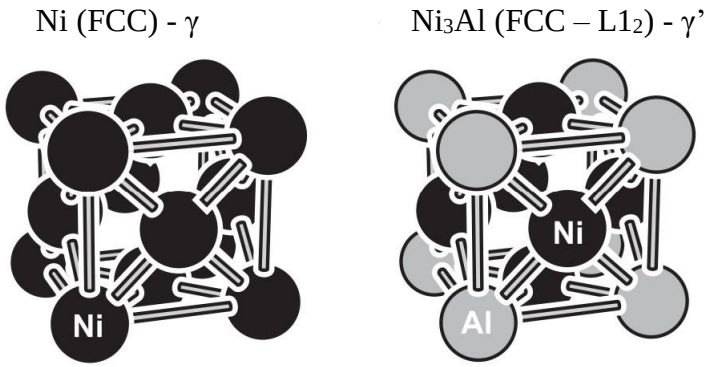

Figure 4 - Schematic diagram of the FCC A1 Ni crystal structure in the γ matrix and the ordered $L1_2$ FCC Ni_3Al crystal structure in the γ' precipitates. Adapted from [16]

Other γ' forming elements such as Ta and Ti can be readily substituted for aluminium throughout the γ' phase[17]. In the case of RR1000, the γ' precipitates contain significant quantities of Ti. The addition of too much Chromium, molybdenum and

tungsten can promote the formation of intermetallic topologically close packed phases (TCP) which can be detrimental to mechanical properties by depleting strengthening elements from the γ matrix and can act as sites for crack initiation [19], [21]–[23]. Many polycrystalline superalloys also contain FCC carbides such as MC, $M_{23}C_6$, and M_6C, where the M is a metal atom usually Cr, Mo, Ti, Ta or Hf. The carbides commonly reside on grain boundaries and can offer strengthening effects by disrupting grain boundary slip[15].

2.2.3 Strengthening Mechanisms

There are many microstructural characteristics that contribute to the high temperature strength capability of nickel superalloys, ranging from grain boundary strengthening mechanisms to complicated dislocation behaviours, induced by the presence of second phase precipitates. Each of these mechanisms provides strength in a different way and shall be described briefly here.

2.2.3.1 Grain boundary strengthening

Critical grain boundaries

The mechanical strength of any metal is partly governed by the structure of the grains within it. Polycrystalline metals are made up of multiple discrete regions known as grains. Each grain has a particular orientation of its crystal lattice structure. The interface between the grains is known as a grain boundary as the miss match in crystallographic orientation prevents them from coalescing. If a dislocation is propagating through one of these grains and meets a grain boundary it will be forced to change its direction in order to propagate into the neighbouring grain, due to its different crystallographic orientation. It is very energy intensive for a dislocation to change its direction which results in the dislocation being halted at the grain boundary, with any dislocations following it piling up behind it. It is this dislocation pile up that makes the propagation of other dislocations more difficult, ultimately providing the strengthening effect. The Hall-Petch relationship states that the strength in polycrystalline materials will increase with decreasing grain size until approximately 20-30nm due to the dislocation density increasing as grain size decreases [24]. This relationship is illustrated in Figure 5.

$$\sigma_{Y.S.} \propto \frac{1}{\sqrt{d}}$$

Figure 5 – Hall-Petch relationship illustrating the relationship between yield stress ($\sigma_{Y.S.}$) and grain size (d).

Although decreasing grain size increases tensile strength and low cycle fatigue properties it has the opposite effect on creep properties and dwell crack growth. This is because the introduction of more grain boundaries increases the number of sites for grain boundary sliding and triple point cracking. As a result, the grain size of superalloys needs to be carefully chosen depending on what type of loading they will experience during service[25].

It is because of this relationship between grain size and physical properties that the two variants of RR1000 exist. During the manufacture of RR1000 compressor disks, a complex heat treatment process is applied to create a dual microstructure. In so doing, the RR1000 disks can have a fine grain size at the bore giving improved strength and fatigue properties, while the rim of the disk has a coarse grain size for improved creep and dwell crack growth properties[26].

Special grain boundaries - Σ3 twin grain boundaries

Heating some strained materials can lead to a type of deformation known as annealing twinning. This deformation mechanism is common in FCC material such as nickel superalloys. Twinning involves the distortion of the crystal lattice to accommodate strain, in doing so creates a coherent 60° grain boundary which can span the length of the entire grain. These 60° boundaries are classed as Σ3 twin boundaries and can offer improvements in mechanical properties such as creep resistance and also corrosion resistance which combine to benefit stress corrosion cracking resistance[27].

It is beneficial to have as high a fraction of Σ3 twin boundaries as possible as they have been shown to cause dislocation pile ups and act as an obstacle to dislocation movement[28].

Σ3 twin boundaries are also more favourable over ordinary grain boundaries due to their coherency with the neighbouring grains, leading to a lower grain boundary energy state. This lower energy state is due to fewer vacancies and defects, which also leads to more sluggish diffusion and mass transport, giving rise to the corrosion resistance benefits[29], [30].

RR1000 contains a significant fraction of Σ3 twin grain boundaries as a result of the processing it undergoes during manufacturing. M. Detrois et al [26], have shown that RR1000 responds well to grain boundary engineering, resulting in an increase in Σ3 boundaries. During their study the specimens were heated to an annealing temperature of 1115°C following the application of the compressive strain. The heating rate used

in this study was very moderate at 0.6°Cs^{-1}, a much lower heating rate than is used in the creation of semi-solid RR1000 microstructures in the present study.

2.2.3.2 Solid Solution Strengthening

Early nickel base super alloys utilised solid solution strengthening in order to retain their strength at temperature; the first Inconel and Nimonic alloys are examples of these. There are two types of solid solution strengthening. The first occurs if the alloying element is of a similar size to Ni and can replace a Ni atom in the lattice of the γ matrix; this is known as substitutional solid solution strengthening.

In nickel alloys, substitutional solid solution strengthening, can happen over a wide range of compositions if the alloying element is of a good fit with the γ matrix. An example of this is chromium that can remain in solid solution at room temperature even at 30wt.%. In the case that the lattice parameter of the alloying element differs from nickel by more than 15% the solid solution solubility is less than 1%. If the atomic radius of the alloying elements is drastically smaller than that of Ni, then a second form of solid solution strengthening occurs where the solute atoms diffuse into interstitial locations in the lattice of the γ matrix, hence named interstitial solid solution strengthening.

Elements that commonly do this in the Ni γ matrix are C, O, H, and B. The solute elements provide strength to the γ matrix by disrupting the movement of dislocations in different ways. An example of this is the elastic effect of having a solute atom in the γ matrix. A difference in atomic radius between solute atoms and the Ni, in the γ matrix, causes an elastic stress field in the lattice surrounding it, this stress field means that any dislocations moving through this stress field will need more energy input to do so, this strengthening effect is directly proportional to the difference in atomic size[15], [17], [31] .

2.2.3.3 Stacking Faults

Stacking faults in FCC materials are associated with dislocations on the (111)[110] type slip system. In materials with a low stacking fault energy it becomes more favourable for a dislocation to split into two partial dislocations with a stacking fault between them. This means that, between the two partial dislocations, the lattice no longer has an FCC structure but is now more like a hexagonal close packed (HCP) lattice. The presence of these stacking fault regions reduces the mobility of dislocations and increases the amount of stress needed for dislocation cross slip thus providing a strengthening effect.

Alloying additions can also reduce the energy needed to create stacking faults in the γ matrix and can be attracted to the stacking fault increasing its distance[16], [32].

2.2.3.4 γ' Second Phase Strengthening

The greatest advance in nickel superalloys properties followed the addition of 2-3% aluminium and titanium. Adding these elements in sufficient quantities promotes the formation of a second phase precipitate known as γ'. γ' precipitates are an FCC $L1_2$ structured superlattice which displays long range order up to its melting point. Long range order means that the γ' crystal lattice has a repeating structure in the general form A_3B where A is a relatively electronegative element in this case Ni and B is a relatively electropositive element like Al, Ti and Nb. The γ' precipitates found in RR1000 are a mixture of Al and Ti. It's this difference in electronegatively that creates the long-range order of alternating A and B atoms [17].

This difference in electronegativity of the γ' forming elements also gives rise to one of the main strengthening effects that γ' provides, namely, the anti-phase boundary. When the γ' precipitate is in its ordered state, all of the Ni and Al atoms are aligned opposite one and other in a repeating fashion. If a dislocation is introduced to the γ' precipitate, it will disrupt this long-range order resulting in a series of alternating Ni-Ni and Al-Al bonds that are energetically unfavourable. If a dislocation was to propagate throughout the length of a γ' precipitate in this way it would require a significant amount of energy. Because of this, dislocations split into two partial dislocations which reduces the energy needed for propagation. The first partial dislocation enters the γ' precipitate creating the miss match of Ni-Ni and Al-Al bonds, then a second partial dislocation is created and follows behind the first undoing the miss match it is creating. The disordered lattice created between these two partial dislocations is known as the antiphase boundary. It is the energy needed in the creation of this antiphase boundary that contributes to the strengthening effect of γ' in nickel superalloys, as without the creation of an antiphase boundary cutting of γ' precipitates cannot occur[17], [33].

γ' size effects.

The size of the γ' precipitates has a significant effect on how they interact with dislocations and therefore, has an impact on the strength they can provide. The size of γ' precipitates is controlled through a heat treatment process called aging where a superalloy is held at an aging temperature to promote the growth of certain γ' precipitates. Before the aging heat treatment can be applied the alloy must first be slowly heated to a solution heat treatment temperature, this is a temperature where all of the γ' precipitates diffuse into the γ matrix to create a supersaturated solid solution γ matrix. The alloy is then cooled to a lower temperature known as the aging temperature, it is here where the supersaturated γ matrix can no longer contain the γ' forming elements in solid solution and therefore precipitates out these elements as γ' precipitates. The longer the alloy is held at the aging temperature the greater in size the γ' precipitates grow[34], [35].

The size of γ' precipitates influences the coherency they have with the γ matrix. If a γ' precipitate is small, then it is very coherent with the γ matrix and any dislocations propagating through the γ matrix will have to cut through the γ' precipitate via the antiphase boundary mechanism. The stress needed for dislocations to cut through a γ' is directly proportional to the size of the precipitate. Increasing the precipitate size too much leads to another mechanism for dislocation movement, known as Orowan bowing, which requires less stress than precipitate cutting if the precipitate is large enough.

The stress required for dislocation bowing has been shown to decrease when particle size and spacing is increased. The combination of these two mechanisms means that there is an optimum size that the γ' precipitates can be aged to, in order to promote the highest stress requirement for dislocation movement for both mechanisms. It is for this reason that aging heat treatments need to be selected carefully, to produce the best strength benefits from precipitation of γ' in superalloys[36].

In the case of RR1000 the two variants are heat treated and aged differently to produce the desired microstructure. The FG variant is solution heat treated below the γ' solvus temperature of 1140°C, so that the primary γ' particles are not removed. Doing this means that the grain boundaries are still pinned by the incoherent intergranular primary γ', preventing grain growth and retaining the fine grain size produced by the powder processing route.

After the FG variant has been subject to this sub γ' solvus solution heat treatment, it is then cooled to an aging temperature (760°C), which refines the secondary and tertiary γ' to a size that is optimal for mechanical strength.

The CG variant undergoes a different heat treatment regime with the aim of allowing the grains to grow. This improves creep properties by limiting the extent of damage accumulation and sliding of grain boundaries at prolonged temperature exposures. The CG variant is produced by solution heat treating as forged RR1000 material for 2 hours at 1170°C, followed by an aging heat treatment for 16 hours at 760°C. During the solution heat treatment all of the γ' precipitates diffuse into solid solution in the γ matrix. During this solution heat treatment, the loss of the pinning effect of primary γ' on the grain boundaries results in grain growth until the grains reach a size where they are stable and will grow no further. The CG variant is then cooled to the ageing temperature at a cooling rate below $1°Cs^{-1}$. This ageing heat treatment produces the bimodal distribution of secondary and tertiary γ' that is found in the CG variant that is optimal for mechanical strength[37], [38].

2.2.3.5 Yield Stress Anomaly

In superalloys that possess high volumes of γ' the high temperature strength can be mostly attributed to the strength of the γ' precipitates. This high temperature strength is a result of a yield strength anomaly where the γ' precipitates actually increase in strength when temperature is increased up to about 700°C. This increase in strength is due to a dislocation phenomenon known as Kear-Wilsdorf locking.

γ' precipitates have an $L1_2$ ordered structure with a slip plane on the {111} plane. For dislocations to propagate through γ' on this slip plane, they must become two partial dislocations and form an antiphase boundary between them, as discussed earlier. As temperature is increased cross slip of these partial dislocations onto the {100} becomes more energetically favourable, but in doing so the partial dislocations become locked and are rendered immobile. It is this immobilisation of dislocations that creates the anomalous yield effect, as more cross slip of dislocations becomes favourable with increasing temperature therefore increasing the occurrence of the Kear-Wilsdorf locking phenomena. It is because of this high temperature strength of γ' that high volume fractions are sought after in the development of nickel superalloys [16].

2.3 Processing of Nickel Alloys for Turbine disk applications.

Superalloy components for disk applications are produced via three processing methods; casting, wrought processing and powder metallurgy. Initially casting was the only way to produce near net shape components, with minimal after machining, but advances in forging methods has resulted in near net shape components being produced via wrought processes.

Wrought alloys are essentially a cast billet that has undergone a series of heat treatments and forging procedures, in order to manipulate the microstructure to produce the desired materials properties. Wrought alloys produce a more homogenous alloy than cast alloys, as the solidification process during casting can cause elemental segregation. If the complexity of the nickel super alloys constituents is further increased, then traditional cast and wrought methods will no longer be sufficient as highly alloyed super alloys have the tendency to crack during the post casting hot working procedures due to their high flow stress.

This susceptibility to cracking and the elemental segregation during casting led to the development of a more advanced manufacturing method, known as powder processing. Ultimately the manufacturing route is governed by the complexity of the nickel super alloys composition[17].

2.3.1 Wrought & Cast Alloys

The first step in producing any nickel super alloy is vacuum induction melting (VIM). During VIM, the raw metallic ingredients required to produce your desired composition are placed in a crucible within a vacuum chamber. The metallic ingredients are then heated via induction heating until they reach melting point, where adjustments to the chemical composition of the melt can be made if needed. The melt is then decanted into a mould in an inert argon atmosphere. The VIM process reduces interstitial gasses to low levels which allows the use of higher quantities of relatively reactive elements such as Al and Ti, while reducing slag contamination in the final product. Nickel superalloys that are commonly cast in this way are Waspaloy, René 100 and IN718.

If an alloy is intended to be subject to wrought processing, then a secondary melting phase is usually added. This secondary melting is often carried out by vacuum arc re-melting (VAR). The purpose of secondary melting is so that the solidification structure

can be more accurately controlled in order to reduce the formation of solute rich defects which can be detrimental to mechanical properties. Before the wrought processing can be carried out, the ingot produced in the VAR process must be heat treated to homogenise any elemental microscale segregation. A series of hot forging processes can then be applied to the homogenised billet to induce recrystallisation in order to refine the grain size. Nimonic 90 and Inconel 625 are examples of wrought processed nickel super alloys. The need for superalloys with better high temperature strength has led to their compositions becoming very complicated and the volume fractions of strengthening phases such as γ' to be increased. In doing this the susceptibility of cracking during the wrought forging procedures has risen with the high temperature strength. As a result, the need for a more advanced superalloy production method led to the development of superalloys manufactured via powder metallurgy processing [39].

2.3.2 Powder Processed Alloys

Powder processed alloys are mostly used as high strength alloys for gas turbine disk applications where high temperature strength is paramount. Powder processing is usually used when an alloys composition is too complicated to manufacture through casting or if it is too difficult to apply wrought forging techniques because of the high temperature strength of the alloy. There are several steps to the powder processing technique as can be seen in the schematic diagram in Figure 6 adapted from [40].

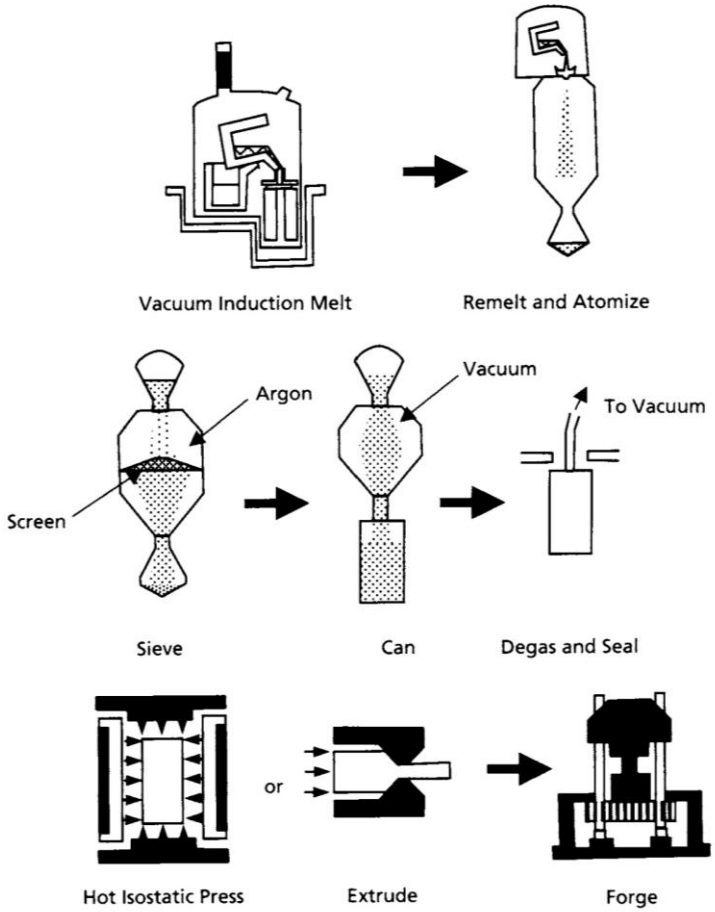

Figure 6 - Schematic diagram of the powder metallurgy process for manufacturing gas turbine disks. Adapted from [40]

Firstly, the desired alloying elements are melted via vacuum induction melting (VIM) to produce liquid metal with the composition of the final alloy. The liquid metal is then fed into a stream of argon gas to atomise the liquid into small particles, each of which has the same composition as the melt and the final alloy. The powdered alloy is then screened to remove any irregular sized particles. Following screening the powder is blended to create a uniform particle distribution which will allow good packing factors

during consolidation. The blended powder is then placed into a container usually made of stainless steel. The container is then outgassed while at a slightly elevated temperature to remove any air or adsorbed water from the powder mixture, then the container is sealed. The degassed powder sealed in the container is now ready for consolidation, this is usually accomplished via hot isostatic pressing (HIP). The HIP process can produce near net shape products that only need machining or produce a billet suitable for subsequent hot working. IN100 and Astroloy are alloys that are produced via powder metallurgy [39].

The alloy RR1000 being investigated in this study is also produced via this method. A post-HIP extrusion operation is performed to break up previous particle boundaries that arise from oxide films on the surfaces of the particles. The extrusion operation of RR1000 creates a fine grain size of <4μm, which aids the next step of its manufacture. The final mechanical stage of RR1000's manufacture is slow strain rate isothermal forging conducted below the γ' solvus temperature. The exact forging temperature is sensitive information as the intellectual property is partly owned by the forging companies, but it can be stated that the forging temperature would likely be 20-100°C below the γ' solvus temperature (γ' solvus ~1140°C in RR1000). This temperature range is supported by research conducted by I. Parr et al [38] who replicated RR1000's isothermal forging process at 1099°C. During this process sections of the extruded RR1000 billets are forged in molybdenum alloy dies, which are heated to the forging temperature to prevent temperature gradients. The isothermal forging is conducted in an inert atmosphere using slow strain rates, which results in superplastic flow. This forging operation produces the near net shape needed for the manufacture of RR1000 gas turbine disks. The forgings are then subject to a range of heat treatments to produce the desired microstructure. The microstructures of both FG and CG RR1000 have been characterised and discussed in detail in section 3.1.

2.4 Joining of nickel superalloys

Nickel superalloys can make up to 40% of the weight of a gas turbine engine, therefore their overuse can have a severe impact on the fuel efficiency of the engine [41]. In order to minimise the quantity of nickel super alloy components in a gas turbine engine, advanced joining techniques are used to remove the need for fastening components which would add more unnecessary weight.

The complicated composition of nickel super alloys brings with it challenges associated with weldability, with elemental segregation upon liquation and heat affected zone (HAZ) cracking being commonplace[42], [43].

RR1000's chemistry is very complicated and as a result conventional welding methods, such as tungsten inert gas (TIG) welding, are not appropriate, due to the large weld pools it requires, which would cause mass elemental segregation[44]. Even more advanced welding methods such as electron beam melting (EBM) and laser beam welding (LBW) are not appropriate with the requirement of a weld pool and large heat affected zones again leading to elemental segregation and HAZ cracking[45]–[49]. The HAZ cracking experienced in alloys with poor weldability is usually the result of intergranular liquid films that are created by sub-solidus liquation mechanisms. These mechanisms include, liquation of low melting point phases and eutectic products and constitutional liquation of second phase precipitates, both of which will be described in detail later [50], [51].

2.4.1 Friction Welding

The favoured joining technique for alloys that exhibit poor weldability is friction welding as it is nominally a solid-state process and does not require the formation of a large melt pool during welding, although the conditions experienced at the weld interface are such that liquation could occur with some alloys. The most common form of friction welding is rotary friction welding. Figure 7 illustrates the rotary friction process adapted from [52].

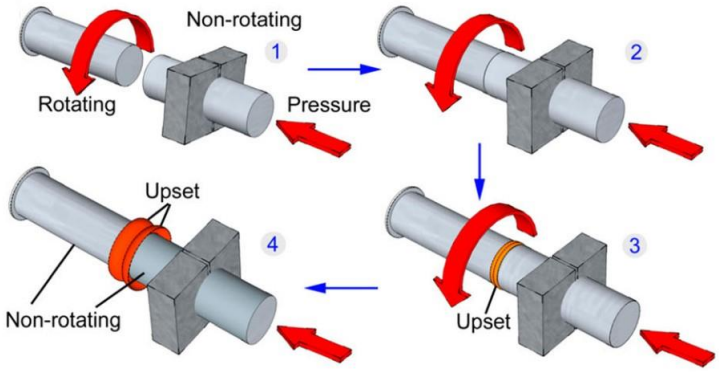

Figure 7 - A schematic diagram outlining the steps of a rotary friction welding process adapted from [52].

During rotary friction welding one part is held stationary (the fixture) while the other is rotated (the spindle). The two parts are then brought together under a set welding pressure and the kinetic energy in the rotating part is converted into heat energy via friction between the two parts. The resultant heating rates from this friction are very rapid with peak temperatures reaching up to 1300°C at the weld interface. Strain rates at the weld interface are also very high with some material being deformed at $1000s^{-1}$[1].

There are two types of rotary friction welding: continuous drive friction welding (CDFW) and inertia friction welding (IFW). The kinetic energy in CDFW is provided via a motor rotating the spindle part and allows a constant rotation speed to be achieved throughout the whole welding process. IFW involves the use of a flywheel which is attached to the spindle part and spun up to a desired rotational speed to provide a chosen inertia. The fixture part is then driven into the rotating spindle part until the speed of the flywheel progressively decreases to zero as the weld consolidates [52].

Friction welding offers some distinct advantages over conventional welding methods which make it a very attractive joining process. Some of these advantages are:

- Friction welding does not involve large melt pools which bring with them inherent solidification problems such as hot cracking, elemental segregation and porosity due to shrinkage during cooling[2].
- The intensity of the deformation and temperature during a friction weld, usually results in a fully recrystalised microstructure at the weld line, in which the smaller grain size results in an increase in strength over the base material due to the Hall-Petch relationship[53].
- No shielding is required via inert gas or vacuum during welding[54].
- Friction welds are a relatively quick method of producing high integrity welds with narrow weld lines and heat affected zones.

During a friction weld the microstructure of the material being welded undergoes several changes due to the extreme heating and plastic deformation involved. These microstructural changes include grain size changes due to recrystallisation and grain growth and solid-state transformations such as the dissolution and reprecipitation of second phase precipitates. The combination of all these phenomena, occurring in such a short time during friction welds, means that friction weld microstructural evolution is very complex and is not fully understood, especially in alloys with intricate compositions, such as the alloy used in this study RR1000 [54].

2.4.2 Microstructure of inertia friction welded RR1000

The alloy studied in this project, RR1000, is routinely welded via IFW in its fine grain variant. RR1000 disks are joined together during the manufacture of high-pressure compressor components for gas turbine engines. The coarse grain variant has also been welded for research purposes but is not currently welded during the manufacture of gas turbine engines.

As mentioned, the complexity of RR1000's microstructure has meant that the dynamic evolution of the microstructure during welding is complicated and not fully understood. Although, the resultant microstructure and mechanical properties of inertia friction welded RR1000 has been documented well and is as follows.

All friction welds consist of three distinct regions, the weld line (WL), the thermo-mechanically affected zone (TMAZ) and the HAZ, this is no different for RR1000. The microstructural changes across these regions in an RR1000 friction weld are dramatic. The weld line zone is approximately 200μm in width for fine grain welds and approximately 600μm in width for coarse grain welds[55].

The weld line zone in both variants is completely denuded of primary and secondary γ' with only reprecipitated tertiary gamma prime present. This is common among nickel superalloys with high volume fractions of γ' where the wt. % of γ' forming elements Al and Ti are enough to cause a strong driving force for reprecipitation even when under rapid cooling[56]. The result of this very fine reprecipitated gamma prime is an increase in strength due to the strengthening effect of increased volume fraction of tertiary γ'[57].

Other nickel super alloys containing lower volume fractions of γ', such as Waspaloy, can widen the lattice parameters of the γ matrix phase enough to retain the Al and Ti in solid solution during cooling to room temperature[58]. The grains at the weld line zone of both fine grain and coarse grain RR1000 welds are fully recrystallised and range in size from 7.1μm to 7.6μm therefore similar in size to the parent fine grain variant of RR1000. Although the recrystallised grains were similar in size to the parent fine grain material the grain boundaries in the weld lines were found to be straight and smooth whereas both variants of parent material feature serrated grain boundaries resultant from slow cooling during forging [55].

Z.W Huang et al [55] also performed a dissimilar IFW of the FG RR1000 variant to the CG variant. The welded part was sectioned and prepped for Vickers hardness testing. A second section of the weld was subject to a standard post weld heat treatment. The results of the hardness maps are illustrated in Figure 8 adapted from [55].

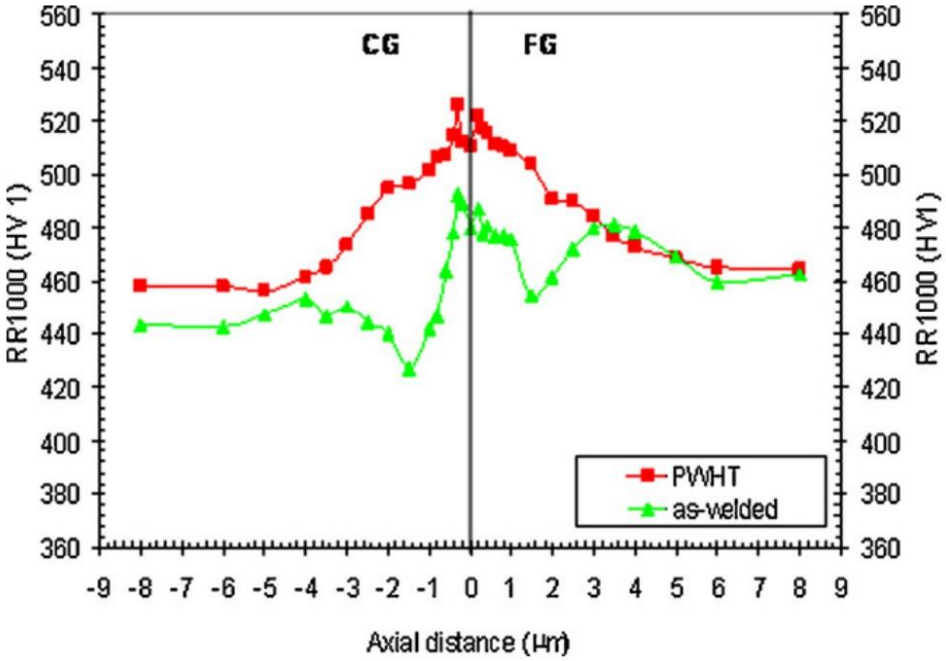

Figure 8 - Microhardness profile of a dissimilar IFW of FG & CG RR1000 before and after post weld heat treatment. Adapted from [55].

Both the as welded specimen and the post weld heat treated specimen experienced a peak in hardness at the weld line. This hardness peak is the result of the reprecipitation of the fine γ' during cooling, as the bi-modal and tri-modal distribution of γ' in the parent CG and FG variants respectively has now been redistributed as a unimodal tertiary γ'. Research conducted by Torster et al [57] on the nickel superalloy U 720 LI has shown that increasing the volume fraction of fine γ' precipitates via increasing cooling rates from a solution heat treatment results in increased yield stress. Therefore, an increase in hardness would also be expected. The slightly lower hardness in the CG side of the as welded specimen was attributed to the parent CG alloy being slightly softer than the FG due to its grain size. Both variants also exhibited a drop in hardness either side of the weld line, in the as welded condition, with the CG experiencing a larger trough than the FG, although no explanation was given for this.

During the present research project the microstructural evolution of both RR1000 variants, when subject to rapid heating rates, was characterised. The results of this assessment gave an insight into the potential causes of the disparity in hardness drop between the two variants, which was reported by Z. W. Huang et al [55].

2.5 Liquation sources during welding

During most welding techniques liquation is expected at the weld interface/weld pool in order to join the two materials. Liquation is rarely constrained to this region and often partial liquation also occurs in the heat affected zone (HAZ) as a result of the rapid heating rates experienced. It is this partial liquation, of regions near the weld, that can cause problems with cracking on cooling and therefore it has been an area of interest in research[51].

As the heating rates experienced in IFW of RR1000 are similar to what would be experienced in the HAZ of traditional welding techniques the liquation mechanisms experienced are likely to be similar. HAZ cracking has been investigated for many years and has been given many different names such as: liquation cracking [59], edge of weld cracking [60] and hot cracking [61]. During this study this form of cracking has been referred to as HAZ cracking.

There can be many causes for HAZ cracking, but the majority can be linked to sub-solidus liquation mechanisms creating intergranular liquid films. It is these liquid films and their inability to withstand thermally or mechanically induced stresses produced by cooling that results in HAZ cracking. [62] As the conditions experienced in the HAZ of any weld are similar to that experienced at the weld line during IFW, the liquation mechanisms that cause HAZ cracking have been investigated as potential sources of liquation during IFW.

The two main mechanisms for sub-solidus liquation are the constitutional liquation of second phase particles such as carbides, sulphides and borides; in each case the particle in question reaches its eutectic melting temperature below the matrix solidus temperature resulting in pockets of liquation being distributed throughout the material. More recently in constitutional liquation of the γ’ phase in nickel superalloys has been reported as a result of rapid heating rates [63].

The second most common cause of HAZ cracking is due to the incipient melting of localised regions in a material, due to either the presence of a lower melting point phase such as Ni-Hf intermetallics or Laves phases but can also be due to chemical inhomogeneity caused by elemental segregation during manufacturing[64].

Both sources of HAZ liquation are likely to occur at the weld interface of an inertia friction weld due to the extreme temperature and heating rates experienced. Constitutional liquation of γ’ precipitates has been studied in detail, as this phenomenon has already been reported to occur in FG RR1000 by M. Attallah et al[4].

Incipient melting causes, applicable to RR1000's microstructure have also been studied. Both are detailed here.

2.5.1 Constitutional liquation

Constitutional liquation of second phase particles is a phenomenon that was first proposed by Pepe and Savage[50] in their study on the weld heat affected zone of a 18Ni maraging steel that had been gas tungsten arc welded. Their study proposed a new liquation mechanism whereby the titanium sulphide particles within the material, had constitutionally liquated during the rapid heating of welding. The constitutional liquation of these particles led to liquid film being produced on the grain boundaries, which resulted in grain boundary pinning limiting grain growth. Since their publication, their proposed method of constitutional liquation of second phase particles has been adapted to other alloy systems, in particular nickel super alloys and the constitutional liquation of MC type carbides as well as M_3B_2 Borides and M_2SC sulphocarbides[65]–[70].

A significant body of work has been conducted by O.A Ojo et al ([63], [71], [72].) on applying the concept of constitutional liquation to γ' precipitates in nickel super alloys. The bulk of their studies were conducted on Inconel 738LC. They initially investigated the resultant microstructures of TIG weldments, where they found the first signs of constitutional liquation. Further studies by the authors, confirmed the occurrence of constitutional liquation of γ' precipitates by conducting a series of heat treatments via a Gleeble thermomechanical simulator, with the aim of recreating the heating regime experienced during TIG welding. It was during this work that they proved that if γ' precipitates were heated fast enough, they could survive up to temperatures where they liquated via a eutectic type reaction with the surrounding γ matrix therefore proving the concept of constitutional liquation of γ' precipitates in nickel super alloys[63], [73].

Work conducted by P. Willemin et al[74] on the Ni-Al-Ti ternary system supports the idea of constitutional liquation of γ' in nickel super alloys. They proposed a projection that suggested that the γ- γ' eutectic reaction in nickel super alloy systems can happen over a range of temperatures. Therefore, if a γ' precipitate was to survive to this temperature it could liquate with the surrounding γ matrix via the eutectic reaction. F. Tancret [5], carried out a simplified simulation of constitutional liquation of γ' precipitates in nickel super alloys via the thermodynamic and multicomponent

diffusion software Thermo-Calc and Dictra. Their model used a Ni-9 wt.% Al alloy for simplicity and computing efficiency. Their model predicted that at high enough heating rates the γ' precipitates of sufficient size will not have enough time to diffuse into the γ matrix because of kinetic reasons and will liquate via a eutectic reaction with the surrounding gamma matrix, as described earlier as constitutional liquation. They also predicted that this effect is strongly dependent on initial precipitate size, meaning that larger particles are even more likely to survive to a temperature where they can constitutionally liquate.

The predictions of Tancret's model were in alignment with the experimental data produced by M. Soucail et al [75]during their experimentation with rapid heating rates on the powder metallurgy superalloy Astroloy. During this research they found the effective solvus temperature of γ' precipitates deviated from the equilibrium solvus temperature if a rapid heating rate was used. The rapid heating rates resulted in the effective solvus temperature of the γ' precipitates to be much higher than the equilibrium solvus temperature (Primary γ' experiencing a 125°C increase with $10°Cs^{-1}$ + heating rates). They also reported that the magnitude of the increase in effective solvus temperature was also dependent on initial precipitate size, with larger precipitates experiencing a larger increase in effective solvus temperature.

The combination of these findings suggests that it is highly likely that if a large enough γ' precipitate is heated at a sufficient rate it will survive to a temperature where it can constitutionally liquate with the surrounding gamma matrix.

The FG RR1000 variant has significantly large primary γ' precipitates (~1.7 μm) which undergo extremely fast heating during an IFW. This would imply that the FG variant is likely experiencing constitutional liquation of its primary γ' during an IFW welding cycle. Research conducted by M. Attallah et al [4], confirmed the likelihood of this, by using high temperature confocal laser scanning microscopy (HT-CLSM) to investigate the constitutional liquation of primary γ' precipitates in fine grain RR1000 when subject to weld like heating rates. The study involved heating the surface of fine grain RR1000 specimens to 1200-1300°C, at heating rates of $5°Cs^{-1}$ and $50°Cs^{-1}$. During their research, the authors provided microstructural evidence of the constitutional liquation of the primary γ' at both heating rates, when heating to above the γ' solvus temperature. The microstructural evidence included in situ observations of the constitutional liquation of the primary γ' from the HT-CLSM, as well as SEM micrographs illustrating the presence of dendritic γ- γ' eutectic structures within the

liquated regions. The authors noted that HT-CLSM surface observations are generally in alignment with the bulk material behaviour but also stated the importance of combining the simulations performed via HT-CLSM with other post cycling or ex-situ microstructural investigation. This is because HT-CLSM tests are performed on a free surface and therefore may alter the behaviour compared to heating a bulk specimen uniformly. Therefore, it was thought to be beneficial to build on this work by finding or creating a semi-solid testing facility capable of heating bulk RR1000 specimens at heating rates between 5 Cs^{-1} and 50°Cs^{-1}, while remaining free from temperature gradients. A testing facility with this capability could replicate the heating cycle of an IFW, while removing the concern of free surface effects. Being able to heat bulk RR1000 specimens in this fashion would also allow the quantification of liquid propagation through the bulk material and offer the opportunity to investigate the effect semi-solid microstructures have on the flow stress of RR1000. Because of this, an assessment of possible semi-solid testing methods was conducted, which is detailed later in section 2.6. This assessment led to a decision to design and commission a novel semi-solid testing facility for the present study.

The semi-solid testing facility designed and created in the present study required a capability of heating bulk RR1000 specimens at heating rates between 5 Cs^{-1} and 50°Cs^{-1}, to reproduce the constitutional liquation of primary γ' in the fine grain variant of RR1000, as observed by M. Attallah et al [4].

This newly developed semi-solid testing facility required numerous modifications and optimisation steps before it could reliably heat bulk RR1000 specimens at the required heating rate, while maintaining a temperature gradient free specimen.

Once this heating capability had been demonstrated, the semi-solid testing facility was used to heat FG RR1000 specimens at 25°Cs^{-1} to 1200°C. During these tests, the constitutional liquation of primary γ' in FG RR1000 observed by M. Attallah et al was replicated, deeming the novel semi-solid testing facility fit for purpose. Only then was it used to expand on this research, by investigating sub-solidus liquation mechanisms of coarse grain RR1000 and the liquid propagation rates in both variants.

2.5.2 Incipient melting

Incipient melting is defined as the liquation of localised areas due to a difference in chemical composition in comparison to the bulk material. This difference in composition can either be the presence of discrete lower melting point phases or inhomogeneous distribution of elements in the matrix phase due to elemental segregation during manufacturing.

Usually the regions susceptible to incipient melting are the last to solidify during the manufacturing process because they have the lowest melting point. This makes them at risk of re-melting during heat treatments or during the thermal stresses of welding[76], [77].

Incipient melting is a liquation mechanism that is seen in many different alloy systems and in particular, alloys that are commonly strengthened by a second phase precipitate. Examples in nickel based super alloys are; the melting of Laves phase in IN718 [78], incipient melting of Ni_7Hf_2 and Ni_5Hf intermetallic phases in as cast DS200 [79] and the melting of γ-γ' eutectic features in CM247 [80]. Incipient melting is also common in aluminium alloys mostly due to the incipient melting of eutectic compounds such as Al_2Cu and Al-Al_2Cu [81], [82].

Most of the research into incipient melting has focussed on the liquation of discrete phases on reaching their own melting point. However, the research conducted by F. Tancret [5] on constitutional liquation of γ' in nickel alloys during rapid heating also discovered a second liquation mechanism, which adheres to the definition of incipient melting. During their simulations of constitutional liquation of γ', their model had shown that even if the γ' precipitates did not survive to a temperature where they could constitutionally liquate during a rapid heating event, the rapid diffusion of the γ' forming elements into the surrounding γ matrix would cause a momentary drop in melting point. This is because Al and Ti are melting point depressants and the rapid heating rate results in a sudden change in composition and a lack of sufficient time for homogenisation of the γ' forming elements throughout the γ matrix. This results in a kind of incipient melting of the enriched γ matrix.

The secondary γ’ in the CG variant of RR1000 are likely to be too small to constitutionally liquate. But the sheer volume of secondary γ’ diffusing into the γ matrix during the heating cycle of an IFW could lead to liquation via this mechanism. Evidence to support this mechanisms occurrence in RR1000 was discovered in the present research and is given later in section 4, results and discussion.

2.5.3 Identifying liquated material in superalloys

Liquated material can be identified by the presence of differential etching. These differentially etched regions are caused by the re-solidification of solute rich liquid on cooling, after a liquation event. The differentially etched new regions appear contrasted from the original matrix, when viewed under optical microscopy and SEM. These differentially etched liquated regions were first reported in nickel superalloys by W.A Owczarski et al in their work on Udimet 700 [83]. Since then the presence of differentially etching liquid films has been reported in multiple nickel superalloys such as IN718 in the work of B.Radhakrlshnan et al [84], and in Incoloy 903 in work conducted by R. Nakkalil et al [85].

More recently, in work carried out by A.P.I Popoolaa et al, differentially etching liquid films have been used to identify liquation during rapid heating of Astroloy, a nickel super alloy with a very similar microstructure to that of FG RR1000. Here they also reported the occurrence of constitutional liquation of primary γ' precipitates. [86]

Another way of identifying liquation is the presence of distinct solidification products that reside in the differentially etched regions. The size and morphologies of these solidification products can vary, but usually in superalloys they will contain some form of eutectic structure and/or intermetallic features. These eutectic features are common in cast nickel superalloys therefore it is not surprising to find them in powder metallurgy nickel superalloys that have experienced a liquation event.

During the solidification of liquated material in a nickel based super alloy, the γ matrix phase is the first to solidify and is usually enriched in Cr, Co and Mo as these elements partition to the γ phase. The solidification of this γ phase leaves the remaining liquid enriched in γ' forming elements, Al, Ti and Ta. The enriched liquid then solidifies last firstly forming γ-γ' eutectic features then occasionally Ni based intermetallics depending on the composition of the alloy [77]. Examples of these solidification products are the lamella γ-γ' found in the HAZ of tungsten arc welded Inconel 738 found by O.A Ojo et al as shown in Figure 9 [63].

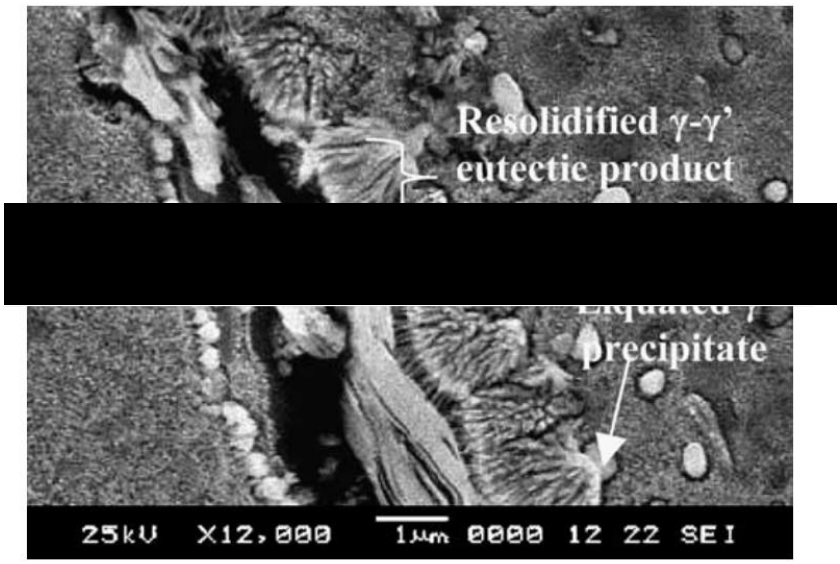

Figure 9 - Eutectic found in the HAZ of tungsten arc welded Inconel 738 found by O.A. Ojo et al [63].

Examples of alloys that have exhibited both γ-γ' eutectics and Ni rich intermetallics are: Tungsten arc welded Mar-M004 in research conducted by Y. Cheng et al illustrated in Figure 10. [87]

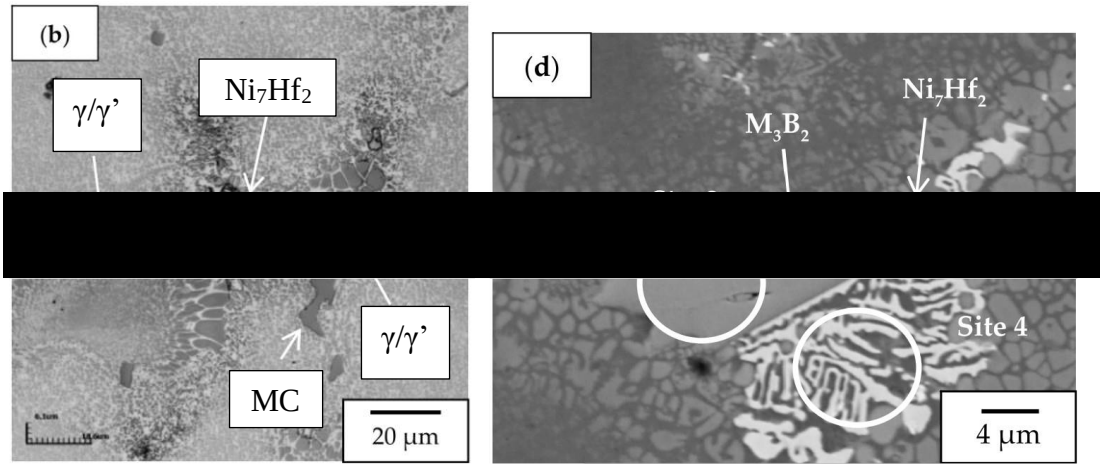

Figure 10 - Examples of solidification products containing eutectics and Ni-Hf intermetallics found by Y. Cheng et al [87].

Similar solidification products were found by V. Ming during their study on solution heat treatments on MarM-002, where they witnessed pockets of liquated material caused by incipient melting. SEM micrographs of their findings are illustrated in Figure 11 [88].

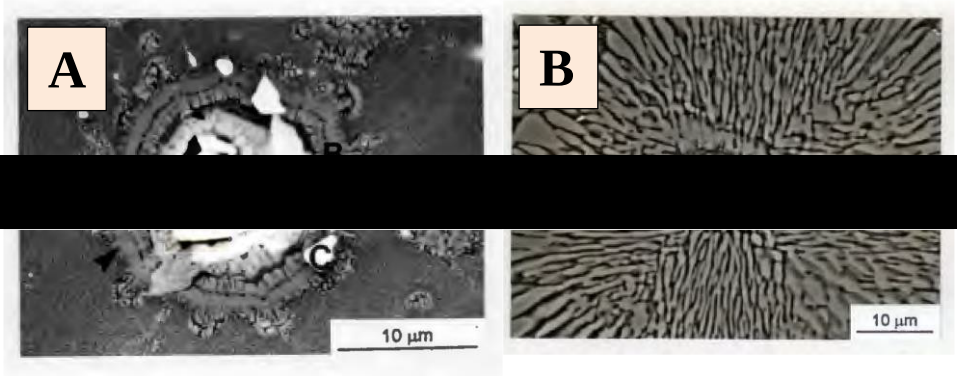

Figure 11 - Examples of lamella γ-γ' eutectic features and NiHf intermetallics found in incipient melted MarM-002 by V. Ming. A) Amorphous Ni-Hf intermetallic centre surrounded by lamella γ-γ' eutectic features and hafnium carbides. B) Lamella γ-γ' eutectic in characteristic rosette formation [88].

2.5.4 Propagation of liquated material

If temperature is sustained following a sub-solidus liquation event, the resultant liquid tends to propagate along grain boundaries, further increasing the fraction of liquid in the material. The liquid propagation is thought to be the result of a reaction of the metastable liquid with the grains surrounding it. If the surviving grains are undersaturated, back diffusion of solute across the solid-liquid interface can occur which can lower the non-equilibrium solid-liquid interfacial energy promoting intergranular wetting and therefore propagation of the liquid[89], [90].

Liquid propagation in RR1000 has not been widely researched. The only mention of liquid propagation in RR1000 that has been reported previously was when it was briefly commented on by M. Attallah et al [4]. The authors reported that the liquated material from constitutionally liquated primary γ' would link up along the specimen's surface to form equiaxed cells but gave no insight into the propagation rate. No research has been conducted on the liquid propagation rate in CG RR1000 or the liquid propagation through bulk specimens of either RR1000 variant. Therefore, the present study aimed to populate this knowledge gap by characterising the liquid propagation rates in both RR1000 variants, both of which were achieved.

2.6 Semi-Solid Testing

When a solid metal is heated to a temperature above its solidus temperature it will begin to melt and result in some liquated material within the solid metal. This state is known as the ‘mushy state’ and the resultant metal is known as a ‘mushy metal’. The opposite scenario to this is when a molten metal is cooled to below its liquidus line and some solidified grains nucleate within it, this is known as a ‘semi-solid state’ and the resultant metal is known as a ‘semi-solid metal’, although the term semi-solid is often used to describe both scenarios.

The mechanical properties of a metal starting to melt and a metal starting to solidify vary greatly. It is only when the fraction of liquid in both cases are similar, that the mechanical properties begin to reflect each other[91].

Most of the research on semi-solid mechanical testing is conducted to further understand the mechanical properties and microstructural evolution during thixoforming, also known as Rheocasting.

Thixoforming is a casting method that involves the injection of semi-solid material, rather than completely liquated material, into dies or moulds. The benefits of thixoforming over conventional casting methods are reduced part defects from air entrapment due to the lower macroscopic turbulence as a result of the higher viscosity. Shrinkage porosity defects are also reduced due to less loss of volume on complete solidification.

Because of these advantages semi-solid testing for thixoforming is a well-researched field, with multiple testing methods, although most of these testing methods focus on calculating the viscosity of semi-solid materials and are aimed at scenarios where there are high fractions of liquid. Examples of semi-solid mechanical tests for high volume fractions of liquid are, rotational rheometers and capillary rheometers.

The main method used for testing semi-solid materials of low to medium fraction of liquid content is compression testing in order to generate flow stress data [92].

The current research focusses on testing samples with a low fraction liquid caused by sub-solidus liquation mechanisms induced by rapid heating. Therefore, low fraction of liquid testing is more applicable, so a focus was made on compression testing methods. These methods have been investigated thoroughly and are detailed in the section 3.5 later. While some semi-solid compression testing research using different testing methods is outlined here with a focus on nickel superalloy testing where possible.

2.6.1 Semi-solid compression testing - equipment & methods

Gleeble thermo-mechanical simulator

Gleeble thermo-mechanical simulators are a series of mechanical testing equipment designed and built by Dynamic Systems Inc. (DSI). They utilise electrical resistance as a heating source by running a current through the load train. The load train is commonly mounted horizontally, although some Gleeble systems do have vertical load trains. A wide range of mechanical tests can be conducted within Gleeble systems. As this program of work focusses on semi-solid compression testing, two relevant examples are detailed below.

A study conducted by M.S. Lewandowski et al [93] investigated the semi-solid compression testing of IN718. The compression tests were carried out using a Gleeble 1500 on 12.5mm height by 7.45mm diameter compression specimens, heated to temperatures above and below the eutectic temperature of 1150°C, in order to test completely, solid specimens and semi-solid specimens.

The fraction of liquid was estimated from data generated from continuously cooled samples of IN718. The heating rates in this study were very slow at $0.4°Cs^{-1}$ and specimens were held at the test temperature for 5 minutes before the compression test was initiated. The compression tests were conducted using constant stroke, at strain rates of $0.0001\text{-}0.001s^{-1}$, which are also very slow. To get around problems associated with friction during compression testing, the authors calculated the compressive stress using the instantaneous area of the mid-section of the specimen. This stress calculation was based on three assumptions; the volume of the specimen remained constant, the barrelling of the sides of the specimen resulted in an ellipse shape and that the friction at each end of the specimen in contact with the Gleeble anvils, was sufficient enough that no sliding occurred resulting in a change in diameter. The main findings from this research were that the semi-solid tests conducted above the eutectic temperature were not very repeatable in comparison to the tests conducted on fully solid specimens, but they did report a distinct drop in flow stress when a semi-solid microstructure was introduced. They also reported a large reduction in activation energy for plastic flow in the semi-solid specimens, compared to the solid specimens but went on to explain that this is not a true change in activation energy and is rather the transition from diffusion controlled plasticity to viscous flow of the liquid when sufficient fraction of liquid was present.

A more recent study utilising a Gleeble thermo-mechanical simulator to conduct compression tests on partially liquated nickel superalloy specimens, was published by A.P.I Popoolaa [86]. The testing was conducted on the powder metallurgy nickel super alloy Astroloy, similar in composition to RR1000. The work was conducted on 8mm diameter by 12mm height compression specimens. The specimens were subject to rapid heating at $20°Cs^{-1}$ to temperatures below the γ' solvus at 1150°C and temperatures above the γ' solvus at 1175°C, 1200°C and 1225°C, with each specimen being held at the test temperature for 3s.

At the temperatures above the γ' solvus this rapid heating induced constitutional liquation of primary γ' precipitates which originally measured 0.8 - 3μm in size. The liquated material in these tests also exhibited the characteristic differentially etched regions, described previously, in section 2.5.3.

Within these differentially etched regions, γ-γ' eutectic features were also found. EDS analysis of these regions found the re-solidified material to have an intermediate composition between that of the γ matrix and the primary γ' precipitate. An interesting finding of this study was that it was claimed that some of the γ-γ' eutectic features could be dissolved into the γ matrix if a 50% compressive strain was applied when the specimen was at temperature. This may be a misconception, as the compressive strain was applied when the specimen was still at the target temperature of 1175°C and therefore the liquated material has not yet cooled in order to form the γ-γ' eutectic features. Instead this compressive strain should be seen to prevent the formation of γ-γ' eutectic features on solidification.

Although the Gleeble is an attractive semi-solid testing method due to its vacuum testing environment and reasonably fast heating rates, it has its drawbacks. Namely, the strain rates possible in Gleeble thermo-mechanical simulators are relatively slow, ranging from $0.001\text{-}5s^{-1}$, compared to other test types such as servo-hydraulic compression machines [86], [93], [94]. Also, the specimen must always be in contact with the compression anvils for the electrical resistance heating to work, this raises the issue of accelerating to the desired strain rate while deforming the specimen, meaning the compression test is not conducted at a uniform velocity. None the less, semi-solid solid investigations have clearly been conducted on Gleeble systems in the literature. Therefore, an investigation into the potential use of the Gleeble 1500 that was available to use in the department was conducted.

Gleeble 1500 assessment

An investigation was conducted looking into the suitability of a Gleeble 1500 thermo-mechanical simulator to carry out semi-solid compression testing (pictured in Figure 12). The Gleeble in question possessed the power to heat to nickel specimens to semi solid temperatures at the required heating rate (1140-1300°C at 5°Cs^{-1} +) but had limitations that prevented its use.

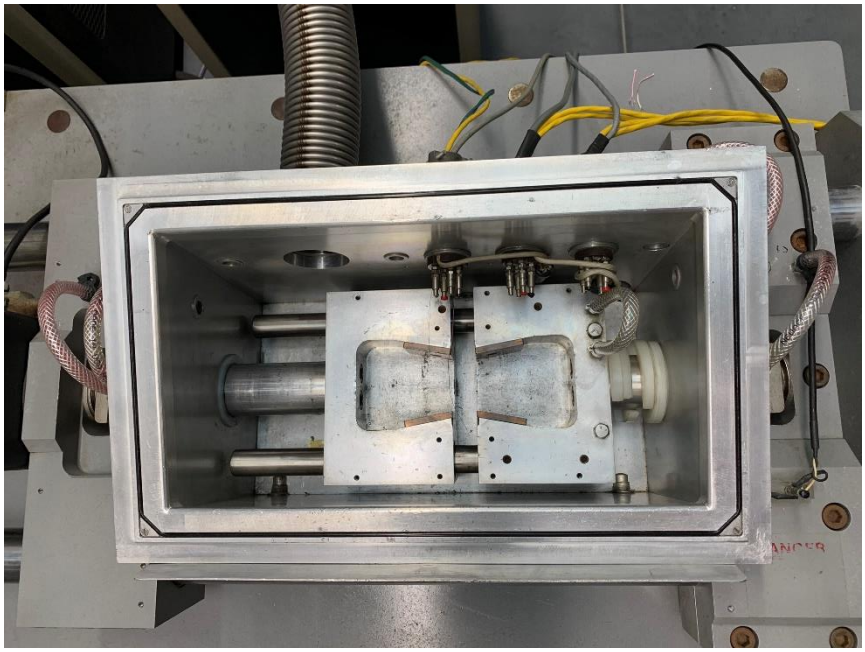

Figure 12 - Gleeble 1500 thermo-mechanical simulator test chamber consisting of two water cooled grips, hydraulic actuator, load cell and thermocouples for temperature measurement.

The Gleeble 1500 consists of a horizontally loaded vacuum chamber in which tests are conducted. Specimens are heated via resistance heating as a current is passed through the specimen via water cooled copper grips, with temperature being controlled via spot welded thermocouples. One of the main issues with using a Gleeble for semi-solid testing is the horizontal orientation of its load train. If a specimen was heated to produce a semi-solid microstructure while it is horizontal this would cause the specimen to bow under its own weight. In order to conduct compression tests within a Gleeble thermomechanical simulator, a set of ISO-T tungsten anvils manufactured by DSI are required (Technical drawings in Figure 13 A adapted from [95]).

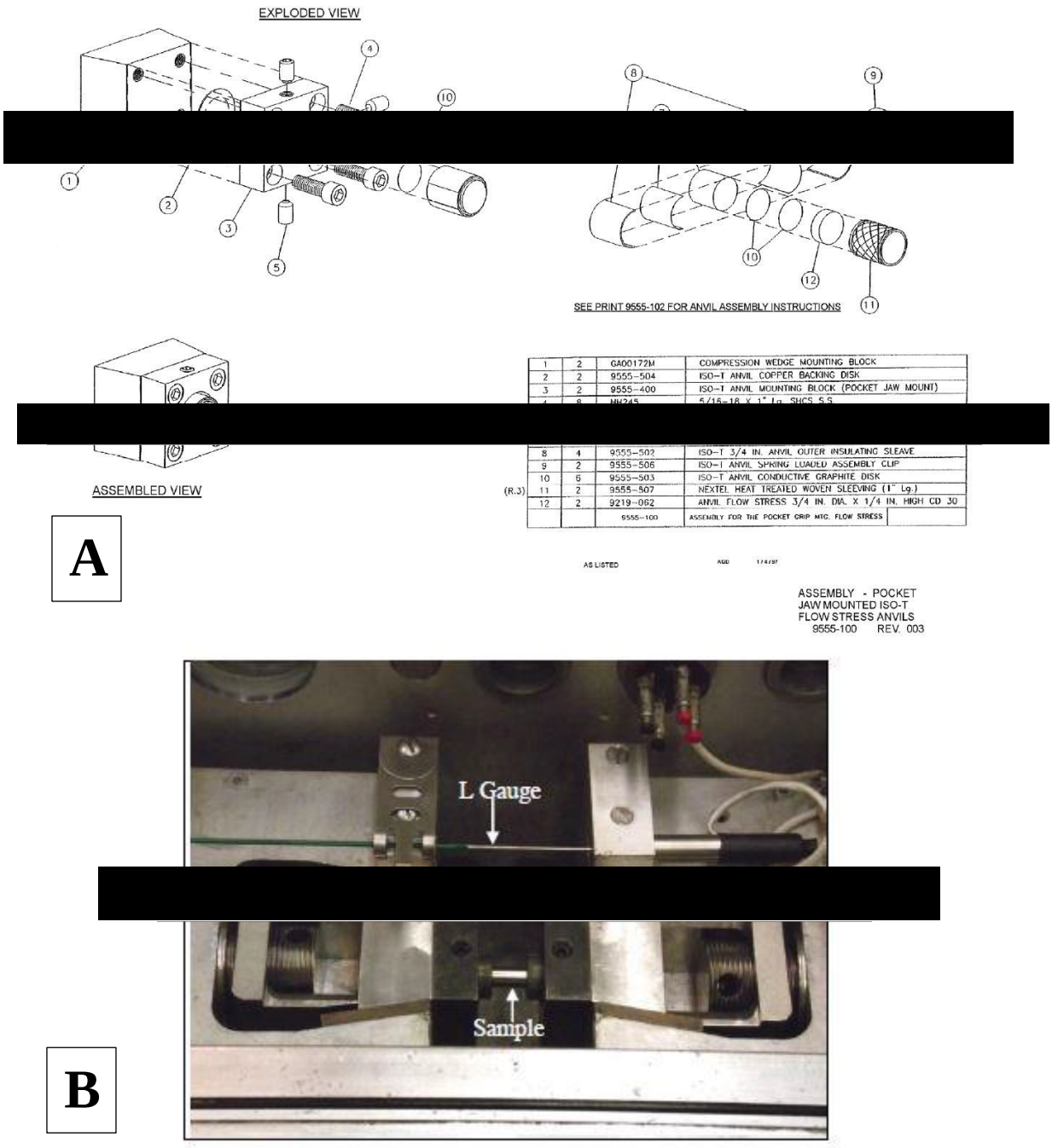

Figure 13 - A) Schematic drawing of ISO-T tungsten anvils to conduct compression tests in Gleeble 1500. B) ISO-T tungsten platens and strain gauge fitted to a Gleeble 1500 [95].

The tungsten anvils raised another limitation which was the maximum heating rate. Although the literature suggested that heating rates of 20°Cs^{-1} are possible using a Gleeble, the Gleeble manual stated the maximum achievable without welding the anvils to the specimen was approximately 5°Cs^{-1} [95]. While 5°Cs^{-1} is enough to cause constitutional liquation in RR1000, being limited to this heating rate would narrow the scope of experimentation too much.

An important requirement for the proposed semi-solid testing facility was the ability to rapidly quench the specimen in order to prevent any microstructural evolution after the test has been conducted. When using the ISO-T anvils the cooling rate is limited to $10°Cs^{-1}$ from 1000°C to 800°C and $4°Cs^{-1}$ from 800°C to 500°C with the majority of the heat dissipating from the cylindrical surface rather than through conduction axially [95]. This cooling rate is a much more moderate cooling rate than the preferred method of water quenching.

Another inherent problem of the Gleeble's heating method is that of the temperature gradients throughout the specimen, which are caused by the water-cooled anvils having to be in contact with the specimen during heating. The undeformed material at each end of the specimen caused by this temperature gradient can be clearly seen in Figure 14 adapted from [95]. These temperature gradients would make it difficult to accurately quantify the liquid propagation rate in bulk RR1000 specimens. The constant contact between the specimen and the anvils that is required for the Gleeble's heating system to work, also means that at the beginning of the test the anvils must accelerate to the required velocity for a desired strain rate while being in contact with the specimen. This means that the whole test was not carried out at a uniform velocity.

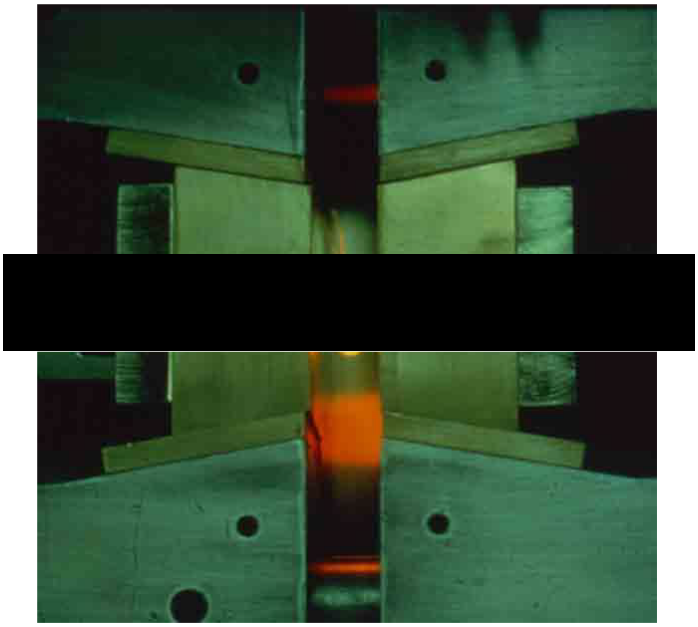

Figure 14 - Example of temperature gradient throughout specimen when conducting compression work with copper jaws in a Gleeble 1500 [95].

For these reasons, the Gleeble 1500 was considered unfit for the purpose of the present research. This prompted the decision to design and commission a novel semi-solid testing facility as part of this research program.

Servo-hydraulic compression

Servo hydraulic compression machines can operate at a range of ram velocities allowing for many strain rates to be used ranging from 0.001-300s^{-1}. Typically, semi solid compression testing has been conducted at lower strain rates to simulate the conditions experienced during thixoforming procedures [96]–[101]. Another advantage of servo-hydraulic compression machines is the ability to use a range of heat sources, from traditional radiant resistance element furnaces [96], [102], [103], to induction heating [98], [101].

Being able to use a range of heating methods is an advantage of using the servo-hydraulic compression method over using a Gleeble thermo-mechanical simulator as the upper compression platen does not need to be in contact with the specimen during heating. Therefore, it can be accelerated up to the testing velocity before it contacts the specimen to conduct the test. Servo-hydraulic compression machines also allow the use of different lubricating agents so that homogenous deformation can be achieved, meaning more accurate flow stress data can be generated [92], [100].

The versatility of servo-hydraulic compression machines and the range of possible heating methods that it could be combined with made it a very appealing. Because of this, the novel semi-solid testing facility designed and commissioned during the present study was built around a servo-hydraulic compression machine.

Advanced semi-solid testing

The most recent advancements in semi-solid testing involve the use of X-ray tomography, enabling the complex interactions of grains in semi-solid materials, to be observed in situ. X-ray tomography has led to great developments in the understanding of microstructure evolution of semi-solids during mechanical testing. Research conducted by K.M. Kareh et al [104], involved compression testing of Al-Cu alloys at fractions of solid between 64% - 93%, to a true strain of 25%.

The grain response to the compressive force was captured during the tests via synchrotron X-ray tomography. During their study they revealed that the grains in a semi-solid material move as independent bodies and deform as near-cohesionless granular materials. This implies that the characteristic peak in flow stress (Figure 15), experienced during compression testing of semi solid materials, is not due to the breaking of welds between grains, but rather is the work required to push the grains apart, inducing a volumetric strain and dilation.

This dilation effect also acts to draw in the liquated material resulting in intergranular porosity, which was more prevalent at higher fractions of solid due to the greater amount of interaction points between grains. A 2D section of the centre of the specimen taken from the X-ray tomography data is shown in Figure 16, this shows increased porosity at higher solid fractions.

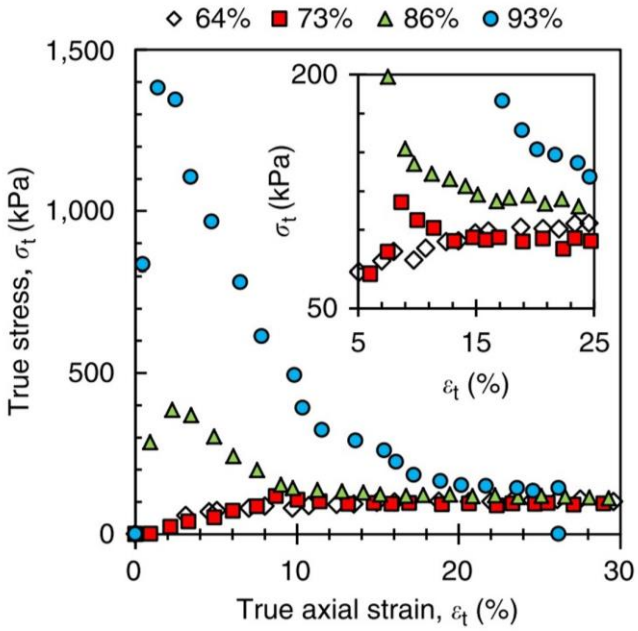

Figure 15 - Flow stress curves for an Al-Cu alloy compressed at varying fractions of solid (64%-93%) adapted from [104]

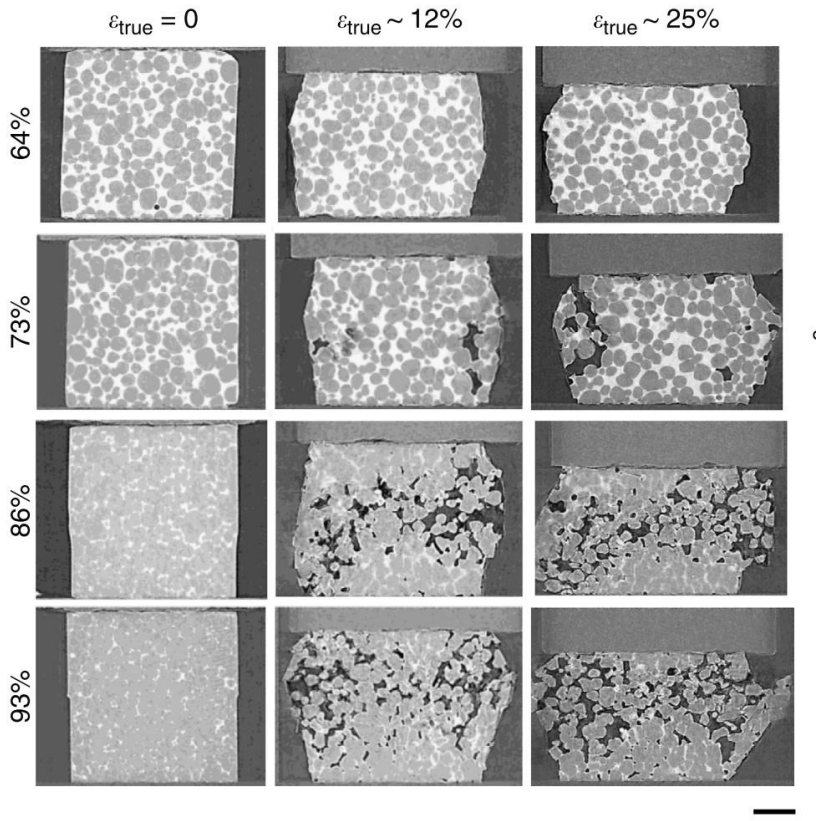

Figure 16 - 2D section of X-ray tomography data of an Al-Cu alloy compressed at a range of solid fractions. Adapted from [104]

In another similar study, conducted by K.M. Kareh,this semi-solid dilatancy phenomena was also reported to occur in a carbon steel alloy when a shear load was applied at a fraction of solid of 90% [105].

Calculating fraction of solid

In order to test materials in a semi-solid state and accurately correlate the mechanical properties to the liquid fraction that was present during testing, an accurate method of predicting the liquid fraction is needed.

In the majority of semi-solid testing this is either done from data obtained from differential scanning calorimetry (DSC) [99], [106], [107], or by experimental data generated by comparing resultant microstructures with specimens cooled from complete liquid to form a continuous cooling curve [98], [108], or by simply estimating the liquid fraction from calculations based on phase diagrams [96].

The problem with the above methods, is that they rely on slow heating rates and/or cooling, from a completely liquid specimen. Thus, not applicable for this study as the liquation mechanisms being investigated rely on the rapid heating rate of inertia friction welding. The most appropriate method for fraction liquid calculation, in the present research, was estimating the amount of differentially etching liquated material from optical micrographs of specimens heated to different temperatures, to produce varying liquid fractions. In conjunction with DSC, the above method was effectively used by A. Bolouri et al [103].

The present research adopted the above method to generate a series of calibration curves, which illustrate the volume of liquid that can be produced by different heating rates, peak temperatures and hold times. These calibration curves also allowed the liquid propagation rate to be characterised in both RR1000 variants during the research study.

2.6.2 Compression testing fundamentals

The fraction of liquid experienced during an inertia friction weld is likely to range from small volumes, caused by constitutional liquation of the primary γ' precipitates in the HAZ, to potentially quite large liquid fractions in the later stages of welding, where temperatures are at their peak. For this reason, compression testing is considered the most suitable semi-solid testing method, as it allows testing up to 100% solid fractions.

Compression testing is usually performed on cylindrical specimens with a height to width aspect ratio of 0.75-1.75, as larger aspect ratio specimens are prone to inhomogeneous deformation via buckling. Compression testing produces raw data in the form of load and displacement, which needs to be converted into true stress and true strain to create a flow stress curve. The true stress is a function of the load (P) divided by the instantaneous cross-sectional area of the specimen being tested. If the deformation is assumed to be homogenous and the specimen volume remains constant throughout the test the true stress can be calculated via equation (1).

$$\sigma_0 = \frac{4P}{\pi D^2} = \frac{4Ph}{\pi D_0^2 h_0} \tag{1}$$

The true strain of a compression test is also a function of specimen height and can be calculated via equation (2). Here, h is the instantaneous height of the specimen, while h_0 is the original height of the specimen, therefore, Δh is the distance travelled by the compression platen since the compression test was initiated. The strain rate can be calculated via equation (3), where v is the velocity of the compression platen[109].

$$\varepsilon = ln\frac{h}{h_0} = \ln\left(1 - \frac{\Delta h}{h_0}\right) \tag{2}$$

$$\dot{\varepsilon} = \frac{d\varepsilon}{dt} = \frac{d(ln\frac{h}{h_0})}{dt} = \frac{1}{h}\frac{dh}{dt} = \frac{v}{h} \tag{3}$$

Often deformation is not completely homogenous because of friction between the compression platens and the specimen surface. The result of these frictional effects results in barrelling of the specimen. These frictional effects can be accounted for by applying corrections to the true stress - true strain data. This can be achieved via validated finite element (FE) models such as the one developed at Swansea University by R.W. Evans et al. [110]. This FE model takes into consideration the final dimensions of the specimen, along with test temperature, in order to calculate the friction factor and amount of adiabatic heating expected. The model then determines the relative errors in the true stress for each strain value allowing the original data to be corrected.

2.6.3 Mechanical behaviour of semi-solids

The fraction of solid present in a semi-solid material is the most important factor when mechanical properties are concerned. As the amount of liquid increases the way the material will respond to mechanical deformation changes dramatically. Semi-solids with high fractions of solid ~95% and above, usually behave like a solid metal.

Solid fractions of 60-95% will often deform like a clay and can be made to flow relatively easily. If the fraction of solid is reduced to less than 60% the material will behave more like a slurry and will flow under the force of its own weight [91]. As a result, the flow stress of a semi-solid material is very dependent on solid fraction, with most materials experiencing a similar relative drop in flow stress as the fraction of solid is decreased. This can be seen in Figure 17 adapted from [111], where, for every alloy tested, the flow stress decreases rapidly as solid fraction is reduced, with the relative reductions lying on the same trend line. This suggests that the dominant factor in a semi-solid materials strength is the fraction of solid present.

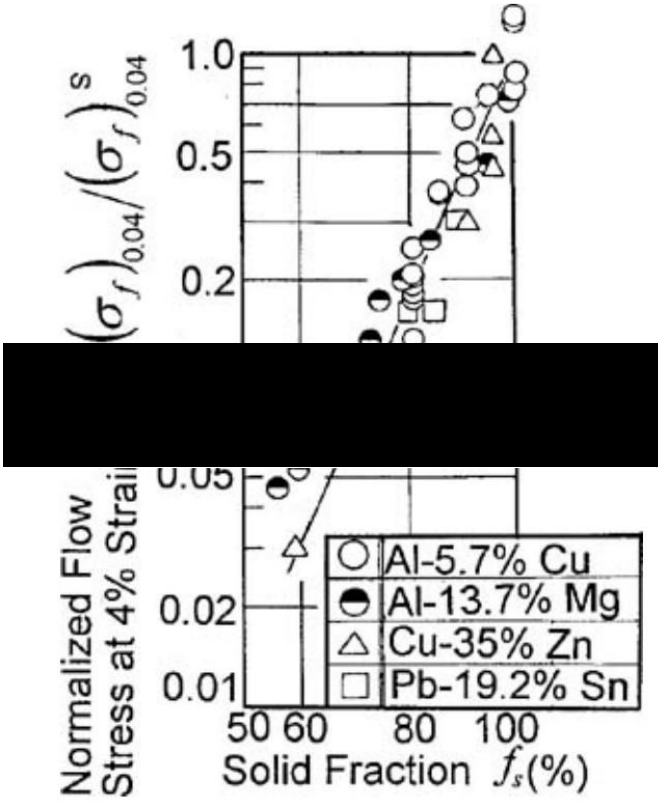

Figure 17 - Plot of 4% strain proof stress against fraction of solid for multiple alloys tested. Adapted from [111]

The sudden drop in flow stress, as the fraction of liquid is increased, is thought to be a result of a change in grain interaction when an intergranular liquid is introduced. In a completely solid metal, the grains exert strong mechanical forces on one another, preventing their deformation and movement. When grain boundary liquation occurs, these intergranular forces diminish allowing the grains to slip past each other rotating and displacing freely, as depicted in Figure 18, adapted from [91]. If the fraction of liquid is increased to sufficient quantities, the intergranular interactions will be so small that the semi-solid material will flow like a non-Newtonian fluid [91].

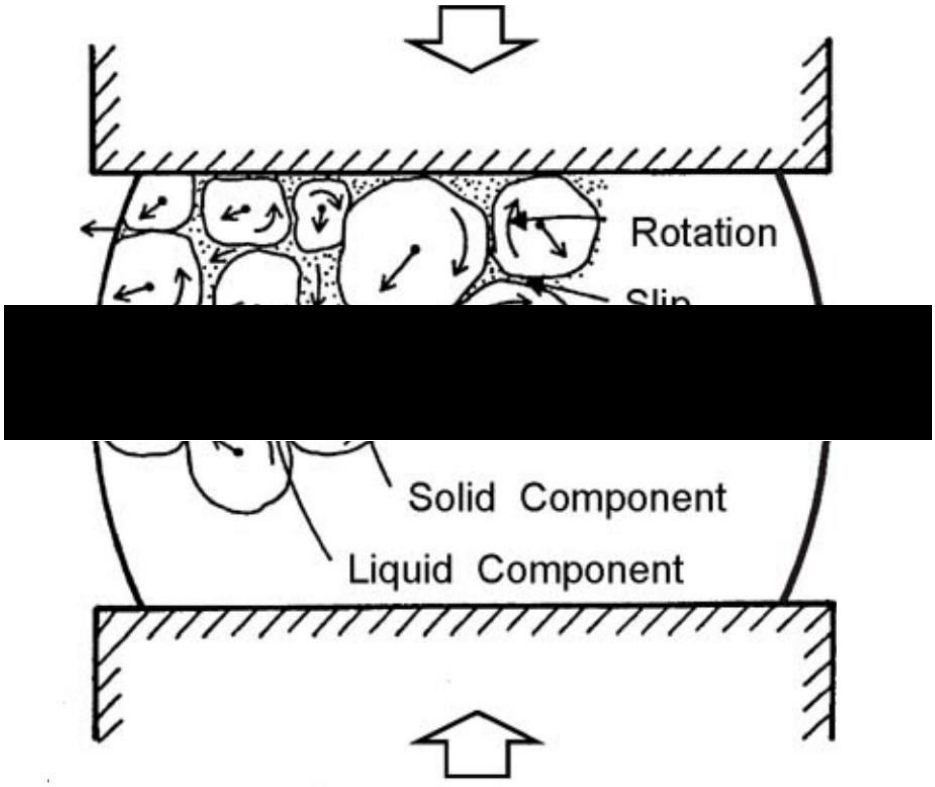

Figure 18 - Schematic diagram of grain interactions in the presence of intergranular liquid. Adapted from [91].

2.7 Heating sources

The heating rates experienced during an IFW are extremely fast, therefore, if the microstructural changes during an IFW are to be replicated in a mechanical testing machine, the heat source used during testing would also have to be capable of rapid heating rates.

This prevents the use of conventional resistance element furnaces that rely on heat transfer through radiation and convection, as the heating rates are relatively slow. The use of conventional furnaces also means a soak time is needed to make sure the specimen temperature is homogenous. This also means the final specimen temperature is governed solely by the temperature of the air in the furnace. As a result, the exact specimen temperature cannot be recorded during the tests and can only be predicted via process modelling.

Resistance heating the specimen directly can produce the necessary heating rates, but imposes limitations on test set up, as a current needs to be passed through the specimen in some way.

Induction heating is an attractive heating method because of its ability to provide non-contact heating at very fast rate. The work head of the induction coil can also be manufactured in a variety of different shapes and sizes. This allows a range of specimen geometries/testing equipment to be heated, while leaving enough room for thermocouples and or line-of-sight, for non-contact temperature measurement. Induction heaters work by passing a high frequency alternating current through coiled copper tubing, the alternating current creates a magnetic field within the coil. If a metallic object is then placed within the coil the alternating magnetic field induces eddy currents within the metal. It is the electrical resistance of the metal to these currents that causes the heating effect. The coiled copper tubing must be water cooled to prevent the heat exposure from softening or melting the copper.

The rapid heating rates capable via induction heating, as well as the flexibility to design multiple work head coils during performance optimization, made induction heating the ideal choice for the novel semi-solid testing facility designed and commissioned during this project.

2.8 Temperature measurement

In order to accurately replicate the heating profile of an IFW the specimen temperature must be controlled and recorded at all times. Temperature control is often carried out with the use of a Proportional-Integral-Derivative (PID) controller. PID controllers and the methods used to tune them, are explained in detail in section 3.7.3.4 . In simple terms, their basic function is to adjust the power output to a heat source in order to remove any error between the specimen temperature and the desired setpoint temperature [112].

A PID controller needs a reference for the specimen's temperature for it to function. This reference temperature reading is usually provided via a thermocouple attached to the specimen. Thermocouples are not ideal and have some drawbacks. Research into the thermal shadowing caused by spot welded thermocouples was conducted by J. Jones et al [113]. The study revealed multiple inaccuracies when using thermocouples to measure the temperature of specimens being heated via induction heating. The study compared the temperature readings from thermocouples spot welded to the specimen to readings from an infrared pyrometer and an infrared thermography camera. The comparison revealed that the thermocouples were drawing heat out of the specimen creating temperature gradients in the specimen. They also reported that the thermocouples would often give false readings, indicating faster heating rates and higher peak temperatures than the true temperature being read by the pyrometer and thermography camera. This was due to the thermocouple itself being heated by the induction coil in addition to being heated by the specimen via conduction. Jones et al concluded that both the pyrometer and thermography camera read temperature accurately to +/- 2°C if the specimens were coated in high emissivity thermal paint. These tests were conducted on quite large thermo-mechanical fatigue specimens in comparison to the smaller cylindrical specimens usually used in compression testing. It can be assumed that the thermal shadowing would be amplified on a smaller specimen with a lower heat capacity.

2.9 Literature review conclusions

IFW is a high integrity joining method that produces narrow heat affected zones and is therefore useful for joining highly alloyed nickel superalloys, as it avoids the necessity of a large weld pool associated with conventional welding methods. The conditions experienced at the weld line region are extreme, including rapid heating rates and large strain rates. Although IFW is nominally stated to be a solid-state joining process, these extreme heating rates make some nickel superalloys susceptible to sub-solidus liquation mechanisms during IFW. The occurrence of hot tearing in the TMAZ of some FG and CG RR1000 inertia friction welds provides further evidence that liquation is occurring during the IFW of both variants.

A range of sub-solidus liquation mechanisms in nickel superalloys have been studied in the literature in **section 2.5**, and the mechanisms applicable to RR1000 have been identified.

M. Attallah et al [4] have demonstrated:-

- Constitutional liquation of primary γ' occurs when the surface of FG RR1000 specimens is heated at 5°Cs^{-1} and 50°Cs^{-1} to above the γ' solvus temperature.
- Evidence of the occurrence of this liquation via in situ observations from the HT-CLSM as well as micrographs of eutectic re-solidification structures.
- The liquated material from the constitutional liquation would join up to form equiaxed cells on the specimen surface.
- Their method of testing using a HT-CLSM involved heating the free surface of FG RR1000 specimens and therefore could be susceptible to free surface effects which may alter the material behaviour compared to heating bulk specimens.

Their research did not, however: -

- Conduct any tests on CG RR1000 to investigate the sub-solidus liquation mechanisms and liquid propagation in this variant of RR1000.
- Characterise the liquid propagation rate in FG RR1000.
- Heat bulk RR1000 specimens, free from temperature gradients, to allow the characterisation of the liquid propagation rate through bulk material.

- Investigate the effect of liquated material on mechanical strength or the effect of re-solidified material on mechanical properties, e.g. hardness.

The present study has aimed to address these previously unexplored areas of research.

As CG RR1000 does not contain any primary γ' it is unlikely that the secondary and tertiary γ' it does contain are of a sufficient size to be susceptible to constitutional liquation at the heating rates experienced in the TMAZ and HAZ of IFW. Hot tearing has been found to occur in both variants of RR1000 during IFW and so it was suspected that the CG variant was experiencing another type of sub-solidus liquation during IFW.

The sub-solidus liquation mechanisms of CG RR1000, when subject to rapid heating rates have not been researched previously. Therefore, the potential mechanisms that could cause the mass sub-solidus liquation have been investigated in **section 2.5.2** and a mechanism applicable to CG RR1000 has been proposed.
The mechanism proposed here, is based on the findings of F. Tancret [5], who conducted a study modelling the constitutional liquation of γ' in nickel superalloys.
Tancret's model confirmed the possibility of constitutional liquation of large γ' precipitates if the heating rate was sufficient but also reported that a form of incipient melting of the γ matrix was possible during rapid heating.
Tancret stated that if the γ' precipitates were too small to survive to a temperature where they could constitutionally liquate, the mass diffusion of their γ' forming elements into the surrounding γ matrix, during their dissolution, could lead to incipient melting. This incipient melting mechanism was reported to be the result of insufficient time for the γ' forming elements to homogenise throughout the γ matrix during rapid heating. The mass diffusion of γ' forming elements into the γ matrix leads to highly alloyed localised areas of γ, which causes momentary drops in melting point in these regions. This combined with the lack of time for homogenisation during rapid heating results in liquation as the temperature is increased further.
This mechanism was identified as a potential cause of the mass sub-solidus liquation experienced by CG RR1000 in the present study, when it is rapidly heated.

To allow the sub-solidus liquation mechanisms and the ensuing liquid propagation in both variants of RR1000 to be characterised, methods of identifying liquated material in superalloys and liquid propagation mechanisms have been investigated. Details of the investigation undertaken are included in **sections 2.5.3** and **2.5.4**. Two main methods were apparent. Liquated material has been reported to differentially etch from the original surviving γ matrix with a clear contrast between the two, when examined via optical microscopy and SEM. Liquation in nickel superalloys had also previously been identified by the presence of distinct re-solidification products, such as eutectic structures. The morphologies of these structures in the literature have been studied, so their presence could be identified in RR1000.

Liquated material in semi-solid metals has been reported to propagate under sustained temperature, usually via grain boundary wetting. Liquid propagation in FG RR1000 was briefly commented on by M. Attallah et al [4] as discussed earlier, but no analysis of the propagation rate was conducted in their study. The liquid propagation rate in either RR1000 variant has not been characterised previously and therefore was a valuable way of building on the work of M. Attallah et al, expanding liquation in RR1000 research further.

To conduct a study capable of the previously unexplored areas of RR1000 sub-solidus liquation research, a semi-solid testing method capable of rapidly heating specimens free from temperature gradients needed to be identified.

Semi-solid testing methods have been investigated in **section 2.6**. Numerous semi-solid testing studies have been conducted via the use of Gleeble thermomechanical simulators and therefore, this method of semi-solid testing was investigated thoroughly to assess its suitability for use in the present research.

Inherent problems were identified with Gleeble testing due to the resistance heating method it uses. These problems included: large temperature gradients throughout the specimens during testing that resulted in inhomogeneous deformation; limits on the heating rate due to problems of welding the specimen to the compression anvils at fast rates; and the necessity to accelerate up to the desired strain rate while in contact with the specimen.

The above reasons deemed the on-site Gleeble 1500, unfit for purpose and so the decision was made to design, develop and commission a novel semi-solid testing facility to carry out the necessary research.

The new semi-solid testing facility needed to be able to rapidly heat RR1000 specimens at heating rates between $1°Cs^{-1}$ and $50°Cs^{-1}$ to replicate the heating rates experienced during IFW. The semi-solid testing facility would need to be capable of this, while maintaining a temperature gradient free specimen to avoid the problems that were evident in Gleeble testing.

Servo-hydraulic compression testing was found to be the best platform for the novel semi-solid testing facility to be built around, due to the range of heating sources that it could be combined with.

An investigation into multiple heating methods was conducted in **section 2.7**. This investigation found that induction heating was the ideal choice for the novel semi-solid testing facility due to its high performance and versatility. A review of the heating methods that were available during the project is also detailed later in section 3.6. Temperature measurement methods were studied in **section 2.8**. This study found that the use of contact temperature measurement methods, such as thermocouples, can draw out heat from specimens and create temperature gradients [113], something that needed to be avoided in the semi-solid testing facility. Therefore, a non-contact temperature measurement method was needed, such as pyrometers, which were reported to be a suitable option.

Research on inertia friction welding of RR1000 has been studied in detail in **section 2.4.2**. Studying this literature provided a good understanding of the final microstructure and resultant mechanical properties of inertia friction welded RR1000. This provided a comprehensive knowledge base to understand the microstructural evolution and liquation mechanisms that occur before this final microstructure. During the study it was apparent that although the final microstructure of IFW RR1000 has been documented well, some of the resultant characteristics have not been fully explained.

A study conducted by Z.W Huang et al [55] reported that when FG and CG RR1000 were joined together via IFW both variants experienced a drop in hardness in the HAZ. This drop in hardness was more severe in the CG variant, but no explanation had been given. When the weld was given a post weld heat treatment to alter the γ’ distribution in the HAZ, the hardness profile in both variants became comparable. This suggested that the γ’ distribution is likely to be the governing strength factor.

Because of this, investigating the effects of rapid heating rates on the microstructural evolution, including γ' distributions and other microstructural characteristics, followed by correlating this evolution with the resultant hardness in both variants, was thought to be beneficial and became an objective of the project.

In order to fully understand the microstructural evolution of RR1000 during rapid heating and the effect the microstructural changes would have on the resultant mechanical properties, the fundamentals of nickel superalloys have been studied in depth in **section 2.2**.

These fundamentals included, but were not limited to, alloying elements, common phases and strengthening mechanisms. Several different factors contribute to the strength of a nickel superalloy. The main contributors are grain size effects, and the presence of a second phase precipitate γ' and its size and distribution. The strength is also improved by lesser strengthening mechanisms such as the presence of special grain boundaries.

The current research built on the existing literature on sub-solidus liquation mechanisms in RR1000, by extending the work of M. Attallah et al [4]. This has been achieved by designing and commissioning a novel semi-solid testing facility capable of rapidly heating bulk RR1000 specimens of both the FG and CG variants, while remaining free from temperature gradients.

This allowed the liquid propagation rate through bulk FG and CG RR1000 specimens to be investigated, removing the possibility of any free surface effects that may have been occurring in the experiments conducted by M. Attallah et al.

The background research into semi-solid testing methods was used to aid the design of the novel semi-solid testing facility, commissioned in the current research. The facility required many developmental alterations before it was fit for the purpose of characterising the microstructural evolution and liquation mechanisms in RR1000. The facility was optimised throughout the entirety of the project and many commissioning tests were undertaken, until confidence was gained in the rig's ability to rapidly heat RR1000 specimens at up to $25°Cs^{-1}$ with no temperature gradients.

The findings of M. Attallah et al [4] were used as a benchmark for the novel semi-solid testing facility. Indeed, the new facility was not declared fit for the purpose of investigating liquation mechanisms of RR1000 until it could be used to replicate the

findings of M. Attalah et al; showing evidence of constitutional liquation of primary γ' in FG RR1000 when heating specimens to above the γ' solvus temperature at heating rates between $5°Cs^{-1}$ and $50°Cs^{-1}$. The findings of the current research aligned with that of M. Attallah et al, with evidence of constitutional liquation of primary γ' in FG RR1000 specimens being heated at $25°Cs^{-1}$ to above the γ' solvus temperature. Clear evidence was presented in the observation of intergranular liquated material, where the primary γ' had once existed and eutectic re-solidification structures were found within these regions.

After the novel semi-solid testing facility had been declared fit for purpose, it was used to conduct an array of heat and quench only tests so that the microstructural evolution and liquation mechanisms of both RR1000 variants could be investigated. This investigation was conducted by rapidly heating both RR1000 variants at $25°Cs^{-1}$ to temperatures between 900°C and 1200°C and assessing the resultant microstructures and hardness. The results of this investigation gave a potential explanation of the disparity in hardness drop between the two alloys that was reported by Z.W Huang et al [55]. This is detailed in the results and discussion section.

The heat and quench only tests were also used to investigate the sub-solidus liquation mechanisms of CG RR1000, something that had not been done previously. Evidence was found to support the occurrence of the proposed incipient melting of the γ matrix mechanism in RR1000. This type of melting, in RR1000, had not been reported until this current research project. Evidence to support this finding has been included in the results and discussion section.

Once the occurrence of rapid heating induced sub-solidus liquation had been established in both variants of RR1000, the liquid propagation rate in both variants of RR1000 was characterised.

A series of heat, hold and quench only tests, where specimens were heated rapidly to induce liquation then held at a target temperature to allow the liquid to propagate, were conducted.

The microstructure of these specimens was then analysed to quantify the resultant fraction of liquid. The methods of identifying liquated material in superalloys that had been studied proved to be invaluable during this stage. The resultant liquid fractions from a range of heating rates and hold times were compared to characterise the liquid propagation rate in both RR1000 variants. On top of quantifying the liquation rate in

each RR1000 variant, this exercise also provided a series of calibration curves which would have been used to conduct compression testing of RR1000 at a range of fraction of solids if the testing had gone to plan.

The experimental methods used in the present research, to populate the gaps in the literature around RR1000's microstructural evolution and liquation mechanisms when rapidly heated, are detailed in the subsequent section.

Following this the results from these experiments are discussed.

Although the planned compression testing was not completed during the current research due to unforeseen problems during testing, the fundamentals of compression testing and the strength of semi-solid materials have been investigated in **sections 2.6.2** and **2.6.3.** These sections therefore provide a strong base for continuation of the present research by further developing the testing facility until it can heat specimens and compression platens simultaneously, for semi-solid compression testing to be conducted.

3 EXPERIMENTAL PROCEDURES

3.1 Materials.

All tests conducted throughout this study were conducted on the nickel superalloy RR1000, provided by Rolls-Royce Plc. RR1000 is a polycrystalline powder processed nickel superalloy intended for use as a gas turbine disk material and is manufactured in a range of different pedigrees. This study focuses on two variants: fine grain and coarse grain. The two variants not only differ in grain size, they have vastly different gamma prime distributions which will play a significant role in their liquation characteristics. The details of each variant's microstructure are as follows:

3.1.1 Fine grain (FG)

- Fine grain size 5-10μm
- Tri-modal distribution of gamma prime precipitates (γ')

  Typical sizes:
  - Primary γ' 1-10μm
  - Secondary γ' 50-500nm
  - Tertiary γ' <50nm

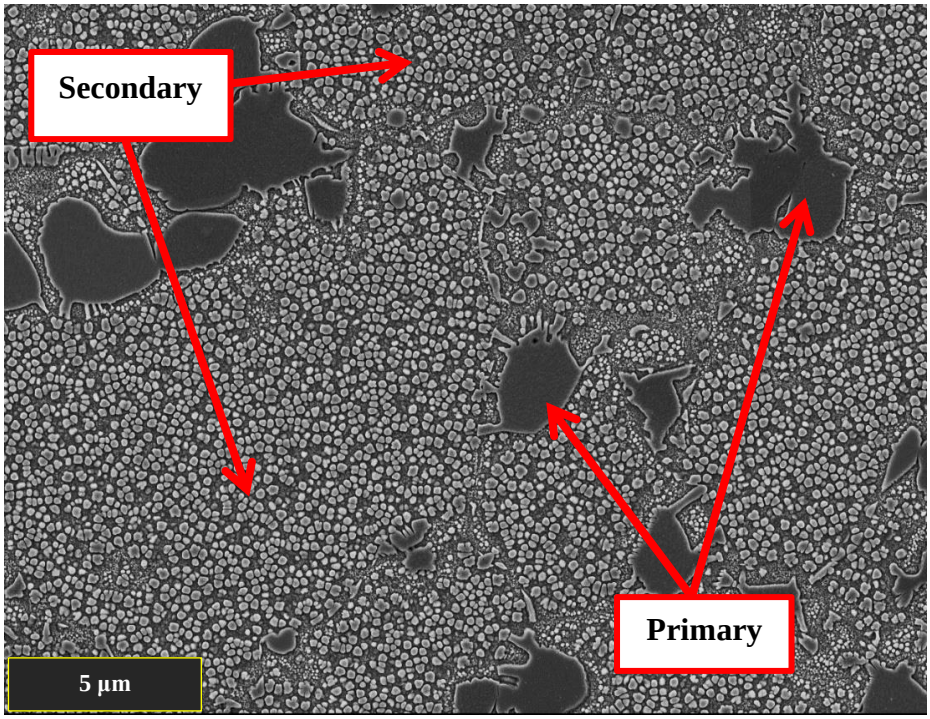

Figure 19 – SEM micrograph of fine grain RR1000, electro etched with 10% Phosphoric acid.

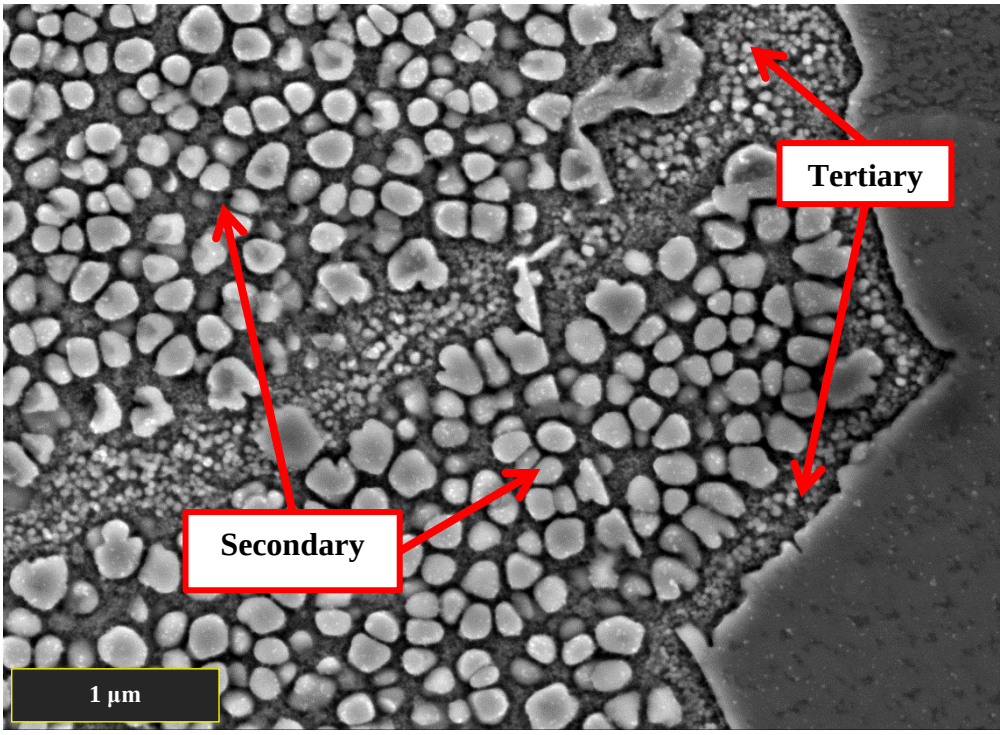

Figure 20 – SEM micrograph of fine grain RR1000, electro etched with 10% phosphoric acid.

For the current study two pedigrees of fine grain RR1000 were supplied from two centre drop forgings with serial numbers 431 & 443, subsequently referred to as FG 431 & FG 443 respectively. Both forgings were subject to a standard heat treatment of 4 hours at 760°C therefore being in pre-weld condition. Both variants were fully characterised before testing and any microstructural differences taken into consideration when interpreting results.

Variant	Average primary γ' size (µm)	Average primary γ' volume fraction (Vol.F.) (%)	Average secondary γ' size (nm)	Average secondary γ' volume fraction (Vol.F.) (%)
FG 431	1.71 (+/- 0.02)	10.2% (+/- 0.7%)	137 (+/- 2)	33.4% (+/- 5.0%)
FG 443	2.02 (+/- 0.02)	11.5% (+/- 4.8%)	124 (+/- 3)	37.7% (+/- 1.7%)

Table 1 - Measured data from fine grain base material characterisation (95% confidence intervals given in brackets).

3.1.2 Coarse grain (CG)

- Coarse grain size 30-50µm
- Bi-modal distribution of gamma prime precipitates (γ')

  Typical sizes:

  - Secondary γ' 50-500nm
  - Tertiary γ' <50nm

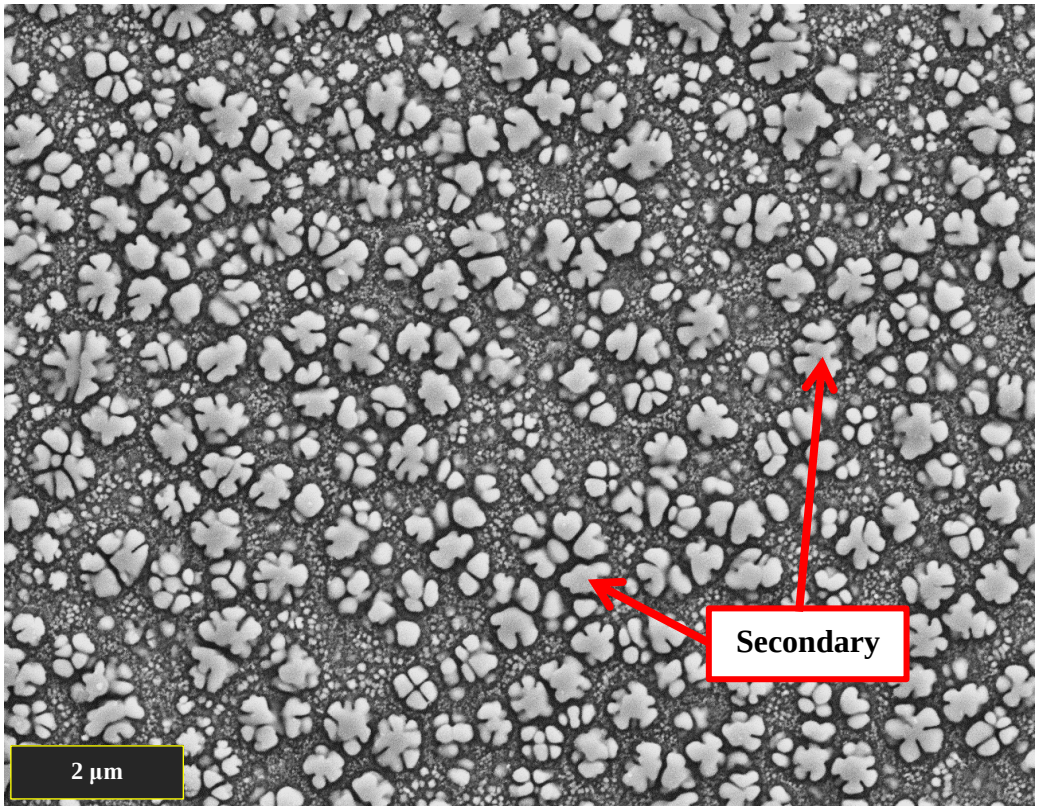

Figure 21 - SE SEM image of coarse grain RR1000, electro etched with 10% phosphoric acid.

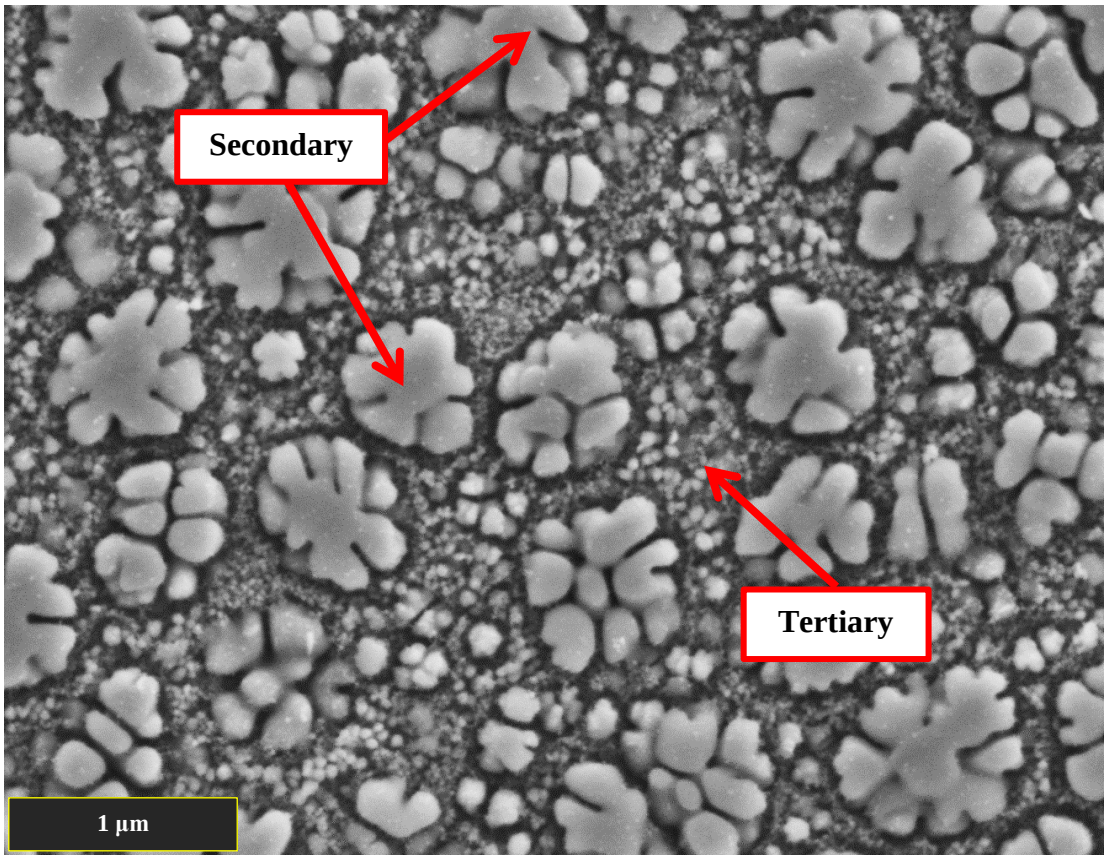

Figure 22 - SEM micrograph of coarse grain RR1000, electro etched with 10% phosphoric acid.

For the current study one pedigree of coarse grain RR1000 was supplied, subsequently referred to as CG. The CG variant was fully characterised before testing. The CG variant is produced by solution heat treating as forged RR1000 material for 2 hours at 1170°C, followed by an aging heat treatment for 16 hours at 760°C. This heat treatment above the γ' solvus temperature causes complete dissolution of the γ', including the incoherent primary γ' which reside on the grain boundaries. This allows the grain size to coarsen to a larger grain size, which will not coarsen further even with further heat treatment. The 'floret' shape of the secondary γ' in the CG variant is caused by a slower cooling rate from the solution heat treatment.[38], [114].

Variant	Average secondary γ' size (nm)	Average secondary γ' volume fraction (Vol.F.) (%)
CG	147 (+/- 4)	31.9% (+/- 6.1%)

Table 2 - Measured data from coarse grain base material characterisation (95% confidence intervals given in brackets).

The methods used to measure these microstructure properties is detailed later in section 3.2 Materials Characterisation Methods. Tertiary γ' size and volume fraction measurements were not conducted in this study, as this involves transmission electron microscopy, which was outside the scope of this work.

3.1.3 RR1000 composition

	Cr	Co	Mo	Ta	Al	Ti	Hf	C	B	Zr	Ni
RR1000	15	18.5	5	2	3	3.6	0.5	0.027	0.015	0.06	Balance

The most abundant element in RR1000 is nickel which forms the FCC γ matrix. The additions of cobalt, chromium and molybdenum partition to the γ matrix whereas aluminium, titanium and tantalum segregate to the second phase precipitate γ'. Primary MC carbides are formed with titanium, tantalum, zirconium and hafnium where was grain boundary $M_{23}C_6$ carbide particles and borides are formed with molybdenum and chromium. This partitioning of elements is illustrated in the EDS maps in Figure 23.

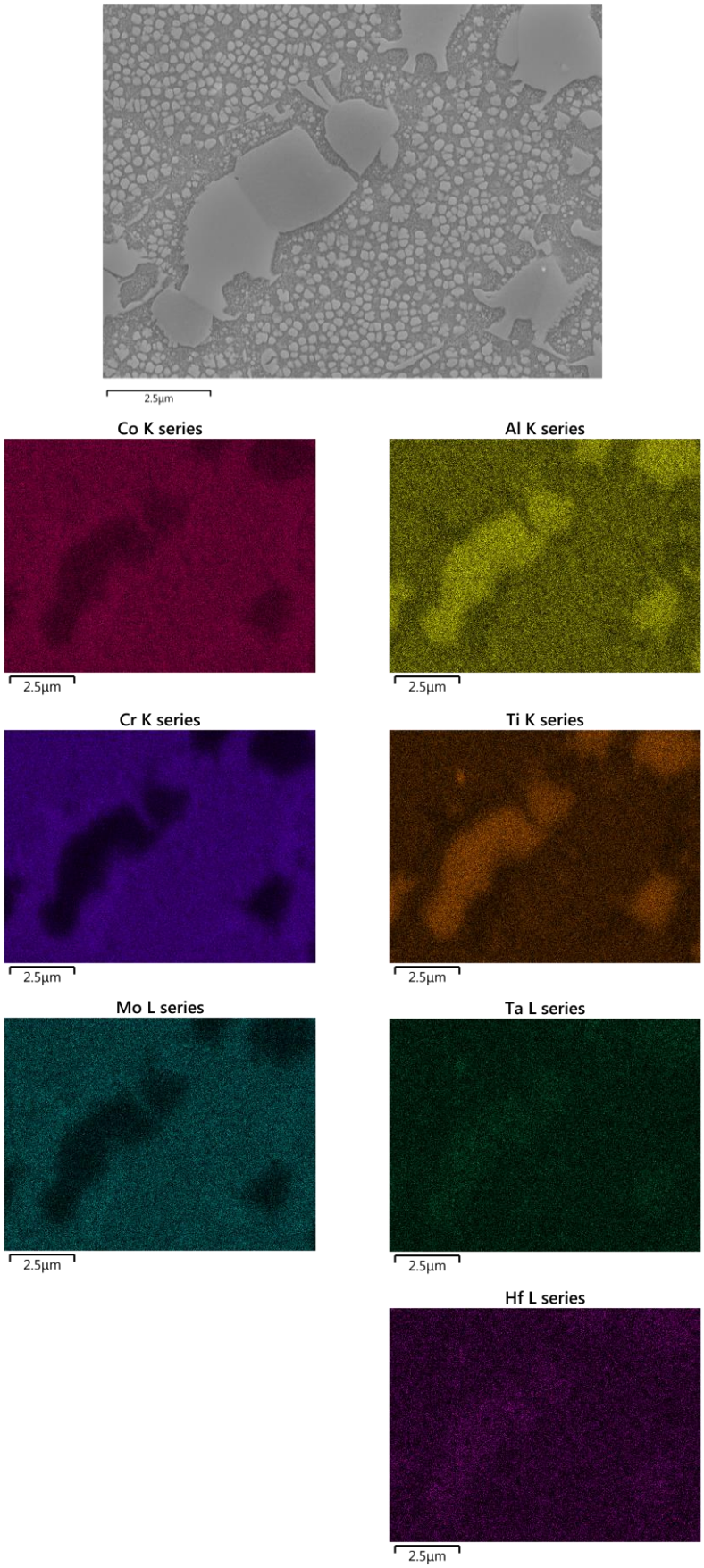

Figure 23 - EDS maps illustrating the elemental partitioning to γ & γ' in RR1000.

3.1.4 Specimen Geometry

The FG RR1000 material was supplied in the form of cylindrical cores that had been electrical discharge machined (EDM) from large pancake forgings, from the mid diameter position. The cylindrical cores measured approximately 40mm in height with an approximate diameter of 27mm.

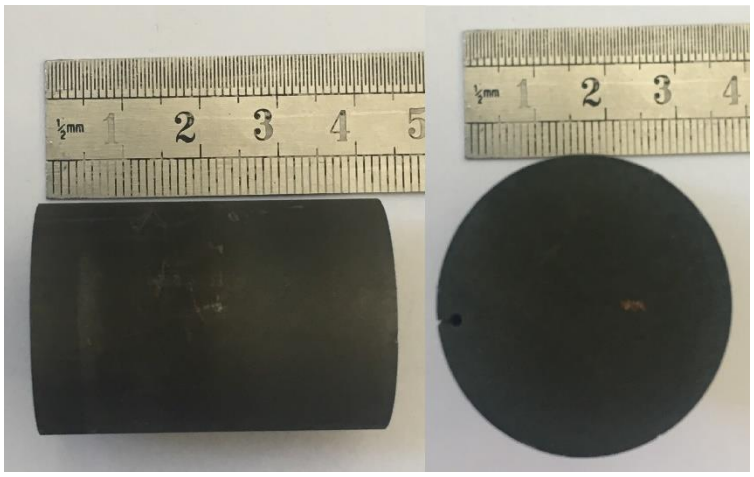

Figure 24 - RR1000 pancake cores supplied to be machined into specimens.

Each core was then sent for further EDM to machine out four rods measuring 9.5mm diameter by 40mm length from each core as detailed in Figure 25.

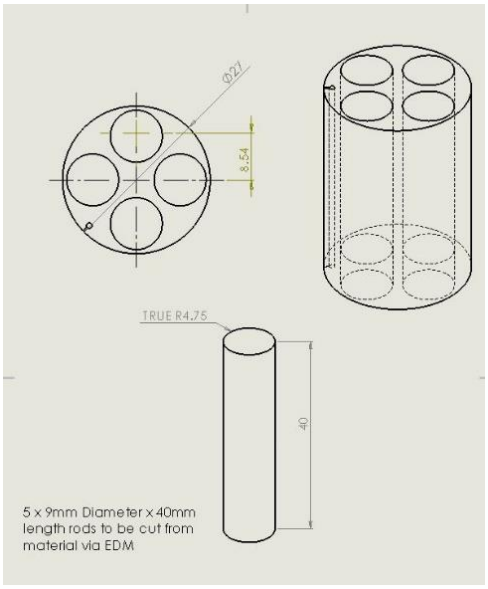

Figure 25 - Technical drawing for EDM'ing of four rods from each supplied RR1000 core.

The CG RR1000 material was supplied in the form of cylindrical rods that had been electrical discharge machined from the rim position of a large pancake forging. The cylindrical rods measured approximately 50mm in height with a diameter of 9.5mm.

Each rod was then turned down on a lathe to the required diameter of 8mm and sectioned into 12mm height compression specimens to a tolerance of +/- 15μm. The aspect ratio of 1.5 for the compression cylinders used in this work was chosen based on the guidelines set out in the handbook of workability and process design, stating aspect ratios should be no more than 2.0 to prevent buckling, with common aspect ratios ranging between 0.75 and 1.75 [109]

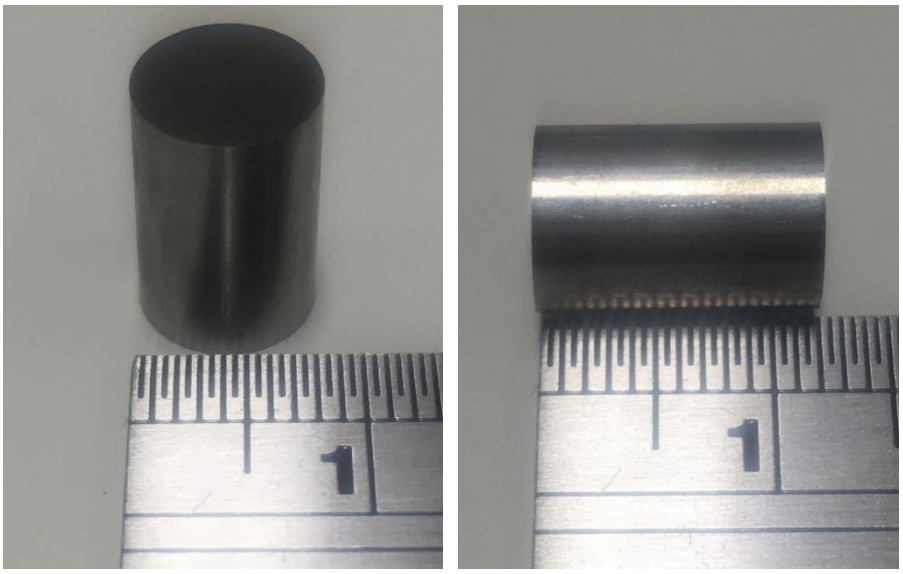

Figure 26 - Standard size 8mm diameter by 12mm height RR1000 compression specimen machined to a tolerance of +/- 15μm.

3.2 Materials Characterisation Methods

3.2.1 Metallography

Prior to any microstructural characterisation all specimens were subject to a specimen preparation procedure detailed below:

1. **Sectioning**

   Specimens are sectioned into an appropriate size and geometry in order to gain access to the area of interest within the specimen. In the case of the compression cylinders used throughout this study, each cylinder was cut in half along the radial-axial plane in order to gain access to the microstructure throughout the specimen assuming the specimen's microstructure is symmetrical around the centre point. All sectioning was carried out on an ATM Brilliant 240 cut off machine.

2. **Mounting**

   Following sectioning each specimen was mounted in 32mm diameter conductive Bakelite cylinders via an ATM Opal 410.

3. **Grinding & Polishing**

   Mounted specimens were then prepared for analysis via a 4-stage polishing routine outlined in Table 3 below

Stage	Polishing Cloth	Polishing media	Force (N)	Cloth speed (RPM)	Polishing time (mins)
1	Struers piano 120	Water	25	300	2
2	Struers Allegro	MetPrep Polymet 9µm	25	150	4
3	Struers Dac	MetPreo Polymet 3µm	25	150	6
4	Struers Chem	MetPrep OPUS 0.04µm Spheroidal silica	20	150	12

Table 3 - Polishing procedure.

3.2.2 Etching techniques

Two etching techniques were used throughout the present study depending on what microstructural features needed to be revealed. If it was necessary to reveal grain boundaries, then a chemical etch with kalling's reagent was used but at the cost of also removing the gamma prime precipitates leaving recesses where they once were. If the size and morphology of gamma prime precipitates and carbides etc. were of interest, then the specimens would be electrolytically etched with 10% phosphoric acid. The etching procedure for each method is detailed below.

Kalling's reagent 1&2 method

1. Specimens cleaned with warm soapy water.
2. Specimens cleaned with acetone and blow dried.
3. Clean specimen surface then immersed in kalling's reagent or alternatively kalling's can be applied to the surface with a clean cotton swab.
4. Specimen exposed to kalling's reagent for 20s.
5. Specimen rinsed with water to remove all etchant.
6. Specimen cleaned with acetone and blow dried.
7. Microstructure was then examined under an optical microscope to check if desired level of etching was achieved, if not sufficient steps 3-6 were repeated.

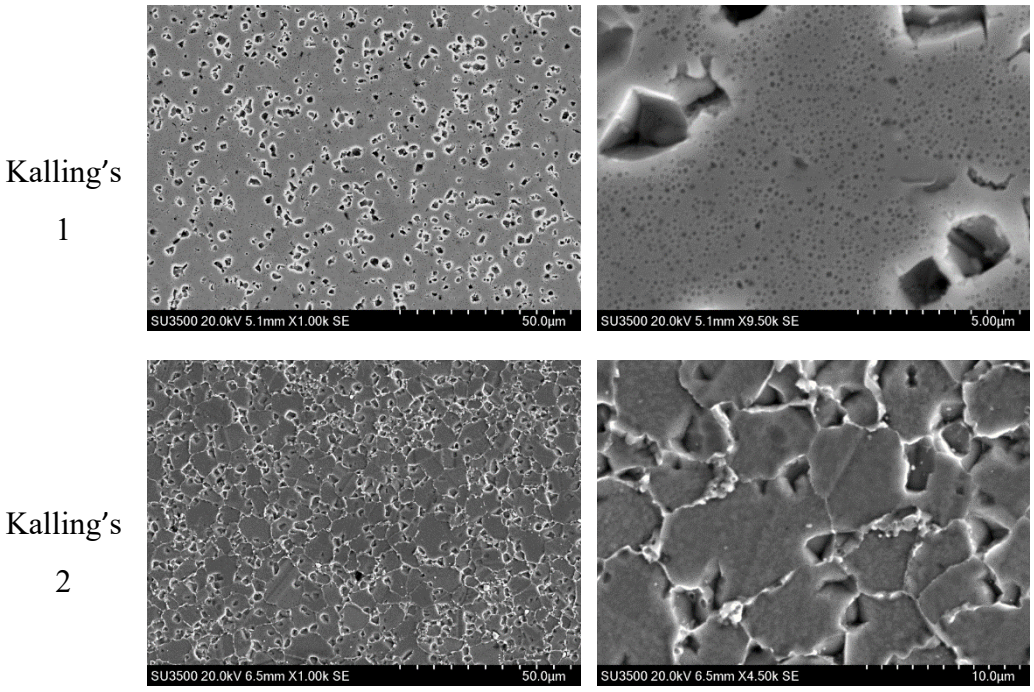

Figure 27 - Example microstructures produced by kalling's 1 & 2 etchants.

10% phosphoric acid electro etch method

1. Specimens cleaned with warm soapy water.
2. Specimens cleaned with acetone and blow dried.
3. Specimen was clamped with a jubilee clip.
4. The positive terminal of the power pack was clamped to the jubilee clip via a crocodile clip.
5. 10% phosphoric acid was applied to the surface of the specimen with a pipette ensuring that all areas of the sample to be etched were fully submerged in phosphoric acid.
6. The power pack was set to 2.5 V and 100 mA.
7. The power pack was activated, and the negative terminal was passed through the phosphoric acid on the specimen making sure that the terminal did not come into contact with the specimen surface.
8. After 10 seconds or when the specimen surface changes colour the negative terminal is removed.
9. Specimen rinsed with water to remove all etchant.
10. Specimen cleaned with acetone then blow dried.

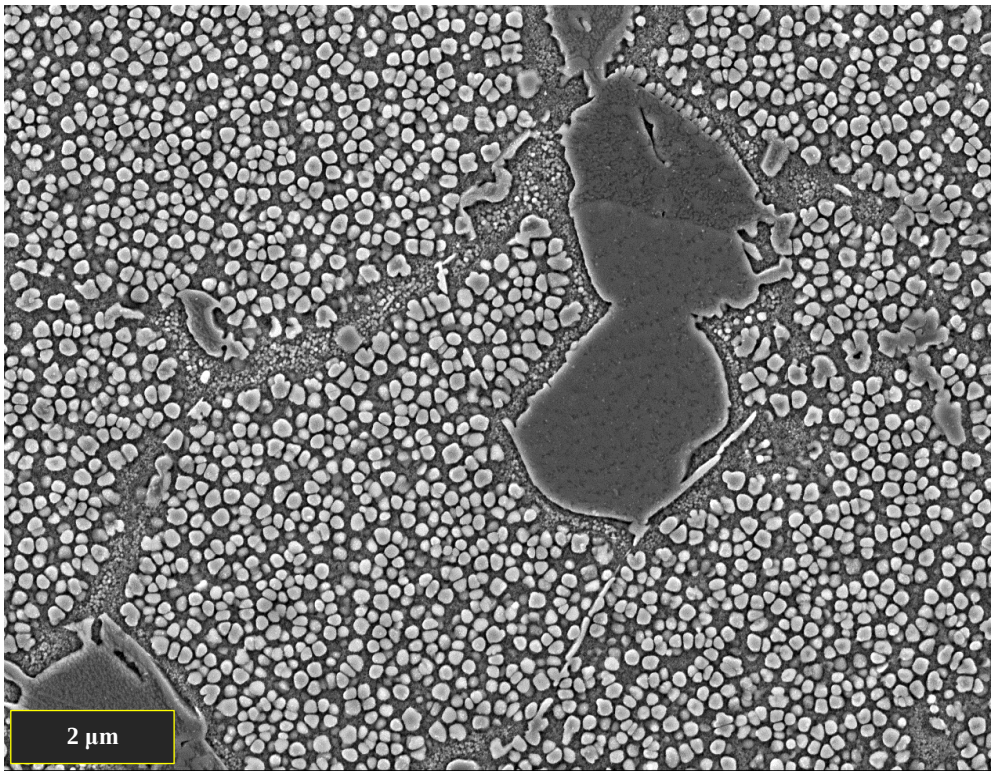

Figure 28 - Example microstructures produced by Electrolytical etching with 10% phosphoric acid.

3.2.3 Microscopy

3.2.3.1 Optical microscopy

All optical micrographs were taken on a Keyence digital microscope fitted with a Z100R 50-1000x magnification lens.

3.2.3.1.1 Mean linear intercept via optical micrographs

The grain size of each pedigree of RR1000 used was initially quantified via the mean linear intercept (MLI) method on optical micrographs of chemically etched specimens as shown in Figure 29 (to ASTM E12 guidelines[115]). Five lines of inspection were used over five images of each RR1000 pedigree so that an average grain diameter could be calculated from the average grain size of each micrograph. Table 4 details the results of the MLI analysis.

Variant	Average Grain Diameter (um)
FG 431	6.4 (+/- 0.8) *
FG 443	6.1 (+/- 0.7)
CG	41.9 (+/- 6.9)

Table 4 - Average grain diameter calculated via the MLI method applied to optical micrographs (95% confidence limit is given in brackets)(* values used in results section comparisons).

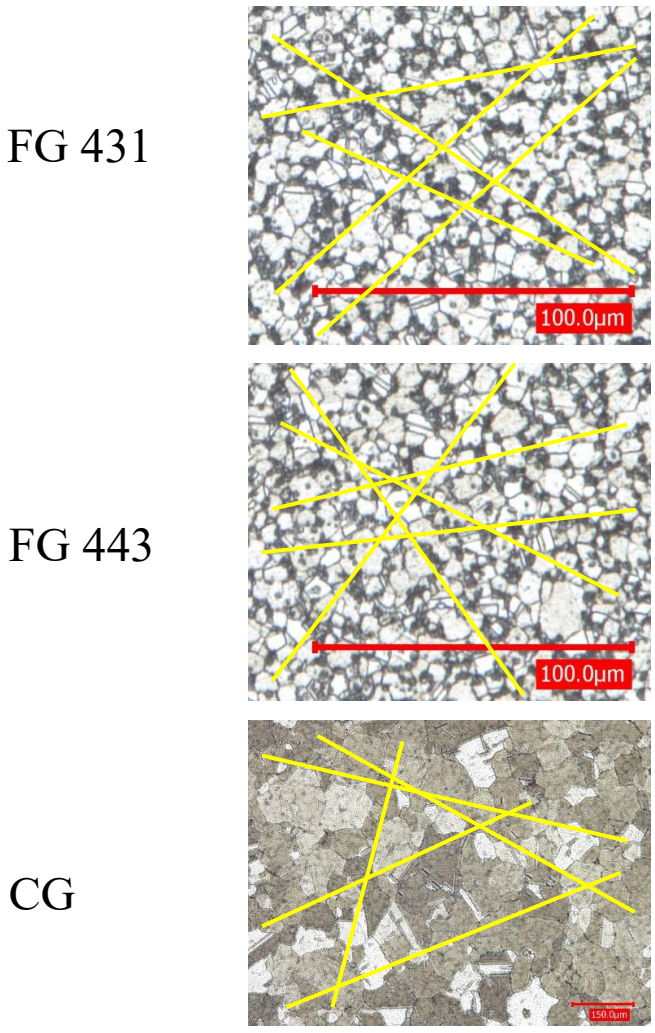

Figure 29 - Images from grain diameter measurement of each RR1000 variant via MLI method.

As grain data gathered via the MLI method is susceptible to human error, EBSD data was used to represent average grain sizes wherever possible.
EBSD data cannot be used to represent the average grain size of the FG specimens that contain primary γ' (i.e. Parent FG - 1100°C test FG) as the primary γ' is incoherent with the γ matrix and is recorded as small grains during EBSD analysis. This results in a smaller average grain size than is present. Because of this, the average grain size for the FG variant 431 stated here was used in the results and discussion section comparisons. This value measurement is starred in Table 4 to signify this. FG 443 was not used during testing and therefore is not used in any results section comparisons.

The CG variant does not contain any primary γ', therefore EBSD data can always be used to represent its average grain size accurately. Because of this, the average grain size value for the CG variant stated here was not used in the subsequent microstructural comparisons in the results and discussion section.

3.2.3.1.2 Primary gamma prime size distribution analysis

The size distribution and volume fraction of primary γ' in each FG variant was quantified via image analysis of optical micrographs using ImageJ software. The image analysis procedure is given in steps 1-4 in Figure 30. This method of analysing primary γ' is in alignment with the Rolls-Royce best practice guidelines [116].

Three optical micrographs of fine grain RR1000 after electro etching were taken.

The primary γ' have a bright appearance under optical microscopy, whereas the γ matrix appears dark. Secondary and tertiary γ' are too small to be seen in optical micrographs and are measured via SEM.

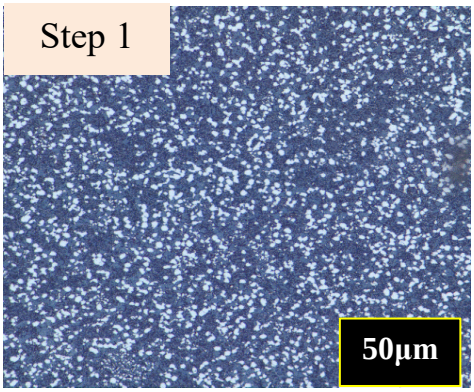

The light coloured primary γ' were then isolated with ImageJ's threshold function. This results in a black and white image with the primary γ' coloured black and the γ matrix being coloured white.

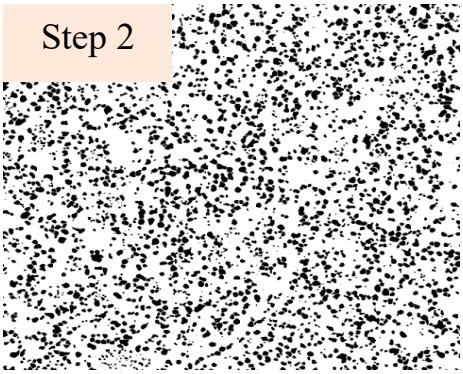

The black thresholded γ' were then measured with the analyse particles function within ImageJ. This function measures the number of black pixels in each primary γ' and uses the image's scale bar size to produce particle areas and total area fraction of particles for the image.

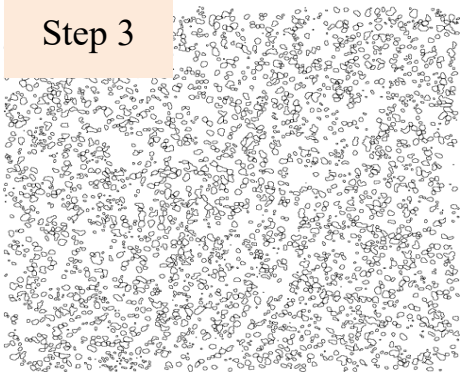

The particle area measurements calculated in ImageJ were then imported into an excel document where they were converted to equivalent circle diameters (ECD). The ECDs were calculated by rearranging the area of a circle equation and are given in µm. The size distributions were then analysed, producing average size values and standard deviation etc.

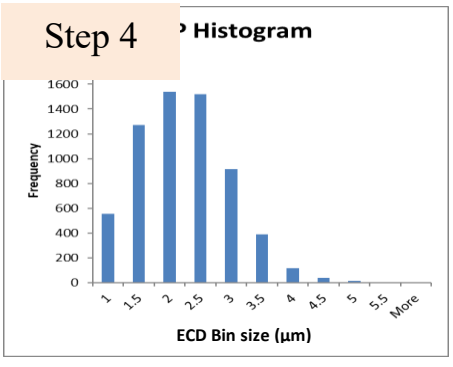

Figure 30 - ImageJ routine for characterising primary γ' from optical micrographs of electro etched specimens.

3.2.3.1.3 Fraction of liquid measurement

A method of quantifying the fraction of liquid produced during testing was needed, so that the liquid propagation rate in both RR1000 variants could be characterised and any mechanical data produced could be correlated to liquid fraction that specimen experienced. When a semi-liquated specimen is electrolytically etched with 10% phosphoric acid, the liquated areas differentially etch to the bulk of the material that remained solid[83]–[86]. The liquated areas appear under optical microscopy as globular structures with a bright blue/white colour. The bulk material that remained solid etches to a shade of yellow with some material etching to a dark blue haze if chemical inhomogeneity is present.

Figure 31 illustrates the globular liquated regions when viewed under optical microscopy. Using the appearance of the differentially etching liquid, a method of quantifying the amount of liquated material was developed. The method utilised ImageJ image analysis software to threshold out the liquated material from the bulk to give an estimation of the fraction of liquid. Figure 32 describes the steps of the ImageJ method developed to quantify the liquid fraction.

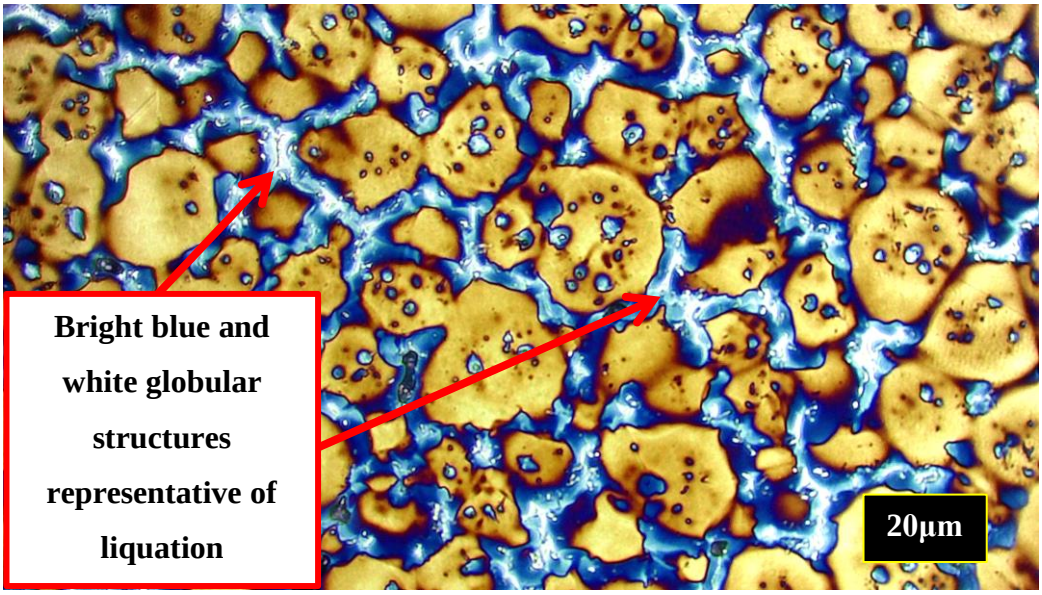

Figure 31 – Optical micrograph of a FG RR1000 specimen that has experienced liquation, illustrating the appearance of the liquated material as a bright blue and white globular structure in contrast to the yellow bulk material that remained solid.

The colour threshold function within ImageJ was used to pick out the differentially etched liquated regions represented by the blue and white globular structures, which are then highlighted red.

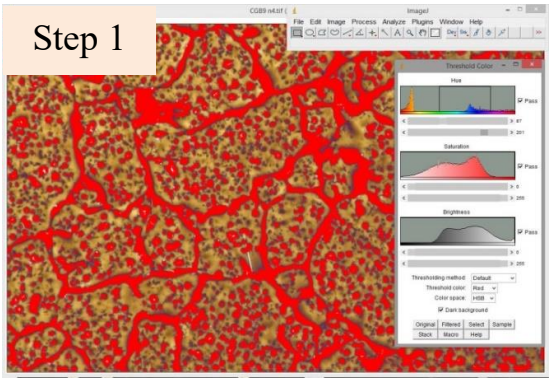

An overlay was created highlighting the regions picked out with the threshold function with yellow outlines. This allows the user to assess the accuracy of the threshold settings and make any adjustments needed.

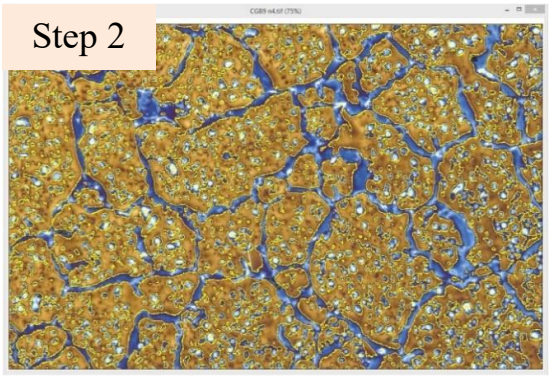

After the threshold is complete the liquated regions are coloured black, with the bulk material that remained solid being coloured white. ImageJ's measure function is then used to measure the percentage of black pixels, giving you an approximate value for the fraction of liquid in that image.

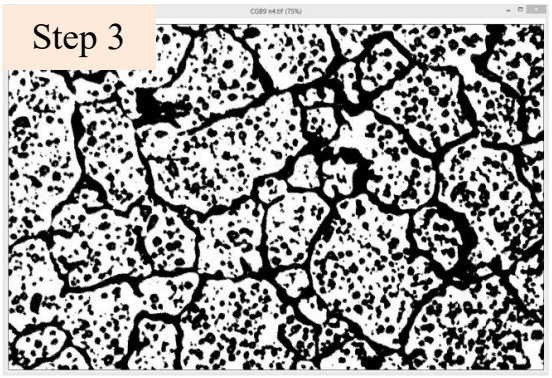

Figure 32 - Method developed to estimate fraction of liquid for semi-solid nickel superalloy specimens.

Modified electro etching method for semi solid specimens

When electro etching RR1000 specimens, the outer perimeter of the specimen tends to etch at a slightly faster rate than the centre of the specimen. This can leave an etch intensity gradient from the perimeter of the specimen towards the centre.

When measuring liquid fractions, a heavy etch across the whole specimen is necessary to highlight the liquated areas. As a result, semi solid specimens etched with the conventional method, detailed earlier in section 3.2.2 '10% phosphoric acid electro etch method', have the liquated regions visible in the heavily etched perimeter but not at the centre of the specimen where the etch has been lighter.

In order to combat this, a second etch is conducted on the specimen in the same fashion as the conventional etch procedure, except on this occasion phosphoric acid is only applied to the centre of the specimen via a pipette. This allows the centre of the specimen to be etched to the same degree as the perimeter, highlighting the liquated regions evenly across the whole specimen.

Image capturing routine for liquation measurement.

After the specimen had been suitably etched to reveal the liquated material across the whole specimen, the fraction of liquid could be measured. Thirteen images were taken across the diameter of the specimen in the arrangement depicted in Figure 33. The images were then subject to the ImageJ liquation measurement routine described in Figure 32. The average liquid fraction for the specimen was then calculated from the results of each image.

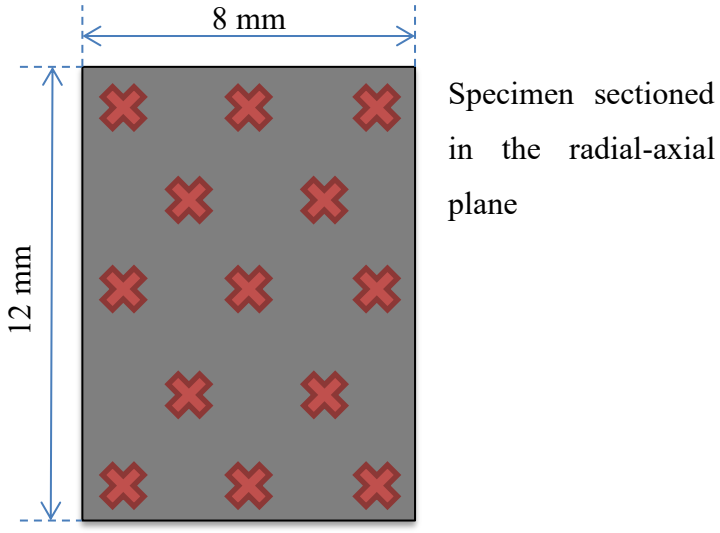

Figure 33 - Approximate location of images taken during liquid fraction measurement.

3.2.3.2 Scanning electron microscopy

All scanning electron microscopy (SEM) was conducted on either a Hitachi SU3500 tungsten filament SEM or a JEOL 7800F field emission gun (FEG) SEM when higher resolution images were required such as secondary γ' analysis.

3.2.3.2.1 Secondary gamma prime distribution analysis

High magnification high resolution images of secondary γ' were taken on the FEG SEM. This produced images with an approximate image width of 12um, suitable for particle size analysis to be conducted via ImageJ software. The secondary γ' analysis procedure is detailed in steps 1-4 in Figure 34. This method of analysing secondary γ' is in alignment with the Rolls-Royce best practice guidelines [116].

Three SEM micrographs of secondary γ' were taken after the specimen had been electro etched. The images were taken in backscattered electron mode to increase the contrast between the γ' and the γ matrix. The γ' appear light grey in colour and the γ matrix is dark grey.

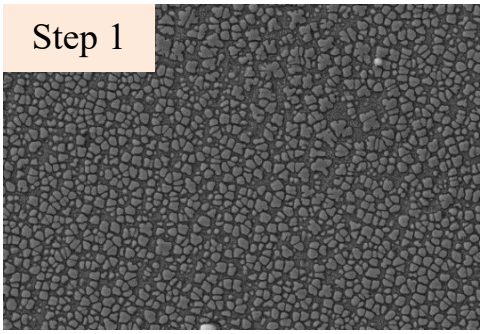

Because the primary γ' appears as a lighter shade of grey in the SEM micrograph it can be isolated with ImageJ's threshold function. This results in a black and white image with the secondary γ' coloured black and the γ matrix being coloured white.

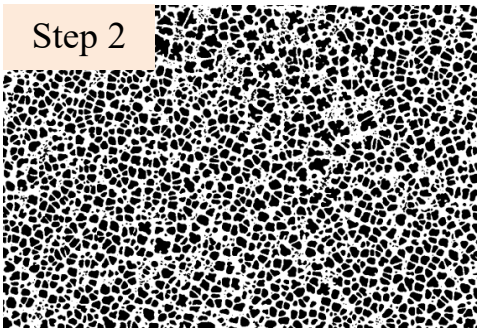

The thresholded γ' was then measured with the analyse particles function within ImageJ. This function measures the number of black pixels in each secondary γ' and uses the image's scale bar size to produce particle areas and total area fraction of particles for the image.

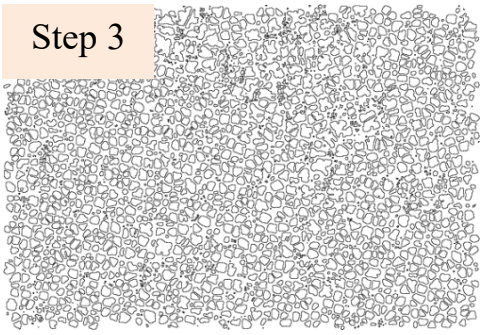

The particle area measurements taken by ImageJ were then imported into an excel document where they were converted to an equivalent circle diameter (ECD). The ECDs were calculated by rearranging the area of a circle equation and are given in nm. Average particle size and standard deviation were then calculated.

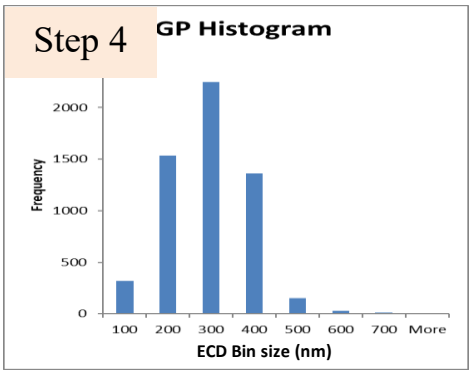

Figure 34 - ImageJ routine for characterising secondary γ' from SEM micrographs of electro etched specimens.

3.2.4 Electron back scatter diffraction (EBSD)

EBSD is a technique used to gain crystallographic data from a material. EBSD is carried out within an SEM and involves the diffraction of electrons. To perform EBSD an electron beam must be projected at a highly polished sample, at an angle of 20° to the sample's surface. The electron beam then interacts with the crystal lattice of the sample. Some backscattered electrons are channelled into different paths, with some of these paths overlapping to create patterns. A phosphor screen placed a short distance from the sample reveals these diffraction patterns by converting the electrons into light, which is detected by a camera. This type of EBSD set up is illustrated in the diagram in Figure 35 adapted from [117]. These diffraction patterns are known as Kikuchi diffraction patterns. The orientation of these patterns is used to calculate the structural characteristics of the material such as the crystallographic orientation. Modern EBSD equipment uses this technique to perform EBSD maps, which give further structural characteristics such as grain size, texture and local misorientation [118].

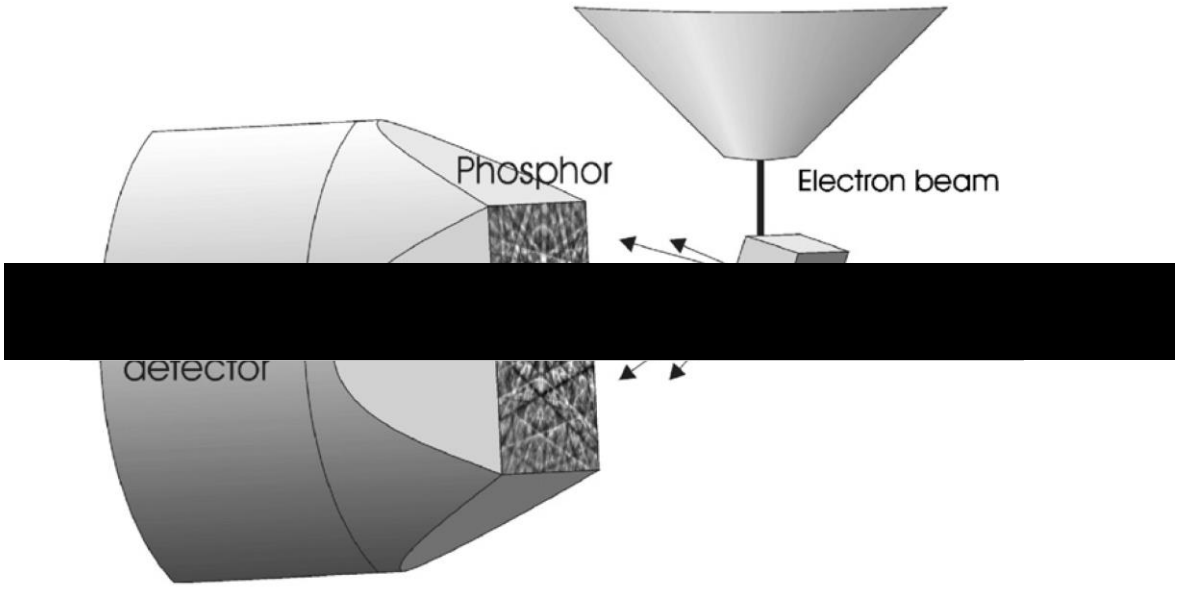

Figure 35 – Schematic diagram illustrating a typical EBSD set up. Adapted from [117]

All EBSD data in this project was captured using a Hitachi SU3500 SEM paired with an Oxford instruments EBSD camera. Aztec HKL software was used to operate the SEM and EBSD camera to create the EBSD maps. Scans were taken at 20kV accelerating voltage and a step size of 0.6µm. All post processing of EBSD data was conducted within Channel 5 software, predominantly using Tango (Figure 36) for the creation of maps detailing grain characteristics of interest. All EBSD scans were taken in the orientation illustrated in Figure 37. A total of three EBSD scans of each specimen were conducted so that average values could be calculated.

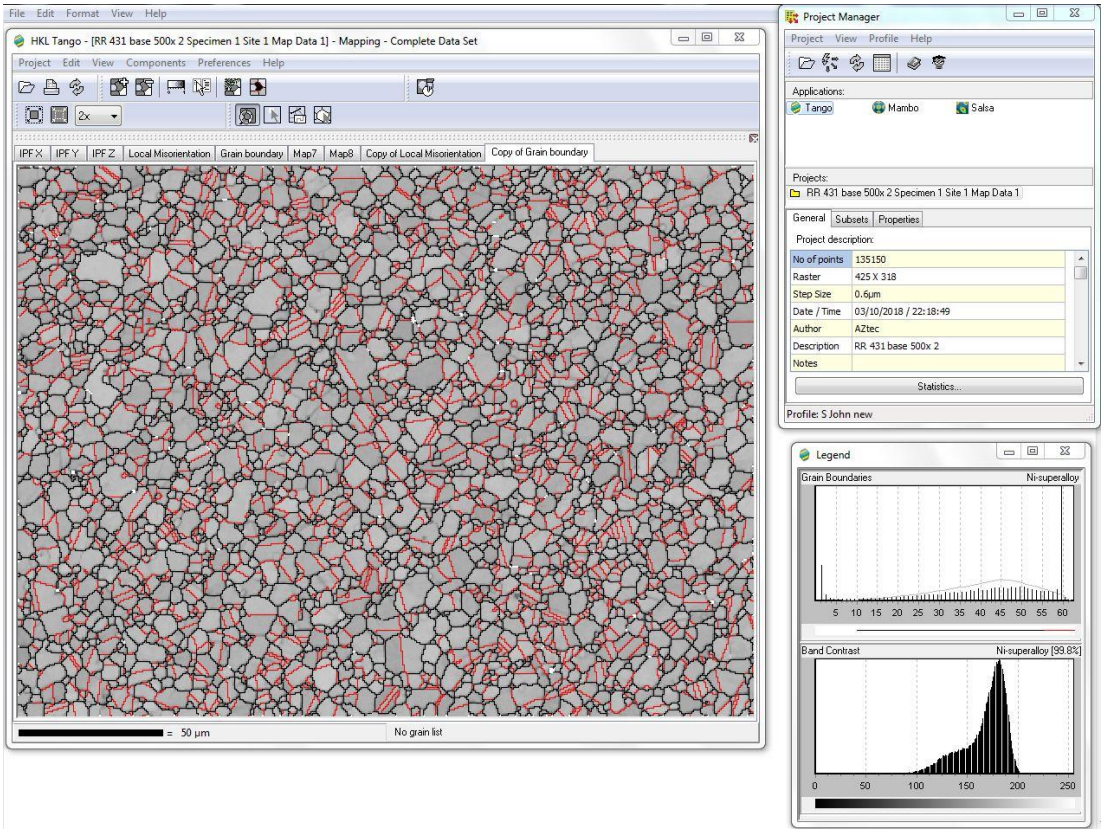

Figure 36 - HKL Channel 5 Tango software

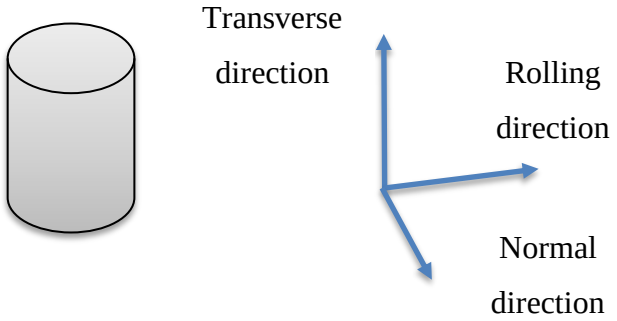

Figure 37 - EBSD scan orientation relative to specimen.

3.2.4.1 Grain orientation

Orientation maps and pole figures were created to assess each variant of RR1000 for grain texture.

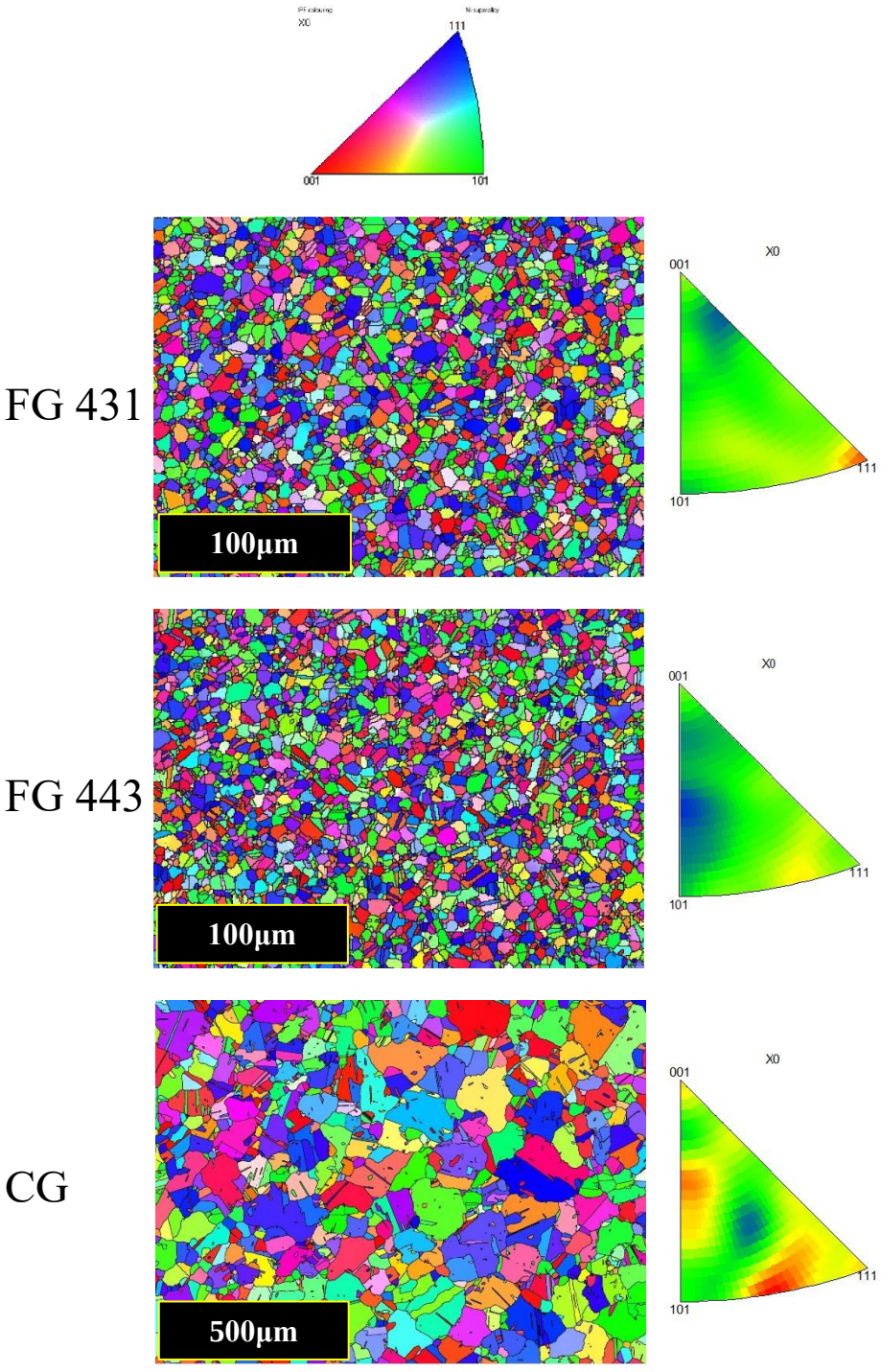

Figure 38 - X axis orientation maps & pole figures for all three RR1000 variants. All maps were generated at 0.6 um step size.

With multiple of uniform density (MUD) values ranging between 0.64 and 1.3, all three variants of RR1000 exhibited random grain orientation with no dominant textures in the X,Y or Z direction [119]. The X direction is shown in Figure 38 as an example.

3.2.4.2 Local misorientation

In order to assess the parent materials for any residual stress within them, local miss-orientation maps were created to illustrate any strain on the crystal lattice caused by residual stress. Each variant was found to be relatively stress free as shown in Figure 39, with no variant displaying an average kernel average misorientation (KAM) value higher than 0.35°. KAM is calculated by comparing the orientation of each data point with the ones surrounding it in a 3x3 grid. The average misorientation is then calculated.

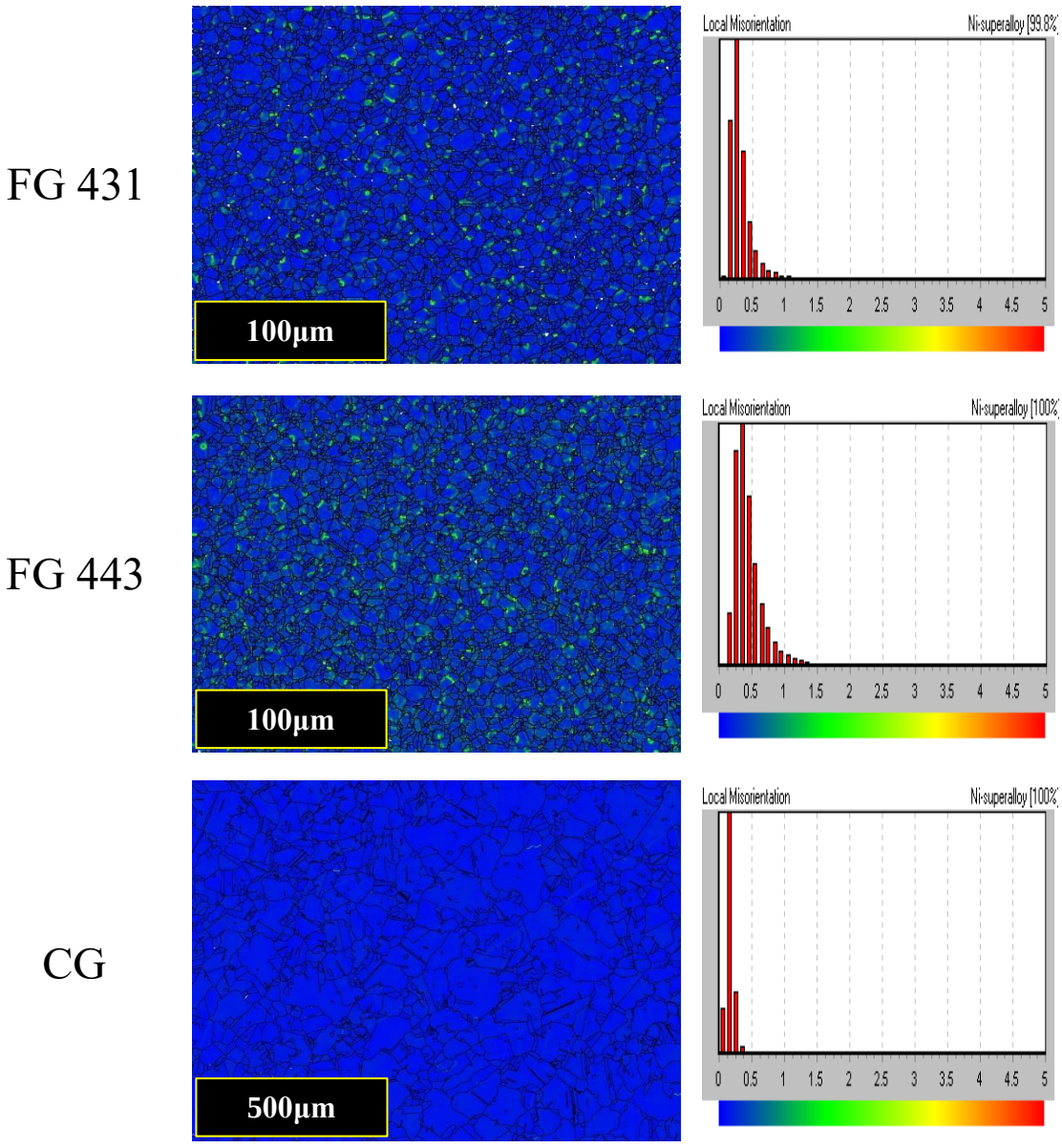

Figure 39 - Local misorientation maps to illustrate any residual stress within the three variants of RR1000. All three variants were mapped with a 0.6 um step size.

3.2.4.3 Grain size & grain boundary characteristics

3.2.4.3.1 Grain size calculations

Channel5 Tango software has inbuilt grain size analysis tools, which can reliably produce grain size data with greater accuracy than conventional MLI methods conducted on optical micrographs. The grain size is calculated as an equivalent circle diameter (ECD) from the area of each grain measured during the scan. A series of 3 EBSD maps were conducted on each of the RR1000 specimens and an average grain size value was calculated from the average grain sizes in each of the three maps. The average grain size of the parent material of each variant is shown in Table 5.

Variant	Average Grain Diameter (um)
FG 431	4.5 (+/- 1.0)
FG 443	4.6 (+/- 1.2)
CG	48.0 (+/- 5.5) *

Table 5 - Average grain diameter calculated as ECD from measured grain area from EBSD data (95% confidence limit is given in brackets) (* values used in results section comparisons).

EBSD grain size data for the fine grain variants can be misleading as the primary γ' is incoherent with the gamma matrix and therefore is detected in the EBSD software as a separate grain. As primary γ' is relatively small compared to the average grain size of the fine grain variants of RR1000, this reduces the EBSD grain size data making it appear smaller than its true value. For this reason, grain size data for RR1000 specimens containing primary γ' must be calculated by the MLI method of optical micrographs as stated earlier. Only the average grain size data for the CG variant parent material stated here was used in the results section comparisons and is starred in Table 5.

3.2.4.3.2 Special Σ3 twin boundaries

All three variants contained a large number of special grain boundaries, namely sigma 3 twin boundaries as revealed in red in Figure 40. In both grain size calculations twin boundaries were not counted as a grain separating boundary. The average quantity of Σ3 twin boundaries in each variant calculated as a percentage of total boundaries was as follows: FG 431 = 22.1% (+/- 1.8%), FG443 = 23.7% (+/- 2.1%) and CG = 46.2% (+/- 1.6%). These average values were calculated by averaging the percentage of Σ3 twin boundaries in each of the three EBSD maps conducted on each specimen. The 95% confidence interval for these average values is given in brackets.

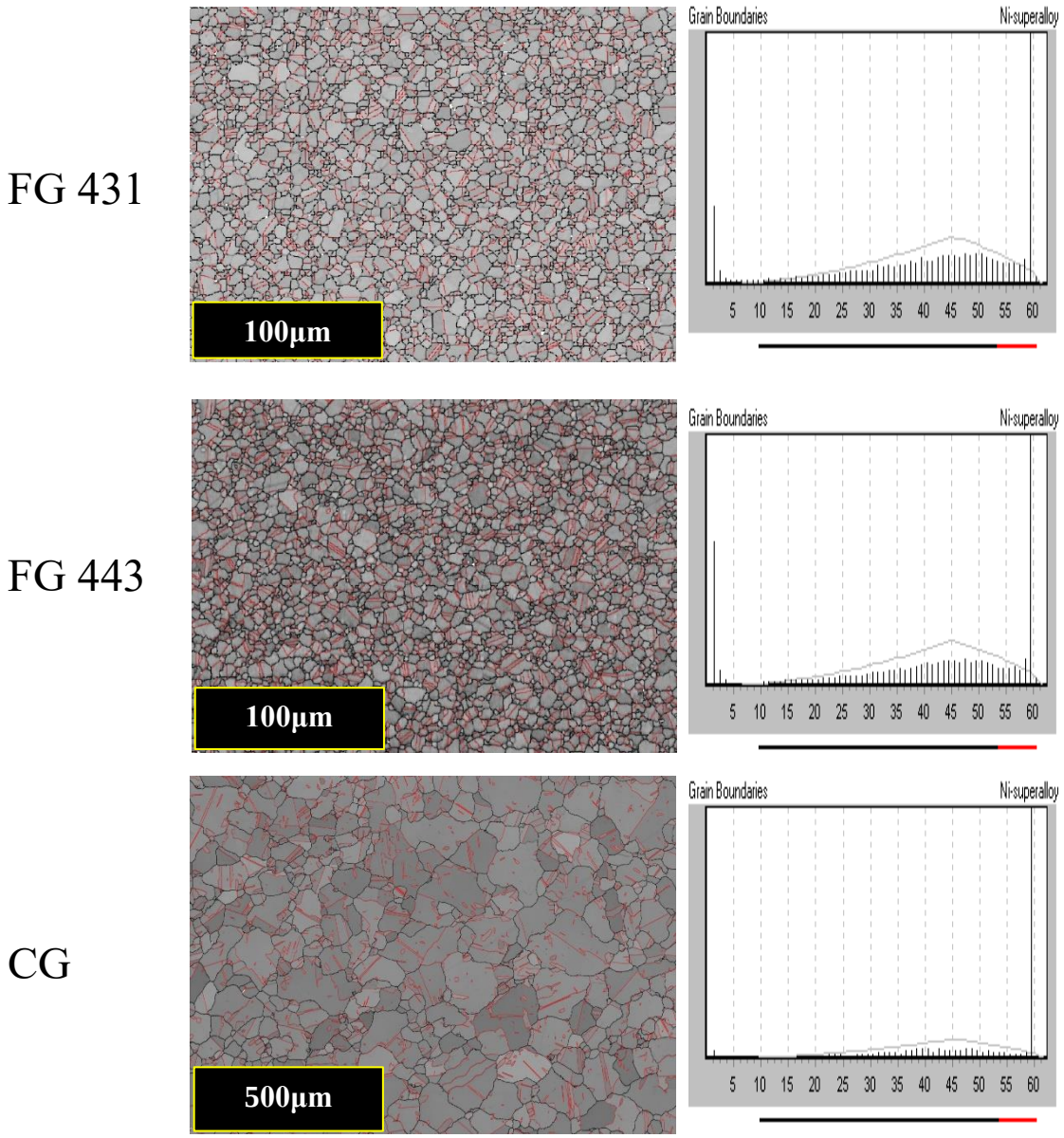

Figure 40 - Grain boundary EBSD map illustrating grain boundaries of 10 - 55° in black and twin boundaries of 55-60° in red. Each grain boundary map is overlayed on a map of band contrast.

3.2.5 Energy-dispersive X-ray spectroscopy (EDS)

All EDS analysis was conducted using an Oxford instruments X-Max 50^N fitted to both SEMs with the data acquisition controlled with Aztec software to produce EDS maps, line scans and point ID's in order to characterise the microstructural features before and after testing.

3.3 Aims of Experimentation.

The experimental objectives of the project were optimistic and included the following:

- Investigate methods of semi-solid testing.
    - Gleeble thermomechanical simulator.
    - Servo hydraulic compression machines paired with:
        - Radiant furnace.
        - Induction heating.
        - Resistance heating.

- Design a novel semi-solid testing facility, investigating:
    - Induction heating as a heat source for hot compression.
    - Methods for inert atmosphere testing.
    - Specimen quenching mechanisms.
    - Load train requirements/design to withstand semi-solid nickel super alloy temperatures.

- Manufacture and commission the novel semi-solid testing facility.
    - Optimise the semi-solid testing facility so that it can accurately heat bulk RR1000 specimens up to 1200°C at heating rates of up to 25°Cs^{-1}.
    - Validate the semi-solid testing facility by replicating the observations of M. Attallah et al [4], causing constitutional liquation of primary γ' in FG RR1000 when heating specimens above the γ' solvus temperature at heating rates of 5-50°Cs^{-1}.

- Utilise the novel semi-solid testing facility to build on previous research and investigate/conduct the following:
    - Sub-solidus liquation mechanisms of the CG RR1000 variant.
    - Liquid propagation in bulk RR1000 specimens, characterising the liquid propagation rate in both the FG and CG variant.
    - Characterisation of microstructural features produced by re-solidification of liquated material.
    - Characterisation of the microstructural evolution that occurs during rapid heating on the lead up to liquation in both FG and CG RR1000 and assess the effect these changes have on the resultant hardness of each variant.
    - The effect of a semi-solid microstructure on the mechanical properties of RR1000, namely the compressive flow stress and the resultant hardness after re-solidification.

- Utilise the new research findings and mechanical properties data to gain a better understanding of the evolution of RR1000's material characteristics during the inertia friction welding process by:
    - Assessing the microstructure of a series of interrupted FG and CG RR1000 inertia friction welds, looking for evidence of liquation.
    - Comparing the microstructures of these interrupted inertia friction welds with the microstructure of the specimens tested in the novel semi-solid testing facility.

3.4 Proposed Test Matrix

In order to characterise the microstructural evolution of both RR1000 variants during rapid heating, a series of heat and quench only tests were conducted. Specimens were heated to a range of target temperatures at different rates and water quenched with no compression applied. Some specimens were also held at the target temperature so that the liquid propagation rate in each variant could be characterised. The specimens were then sectioned, and their microstructure evaluated to assess the microstructural changes that had occurred. This allowed the microstructural evolution of both RR1000 variants when subject to rapid heating rates to be characterised.

During this evaluation, the fraction of liquid was measured by quantifying the area fraction of the differentially etching blue and white globular structures using the method described in section 3.2.3.1.3. From these measurements a series of calibration curves were created, illustrating the fraction of liquid for given temperatures, heating rates and hold times, allowing the liquid propagation rate to be characterised.

The most common way of quantifying the fraction of liquid present in a specimen, in order to conduct a semi-solid test, is by using continuous cooling curves or phase diagrams and simply estimating the amount of liquid expected. As the liquation experienced by both RR1000 variants is suspected to originate from sub-solidus liquation mechanisms resulting from the rapid heating, these methods of quantifying liquid fraction are unsuitable.

The calibration curves created for the characterisation of the liquid propagation rate could also solve this problem by using them to estimate the fraction of liquid during any subsequent semi-solid compression tests. All heat-only tests were conducted successfully allowing the calibration curves to be created. This allowed the microstructural evolution and liquation mechanisms in both RR1000 variants to be characterised. Unfortunately, due to complications with testing equipment the semi-solid compression tests were not completed. The challenges that prevented the compression testing are discussed in detail later in section 3.9.1.

3.4.1 Heat Only Tests

Planned Test	Test not required	✔ = Successful test	✗ = Test not completed

Fine Grain

Heating rate: 25°C s

Hold Time \ Temp	900°C	1000°C	1050°C	1100°C	1160°C	1200°C
1s	✔	✔	✔	✔	✔	✔
15s					✔	✔
45s					✔	✔

Heating rate: 12.5°C s

Hold Time \ Temp	900°C	1000°C	1050°C	1100°C	1160°C	1200°C
1s					✔	✔
15s					✔	✔
45s					✔	✔

Heating rate: 1°C s

Hold Time \ Temp	900°C	1000°C	1050°C	1100°C	1160°C	1200°C
1s						✔
15s						
45s						

Coarse Grain

Heating rate: 25°C s

Hold Time \ Temp	900°C	1000°C	1050°C	1100°C	1160°C	1200°C
1s	✔	✔	✔	✔	✔	✔
15s					✔	✔
45s					✔	✔

Heating rate: 12.5°C s

Hold Time \ Temp	900°C	1000°C	1050°C	1100°C	1160°C	1200°C
1s						✔
15s						✔
45s						✔

Heating rate: 1°C s

Hold Time \ Temp	900°C	1000°C	1050°C	1100°C	1160°C	1200°C
1s						✔
15s						
45s						

3.4.2 Proposed Compression tests

Fine Grain

Semi Solid

25°Cs^{-1} Hold Time	Temp 1160°C	1200°C
1s	✗	✗
15s	✗	✗
45s	✗	✗

12.5°Cs Hold Time	Temp 1160°C	1200°C
1s	✗	✗
15s	✗	✗
45s	✗	✗

Coarse Grain

Semi Solid

25°Cs^{-1} Hold Time	Temp 1160°C	1200°C
1s	✗	✗
15s	✗	✗
45s	✗	✗

12.5°Cs Hold Time	Temp 1160°C	1200°C
1s		✗
15s		✗
45s		✗

The compression tests were not completed during the current research project due to complications during testing. The problems that prevented these tests are detailed in section 3.9.1.

3.5 Assessment of available compression methods

3.5.1 Gleeble Thermomechanical Simulator.

A thorough investigation was conducted, assessing the suitability of a DSI Gleeble 1500 thermo-mechanical simulator to carry out the semi-solid testing needed for this program of work. This assessment is detailed in section 2.6.1 Semi-solid compression testing - equipment & methods, with the main outcomes summarised below.

The main drawback that prevented the use of the Gleeble 1500 was its horizontal load train, which would have caused complications when testing at high fraction of liquid, as the specimen would likely bow under its own weight leading to inhomogeneous deformation. When compression testing in a Gleeble thermomechanical simulator, the specimen experiences large temperature gradients due to the water cooled grips used to cool the load train when the resistance heating system is active. These temperature gradients would make it difficult to accurately characterise the liquid propagation rate in bulk specimens. Although the literature suggested that heating rates of $20°Cs^{-1}$ could be achieved on compression cylinders using a Gleeble, the handbook provided with the Gleeble 1500 at the SMaRT laboratory and application notes from DSI suggested heating rates should be limited to $5°Cs^{-1}$ when using the ISO-T tungsten compression anvils to prevent the specimen welding to the anvils [95]. This limitation on heating rate would have reduced the scope of the project too much, reaffirming that the Gleeble 1500 was not suitable for this program of work.

3.5.2 Servo Hydraulic Compression.

A multitude of compression work has been conducted previously at Swansea university, ranging from hot compression to cryogenic compression. A previous research project conducted at Swansea in collaboration with Rolls-Royce Plc. PROMOTE (Process Modelling for Tomorrows Engines) focused on hot compression of RR1000. The aim of the project was to generate mechanical property data to support the constitutive description of RR1000 within a finite element-based computer model of inertia friction welding. The tests were conducted in air, utilising the servo hydraulic compression machine FG3 paired with a Severn Thermal radiant element furnace capable of temperatures up to 1250°C. An outline of the tests conducted in this project is displayed in Table 6 below:

	Strain Rate s^{-1}					
Temp (°C)	**0.001**	**0.01**	**0.1**	**1**	**10**	**20**
600	CG	CG/FG	CG	CG	CG	CG
700	CG	CG/FG	CG	CG	CG	CG
800	CG	CG/FG	CG/FG	CG/FG	CG	CG
900	CG	CG/FG	CG/FG	CG/FG	CG	CG
1000	CG	CG/FG	CG/FG	CG/FG	CG/FG	CG/FG
1050	CG	CG/FG	CG/FG	CG/FG	CG/FG	CG/FG
1100	CG	CG/FG	CG/FG	CG/FG	CG/FG	CG/FG
1150	CG	CG/FG	CG/FG	CG/FG	CG/FG	CG/FG
1200	CG	CG/FG	CG/FG	CG/FG	CG/FG	CG/FG

Table 6 - Test matrix of compression tests conducted on RR1000 during the PROMOTE program.

Compression testing was carried out on three variants of RR1000; coarse grain, fine grain aged for 4 hours at 760°C and fine grain aged for 16 hours at 760°C. It was found that all three variants experienced strain induced porosity (SIP) throughout the specimen when testing at temperatures above 1150°C (Figure 41, A), with specimens completely disintegrating when tested at 1200°C (Figure 41, B & C). At the time of testing, the cause of the SIP and disintegration was not fully understood but was suspected to be a consequence of the oxidation seen throughout the disintegrated specimens. It is now known that at these test temperatures the presence of liquated material is highly probable and was likely a contributing factor to the SIP and disintegration.

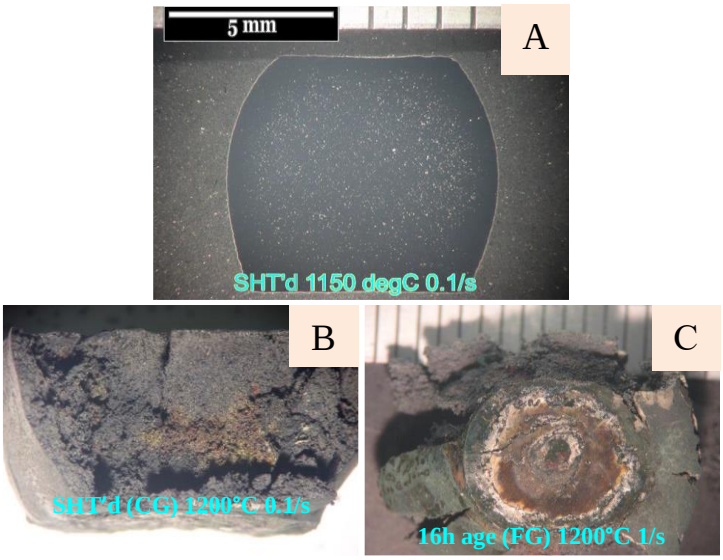

Figure 41 - Macro images / micrographs of RR1000 specimens tested during the PROMOTE program. A) CG variant tested at 1150°C at $1s^{-1}$, B) CG variant tested at 1200°C at $0.1s^{-1}$, C) FG variant tested at 1200°C at $1s^{-1}$.

3.6 Assessment of heating methods

Before designing the semi-solid testing facility, a preliminary investigation into the available heating methods within the SMaRT laboratory was conducted. These included conventional radiant element furnaces, resistance heating and induction heating. Each heating method is described in turn below.

3.6.1 Radiant furnaces.

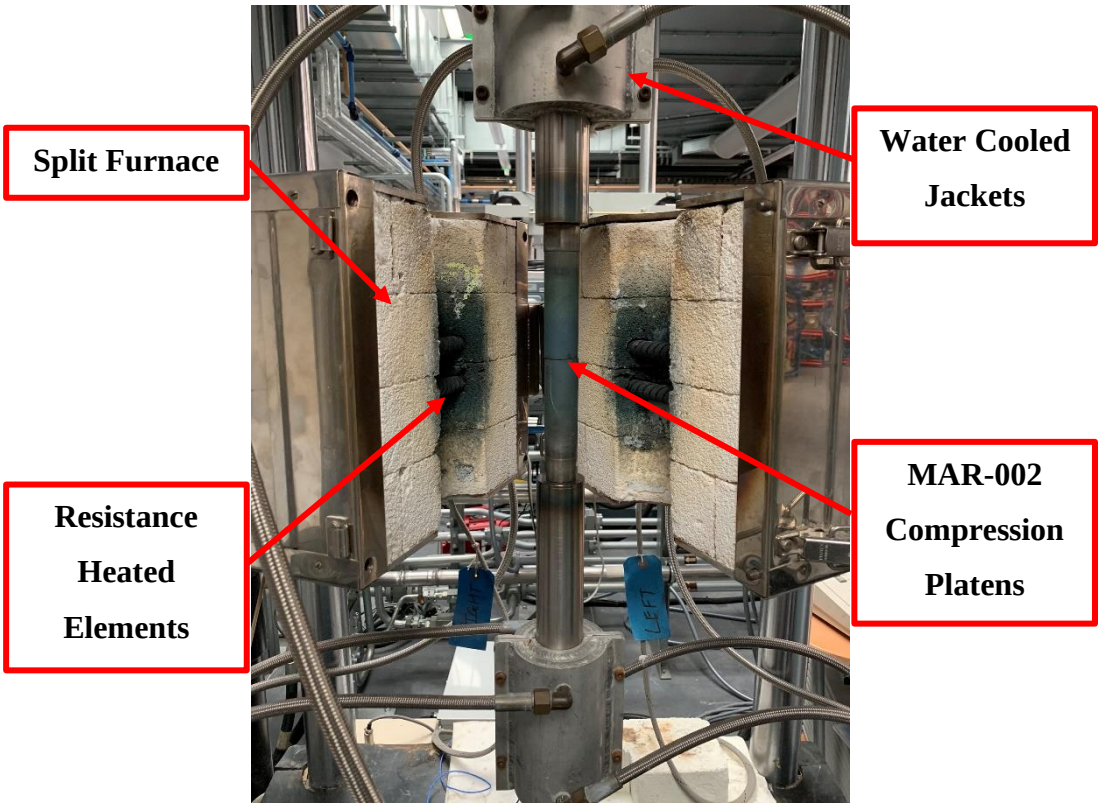

Figure 42 - Radiant element furnace fitted to the servo-hydraulic compression machine FG3 at SMaRT.

Isothermal hot compression tests are regularly conducted using the set up depicted in Figure 42. The set up consists of a split type radiant element furnace in which two high temperature platens made of MAR-002 nickel superalloy are placed. The MAR-002 platens retain their strength up to a maximum test temperature of 1250°C. To ensure no heat damage is done to the stainless-steel loading rods and load cell at these high test temperatures, both loading rods are fitted with water cooled cooling jackets. In order to accurately measure and control the test temperature, the furnace is fitted with two R-type thermocouples which are calibrated to 1300°C. Thermocouples cannot be directly mounted to the sample during testing without being damaged or destroyed during the compression test, therefore two R-type thermocouples are positioned alongside the top and bottom platens respectively so that the air temperature at these

locations is measured. When heating the furnace to the desired test temperature, the furnace, platens and loading rods are left at this temperature for a minimum of 30 minutes so that the platens and furnace reach thermal equilibrium. This allows the R-type thermocouples air temperature reading to be used as an indicator of the test temperature by averaging the two readings. After the furnace has been allowed to heat soak for 30 minutes, the platens must be zero'd at the desired test temperature to account for the thermal expansion of the loading rods and compression platens. When these steps have been completed the setup is ready for testing. A specimen can now be sprayed in boron nitride high temperature lubricant and placed on the lower platen. The specimen must heat soak under no load on the bottom platen for a minimum of 5 minutes, to ensure thermal equilibrium of the specimen at the chosen furnace temperature, removing any temperature gradients throughout the specimen. Immediately after the five minutes soak time has finished, with the specimen at the chosen furnace temperature, the compression test should be conducted. The specimen should then be removed from the furnace and water quenched to prevent any microstructural evolution following the compression.

3.6.2 Resistance heating

Semi-solid testing has been conducted at Swansea university previously as part of a program of work investigating mechanical tests close to the solidus temperature of a range of alloys in order to further understand material behaviour during investment casting. A novel test technique was developed by J. James, R. Evans, J. Spittle and S. Brown in 2004 known as the advanced semi solid elongation test (ASSET)[120], [121]. The test technique is outlined in Figure 43 adapted from [120].

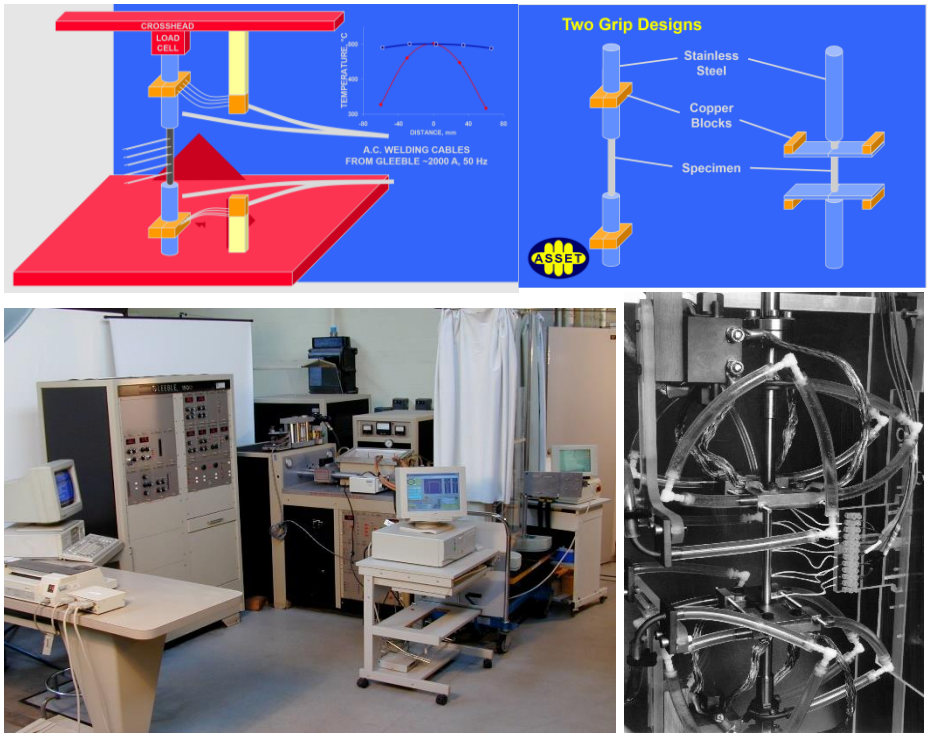

Figure 43 - Advanced semi solid elongation test (ASSET) set up [120].

The ASSET test technique was built around a Hounsfield tensile machine. A specimen was mounted to two stainless steel loading rods and heated via resistance heating by a current passing through copper blocks either end of the specimen. In order to achieve the desired heating rate and peak temperature required for the specimens to become semi-solid a high current was required. This was provided by the Gleeble 1500 thermomechanical simulator, which was attached to the copper blocks each side of the specimen by large copper wiring. The testing temperatures to produce an estimated fraction of liquid for each alloy were then calculated via a thermodynamic calculation. A series of tensile tests were then performed at a number of different fractions of liquid to assess the impact a semi-solid microstructure has on mechanical properties.

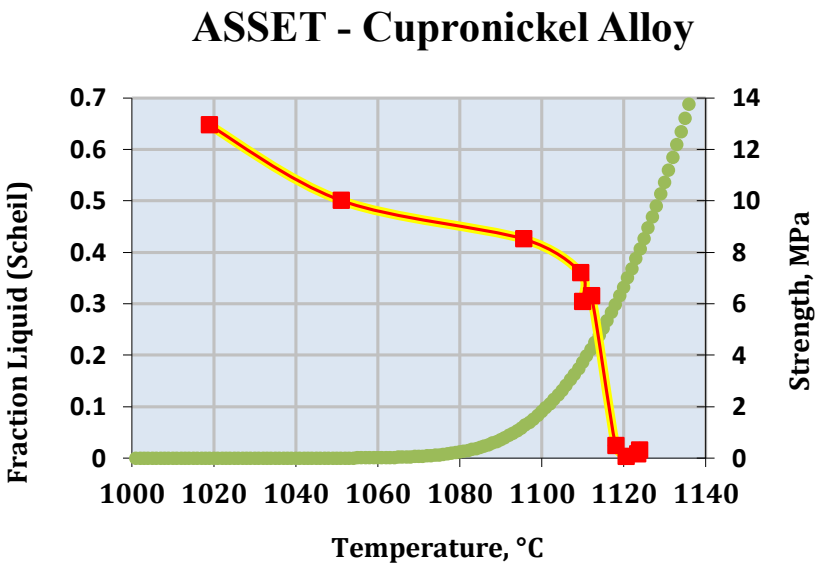

Figure 44 - Graph of tensile strength vs fraction of liquid for cupronickel alloy tested in the ASSET facility [120].

Most of the testing carried out in the ASSET program focused on aluminium alloys (400-650°C), although some testing was carried out at higher temperatures on cupronickel alloy (1100°C). It was found that there was a severe drop off in strength when testing at fractions of liquid above 10-15% liquid as can be seen in Figure 44. Although the ASSET system was very effective at semi solid testing the use of the Gleeble's power system to run up to 2000 amps of current through the specimen via copper cables involves severe health risks. While this was acceptable at the time of testing, getting a system like this to pass modern risk assessment procedures would be impossible preventing its use in this program of work.

3.6.3 Induction Heating.

The suitability of induction heating as a heat source has been considered. Induction heating has been used in a vast array of applications, from heating metals to be melted during casting methods such as VIM to providing heat to set bonding agents in the manufacture of automobile chassis. Induction heating is a non-contact heating method that can produce rapid heating rates. Induction heaters work on the principles of electromagnetic induction. If an electrically conductive object (work piece) is placed within a coil in which an alternating current is passed, the alternating current will create a varying electromagnetic field. The electromagnetic field will then induce circulating eddy currents within the work piece. The resistivity of the workpiece to these currents causes joule heating.

Induction heating trials (2kW)

In order to assess the suitability of induction heating to produce semi solid microstructures in nickel super alloys, a series of heating trials were conducted. The initial trials utilised a 2kW easy heat induction heating package produced by Cheltenham induction. This package consisted of a small AC generator with 2kW power capability. The relatively low power allowed this set up to be cooled with a water-to-air heat exchanger. The cooling water flows through the generator as well as the work head and work coil to combat the heat generated by the large currents.

The first test carried out on the 2kW easy heat system was to test the maximum temperature capable with this power pack when heating a standard 8mm diameter by 12 mm height RR1000 compression specimen. To do this a specimen was placed within a crucible, machined from a refractory brick. The helical induction coil was then placed around the crucible as depicted in Figure 45.

Figure 45 - 2kW easy heat induction heater trials set up.

The power of the induction heater was then gradually increased until the specimen liquated into the crucible as shown in Figure 46. This confirmed that liquation of RR1000 could be achieved with the use of the 2kW induction heating system.

Figure 46 - Liquated RR1000 compression cylinder.

The next assessment to be made was the maximum heating rate achievable with the 2kW system. Another crucible was manufactured to allow a type N thermocouple to be spot-welded to the specimen to monitor the temperature during the experiment as depicted in Figure 47.

Figure 47 - RR1000 specimen with a spot-welded N-type thermocouple being heated to 1300°C with a 2kW induction heater.

The specimen was heated to 1300°C with the induction heater set to its maximum power output. The graph in Figure 48 shows that between 52°C and 1200°C an average heating rate of 48°Cs^{-1} was achieved.

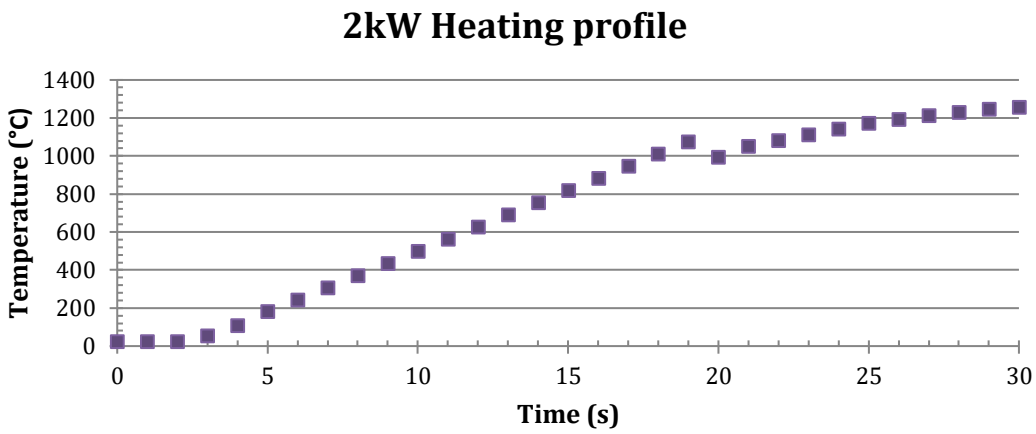

Figure 48 - Heating profile of an RR1000 compression specimen heated at full power in the 2kW induction heating system.

This heating rate is more than enough to cause sub-solidus liquation in RR1000, but the fact that this was an isolated specimen being heated without the presence of compression platens needed to be taken into consideration. Adding two large compression platens to the induction field would dramatically reduce the amount of power being exerted on the specimen, therefore it was decided that the proposed semi-solid testing facility could use induction heating as a heat source but would likely require a higher power induction heater.

The microstructure of the specimen was characterised to determine if liquation had occurred. The specimen was analysed via SEM and EBSD, the results of which are shown in Figure 49. In this test the specimen completely liquated with the specimen becoming essentially an oxide shell containing molten RR1000. The EBSD and SEM micrograph in Figure 49 show that on cooling large columnar grains have grown from the oxide shell towards the centre of the specimen where a few smaller equiaxed grains have nucleated. This grain formation pattern is very common in ingot casting.

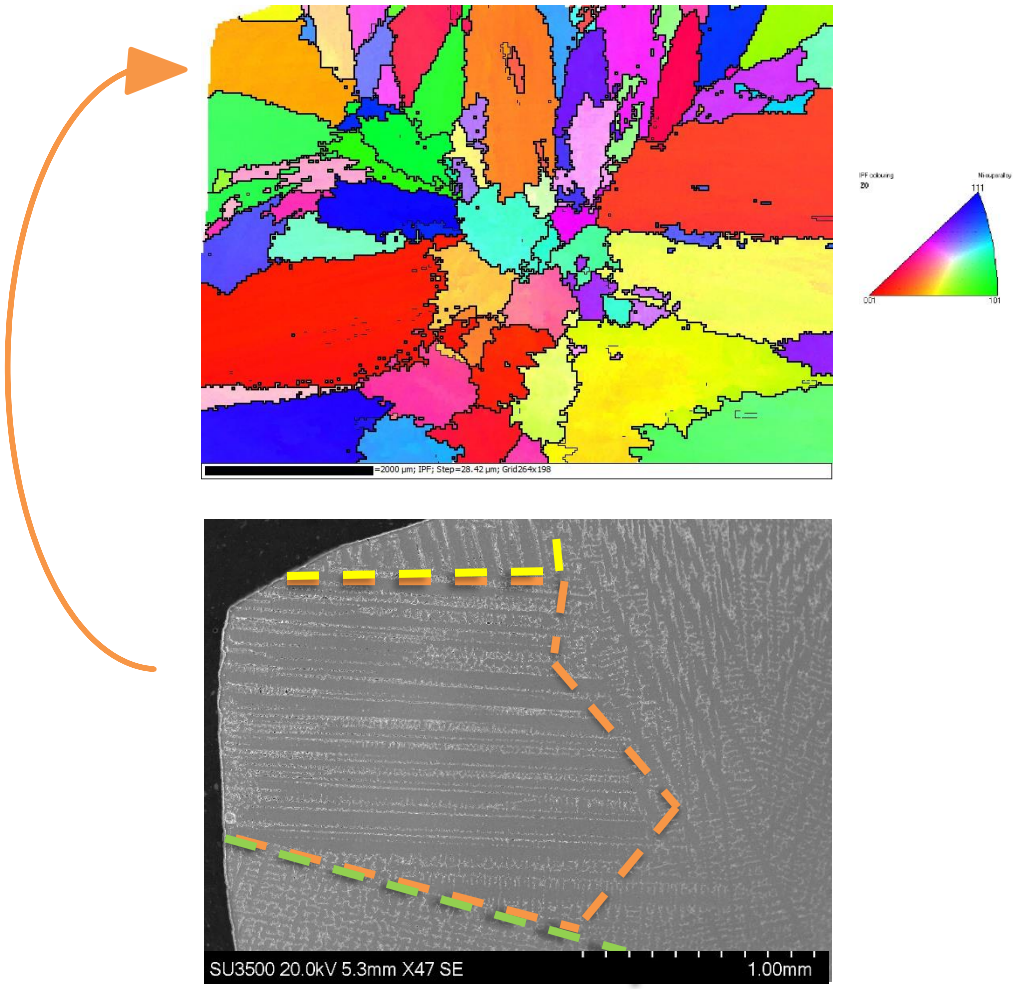

Figure 49 - EBSD IPF map and SEM micrograph of specimen heated to 1300°C during 2kW induction heater trial.

3.7 Semi-solid testing facility design

Taking into consideration each method of semi-solid testing investigated as well as the wealth of knowledge of compression testing RR1000 at Swansea university, it was decided that in order to meet the research objectives of this project, a novel semi-solid testing facility would need to be designed and built around an existing test frame within the laboratory at SMaRT.

3.7.1 Existing servo hydraulic compression machine

Figure 50 - FG1 Servo hydraulic compression machine to be modified for semi solid compression testing.

The proposed semi-solid testing facility was to be built around an existing servo hydraulic compression machine (FG1 - Figure 50) capable of loads up to 100kN based in the main SMaRT laboratory. To assess the capability of FG1, multiple tests were conducted to find the maximum ram velocity and accuracy of the control system.

To assess the accuracy of the position sensor, the loading rod was set to maintain a fixed position and the oscillations in the position reading were recorded. The position data was then put through the error analysis procedure detailed later in section 3.11. From this, a 95% confidence interval of +/- 0.02mm was calculated for the position reading. As this position reading is measured within the compression machine itself, and not at the end of the loading rod where the specimen is located, the error associated

with the position recording is likely larger due to any potential slack or misalignment in the components between the two. The decision was made to use a conservative approach to the position measurement and all position measurements were rounded to the nearest 0.1mm.

In the first test the ram was set to move from a platen position of 30mm to a final platen position of 7mm at 1000mms^{-1}, with the idea that whatever velocity this test produced would be the maximum. The results of this test are illustrated in Figure 51.

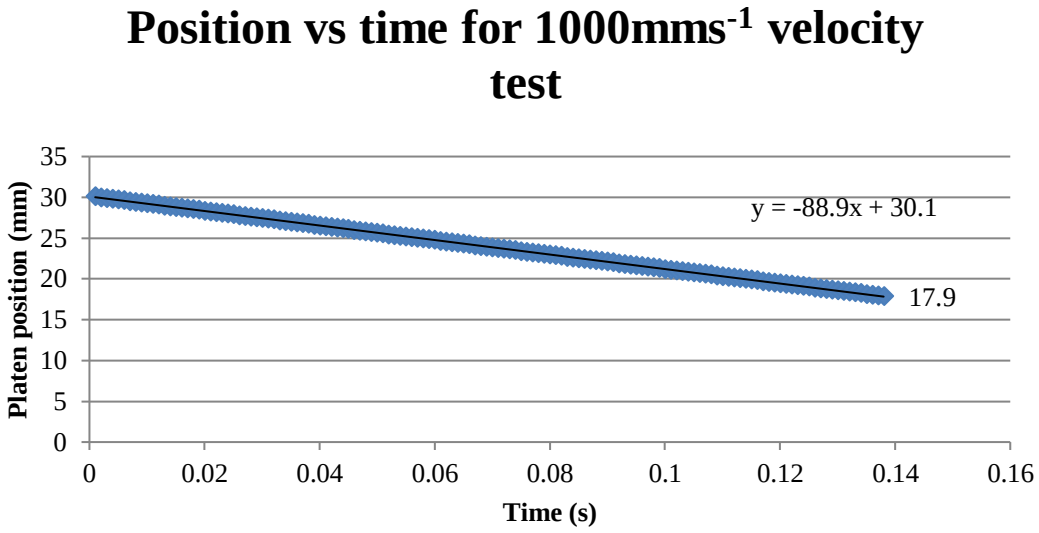

Figure 51 - Graph of platen position vs time for 1000mms^{-1} ram velocity test. Linear trend line fitted with associated line equation indicating a gradient of 88.9, therefore a ram velocity of 88.9mms^{-1} was achieved. The platen position of the final data point is also indicated to show the final platen position achieved in the test.

The graph indicates that the maximum ram velocity achievable by FG1 is 88.9mms^{-1}, as indicated by the gradient of the linear trendline. On further inspection of the data it was noted that the final platen position of 7mm was not achieved and instead the test stopped 10.9mm short, at a final platen position of 17.9mm. This test was repeated multiple times, yielding the same result. Because of this, it was suspected that the PID controller in FG1's control system was not fast enough to accurately reach a final platen position of 7mm at this velocity.

For this program of work a minimum strain rate of $1s^{-1}$ was required for an 8mm diameter x 12mm height compression cylinder. A second test was conducted to assess whether FG1 could reach a final platen height of 7mm at a velocity of $12mms^{-1}$. The gradient in Figure 52 indicates that a velocity of $12mms^{-1}$ was achieved, while also stopping at the required platen position of 7mm. This confirmed FG1 was fit for purpose.

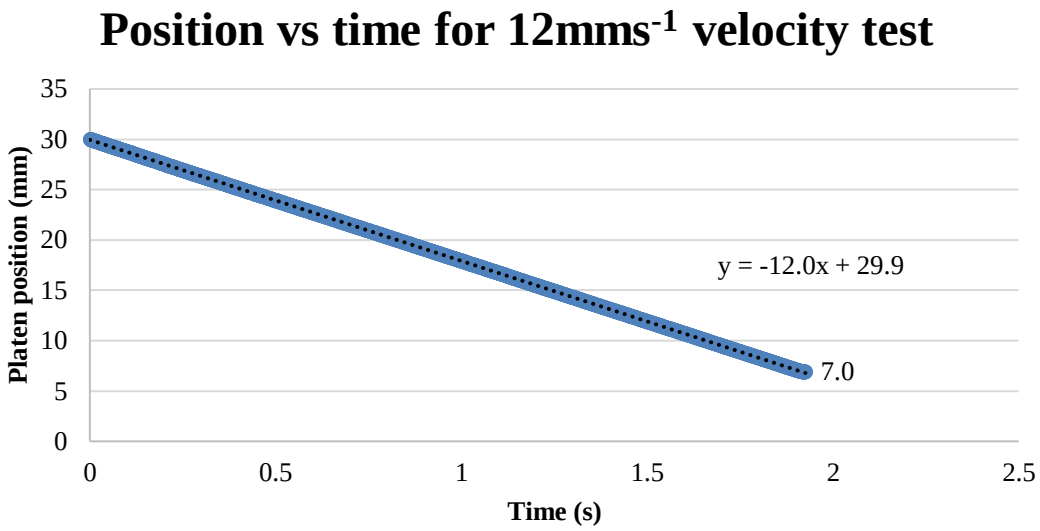

Figure 52 - Graph of platen position vs time for $12mms^{-1}$ ram velocity test. Linear trend line fitted with associated line equation indicating a gradient of 12.0 therefore a ram velocity of $12.0mms^{-1}$ was achieved. The platen position of the final data point is also labelled to indicate the final platen position achieved at the end of the test.

3.7.2 Final design

In designing the bespoke semi solid testing facility, the following factors were considered: -

Inert testing atmosphere – Previous compression work on RR1000 conducted at Swansea University highlighted that high temperature compression testing (1150°C +) resulted in large amounts of strain induced porosity (SIP) leading to complete disintegration of the specimen at 1200°C. One of the suspected causes for the specimen disintegration was oxidation caused by testing in a conventional radiant furnace in air. In order to investigate this theory, the proposed semi solid testing facility needed to be able to conduct tests in an inert atmosphere meaning either a vacuum or inert gas environment. With the added difficulty of chamber strength associated with vacuum testing, the choice was made to use instead an inert gas environment chamber, in this case argon, as the chamber would have to withstand reasonably low forces from the gas pressure compared to the large forces exerted by a vacuum. This would allow large viewing windows to be installed to monitor tests.

Rapid heating rate to test temperatures of 1100-1300 °C – The 2kW induction heater trials established that induction heating was a viable option for providing rapid heating of RR1000 specimens to temperatures up to 1300°C, but raised concerns on the power capability if large compression platens were to be heated also. As a result of the heating trials and on advice of Phoenix calibration & services a higher power, 15kW induction heater, was selected to be the heat source. The induction heater was to be controlled by a PID controller paired with an infrared thermometer in a closed loop.

Post-test quenching mechanism – In order to preserve the microstructure and avoid any microstructural evolution after testing, the specimen needed to be quenched as quickly as possible, following the test. A quench bath was built into the chamber and a pneumatic actuator installed at the back of the chamber to knock the specimen into the bath immediately after it is compressed. The details of this quenching mechanism are discussed in section 3.7.2.1 – Quenching mechanism.

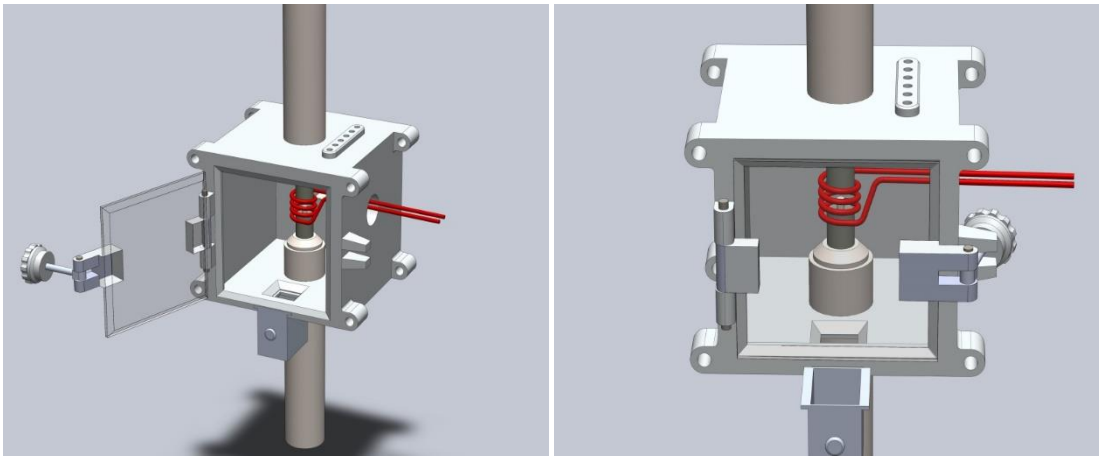

Figure 53 - CAD model built in SOLIDWORKS, illustrating a basic outline of the proposed semi solid testing facility to be manufactured and fitted to FG1.

To assess the effectiveness of water as the quench media, an analysis of the quench rate from 1200°C to room temperature was conducted on a standard 8mm diameter by 12mm height RR1000 compression specimen. A thermocouple was inserted into the centre of the specimen to track its temperature during a heat and quench cycle within the chamber. The specimen was heated to a target temperature of 1200°C then water quenched using the semi-solid testing facilities quenching mechanism. The specimen temperature data recorded after the quenching procedure was activated is shown in Figure 54.

The specimen experiences a very slow quench rate initially as it cools via the argon surrounding it while the chamber moves to align the quenching mechanism with the specimen. On entering the quench bath, the specimen temperature is approximately 1170°C, meaning any liquated material created will still be present, as the research in this study will later show that holding liquated specimens above 1160°C leads to liquid propagation.

When the specimen enters the quench bath two distinct quench rates can be seen, as illustrated in Figure 54, an ‘initial water quench rate’ and a ‘second quench rate’. The initial quench rate was recorded at ~200°Cs^{-1} as indicated by the linear trend line. The

second quench rate was recorded at ~400°Cs^{-1} as indicated by the second linear trend line. The initial quench rate is slower than the second quench rate due to the Leidenfrost phenomenon which causes some of the steam produced around the specimen to act as an insulating barrier. The second quench rate is much higher when the Leidenfrost phenomenon has subsided just below 850°C. This is in alignment with the Leidenfrost transition temperature during continuous casting of steels which has been found to be in the range of 700-900°C [122]. This quench analysis test was repeated and the results of both tests were comparable.

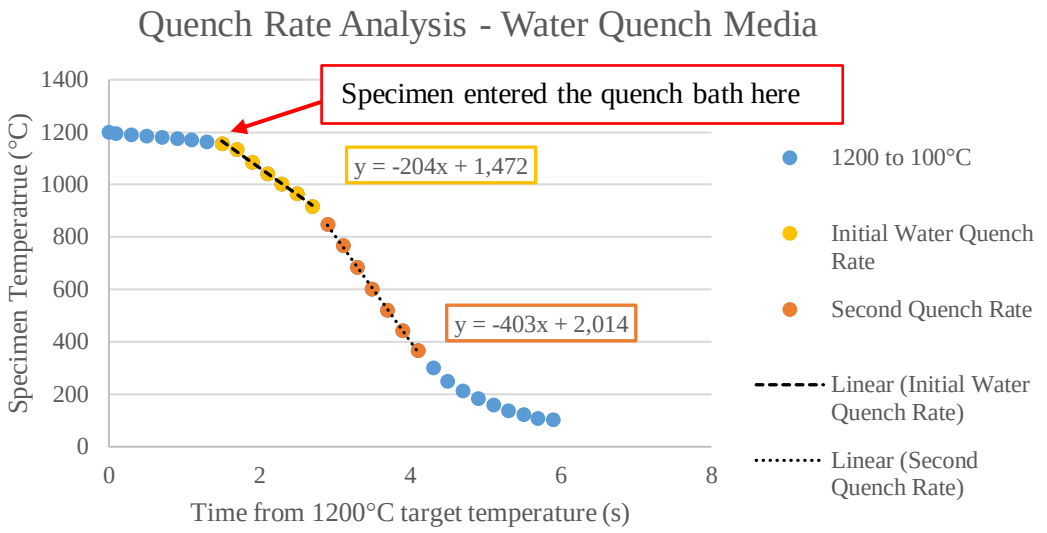

Figure 54 – Specimen temperature profile during quench rate analysis of water quench media.

A study conducted within Rolls-Royce Plc by Simon Bray et al [123] measured the temperature profile of RR1000 inertia friction welds during a welding cycle. The temperature was recorded during the heating phase as well as the cooling phase, post-consolidation. The study recorded temperature data by embedding thermocouples at set intervals in the test piece, so that as the weld pieces upset, the final location of some of the thermocouples corresponded with the weld line, TMAZ and HAZ. Temperature data was collected from several RR1000 welds, including both the FG and CG variants. The study found that the maximum cooling rate in these regions after consolidation ranged from 164 - 405°Cs^{-1}, with an average maximum cooling rate of 278°Cs^{-1}. These cooling rates are comparable to the water quench rates of the quenching mechanism in the semi-solid testing facility measured here. Therefore, the use of water as the quench media in the semi-solid testing facility was considered to provide sufficient cooling rates for replicating the thermal conditions of an IFW.

Argon jets were also considered as a quenching mechanism, but the slower cooling rate compared to water quenching and complications of sudden pressure rises within the chamber prevented their use.

3.7.2.1 Semi solid testing facility full details

Key components of the bespoke semi-solid testing rig are described below.

Environment chamber (Figure 55**)–** The environment chamber was manufactured out of aluminium and fitted with three large Perspex windows for visibility during testing. The bottom of the chamber was fitted with a removable 250ml quench bath sealed with a PTFE O-ring. Argon is fed into the chamber through a diffuser via a Brooks instruments 0-10 litres per minute gas flow meter allowing the chamber fill speed to be adjusted. The air in the chamber is displaced out of the top of the chamber by the heavier argon through a bubble trap with the pressure inside the chamber being regulated by a 0.5bar check valve. The chamber is also fitted with an emergency release valve which prevents over-pressurisation in the event of a blocked check valve. The front of the chamber is mounted on two hinges with four reinforcing clasps to ensure a complete seal of the PTFE O-ring on the door's perimeter.

During testing the chamber exerts two load effects on the loading rods and therefore the load cell - these need to be accounted for.

The first is the load the positive gas pressure within the chamber exerts on the loading rods, acting to push them out of the chamber. To assess this load effect the chamber was filled with argon to the operating pressure and the change in load reading from the load cell recorded. It was found that the load exerted by the gas pressure on the loading rods was 0.01-0.02 kN. As all compression tests would be conducted with the chamber already at operating pressure, the change in compressive load exerted on the loading rod by the specimen would be unaffected by this pre-load of the argon gas.

The second load to be accounted for is the drag force of the chamber's seals on the loading rods, as the loading rod is pushed through the chamber by the force of a specimen being compressed. This seal drag force would need to be overcome to exert a force on the load cell through the loading rod. To measure this seal's drag force, the chamber was manoeuvred up and down the loading rod and the change in load reading from the load cell recorded. The chamber was moved at 1 and 12mms^{-1} to replicate the displacement rates that would be used during compression testing. At both displacement rates the drag force of the seal on the loading rod was found to be 0.05-0.06 kN. Therefore, this seal drag force would be subtracted from any change in force readings recorded during a compression test, to give the true force needed to compress the specimen.

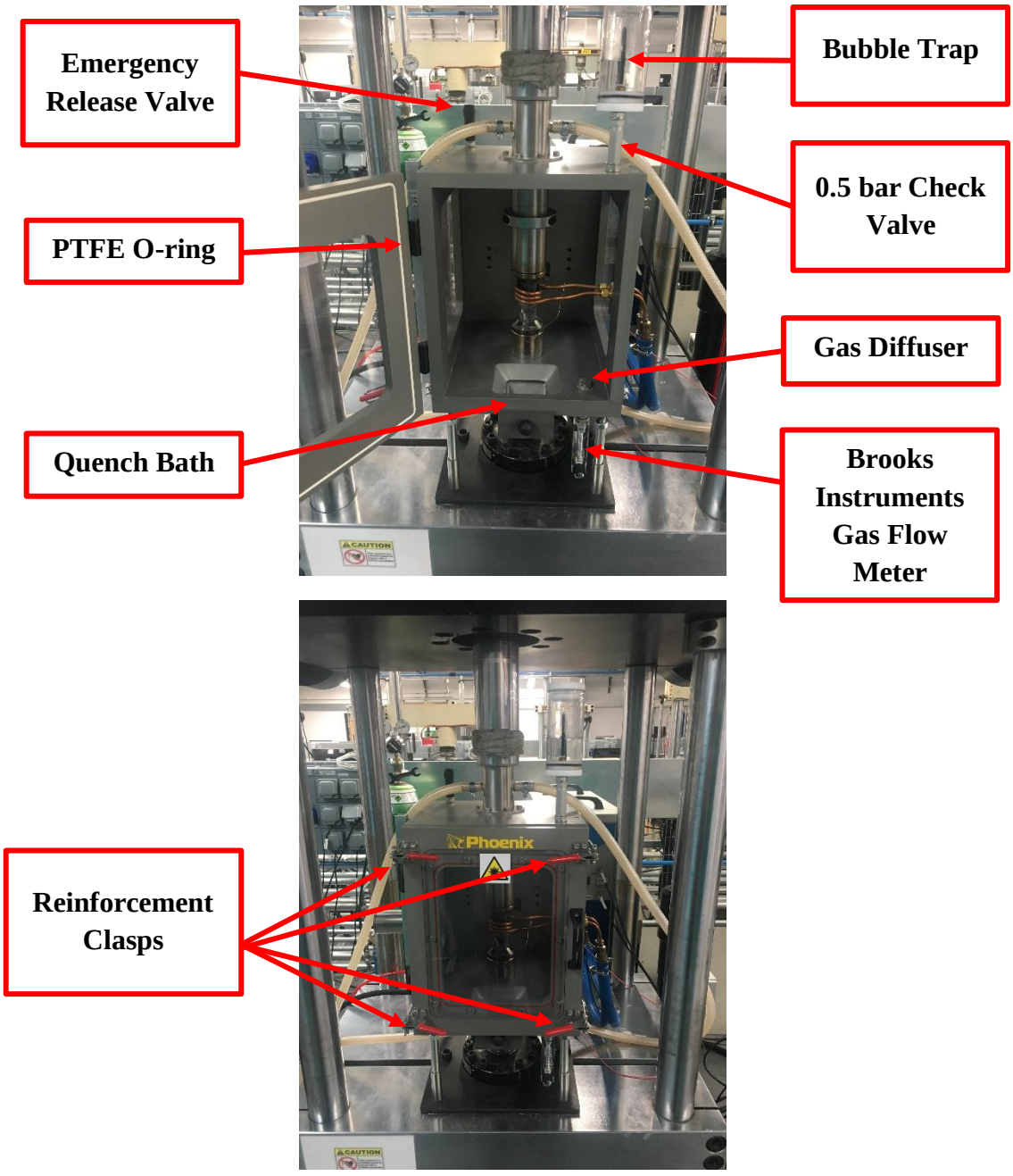

Figure 55 - Inert gas environment chamber fitted to the servo hydraulic machine FG1 with components highlighted.

Load train components – Loads are transferred to the specimen via two stainless steel loading rods. The loading rods in the conventional radiant furnace set up were cooled via two sets of water-cooled aluminium jackets bolted to the loading rods. This set up is quite bulky which prevented its use within an environment chamber. As a result, the new loading rods in the semi solid testing facility have inbuilt cooling channels through which chilled cooling water from the laboratories ring main is pumped, thus regulating the rod temperature to prevent any heat damage to the load cell. The compression platens on which the tests would be carried out are made of tungsten with a slight cobalt impurity, this allows the platens to retain their strength up to the required test temperatures of 1300°C. These platens are bolted to the end of the loading rod allowing for ease of access for removal if damaged.

Heating system & temperature control – Heat is provided by a JKZ CX2030C 15kW induction heater mounted at the rear of the test frame. Flexible copper lined hoses feed the induction current into the chamber via two brass ports in one of the Perspex windows. An induction coil is fitted to the inside of the chamber to the brass ports via wade compression nuts as shown in Figure 56.

Figure 56 - JKZ induction heater configuration within the FG1 test frame.

The induction heater is controlled via a WEST Pro-16 PID controller paired with an Optris 3MH2 200-1500°C infrared thermometer mounted to the opposite side of the chamber on a sliding panel to allow for height adjustment as shown in Figure 57.

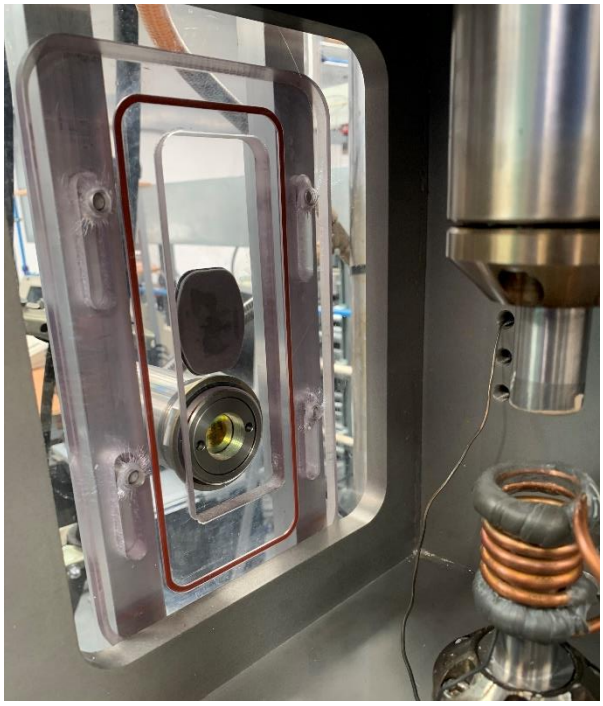

Figure 57 – Optris 3MH2 infrared thermometer mounted on a sliding Perspex panel at the side of the chamber.

The cooling water used in an induction heating system must have a low iron content rendering the laboratory ring main water unsuitable. Instead the induction heater is cooled via a standalone reservoir of distilled water, cooled by a water-to-water heat exchanger as pictured in Figure 58.

Figure 58 - Water-to-water heat exchanger with isolated distilled water reservoir for induction heater cooling.

Quenching mechanism – After a compression test is conducted the chamber is raised up via a locking clamp on the upper loading rod to align the lower platen with a pneumatic actuator mounted to the rear of the chamber. This is illustrated in Figure 59. The induction coil is mounted to the environment chamber, so it is also moved out of the way of the pneumatic actuator exposing the specimen. When the actuator is activated by the control system on the FG1 test frame, the specimen is then knocked forward into the 250ml quench bath at the front of the environment chamber.

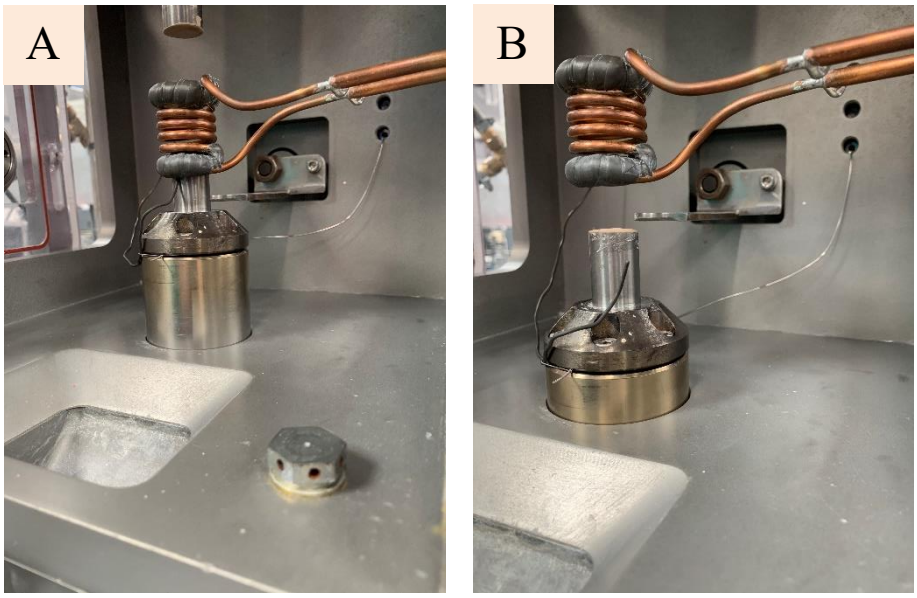

Figure 59 - Quenching mechanism: Pneumatic actuator mounted to the back of the chamber. A) Position during testing, B) Position when chamber has risen to align the actuator with the top of the lower platen.

3.7.3 Set up & optimisation

3.7.3.1 Testing Macros

Two macros were written during the project with the aid of Phoenix Calibration Ltd staff, using the Phoenix virtual control panel (VCP). This enabled testing to be carried out autonomously. The macros include a user-friendly interface, with call outs prompting the user to enter the specimen height, test velocity, acceleration gap and final height. The call outs guide the user through each step of the test set up until the test is ready to run. On running the test, the macro initiates the data logging system and conducts the compression test followed by automatically retracting the chamber with the upper loading rod to the quench height so that the quench mechanism can knock the specimen into the quench bath. A graph of position vs load is then displayed on screen where the data can be saved as a .DAT file.

Figure 60 - Virtual Control Panel (VCP) used to operate the test frame FG1.

3.7.3.2 Commissioning of the Semi-Solid Compression test facility

After installation of the semi solid facility, three trial runs were conducted to determine the maximum heating rate and to assess whether any temperature gradients were present in the specimen during testing.

The first test was carried out on a 14mm diameter by 21mm height FG RR1000 compression cylinder in order to assess the test frame's capability to use larger specimens. The PID controller was set to heat the specimen to a test temperature of 1200°C at maximum heating rate of $4°Cs^{-1}$ where the compression test was conducted at $20mms^{-1}$ to a final height of 7mm. During the test, the bottom of the specimen that was in contact with the lower platen, appeared to be at a higher temperature than the top of the specimen as it was glowing brighter. On compression the specimen deformed inhomogeneously as shown in Figure 61, confirming the presence of a temperature gradient during testing.

Figure 61 - 14mm diameter by 21mm height FG RR1000 compression specimen used in first trial run, exhibiting inhomogeneous deformation due to a temperature gradient during heating.

A second test was carried out on the standard specimen size 8mm diameter by 12mm height FG RR1000 compression cylinder to assess whether the temperature gradient was an artefact of the oversized specimen or if the higher temperature at the bottom of the specimen was due to conduction of heat from the lower platen.

In this test the PID controller was set to heat the specimen to 1200°C as fast as possible (~3°Cs^{-1} achieved). On reaching the target temperature the specimen was compressed at 12mms^{-1}. During this test the lower platen appeared to heat much more than the specimen resulting in the bottom half of the specimen being almost completely molten while the top was still solid (image of compressed specimen below in Figure 62). The molten lower half of this specimen then fused to the lower platen. During cooling the difference in thermal expansion coefficient of the two metals caused the specimen and a layer of tungsten from the top of the platen to shear off (Image below). It was thought that this overheating was either due to conduction of heat from the lower platen into the specimen or possibly a specimen emissivity issue leading the pyrometer to believe the specimen is at a lower temperature than it is.

A spare set of platens was fitted to resume testing while the damaged platens were sent for resurfacing.

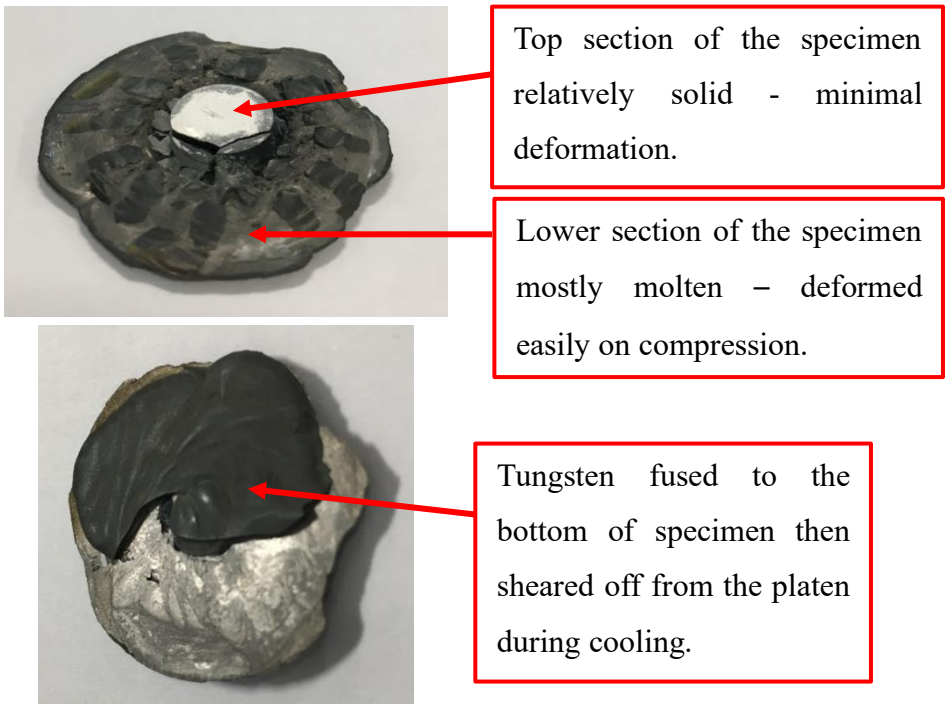

Figure 62 - Over heated specimen fused to tungsten sheared off from the lower platen.

These two initial tests highlighted two problems that needed rectifying to make the semi solid testing facility fit for purpose: -

1. The low heating rate and temperature gradient across the specimen. The large coil and platen diameter compared to the relatively small diameter of the specimen meant that most of the power from the induction heater was acting on the platens rather than the specimen. This caused the platens to become hotter than the specimen therefore conducting heat into the specimen causing the temperature gradient while producing insufficient heating rate of the specimen.

2. The potential lack of a stable specimen emissivity during testing causing the pyrometer to read incorrect temperature readings.

To combat the first problem a specimen holder was designed to isolate the specimen from the lower platen to remove any thermal gradients caused by heat conduction from the platen. The specimen holders were hollow 21mm diameter tubes with an inner diameter of 8mm as pictured in Figure 63. The specimen holders were manufactured from a fibrous high temperature insulation board and were designed to be disposable. The specimen would be slotted into the beginning of the hole in the holder during heating, then on reaching the target temperature the top platen would push the specimen through the holder and onto the lower platen. The holders were designed so that they were taller than the specimen being tested, so when the specimen was pushed completely into the holder the platens would compress the holder causing it to break away from the specimen therefore not influencing the deformation of the specimen during the test.

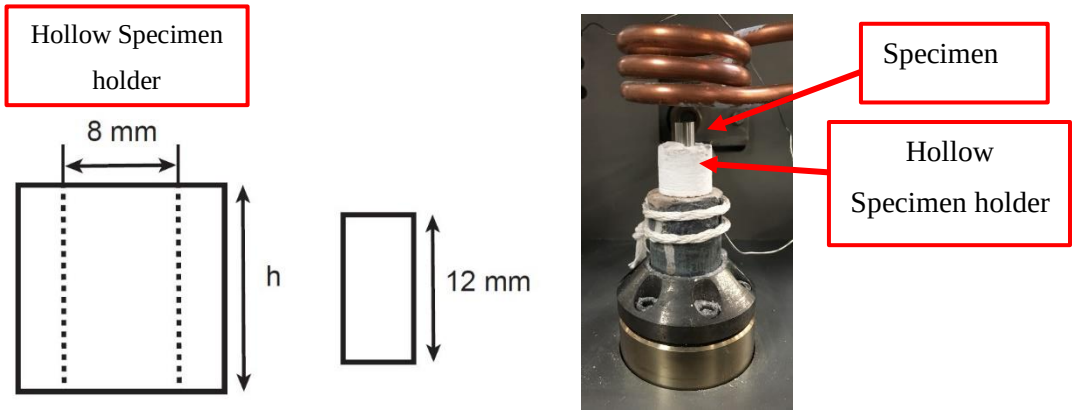

Figure 63 - High temperature insulation board specimen holder design.

While testing the specimen using this method the temperature gradient issue appeared to be resolved, as the specimen had an even glow during heating. The lack of temperature gradient was later confirmed via inspection of the microstructure showing homogenous changes to the gamma prime precipitates throughout the specimen.

The specimen holder also aided the low heating rate. With the specimen now being further away from the platen, more of the induction coil's power was being transferred to the specimen instead of the platens. Utilising the specimen holder technique, the average heating rate to 1200°C was raised to 10°Cs^{-1}. Although this was a good increase in heating rate capability, improvements would need to be made to achieve the desired heating rate of 25°Cs^{-1}.

Specimen emissivity

As a concern about the specimen's emissivity was raised during the initial trials of the semi solid testing facility, an investigation the specimen's emissivity was conducted. To do this six 8mm diameter by 12mm height FG specimens were modified by spark eroding a 1mm diameter by 6mm length hole into the centre as depicted in Figure 64.

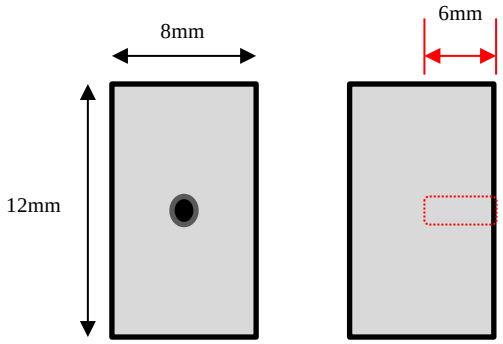

Figure 64 - Graphic illustrating the modifications made to compression specimens in order to conduct specimen emissivity investigation.

This modification allowed a 1mm diameter N-type thermocouple to be inserted into the specimen to measure the internal temperature during heating. The temperature reading from the thermocouple could then be compared with the temperature being read by the infrared thermometer. During the initial compression test trials an emissivity value of 0.9 was used as recommended for nickel alloys in the Optris pyrometer user manual.

As suspected, there was a slight discrepancy of +/- 10°C between the thermocouple and the pyrometer readings. A specimen was held at 1100°C while the emissivity value was changed on the pyrometers controller to tune the emissivity value. The emissivity value was changed until the readings from both the thermocouple and pyrometer matched. The specimen was then further heated to 1200°C to assess whether both readings still corelated. Unfortunately, at this temperature the discrepancy in the readings had returned. Although all testing is being carried out in an argon atmosphere some oxidation of the specimen still occurs at these high temperatures due to the slight impurity of the argon gas (99.998%). Specimen oxidation was considered the likely cause of the unstable emissivity. With the aim of solving this issue, four specimen preparation techniques were trialled to evaluate their emissivity.

Boron nitride only – Emissivity value of 0.3 stable at 500°C but produced temperature fluctuations +/- 50°C when temperature raised to 700°C. Not suitable for accurate temperature measurement.	
High temperature paint – Stable emissivity of 0.885 up to 800°C (+/- 5°C error). Emissivity value then drops to 0.4 when temperature increased to 1200°C (+/- 5° error). This large change in emissivity renders this paint not suitable.	
Pre oxidised at 500°C for 72 hours – Specimen examined in SEM to check for any microstructural changes during pre-oxidation = no obvious changes. Emissivity value of 0.765 at 900°C but with a change in emissivity at 1200°C due to further oxidation leading to a +/- 10°C error.	
HE6 high emissivity paint (R-R) – Paint developed by Rolls-Royce for use in air up to 1300°C. In a study HE6 was shown to have a virtually temperature independent emissivity of 0.95 between 700°C and 1300 °C [126]. When tested the HE6 coated specimen was accurate to +/- 2°C from 900-1200°C.	

Table 7 - Results of emissivity experiment examining different specimen preparation techniques and analysing their ability to produce a stable emissivity.

Table 7 outlines the results of the emissivity experiment. Prior to compression testing all specimens were coated with a boron nitride high temperature lubricant to reduce the effects of friction. Therefore, a specimen coated in boron nitride spray was evaluated first, but its light colour resulted in an unreliably low emissivity value of 0.3 which was completely unstable when temperature was increased. Next a specimen was coated in black VHT high temperature exhaust manifold paint, in the hope that the dark colour would yield a higher emissivity value. Initially this theory held true with the VHT paint having an emissivity of 0.885 up to 800°C. Unfortunately, on further heating to 1200°C the VHT paint began to degrade reducing its emissivity value to 0.4 rendering it unreliable. The third method to be trialled was pre-oxidation of the specimen. The specimen was heat treated at 500°C for 72 hours leaving the specimen surface a dark blue but remaining relatively polished surface roughness. The temperature of 500°C was selected as to not cause any changes to the microstructure. Results from this test were initially promising with an emissivity of 0.765 at 900°C, but on heating to 1200°C the surface oxidation developed further resulting in a change in emissivity giving a +/-10°C error between the thermocouple and pyrometer readings. The time it would take to pre-oxidise the specimen at 500°C to the same extent as heating in argon at 1200°C would be very long and therefore unrealistic as a specimen preparation method for this study. The final preparation method to be tested was a high temperature paint HE6 developed by Rolls-Royce Plc. R. Brandt et al conducted an experiment assessing the suitability of HE6 as a constant emissivity reference paint. They concluded that HE6 shows slight angle dependency but exhibited a practically temperature independent emissivity value of 0.95 between 900°C and 1300°C as shown in Figure 65 [124].

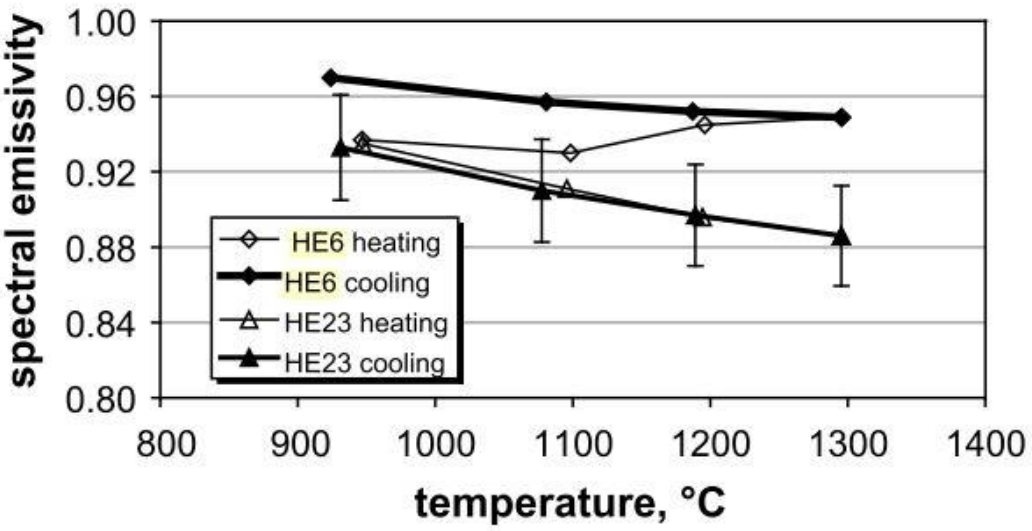

Figure 65 - Emissivity value vs temperature for HE6 high temperature paint adapted from [124].

The specimen coated in HE6 in this evaluation of specimen preparation methods maintained an emissivity of 0.95 up to the desired test temperature of 1200°C, maintaining correlation with the thermocouple with only a +/- 2°C error. All specimens tested from this point onwards were coated in HE6 in order to sustain constant emissivity during heating.

3.7.3.3 Induction coil & platen design

Having established a method of accurately heating the specimen to the desired temperature with no temperature gradients, an intensive program of study was undertaken on coil design to increase the heating rate to 25°Cs^{-1}.

The coil head design was altered and improved via a comprehensive, iterative process. Each coil was set to heat a standard sized specimen to 1200°C as fast as possible and was given approximately 100 seconds to do so. The specifications of each iteration of coil and the average heating rate they produced when heating a standard specimen to 1200°C is detailed below along with notes on the reasoning behind each design:

3.7.3.3.1 Original coil

- Conventional helical style
- 30mm internal diameter
- 6mm copper piping
- 4 turns
- **Heating rate:**

  Average without specimen holder = 3 °Cs^{-1}

  Average with specimen holder = 10 °Cs^{-1}

Figure 66 - Original coil.

3.7.3.3.2 Coil 2

Specification.

- Conventional helical style
- 30mm internal diameter
- 6mm copper piping
- 2 turns
- **Heating rate:**
  Average without specimen holder – 3.5 $°Cs^{-1}$

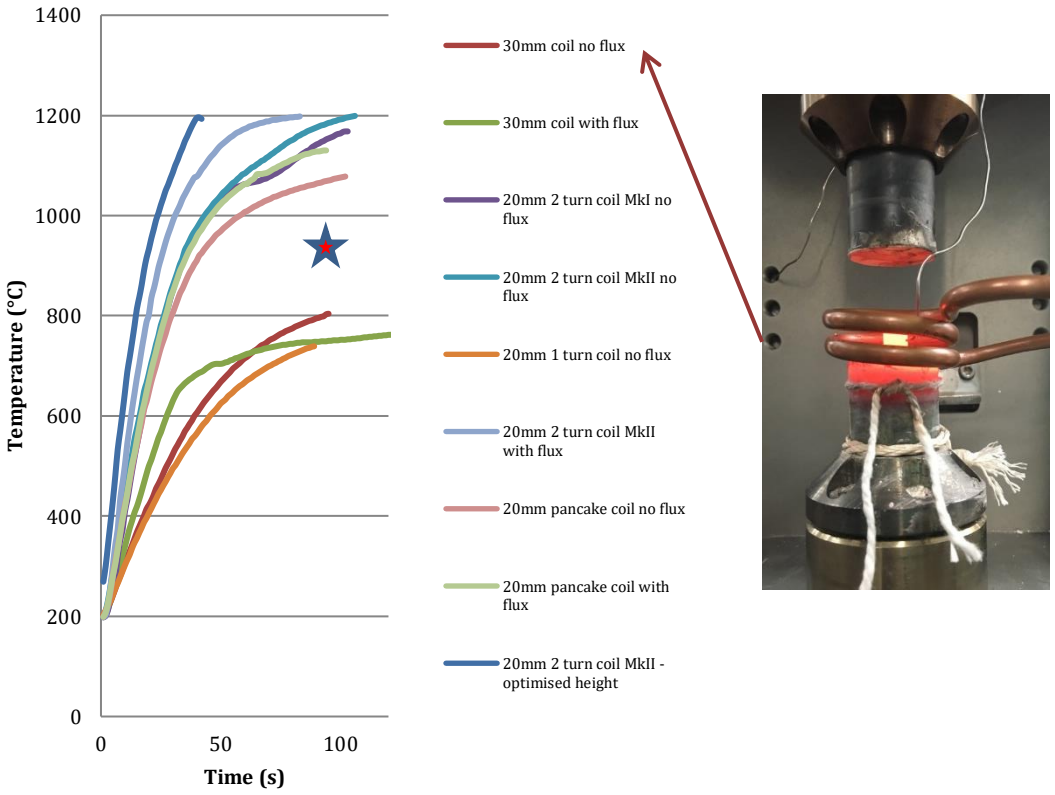

Notes.

Coil 2 was designed with two turns instead of the four turns of the original coil, in the hope that the shorter height of the coil would concentrate more of the power into the specimen and less into the platens. This was true, as during testing the platens appeared to be at a lower temperature compared to when testing with the original coil. Because of this coil 2 was trialled without the specimen holder. The reduction in the number of turns had little effect on the heating rate achievable therefore further modifications were needed.

3.7.3.3.3 Coil 3

Specification.

- Conventional helical style
- 30mm internal diameter
- 6mm copper piping
- 2 turns
- Fluxtrol magnetic flux concentrator applied
- **Heating rate:**

  Initial heating rate - 12.8°Cs^{-1}

  Final heating rate - 1°Cs^{-1}

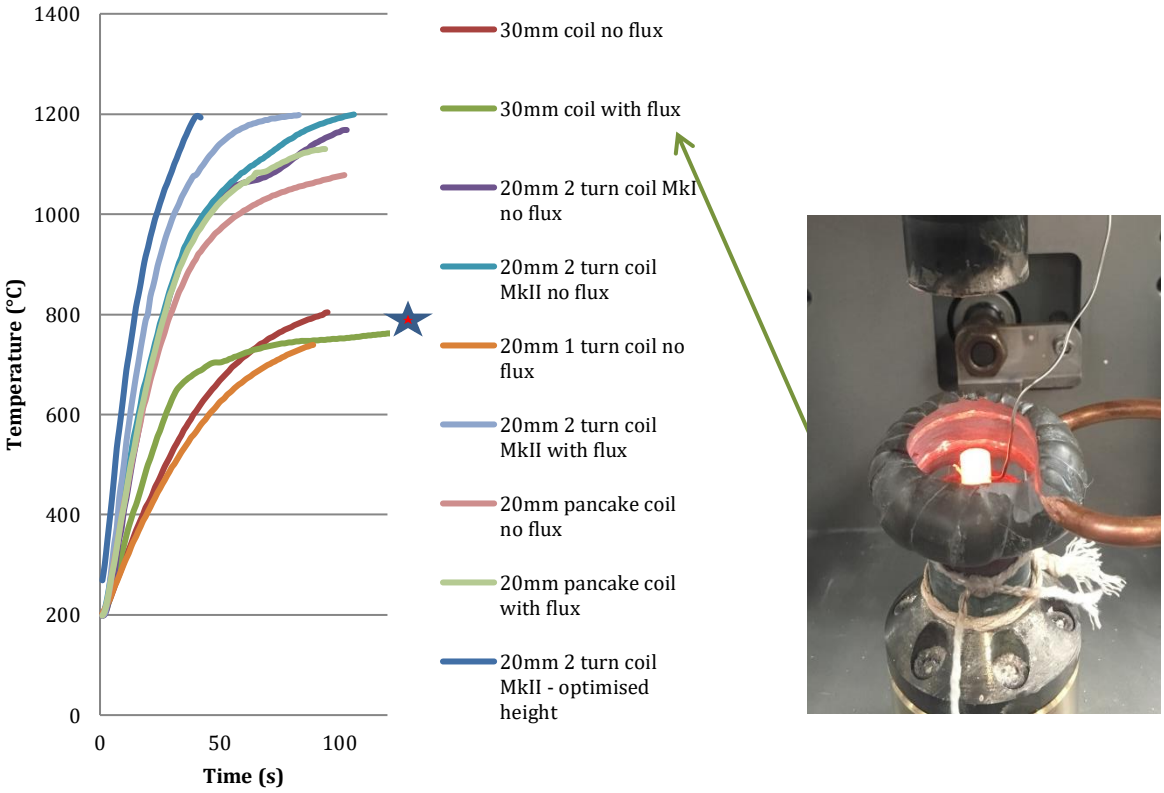

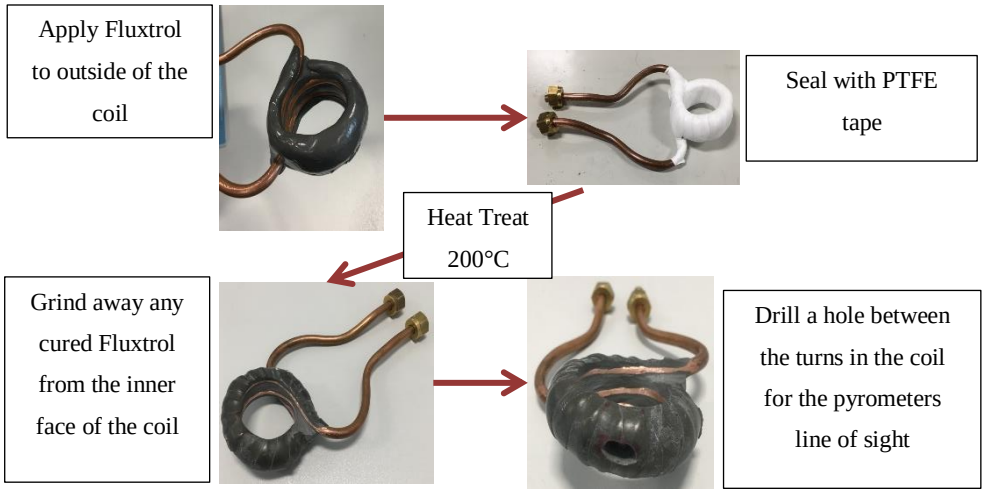

Figure 67 - Application of Fluxtrol to coil 2

Notes.

Before making any drastic changes to the platen dimensions in order to use smaller diameter coils a final attempt was made to increase the effectiveness of coil 2. A magnetic flux concentrator Fluxtrol was applied to the outer perimeter of the coil. Fluxtrol is a magnetic composite that concentrates the magnetic field of the coil in the direction normal to the open face of the copper tubing. The addition Fluxtrol initially looked promising producing a heating rate of 12.8°Cs^{-1} between 200°C and 675°C, but unfortunately this heating rate tapered off severely to as low as 1°Cs^{-1} and failed to reach the target temperature of 1200°C. It was clear that in order to significantly increase the heating rate a reduction in coil diameter needed to be made and therefore a reduction in platen diameter also.

3.7.3.3.4 Platen re-shaping.

If a smaller diameter coil was to be used, the diameter of the compression platens would also need to be reduced to the same diameter to ensure the platens could pass freely through the coil during a compression test. It was calculated that if a standard 8mm diameter by 12mm height compression specimen was compressed perfectly from 12mm height to 1mm height it would have a diameter of 13.86mm. Therefore, a decision was made to reduce the platens to 20mm diameter from 30mm, this would still allow some room for error with specimen positioning and/or inhomogenous deformation.

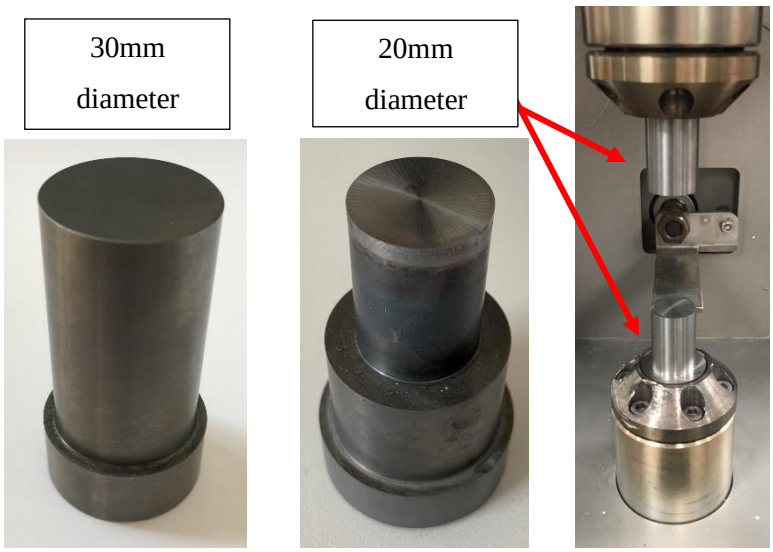

Figure 68 - Tungsten platen modifications - Outer diameter ground down from 30mm to 20mm.

3.7.3.3.5 Coil 4

Specification.

- Conventional helical style
- 20mm internal diameter
- 6mm copper piping
- 1 turn
- **Heating rate:**

  Average heating rate - 6 °Cs^{-1}

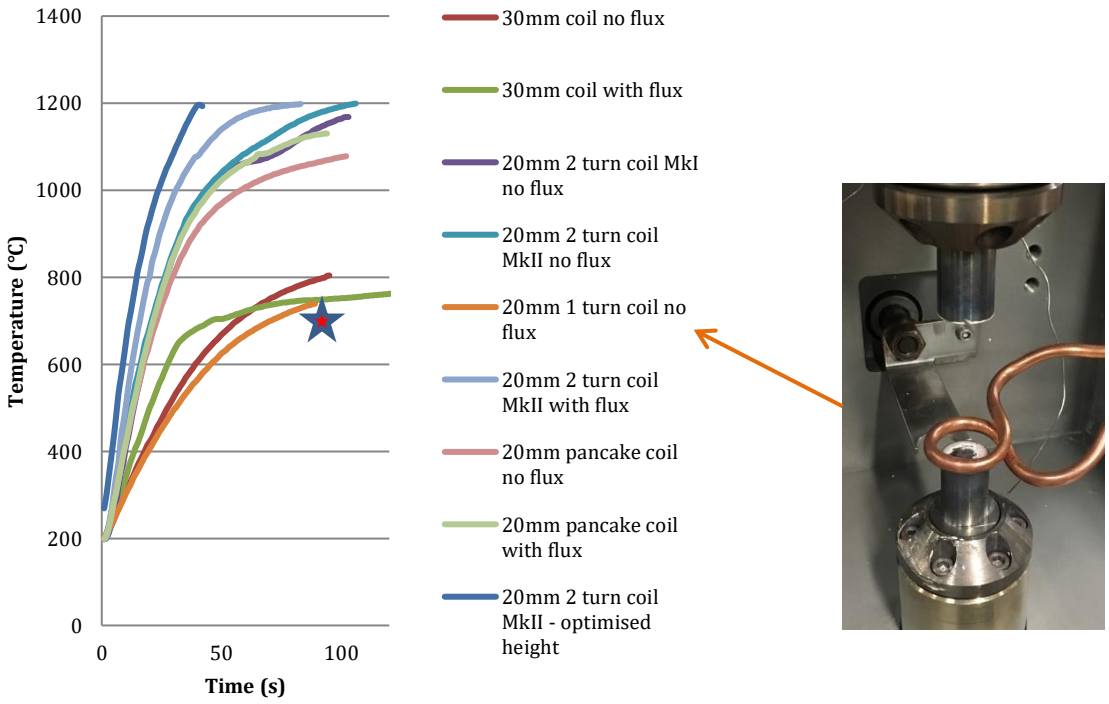

Notes.

The first 20mm diameter coil to be trialled was a single turn coil made from 6mm diameter copper tubing. It was expected that this coil would not perform well as the purpose of having multiple turns is to amplify the magnetic field between them. As a result, coil 4 was the worst performing coil tested, producing an average heating rate of 3°Cs^{-1} and only reaching 736°C not the target of 1200°C.

3.7.3.3.6 Coil 5

Specification.

- Flat radial ‘pancake’ style
- 20mm internal diameter
- 6mm copper piping
- 2 radial turns
- **Heating rate:**

  Initial heating rate - 18°Cs^{-1}

  Tapered off to 3 °Cs^{-1}

Notes.

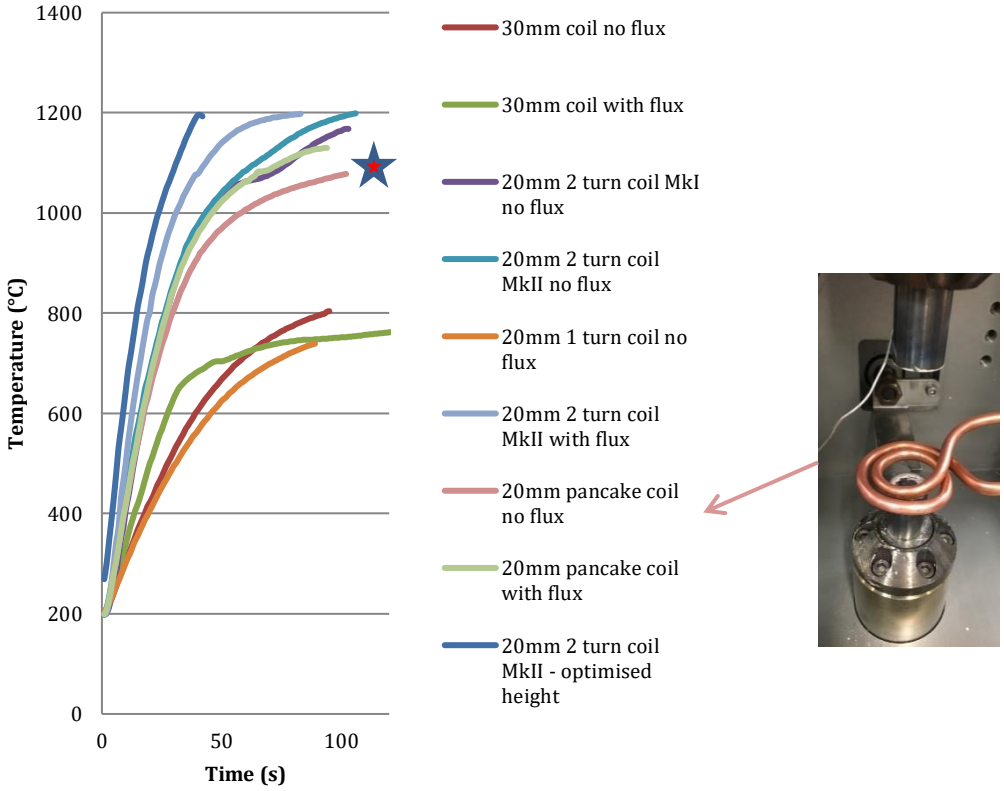

Coil 5 was the first flat radial ‘pancake’ style coil to be trialled. Flat coil designs are usually used to heat large flat surfaces, but the radial turns do also provide a significant amount of power towards the centre of the coil. Coil 5 initially produced a heating rate of 18°Cs^{-1} up to 800°C but then tapered off quite aggressively to only 3°Cs^{-1}.

3.7.3.3.7 Coil 6

Specification.

- Flat radial 'pancake' style
- 20mm internal diameter
- 6mm copper piping
- 2 radial turns
- Fluxtrol magnetic flux concentrator applied
- **Heating rate:**

  Initial heating rate - 20°Cs^{-1}

  Final heating rate - 4°Cs^{-1}

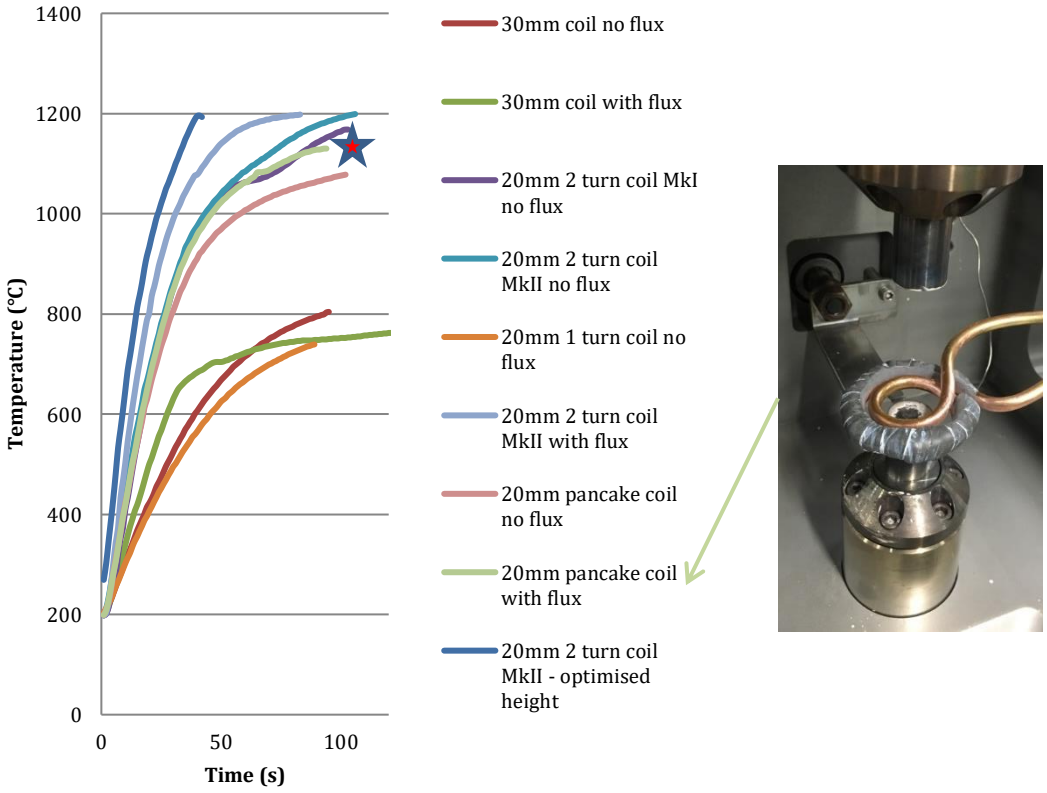

Notes.

With coil 5 exhibiting a strong initial heating rate of 18°Cs^{-1}, Fluxtrol was applied to the outer turn to try and amplify the field at the centre of the coil. This modification resulted in a slight enhancement of 2°Cs^{-1} to the initial heating rate and 1°Cs^{-1} to the final heating rate. Both radial coils failed to sustain an adequate heating rate to the target temperature of 1200°C consequently only conventional helical type coils were to be trialled from this point onwards.

3.7.3.3.8 Coil 7

Specification.

- Conventional helical style
- 20mm internal diameter
- 6mm copper piping
- 2 ½ turns
- **Heating rate:**

  Initial heating rate - 21°Cs^{-1}

  Final heating rate - 4°Cs^{-1}

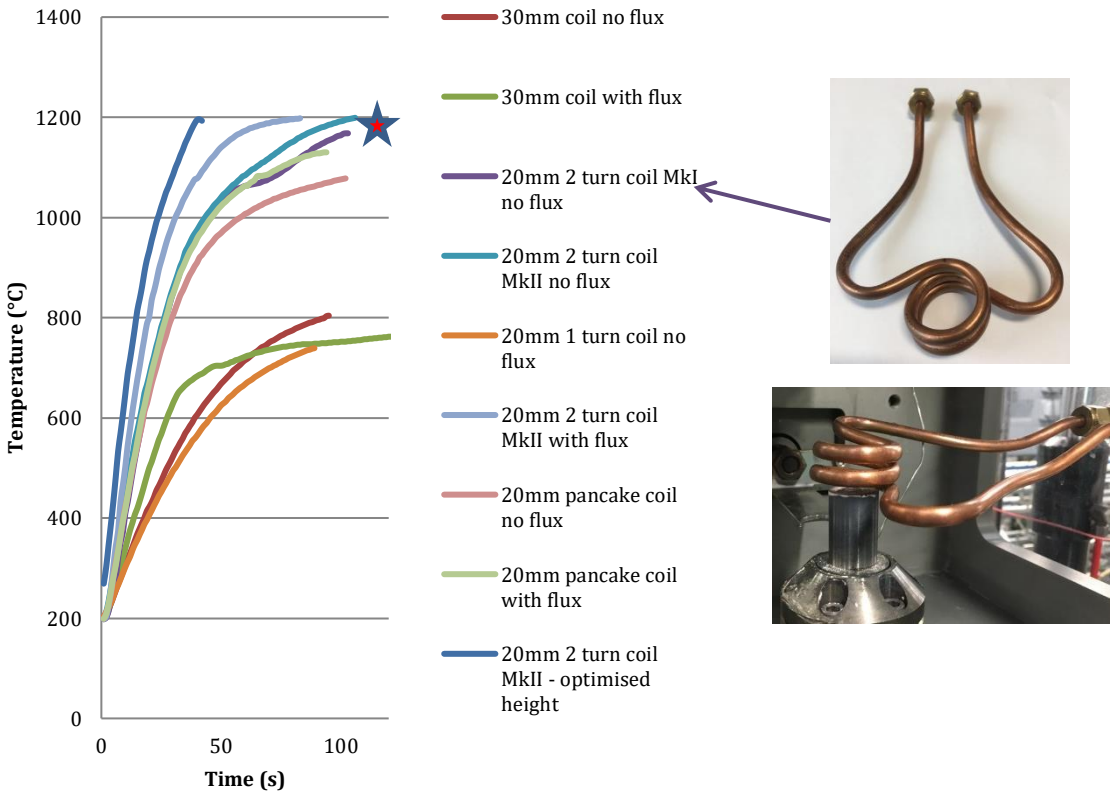

Notes.

Coil 7 was the first multiple turn, conventional helical style coil to be trialled with the new 20mm internal diameter. The arms of the coil were intentionally wrapped further around the coil than usual in effect creating a two and a half turn coil with two turns at the front and three at the back. Coil 7 matched the performance of coil 6 even without the use of Fluxtrol, giving an initial heating rate of 20°Cs^{-1} but tapering off to 4°Cs^{-1} at the end.

3.7.3.3.9 Coil 8

Specification.

- Conventional helical style
- 20mm internal diameter
- 6mm copper piping
- 2 turns

Heating rate:

Initial heating rate - 21°Cs^{-1}

Final heating rate - 5°Cs^{-1}

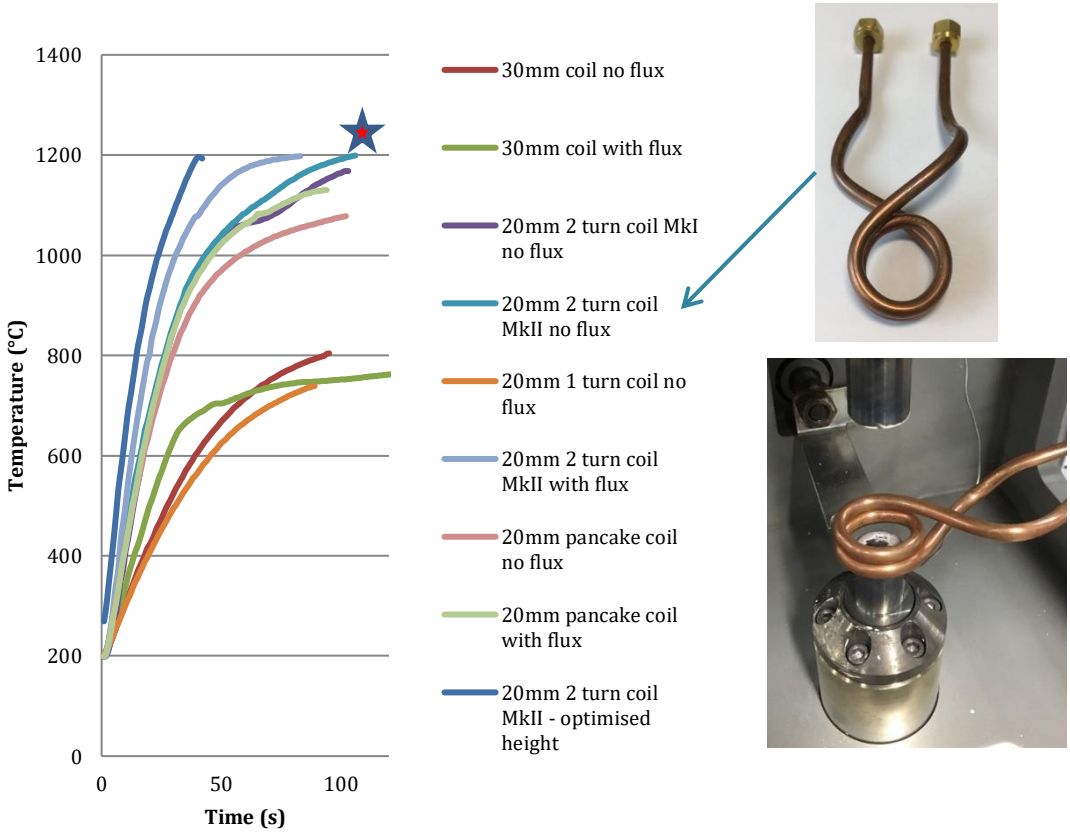

Notes.

Coil 8 was the same design as coil 7 but without the extra coil arm wrap around. As expected, coil 8 performed similarly to coil 7 but with a slight improvement on the final heating rate with 5°Cs^{-1}. Coil 7 was also the first coil to reach the target temperature of 1200°C in the allotted 100s test time.

3.7.3.3.10 Coil 9

Specification.

- Conventional helical style
- 20mm internal diameter
- 6mm copper piping
- 2 turns
- Fluxtrol magnetic flux concentrator applied
- **Heating rate:**

  Initial heating rate - 30°Cs^{-1}

  Final heating rate - 5°Cs^{-1}

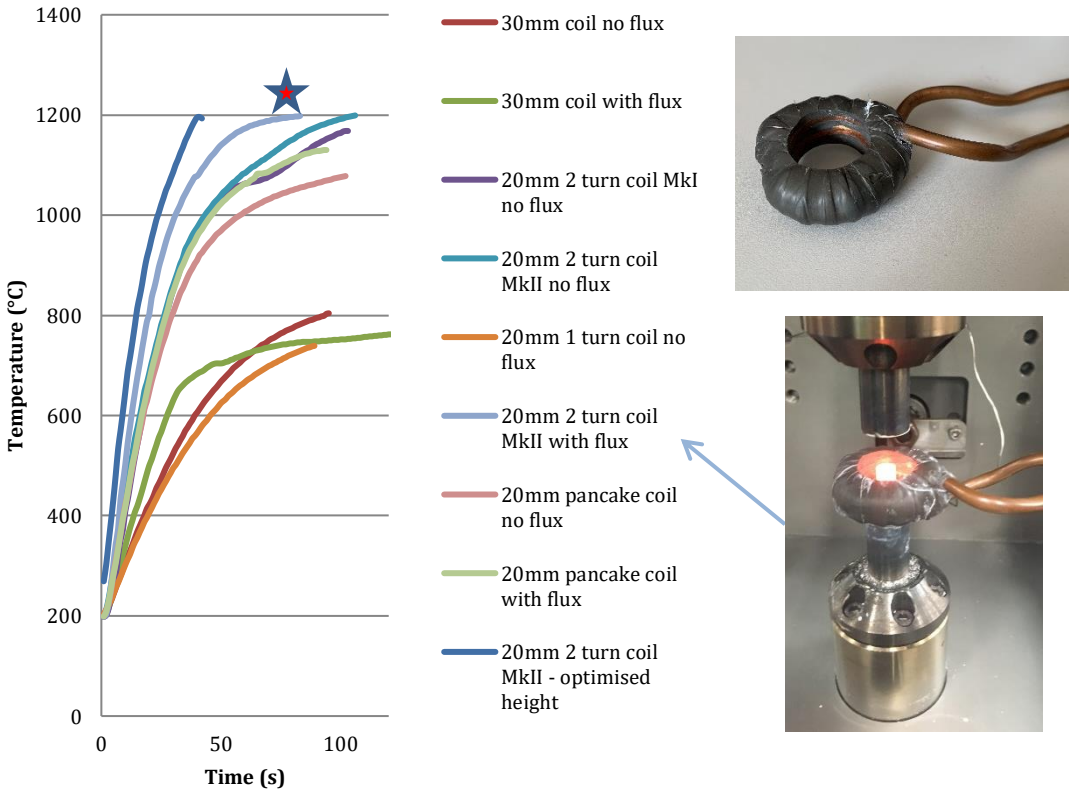

Notes.

With coil 8 being the first design to reach the target test temperature of 1200°C in the allotted test time, an attempt to improve the performance of this design was made with the application of Fluxtrol to the outer diameter of the coil. The Fluxtrol was much more effective on the conventional helical style coil compared to when it was applied to the 'pancake' style coil. In this instance the application of Fluxtrol improved initial heating rate by $9°Cs^{-1}$, thus being the first coil to reach the desired heating rate of $25°Cs^{-1}$.

3.7.3.3.11 Coil 9 – Specimen position optimisation

Coil 9 with the Fluxtrol coating was the best performing design from this batch of coils which were manufactured with 6mm diameter copper tubing. An experiment was conducted to assess at what linear position inside the coil the field was most powerful and could provide the highest heating rate.

To do this coil 9 was fitted to the 2kW induction heating system and a steel rod placed inside it, as shown in Figure 69. The steel rod had four N-type thermocouples spot welded to it in 5mm intervals. The steel rod was then raised through the coil in sequential 0.1mm movements with the temperature reading from each thermocouple being recorded at each. The thermocouple data showed that the hottest section of the coil was between 3.25 and 16mm from the bottom edge of the Fluxtrol bonded to the coil. This suggested that if the top of the specimen was aligned around 15mm from the bottom edge of the coil the specimen will heat at the fastest rate possible.

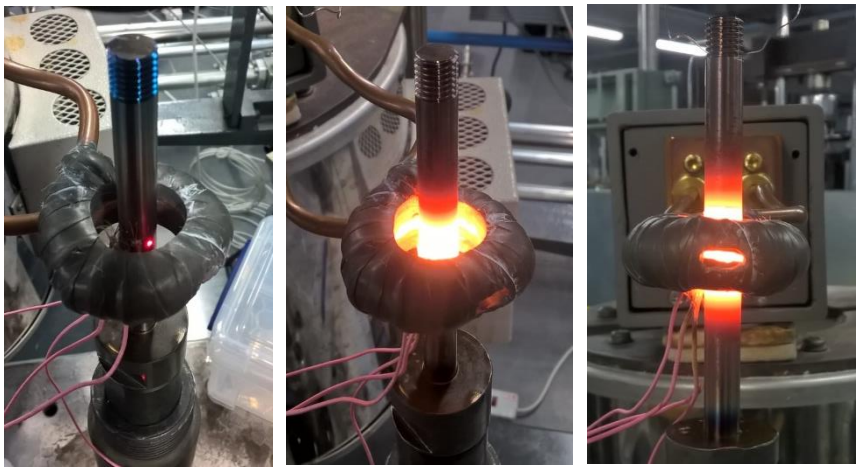

Figure 69 - Steel rod with N-type thermocouples spaced in 5mm intervals being heated within coil 9 to optimise specimen positioning.

3.7.3.3.12 Coil 9 – With optimised specimen positioning

Specification.

- Conventional helical style
- 20mm internal diameter
- 6mm copper piping
- 2 turns
- Fluxtrol magnetic flux concentrator applied
- **Heating rate:**

  Initial heating rate - 32°Cs^{-1}

  Final heating rate - 12°Cs^{-1}

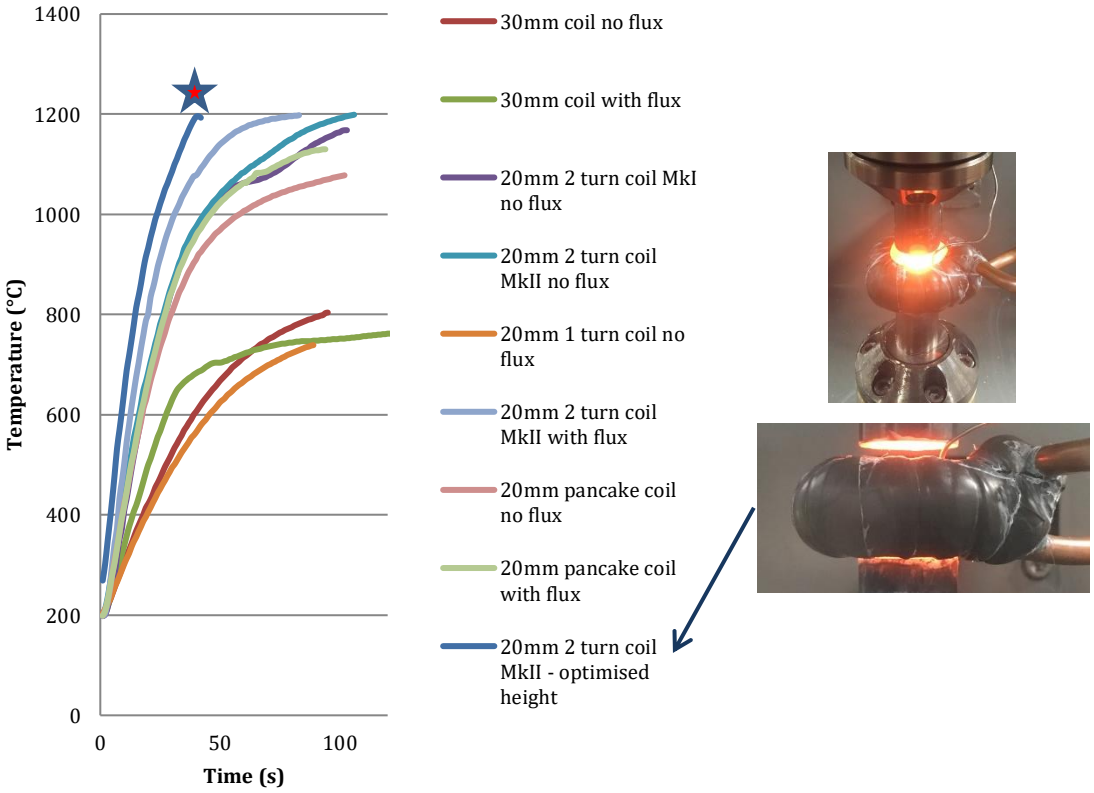

Notes.

Heating a specimen within coil 9 at the optimised specimen height resulted in a further increase of initial heating rate from 30°Cs^{-1} to 32°Cs^{-1} also improving the final heating rate by 7°Cs^{-1} to 12°Cs^{-1}. This sustained heating rate was thought to be sufficient to initiate sub-solidus liquation in FG and CG RR1000. Although a compression test needed to be conducted to assess the effectiveness of the design alterations.

3.7.3.3.13 Coil 9 compression test with specimen holder

A compression test was carried out using coil 9 at the optimum height paired with the specimen holder to assess if the holder would break away as theorised or if it would foul on the specimen during testing thus affecting the specimen deformation.

A standard sized FG specimen was placed onto a specimen holder and placed on the lower platen. The induction heater was set to heat the specimen to 500°C initially followed by a 5 second hold. The controller was then set to ramp the temperature up to 1200°C at 10°Cs^{-1}. The compression test was set to commence as the specimen reached the target test temperature. The specimen was pushed through the specimen holder and compressed as planned but unfortunately, even though the specimen holder was heavily disintegrated, it did not break away as intended and instead remained around the deformed specimen. Following the compression, the chamber aligned the quench actuator with the lower platen where it activated, knocking the specimen and the encapsulating specimen holder into the quench bath.

On inspection of the specimen it was evident that it had not deformed homogenously as can be seen in Figure 70. The centre of the specimen had deformed as expected showing some signs of barrelling, while the top surface looked undeformed and the bottom surface featuring three large shear cracks. It was suspected that on compression the lower temperature tungsten platens had quenched the top and bottom surfaces on contact reducing the temperature significantly before the compression test was completed.

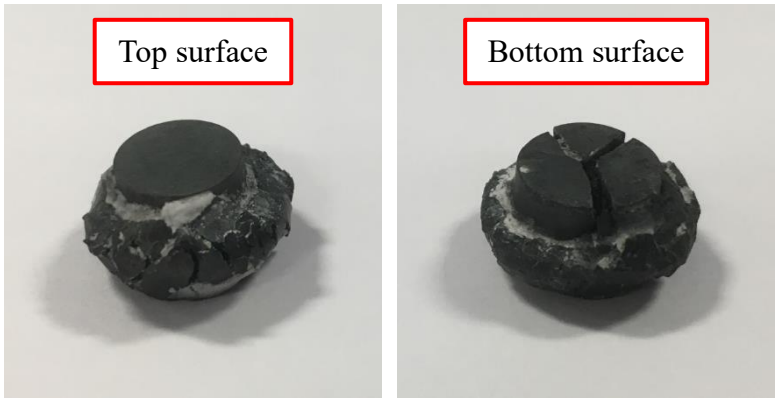

Figure 70 - Standard size FG compression specimen after a trial compression test at 1200°C with coil 9 & specimen holder. Exhibiting

3.7.3.3.14 Gas pressure sintered silicon nitride (GPSN) ceramic platens trials

In an attempt to reduce the quenching effect of the compression platens, on contact with the specimens, a new platen material was trialled, namely gas pressure sintered silicon nitride ceramic (pictured in Figure 71).

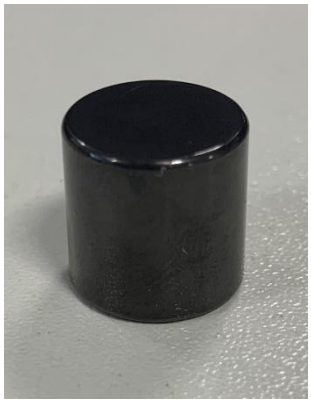

Figure 71 - 12mm diameter by 12mm height GPSN ceramic disk.

The GPSN was to be used as an insulator between the tungsten platens and the specimen as the thermal conductivity of GPSN is much lower than that of tungsten. In order to test the suitability of GPSN a compression test was carried out with a GPSN disk acting as the lower platen. A schematic of the test carried out is illustrated in Figure 72.

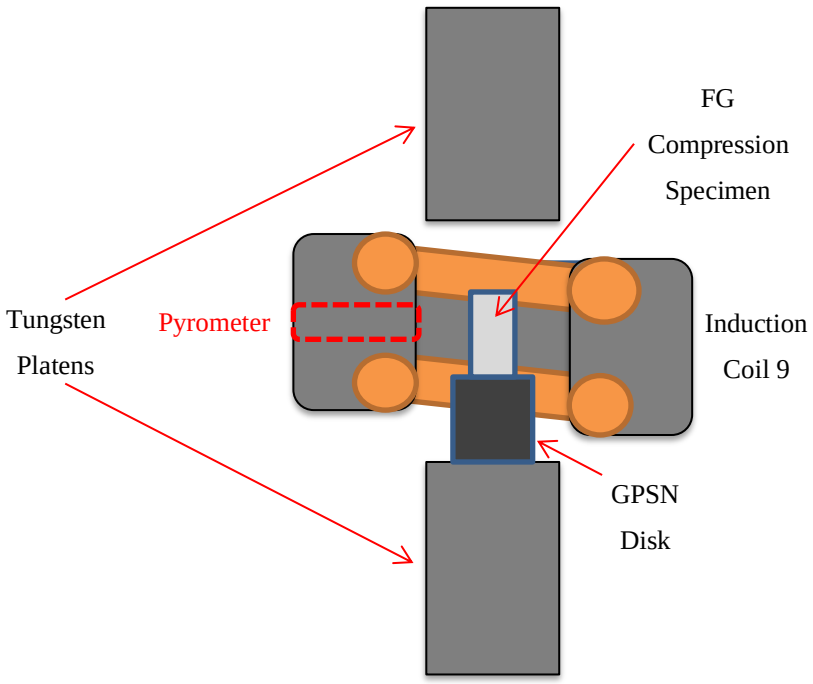

Figure 72 - Schematic diagram illustrating the set up used to trial the GPSN as a platen material.

A standard size FG specimen was placed on top of a 12mm height x 12mm diameter GPSN disk which was resting on top of the lower tungsten platen. Coil 9 was placed around the specimen and a compression test was carried out using the same heating profile as the coil 9 compression test with the specimen holder. On reaching the 1200°C target temperature the specimen was compressed into the GPSN disk, followed by the quench mechanism knocking both the GPSN disk and the Specimen into the quench bath.

Observation of the specimen revealed that a temperature gradient along the specimen's height was still present as the bottom of the specimen was again undeformed with approximately 4mm of the specimen remaining intact, indicating it had suffered heat soak from being in contact with the GPSN disk. The top of the specimen had experienced some deformation, disintegrating in a similar fashion to the specimens tested in the PROMOTE project as can be seen in Figure 73.

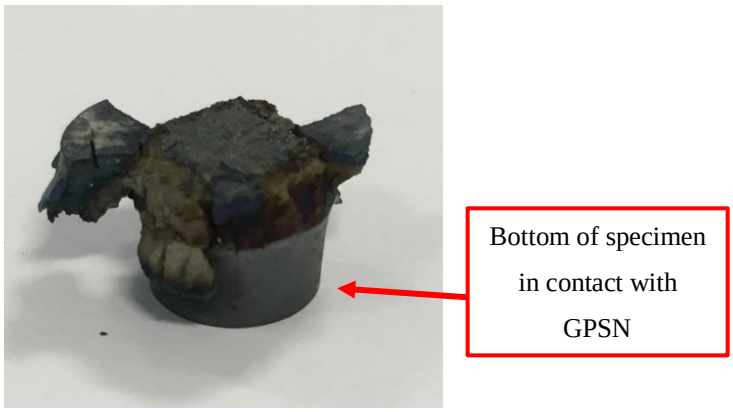

Figure 73 - FG compression specimen used in the GPSN platen trial compression test. Showing inhomogeneous deformation and specimen disintegration.

The specimen was sectioned in half and prepped for electro-etching so that the size and morphology of the gamma prime precipitates could be observed to give an indication of the temperature that the bottom of the specimen had reached. The optical micrograph in Figure 74, A shows a region of material that differentially etched to the rest of the specimen that coincided with the bottom of the specimen that was quenched by the GPSN disk. Further investigation of this region revealed that this area still contained primary γ' although slight spheroidization can be seen in the SEM micrograph in Figure 74, B. The presence of primary γ' indicated that the bottom of the specimen had failed to reach RR1000's gamma prime solvus of 1140 °C.

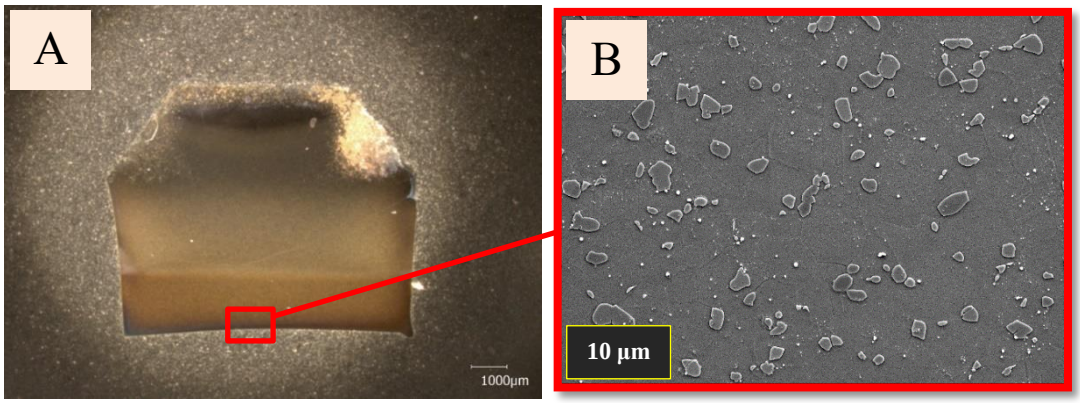

Figure 74 - Micrographs of specimen used in GPSN trial. A) Optical micrograph at low magnification. B) SEM micrograph at higher magnification.

3.7.3.3.15 Coil 10 & measurement of the temperature gradient

In order to assess the temperature gradient through the height of the specimen the experiment was replicated with one of the spark-eroded thermocouple specimens with an N-type contact thermocouple within it. Two additional spot-welded N-type thermocouples were attached 0.5mm from the top and bottom surface of the specimen allowing temperature measurement of the whole specimen. Figure 75 shows a schematic diagram of the test configuration.

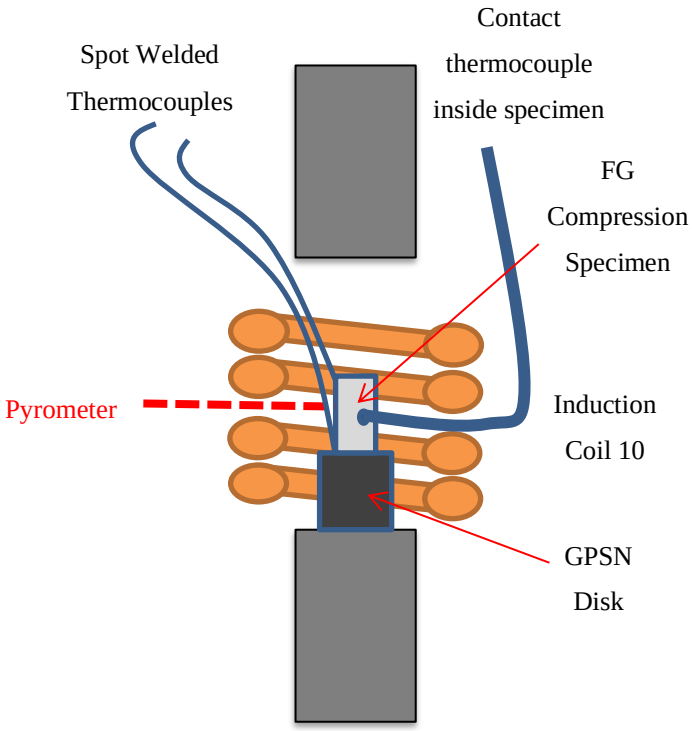

Figure 75 - Schematic diagram illustrating the experiment conducted to measure the temperature gradient across the length of the specimen.

During this test, the specimen was heated incrementally to 1200°C and the temperature reading at each thermocouple was recorded. Figure 76 shows the temperature readings from each thermocouple at three temperature increments during the test, 530°C, 820°C & 1200°C with the maximum temperature difference at that temperature.

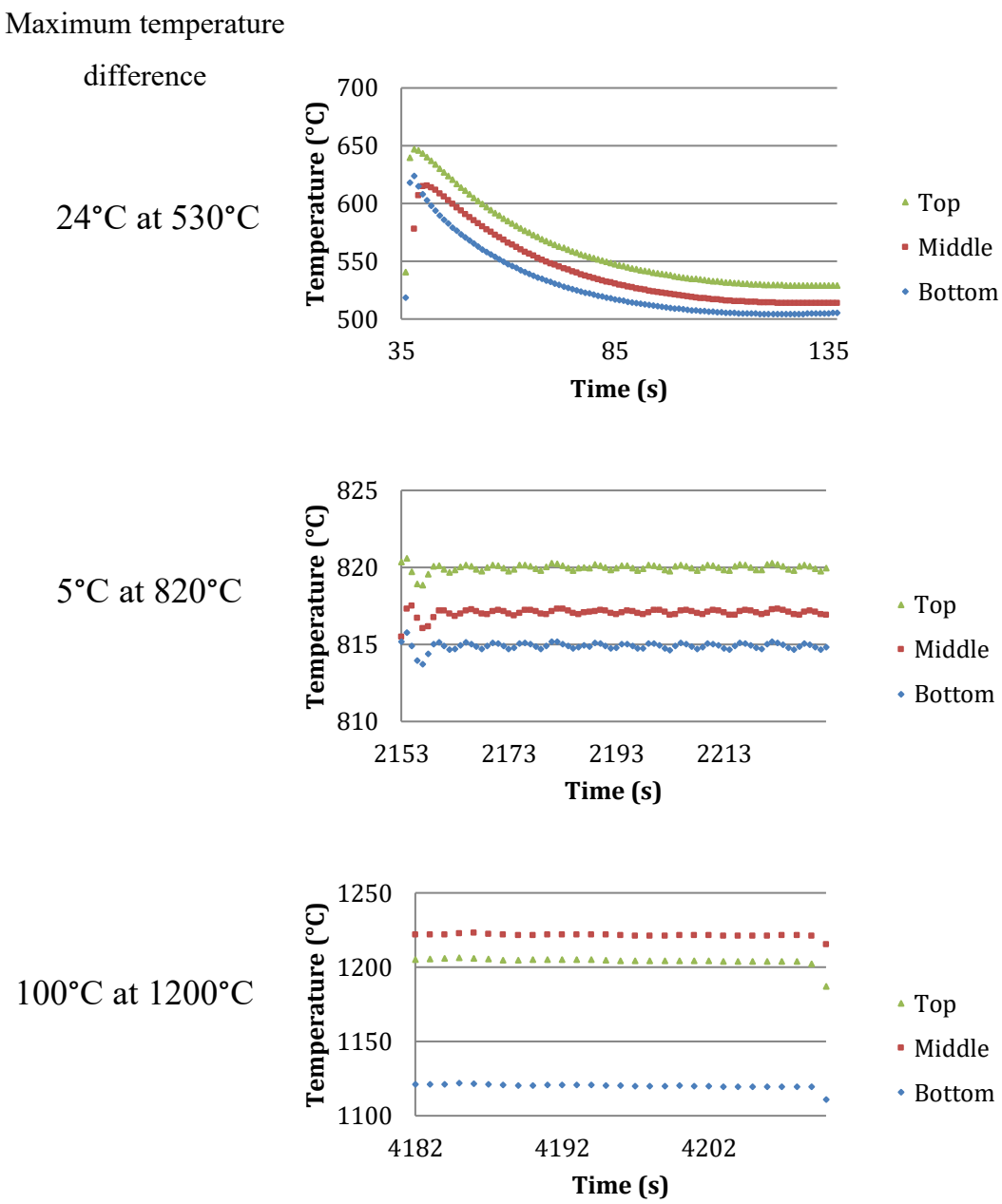

Figure 76 - Thermocouple readings showing the temperature gradient in the specimen created by contact with the GPSN disk at the bottom surface.

The specimen was initially heated as fast as possible to 520°C and held, revealing a gradient of 24°C between the top and bottom of the specimen. Further heating to 820°C reduced the temperature gradient to 5°C but then on heating to the final target temperature of 1200°C the temperature gradient had increased considerably to 100°C. The issue of temperature gradients would need to be resolved before flow stress data could be generated.

This test was also the first trial run of coil 10. This coil was the first of several coil iterations to be made with 4mm diameter copper tubing. The use of 4mm tubing allowed for a coil to have more turns for a given coil height when compared to coils made with 6mm copper tubing. On average, a coil made with 4mm tubing could have 3 turns for every 2 turns in a coil made with 6mm tubing. The increased number of turns and the closer proximity of each turn to its neighbouring turn drastically increased the magnetic field amplification within the coil. As a result, coil 10 produced a much faster heating rate than all the coils before it as detailed below:

Specification.

- Conventional helical style
- 20mm internal diameter
- 4mm copper piping
- 4 turns
- **Heating rate:**

  Initial heating rate - $57°Cs^{-1}$

  Final heating rate - $57°Cs^{-1}$

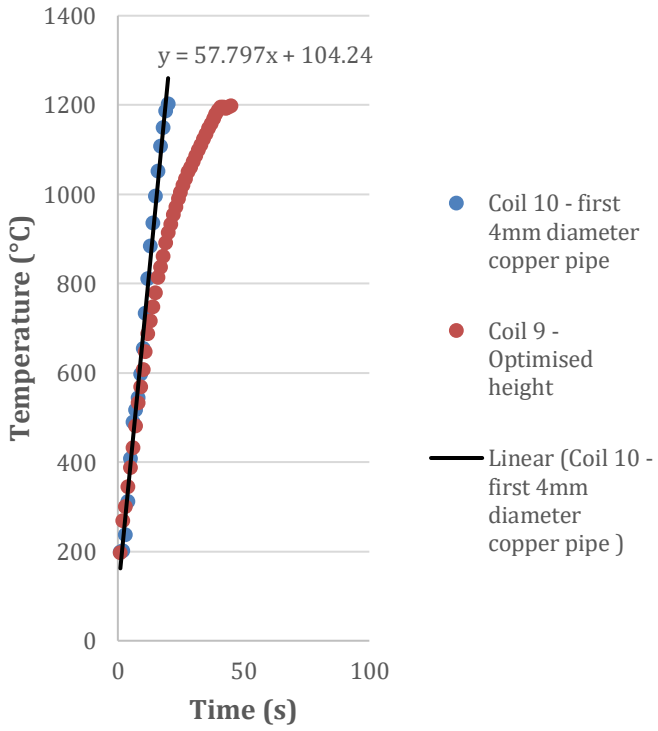

Notes.

The linear trend line applied to coil 10's heating profile indicates a gradient of 57.8°Cs^{-1} was achieved throughout the whole test showing no signs of heating rate drop off unlike the coils manufactured with 6mm diameter copper tubing. The heating profile of coil 9 at its optimum height is also illustrated on the graph for comparison.

3.7.3.3.16 Specimen isolation – 'floating' specimen method

The thermocouple data showed a significant temperature gradient was present during heating, caused by contact of the bottom surface of the specimen with the GPSN disk. An attempt was made to isolate the specimen from the GPSN disk and tungsten platen during heating. This was done by spot welding two 15mm strands of type-N thermocouple to each side of the specimen, the specimen was then lowered inside the induction coil and suspended within it via the two thermocouple strands resting on the turns un the coil. A schematic diagram of this set up is illustrated in Figure 77.

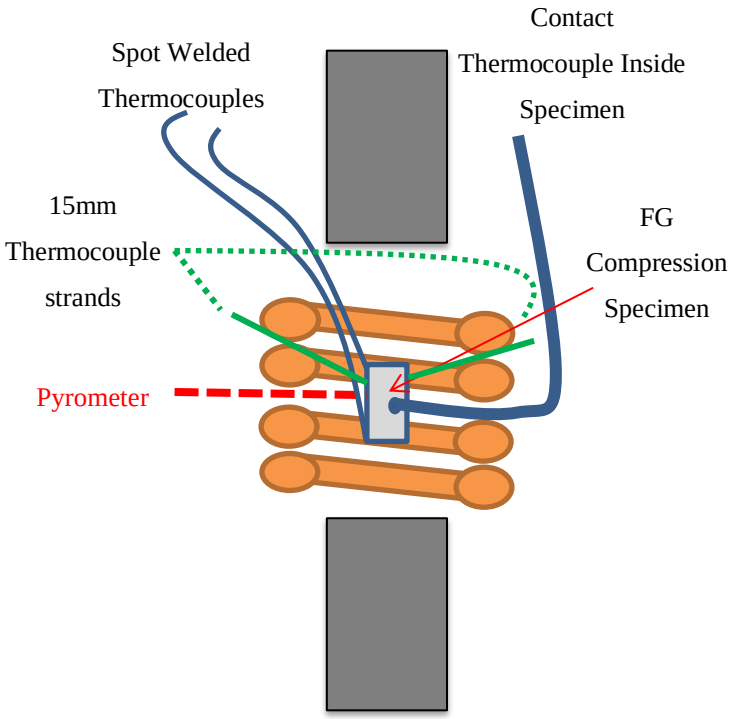

Figure 77 - Schematic diagram illustrating the experiment conducted to assess whether the temperature gradient across the length of the specimen had been rectified with the 'floating' specimen method.

Another specimen with two spot welded thermocouples top (Green) and bottom (Blue) paired with a contact thermocouple at the centre (Red) was used to measure the temperature of the specimen during heating utilising the 'floating' specimen method. An additional contact thermocouple was attached to the top of the steel loading road (Pink) to track its temperature so that any overheating could be noticed and prevented. The specimen was heated to 1200°C incrementally as shown in Figure 78. The temperature profile clearly shows the top and bottom of the specimen heating uniformly indicating that there was no temperature gradient in the specimen. The middle contact thermocouple lagged slightly during heating but reached the desired

temperature fractionally after the top and bottom thermocouples between the required test temperature 900-1200°C. The lag experienced by the centre thermocouple is thought to be the result of the use of a contact thermocouple. Contact thermocouples are not as reliable as spot welded thermocouples as you rely on a good contact area between the thermocouple tip and the surface of the specimen being measured. With the thermocouple being inside the specimen it is difficult to know whether a good mating of the surfaces was present during testing. Large specimens can be susceptible to the skin heating affect associated with induction heating. The skin heating effect is when the outside of the specimen heats slightly faster than the centre due to the surface of the specimen being in closer proximity to the induction coil. As the specimens in this research are so small it is unlikely that the skin heating effect is significant, and that the temperature lag exhibited was thermocouple related.

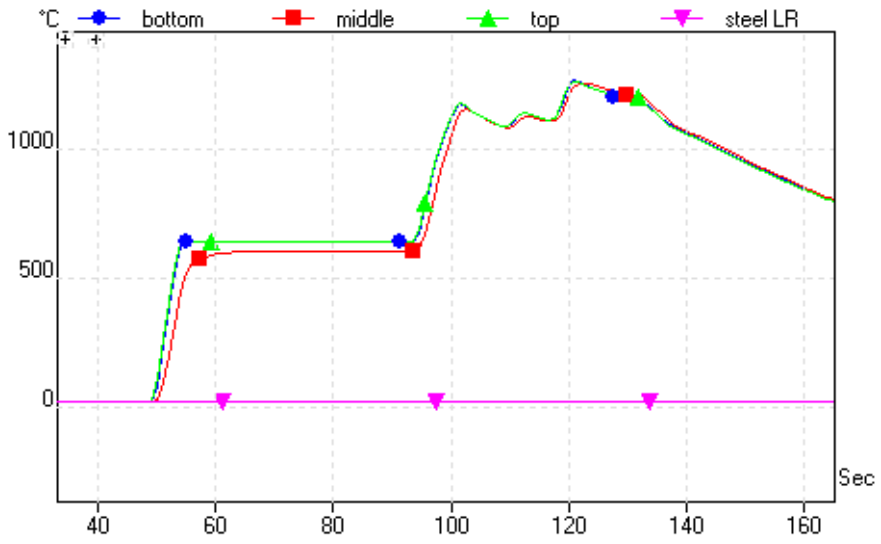

Figure 78 - Thermocouple temperature data indicating no temperature gradient was present throughout the specimen during heating with the 'floating' specimen method.

In order to test the suitability of the floating specimen method a compression test was performed. Figure 79 illustrates the test set up. A standard sized FG RR1000 specimen was held within the coil 2mm above a GPSN disk via the 'floating' specimen method. The specimen was then heated at 25°Cs^{-1} to 1200°C. On reaching the target temperature the top platen pushed the specimen down onto the GPSN disk compressing it at 12mms^{-1}.

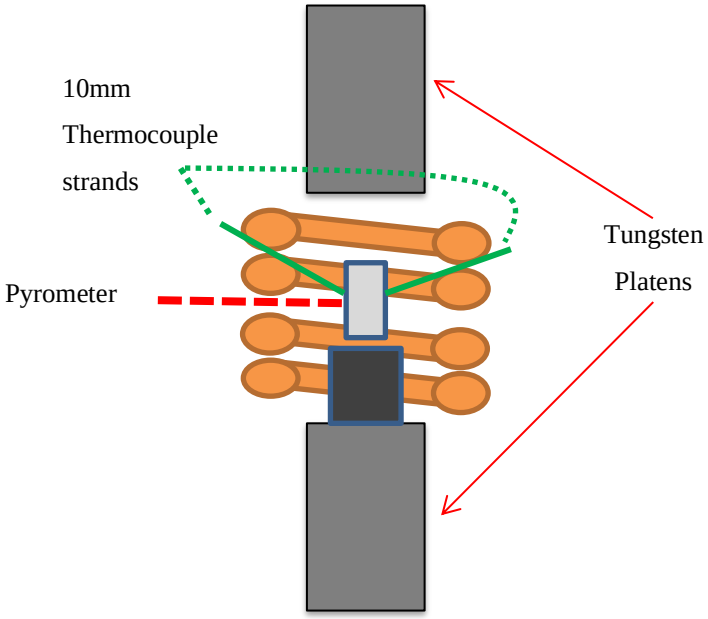

Figure 79 - Schematic diagram illustrating the experiment conducted to assess the suitability of the 'floating' specimen method.

The macro image and optical micrograph of the specimen used in this test shown in Figure 80 clearly shows that on contact with the top platen and GPSN disk the specimen has been quenched before the compression test could be completed. The top and bottom regions of the specimen were relatively undeformed compared to the centre where SIP and disintegration had occurred.

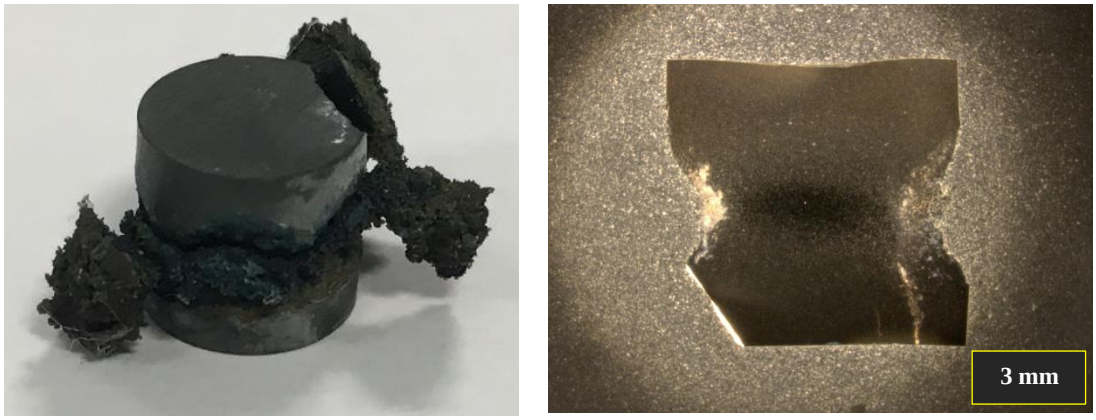

Figure 80 - Macro photograph and optical micrograph of the specimen used in the 'floating' specimen compression trial.

As can be seen in Figure 80 the top of the specimen was quenched more severely than the bottom retaining a larger volume of undeformed material. The cause of this was thought to be due to slightly longer contact time with the top platen as the specimen was pushed through the isolation gap between the bottom of the specimen and the GPSN disk along with the greater thermal conductivity of the tungsten platen compared to GPSN. In order to confirm that the undeformed material was in fact caused by quenching of the specimen on the platens and not by a temperature gradient caused by the induction coil design, this specimen was prepped via the standard metallographic preparation procedure and electro etched. The specimen was then examined in the FEG SEM to assess its microstructure. The SEM micrographs in Figure 81 clearly show eutectic products present at the top and bottom of the specimen confirming that the specimen had reached the target temperature of 1200°C resulting in liquation. This was confirmation that the specimen quenching was caused by contact with the lower temperature platens and that even the reduced thermal conductivity of GPSN was enough to prevent specimen quenching.

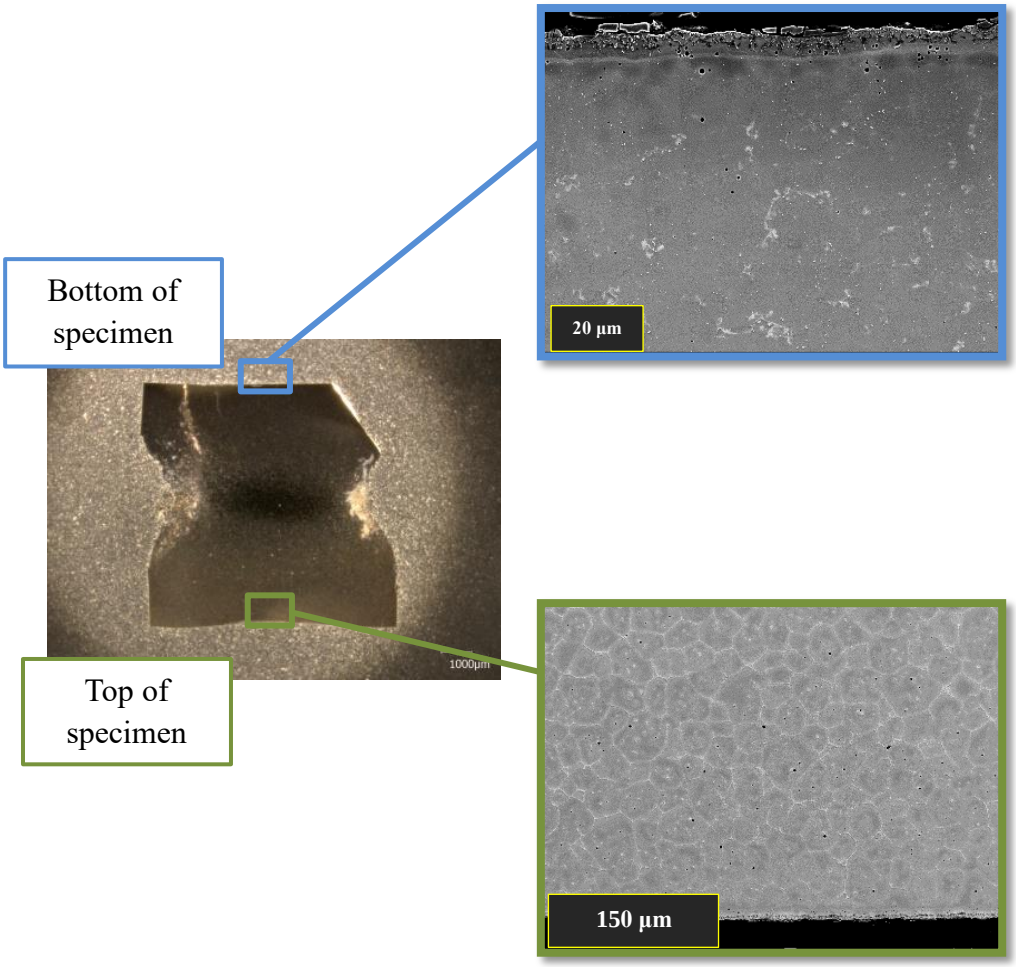

Figure 81 - SEM micrographs illustrating the presence of eutectic products at the top and bottom of the specimen. Optical micrograph included to indicate the area the SEM micrographs were taken.

An attempt was made to decrease the quenching effect of the platens by diverting the cooling water from the loading rods, although this made very little difference. As a result, the only logical progression was to find a way to heat the tungsten platens to the same temperature as the specimen. This would have been impossible with the original batch of coils manufactured with the 6mm copper tubing, but the new coils made with 4mm diameter tubing had proven to be much more powerful, potentially being sufficient to heat the platens as well as the specimen if a larger coil with more turns was used.

3.7.3.3.17 Coil 11

Coil 11 a taller 6 turn coil was manufactured from the 4mm copper tubing in order to have more room to insert the tungsten platens to heat them simultaneously with the specimen. The specification and performance of coil 11 is detailed below:

Specification.

- Conventional helical style
- 20mm internal diameter
- 4mm copper piping
- 6 turns
- **Heating rate:**

  Initial heating rate - 135°Cs^{-1}

  Final heating rate - 75°Cs^{-1}

Notes.

The addition of two more turns improved the performance dramatically raising the initial heating rate capability to 135°Cs^{-1} and the final heating rate to 75°Cs^{-1}. Unfortunately accompanying this newfound performance was a new problem. During the capability testing of coil 11 the induction heater would intermittently emit strong radio frequency (RF) radiation when subjected to high loads. This would usually occur when the induction heater would need to operate at maximum power, such as when a fast heating rate is requested. The RF radiation was strong enough to induce currents in the USB cables that connect the PID controller and thermocouple PICO logger to the laptop computer that was recording the temperature data. The currents induced in the USB cables were enough to overload the USB ports causing a communication drop out, therefore preventing the temperature data to be logged. Fortunately, in the event of a communication drop out the induction heater would be still under control via the PID controller. The communication dropouts have been labelled in coil 11's temperature profile below.

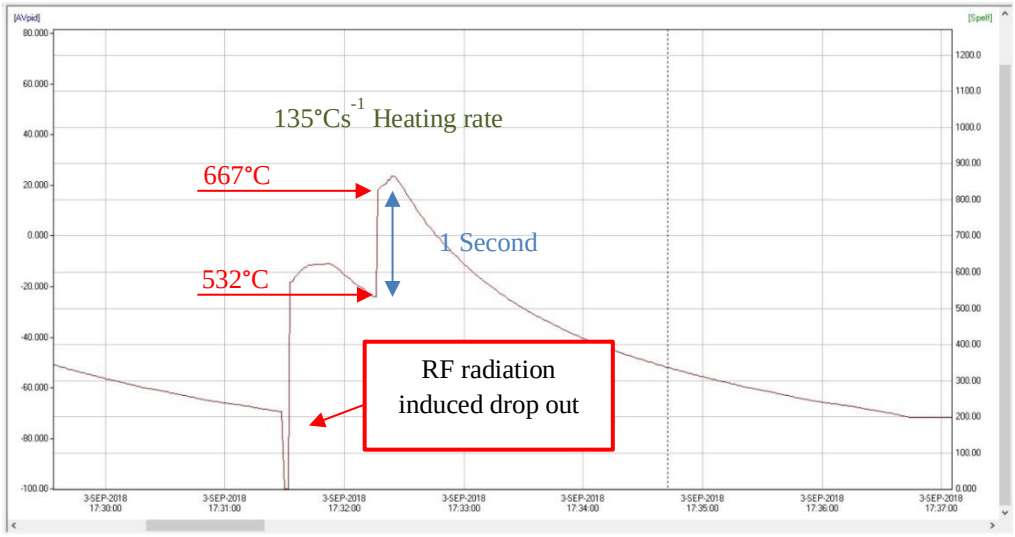

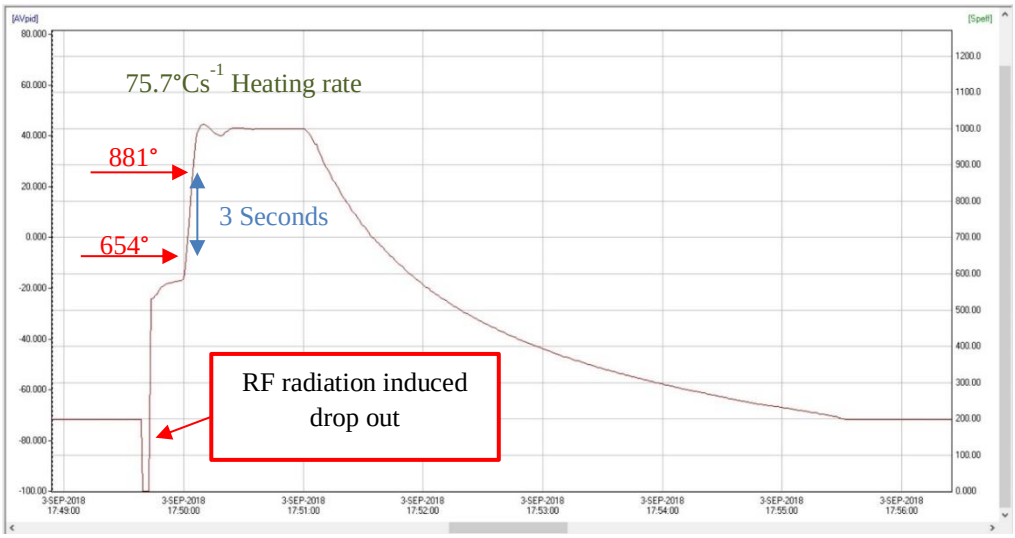

In some instances, the RF radiation emitted would be so severe that it would interfere with the operating systems of other hydraulic test frames within the SMaRT laboratory, causing their actuators to jump around violently. This was obviously a major concern and from this point onwards any testing on FG1 and the use of the induction heater had to be limited to times where no tests were being run on the affected hydraulic test frames.

3.7.3.3.18 Simultaneous heating of the specimen & tungsten platens

Working around the interference problems caused by the RF radiation, a series of tests were conducted with larger coils made of 4mm copper tubing in an attempt to bring the tungsten platens up to testing temperature with the specimen simultaneously. Initially coil 11, with its 6 turns was tested with the set up shown in Figure 82.

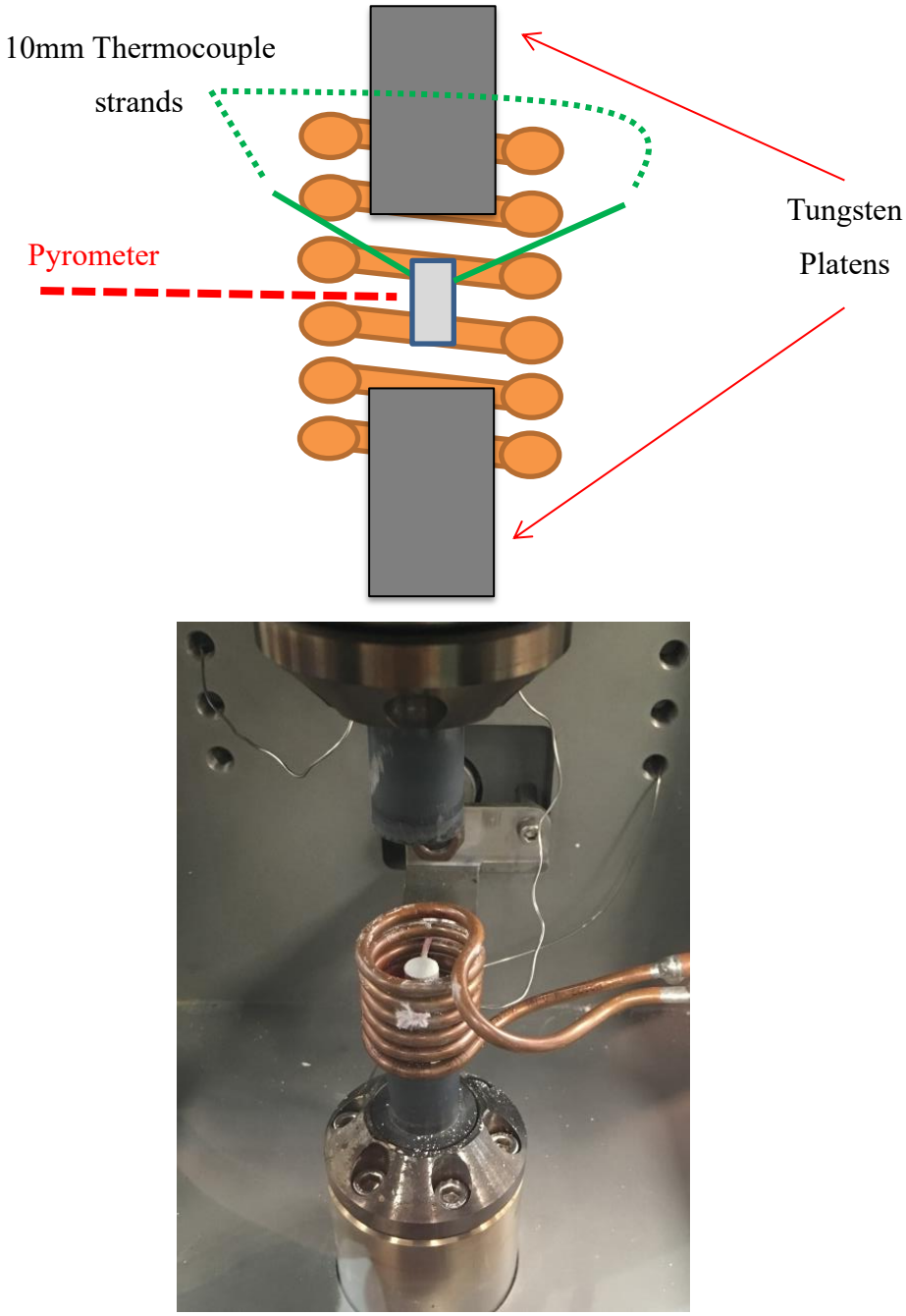

Figure 82 - A) A schematic diagram illustrating the set up used to assess coil 11's ability to heat the tungsten platens to the test temperature. B) A photograph of coil 11 with a 'floating' specimen within it just before the top platen was lowered into the coil.

During this test, the specimen was heated to 1000°C at 25°Cs^{-1} from 520°C^{-1}. The temperature of the tungsten platen was monitored via a N-type contact thermocouple placed at the top of the bottom platen. When the specimen reached 1000°C the tungsten platens had reached 300°C. Although this was an improvement over the original set up used when the semi-solid testing facility was first built, the platen temperature would need to be increased further.

3.7.3.3.18.1Coil 12 – 8 turn 4mm diameter tubing.

Coil 12 was manufactured in the same fashion as coil 11 but with an extra two turns added allowing the tungsten platens to be inserted further into the coil during heating. Coil 12 is pictured in Figure 83.

Figure 83 - A photograph of coil 12 with a 'floating' specimen within it and the tungsten platens inserted ready for testing.

Coil 12 was subject to the same test as coil 11 and produced the same capability in reference to specimen heating rate but with an improvement in platen heating, achieving a platen temperature of approximately 700°C when the specimen was at 1200°C. Progress was being made but improvements were still needed.

3.7.3.3.18.2Coil 13 – 8 turn coil with Fluxtrol

With coil 12 showing promising results, an attempt was made to increase it's capability by applying the Fluxtrol magnetic flux concentrator to the first and last two turns of the coil where the tungsten platens are inserted. The aim was to increase power in these areas to make up the temperature deficit between the specimen and the platens. Figure 84 depicts coil 13 following the application of the Fluxtrol.

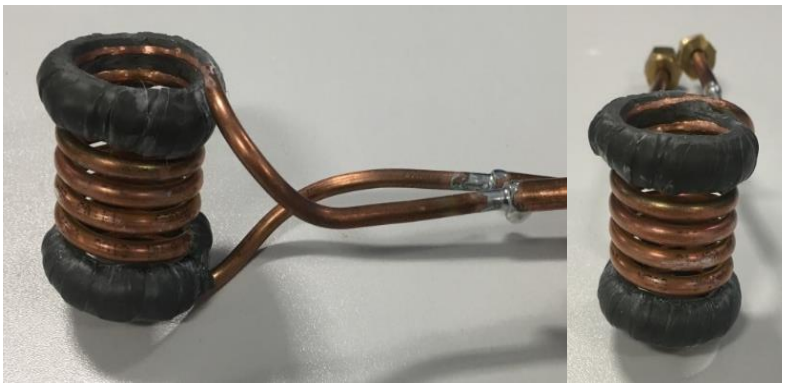

Figure 84 - Coil 13 featuring Fluxtrol applied to the first and last two turns of the coil.

The addition of the Fluxtrol offered a slight improvement over coil 12 with the platens reaching a peak temperature of 822°C while the specimen was at 1000°C. This was considered to be the maximum platen temperature that could be achieved, without drastic equipment changes e.g. a more powerful induction heater.

3.7.3.4 PID controller tuning

Having reached the maximum platen temperature feasible with the 15kW induction heater paired with coil 12 & coil 13, the proportional, integral derivative (PID) controller needed to be tuned to the final set up to prevent temperature overshoots and power oscillations. Several methods exist for tuning PID controllers with many manufacturers having tuning programs built in.

Initially the autotuning function on the WEST pro-16 was used, which sends a command for a momentary burst in power to the induction heater to make a slight change in process variable, in this case the temperature of the specimen. The auto tune then calculates appropriate values for the proportional (P), integral (I) and derivative (D) settings based on the trajectory of the process variable reaction curve in response to the burst of power.

Although the settings chosen by the auto tune produced very reliable control at low temperatures and slow heating rates, the accuracy of control would deteriorate as heating rates were increased above 5-10°Cs^{-1} with the PID controller beginning to oscillate the output variable, in this instance the induction heater power as can be seen in Figure 85.

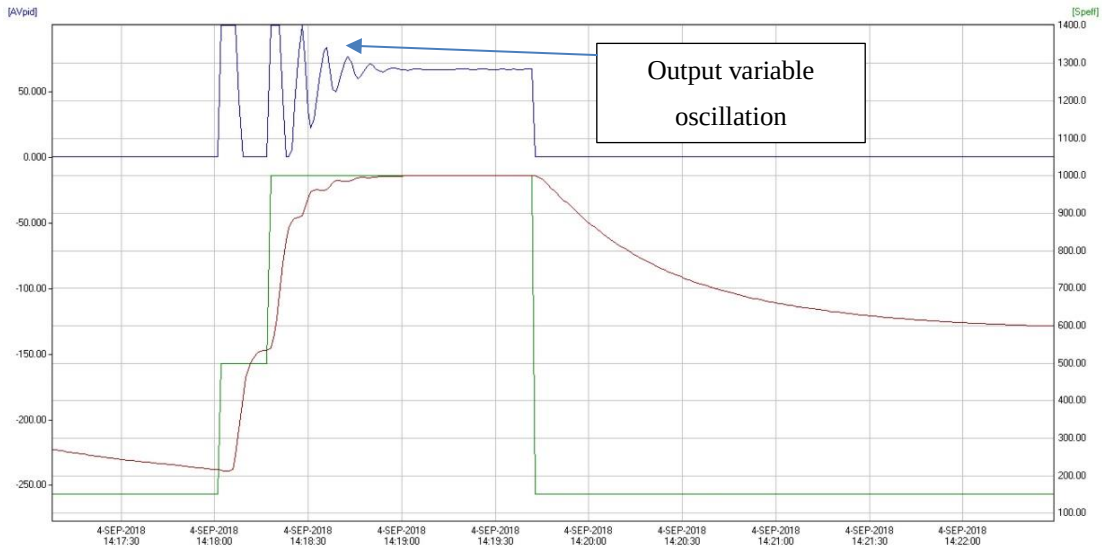

Green = Set point - target temperature (°C)

Red = Process variable - specimen temperature (°C)

Blue = Output variable - Induction heater power output (% of maximum)

Figure 85 - PID output readings illustrating the oscillation in the output variable after the auto tune had been performed.

Oscillation of the output variable is known as ‘hunting’ and is an indication of one or more of the following:

- Proportional setting is too high or too low.
- Integral setting is too low.
- Derivative setting is too large.

It was clear that the autotune program could not handle such high heating rates.
The second tuning method used was the Ziegler-Nichols closed loop method [125]. During this method, the integral and derivative functions of the PID controller are disabled leaving the system under proportional control only. The specimen was then held at a constant temperature of 900°C and the proportional value changed until a slight oscillation was seen in the specimen temperature, this proportional value is known as the ‘ultimate gain’ P_u. The next step is to measure the time period between the troughs of the oscillation, this value is known as the ‘ultimate time period’ T_u. These two values can then be input into the equations in Figure 86 to give the optimum P, I and D settings for the system.

$$\mathbf{P = 0.6\ P_u}$$

$$\mathbf{I = 0.5\ T_u}$$

$$\mathbf{D = 0.125\ T_u}$$

Figure 86 - Ziegler-Nichols equations for closed loop PID tuning, where P_u is the ‘ultimate gain’ and T_u is the ultimate time period [125].

The value for P_u was calculated at 900°C to be 13, with T_u being measured at 2 seconds. Therefore, the following PID settings were used: P = 7.8, I = 1 second, D = 0.25.

Unfortunately, this method produced the same results as the auto tune, with the controller exhibiting large oscillations in the output variable when heating with rapid heating rates. In some cases PID theory can break down, especially when working with very small dead times. With the specimen having such a small thermal mass combined with such a powerful induction coil, the deadtime of this system is very small. It was clear that conventional PID theory could not be applied to this system and that a bespoke set of PID parameters would need to be determined via an iterative process.

3.7.3.4.1 Iterative PID tuning

In order to establish good base settings to work from, the PID was initially tuned to produce no temperature overshoot and power oscillation when using a temperature step function. This was done by sending a command to the PID controller to increase the temperature to 1000°C and observing the specimen temperature and induction heater power output, looking for any changes in heating rate, overshoots in target temperature and oscillations in power output. This process was done in an iterative manner as illustrated in Figure 87. After each iteration the PID settings were altered to reduce any temperature overshoots and output variable oscillations by considering the following statements on PID function: The proportional setting governs the magnitude of the correcting action to a given error in specimen temperature. The integral setting accounts for any steady state errors between the setpoint temperature and the specimen temperature. The differential setting accounts for the rate of change in specimen temperature when approaching a setpoint. By a combination of iterative alterations to all three settings, the system was tamed with the following settings: P = 150°C, I = 2.5 seconds, D = 2.1 seconds. These settings produced a constant heating rate with no temperature overshoot when using the temperature step function from 700°C to 1000°C as can be seen in Figure 88 iteration C.

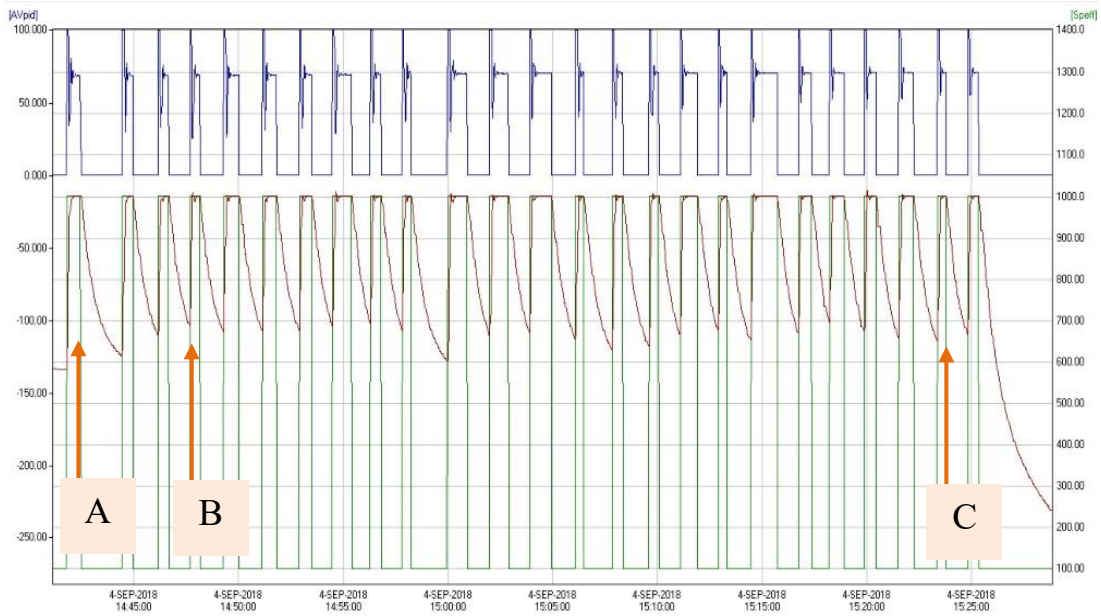

Figure 87 – An overview of the PID outputs to illustrate the iterative tuning method (A, B & C highlight the iterations shown in the next figure).

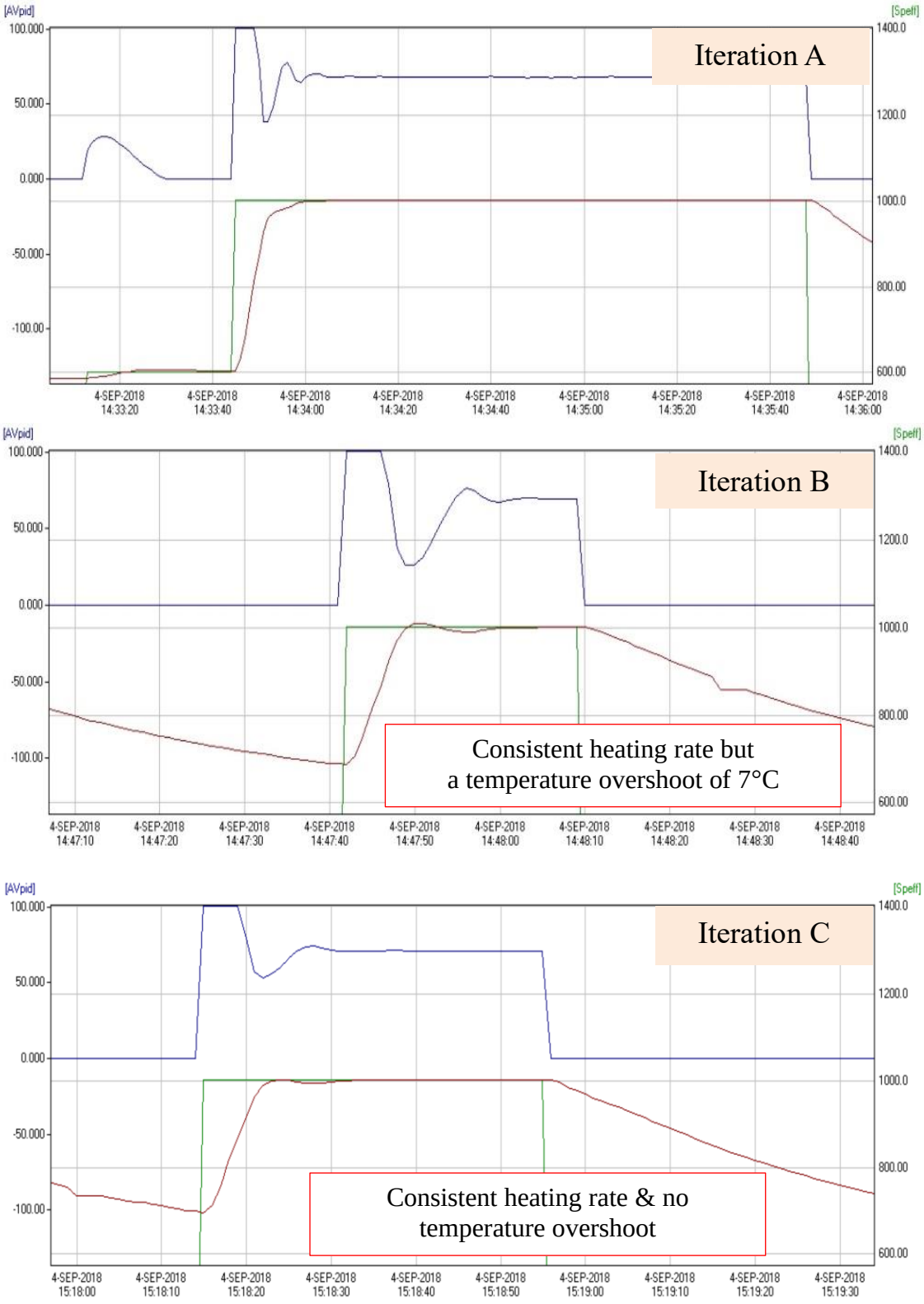

Green = Set point - target temperature (°C)

Red = Process variable - specimen temperature (°C)

Blue = Output variable - Induction heater power output (% of maximum)

Figure 88 - PID outputs during the iterative PID tuning.

Tuning the PID controller to perform well using the temperature step function provided good base settings to work from when tuning the PID controller to follow a pre-programmed temperature profile. The West PID interface software BlueControl was used to program temperature profiles into the Pro-16 PID controller in order to heat the specimens at predetermined rates, rather than heating as fast as possible with the temperature step function. An example of a standard heating profile is pictured in Figure 89. The program is set to initially heat the specimen to 520°C at 5°Cs^{-1} where it is held at temperature for 6 seconds. The specimen is then heated at the desired heating rate for the test in this case 25°Cs^{-1} to the target temperature of 1200°C.

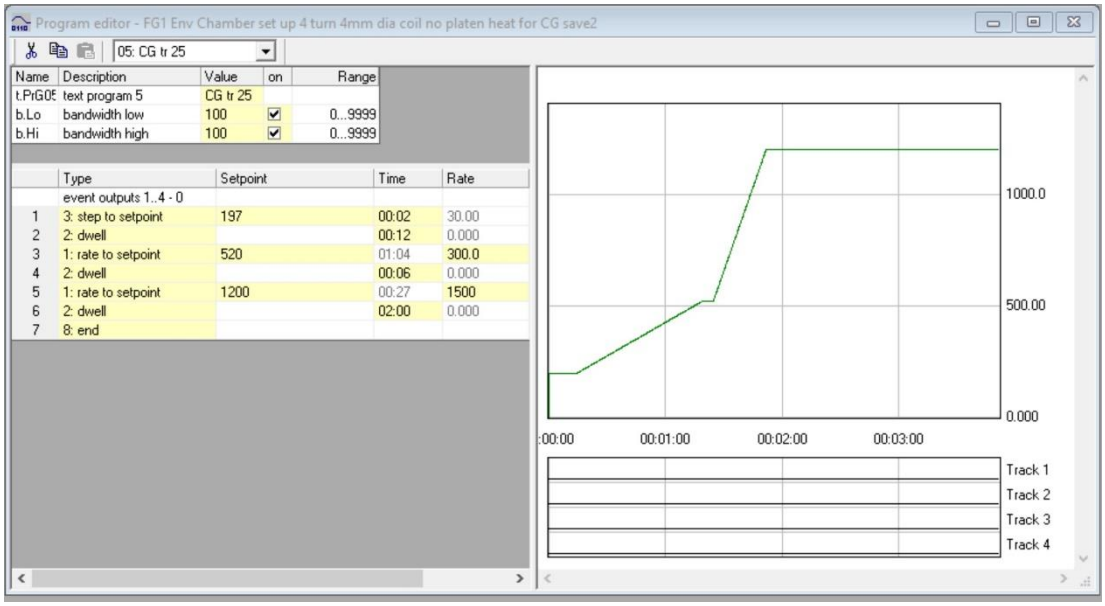

Figure 89 - Example heating profile programmed into the West BlueControl PID interface software.

The heating profiled detailed in Figure 89, and others with altered target temperature, were used to evaluate whether the PID settings established in the iterative method were still suitable when using a heating profile rather than a temperature step function.
Initially the heating profile was altered to change the target test temperature to 900°C, the heating profile function was then activated on the PID controller and the specimen was heated. The PID outputs were monitored to look for any temperature overshoots and oscillations in induction heater power. The resultant PID outputs of this test are shown in Figure 90.

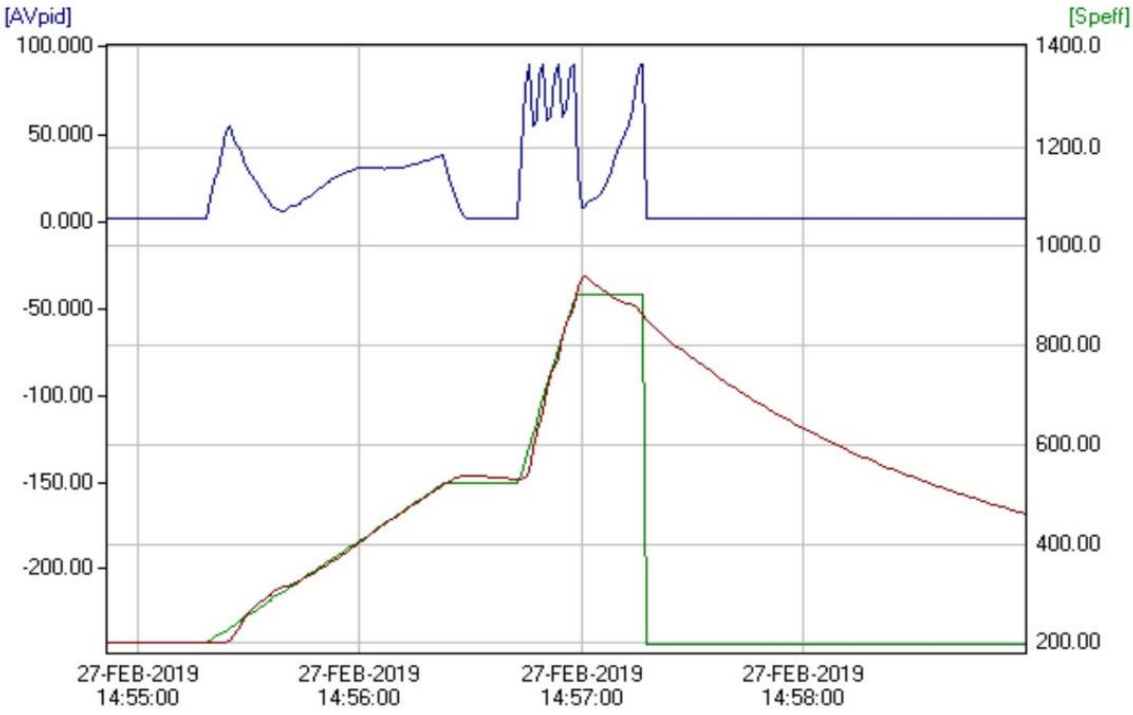

Green = Set point - target temperature (°C)

Red = Process variable - specimen temperature (°C)

Blue = Output variable - Induction heater power output (% of maximum)

Figure 90 - Resultant PID outputs from the first heating profile test with the optimised PID settings for the temperature step function.

At the beginning of the test during the 5°Cs^{-1} to 520°C segment, the specimen temperature tracked the set point temperature very well, although on reaching the dwell segment at 520°C, there was a temperature overshoot of 15°C.

Following the dwell at 520°C the next segment heated the specimen at 25°Cs^{-1} to 900°C, again on heating the specimen, temperature and setpoint tracked well, but unfortunately on reaching the target temperature of 900°C there was another even greater temperature overshoot of 35°C.

Several tests were carried out in this fashion, altering the target temperature each time, but each of these tests yielded the same result. These tests indicated that the PID settings established in the iterative step function method were nearly suitable but would need further adjustment in order to reliably track temperature profiles.

The iterative tuning method was applied once again but instead this time a trial run of the heating profile was carried out between each change in PID settings as can be seen in Figure 91. The PID settings were again adjusted in accordance to the three statements on PID function with the aim of reducing the temperature overshoot in each iteration until the specimen temperature accurately tracks the setpoint during the test.

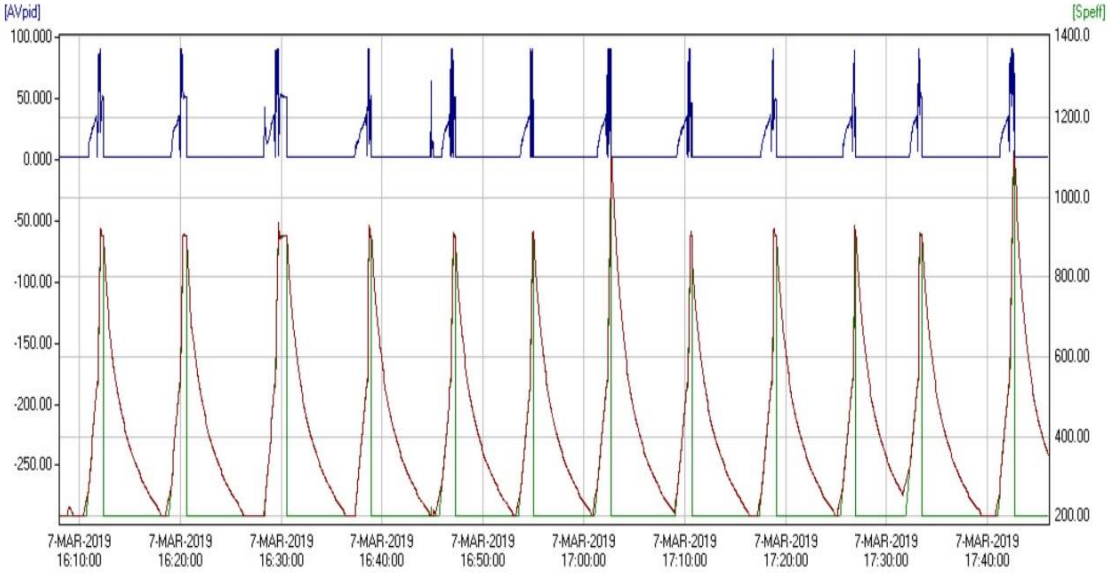

Green = Set point - target temperature (°C)

Red = Process variable - specimen temperature (°C)

Blue = Output variable - Induction heater power output (% of maximum)

Figure 91 - PID outputs during the iterative tuning of the temperature profile function.

The PID was only classified as suitably tuned when it could heat a specimen to within +/- 5°C of the setpoint throughout the whole test when heating to target temperatures between 900°C and 1200°C.

After many trial iterations this was achieved with the following settings:

P = 100°C,

I = 8.2 second,

D = 1.8 seconds.

In order to confirm the PID was suitably tuned a specimen was heated to 900°C, 1000°C, 1100°C and 1200°C using the standard heating profile described earlier. The results of these tests are shown in Figure 92 and Figure 93 which show the specimen temperature accurately tracking the set point throughout all four tests.

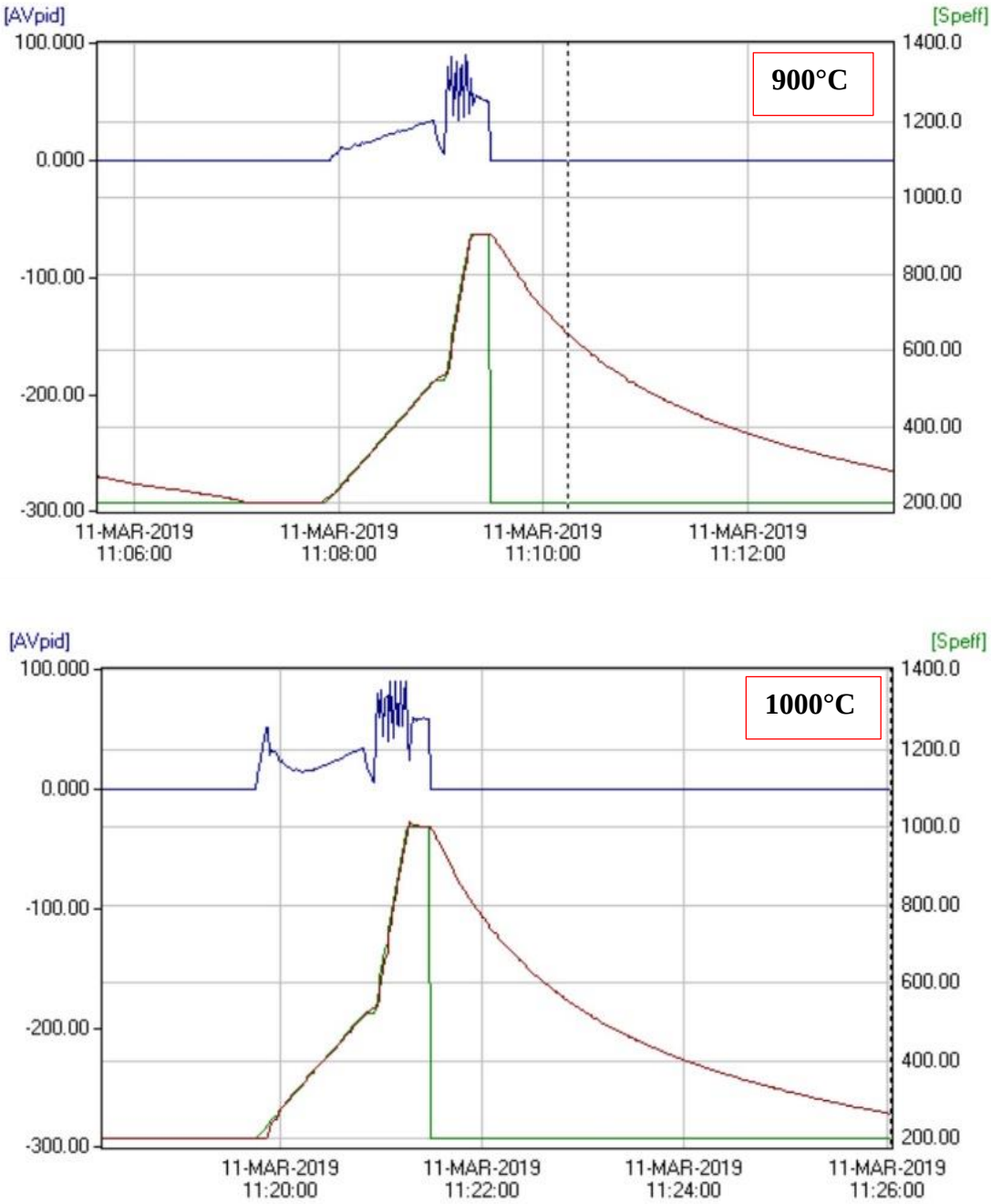

Green = Set point - target temperature (°C)

Red = Process variable - specimen temperature (°C)

Blue = Output variable - Induction heater power output (% of maximum)

Figure 92 - PID outputs from tuning confirmation tests conducted at 900°C & 1000°C.

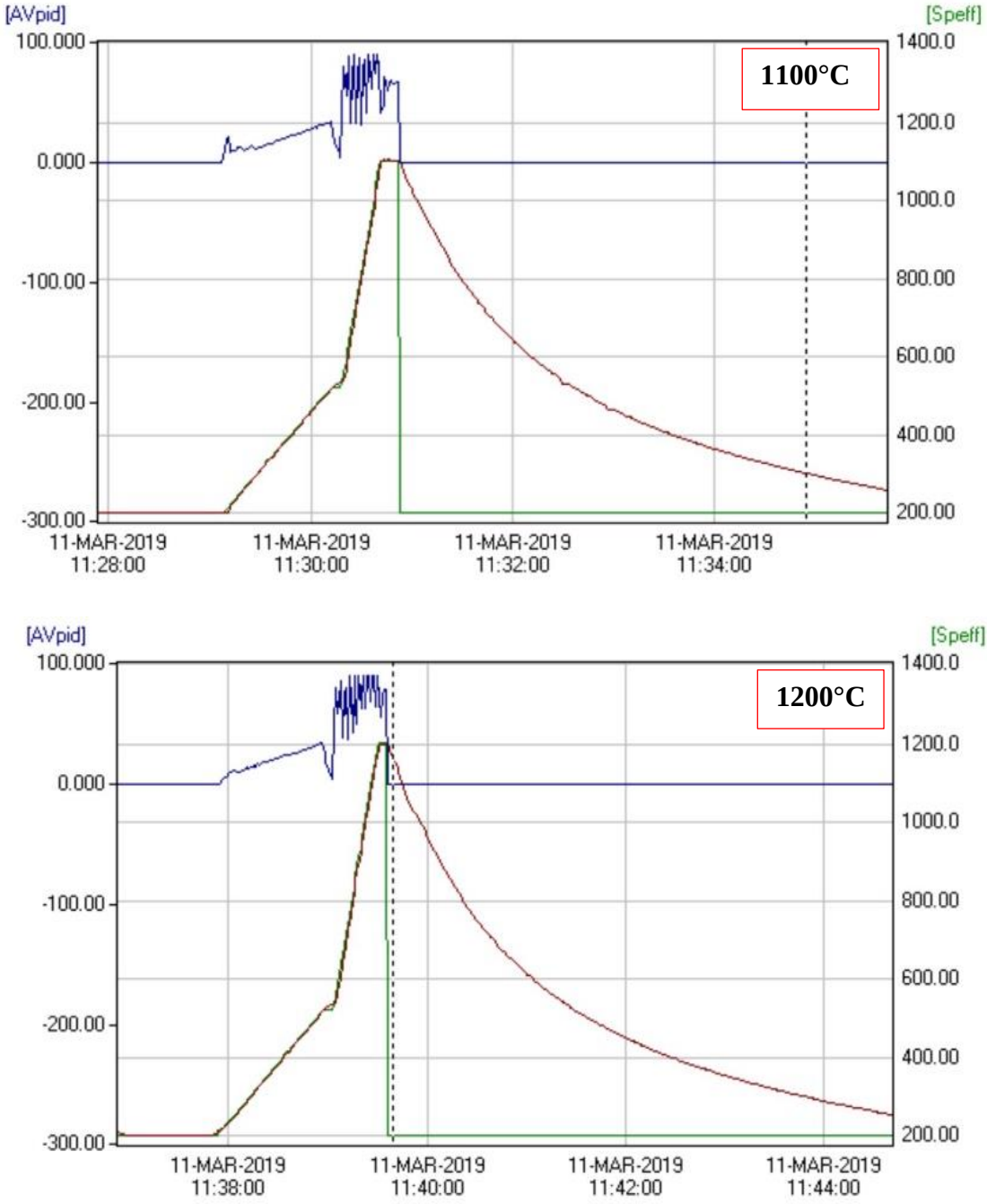

Green = Set point - target temperature (°C)

Red = Process variable - specimen temperature (°C)

Blue = Output variable - Induction heater power output (% of maximum)

Figure 93 - PID outputs from tuning confirmation tests conducted at 1100°C & 1200°C.

3.7.3.5 Lubrication & platen protection

An inherent complication with semi solid compression testing is contact of liquated material with the platens resulting in welding of the specimen to the platens. To reduce the risk of this happening high temperature lubricants were used to protect the platens from liquated material.

The first to be used was the standard high temperature lubricant used in the SMaRT laboratory, Boron Nitride. All specimens tested are sprayed with a thin layer of boron nitride prior to testing. Although boron nitride had good lubricating properties, the coating was not substantial enough to prevent liquated material from meeting the platen resulting in fusion between the two, as shown earlier in section 3.7.3.2 Compression test trial runs in Figure 62.

A more robust platen lubrication was needed so two glass-based lubricants were trialled. Glass based lubricants are commonly used in hot forging and drawing techniques. Glass particles are suspended in a water-based paint which on heating evaporates leaving the glass particles to melt and act as lubrication. The two glass lubricants trialled were Bonderite L-FG2626 and Advanced Technical Products ATP-9, with ATP-9 performing the best out of the two. The platens were coated before each test as shown in Figure 94. The platens were then heated without a specimen to 300°C to evaporate the water from the paste to prevent this water vapour from contacting and oxidising the specimen during testing.

Figure 94 - Tungsten compression platens coated in ATP-9.

3.8 Heat & quench only test procedure

All heat and quench only tests were conducted using the standard heating profile shown in Figure 95.

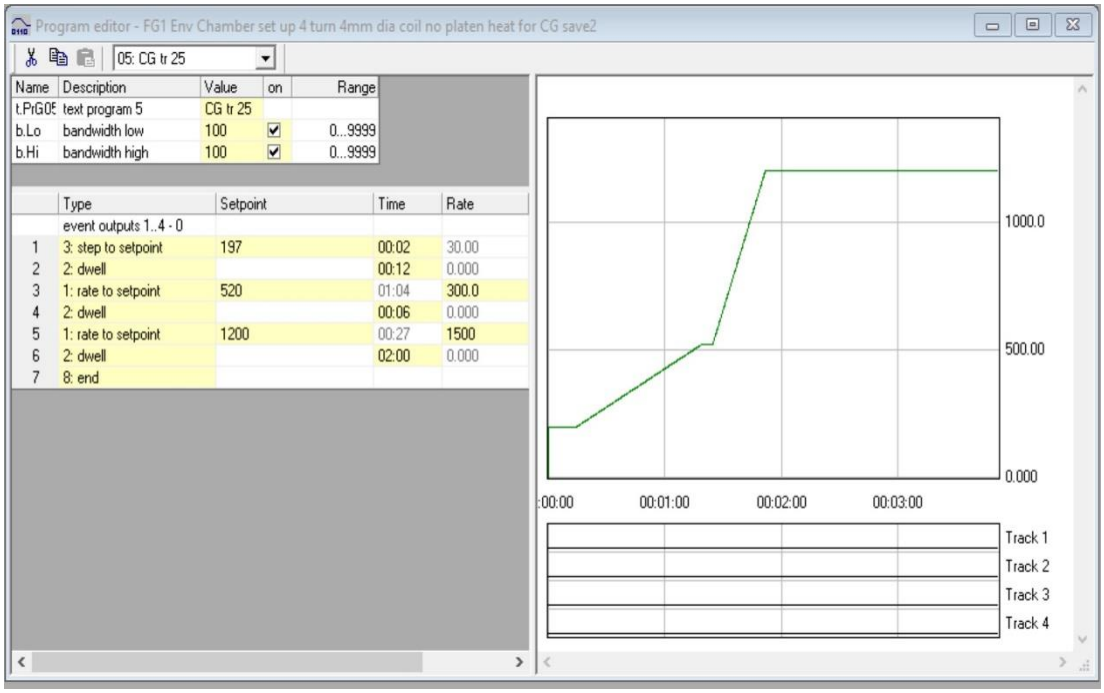

Figure 95 - Standard heating profile used for just heat tests & compression tests.

Segment 5: rate to set point, was altered to change the target temperature of each test as well as the desired heating rate by adjusting the setpoint and rate values, respectively.

All heat and quench only tests were conducted on specimens resting on top of a specimen holder as described in Figure 63, this enabled heating of the specimen while remaining free from temperature gradients and avoiding heating the platens. Doing this prevented the RF radiation problem and allowed the heat only tests to be conducted. When the target temperature was reached the quenching mechanism would knock the specimen and the specimen holder into the quench bath, freezing the microstructure.

3.9 Compression test procedure

Compression tests were carried out using the ‘floating’ specimen method described in section 3.7.3.3.16. The standard heating profile in Figure 95 was also used for all compression tests, changing the target temperature and heating rate as needed.

3.9.1 RF radiation issues prevented testing

As described in the notes of coil 11’s capability testing in section 3.7.3.3.17, the induction heater would emit strong RF radiation when subjected to high loads. This would occur when the induction heater needed to operate at maximum power such as when a fast heating rate was requested. The RF radiation was strong enough to induce currents in the USB cables that connected the PID controller and thermocouple PICO logger to the laptop computer that was recording the temperature data. The currents induced in the USB cables were enough to overload the USB ports causing a communication drop out, therefore preventing temperature data logging. In some instances, the RF radiation emitted would be so severe that it would interfere with the operating systems of other hydraulic test frames within the SMaRT laboratory, causing their actuators to jump around violently.

Due to the severity of the RF radiation and the consequent data dropouts and test frame interference caused, testing was ceased because of health and safety concerns. Consequently, the proposed semi-solid compression tests detailed in section 3.4.2 were not conducted and will be investigated in further work.

Before testing was ceased, two proof of concept tests were attempted during a downtime period at the SMaRT laboratory, the results of which are detailed here.

3.9.2 Proof of concept tests

Despite the RF problem, two proof of concept compression tests were conducted using both coil 12 and coil 13 utilising the 'floating' specimen technique. The first test was carried out using coil 12 to heat a standard size CG specimen to 1047°C with a heating rate of 25°Cs^{-1} followed by compression at a strain rate of 1s^{-1} to a true strain of 0.5. The coil position had been altered for this test to allow the platens to be inserted further to increase the platen temperature further than the 700°C that was produced in coil 12's capability tests. As expected, during the test the RF radiation once again caused currents to be generated in the PID controllers' USB cable causing a communication failure. Because of this, the only way of recording what temperature the specimen was at when the test was conducted was by simultaneously taking a photograph of the display window of the pyrometer's control module as shown in Figure 96.

Figure 96 - Photograph of the specimen temperature reading displayed on the pyrometer control module during the first proof of concept test.

As the RF radiation had also previously caused a communication drop out with the thermocouple PICO logging system, the N-type thermocouple recording the platen temperature was instead plugged into a Fluke handheld thermocouple reader during this test. The Fluke does not have the capability to record data and can only be used as a real time reference, therefore the temperature could only be recorded by again, taking a photograph of the display simultaneously with the compression test being conducted. The photograph of the Fluke reading is shown in Figure 97 indicating a platen temperature of 1281°C, a drastic improvement from the previous capability test with coil 12.

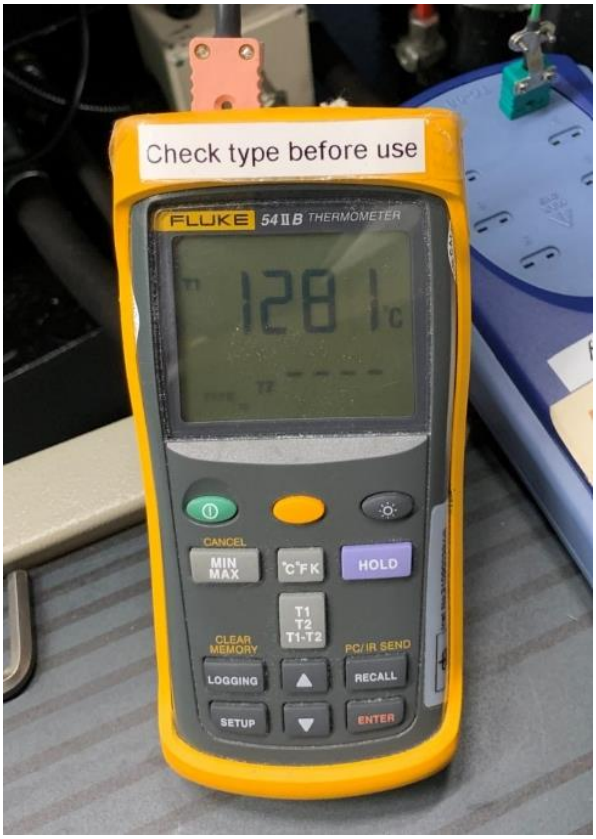

Figure 97 - Photograph of the platen temperature reading displayed on the Fluke handheld thermocouple reader.

Figure 98 - Photograph of the tungsten platens and specimen at temperature prior to compression.

The temperature difference between the platens and the specimen had now inverted resulting in the platens overheating the specimen on contact, rather than quenching it as experienced in earlier tests. The macro image of the specimen used in this test confirmed this as shown in Figure 99.

Figure 99 - Macro image of the CG specimen used in the first proof of concept test exhibiting inhomogeneous deformation at the top and bottom surface.

The top and bottom of the specimen had deformed much more than the centre of the specimen due to the sudden increase in temperature. With the platens being near the liquidus temperature of RR1000 this plastic flow of material was to be expected. This test confirmed that this testing method could heat the tungsten platens to the same temperature as the specimen. Although, the insertion depth of the platens inside the induction coil has a dramatic effect on the final temperature and therefore would need further development to calculate an optimum platen insertion depth.

The second proof of concept test was conducted using coil 13 to heat a standard size CG specimen to 1200°C with a heating rate of 25°Cs^{-1} followed by compression at a strain rate of 1s^{-1} to a true strain of 0.5. Again, the tungsten platens were inserted deeper into the coil to increase their temperature. During this test, the RF radiation problem meant that the test temperature of the specimen and the platens had to be recorded in the same fashion as the first proof of concept test. During this test, the platens reached a temperature of 1211°C when the specimen was at 1202°C. Unfortunately, during this test, the molten glass lubricant stuck the specimen to the top platen resulting in the specimen not being knocked into the quench bath after the test. Some of the molten glass lubricant also bridged the gap between the water-cooled induction coil and the tungsten platen fusing the two together, resulting in the coil being bent downwards during the quenching procedure as shown in Figure 100

Figure 100 - Coil 13 after sustaining damage due to molten glass lubricant fusing the coil to the lower platen.

The macro image in Figure 101 shows the FG specimen after the test. Again, the specimen exhibited inhomogeneous deformation with the top of the specimen deforming much more than the bottom. It was suspected that this was due to the top platen heating to a higher temperature as it descended into the coil to conduct the compression. In future tests the platens will have to be placed as close as possible to the specimen in order to reduce the amount of time the upper platen is descending through the coil before the compression is conducted.

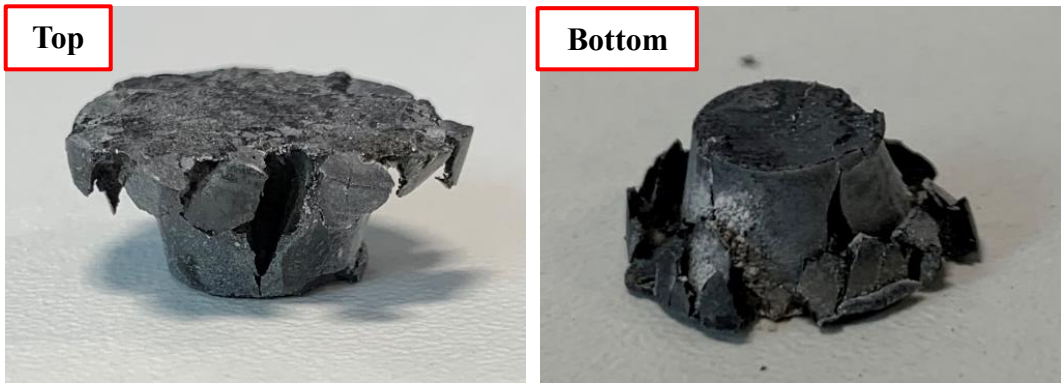

Figure 101 - Macro image of the FG specimen used in the second proof of concept test.

3.9.2.1 Proof of concept conclusion

The proof of concept tests have proven that simultaneous heating of the platens and specimen with a single induction coil is possible, although peak platen temperature is subjective to their insertion depth into the coil. As a result, the optimum insertion depth to achieve matching test temperatures for both specimen and platen would need further investigation. Unfortunately, the development of the RF radiation problem which led to severe complications meant that the proposed compression testing could not be carried out. The source and cause of the RF radiation will need to be investigated and a prevention or containment plan will need to be developed. When this issue is resolved the simultaneous heating of both platens and the specimen via this method is possible and the proposed compression test can be conducted within this semi-solid testing facility.

3.9.3 Test frame compliance correction

All test frames have a compliance that needs to be corrected when analysing any data produced within the frame. The compliance arises from all the small intolerances in the parts that make up the test frame as well as some elastic strain from these parts when a force is exerted on the load train. As a result, the position sensor of the loading rod will record a small amount of movement for a given force, but the recorded movement was not deformation of the specimen but the take up of the machine compliance.

To account for this, the equation of the trend line in Figure 102 can be used to correct the strain data of any tests performed in the test frame. The equation is calculated by bringing together the compression platens in the test frame under load control. A compressive load is then applied incrementally up to and beyond the maximum load that will be experienced during testing in this case 50kN. At each force increment the measured displacement is recorded. The load vs displacement graph in Figure 102 can then be plotted. The equation of the linear trendline can then be used to correct strain data measured in the subsequent compression tests.

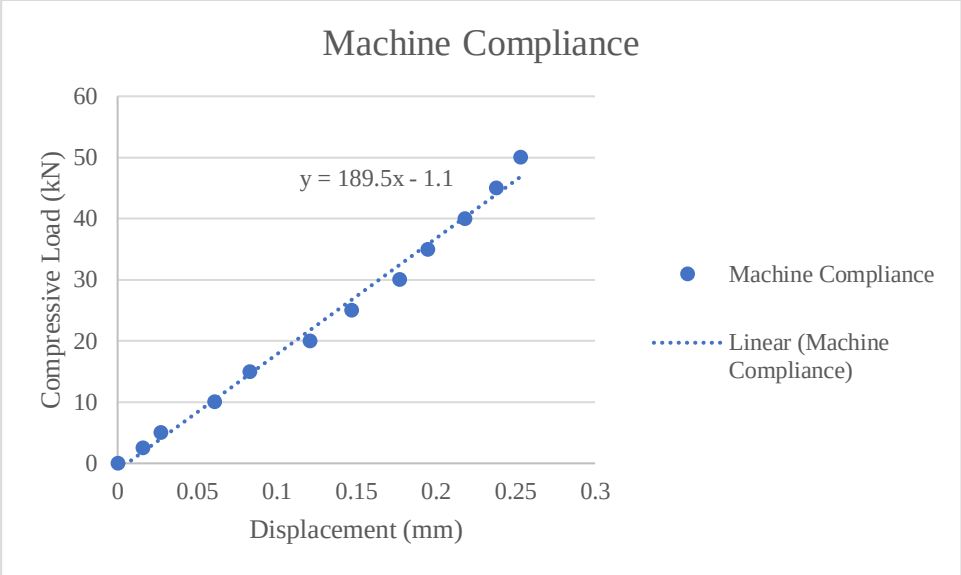

Figure 102 - Machine compliance correction plot.

3.10 Hardness testing

Vickers hardness testing was utilised as a way of quantifying the mechanical properties of specimens after they had been subject to rapid heating to induce microstructural changes. All hardness testing conducted in this project was performed on a Struers Duramin-40 A3. The test standard Hv1 was used, which includes a 1kg load applied via a Vickers indenter for a dwell time of 10s. In order to get a value of the specimens' average hardness, they were sectioned in half along the radial-axial plane and mounted and polished. a 5 by 5 grid of indents was then conducted. The indents were spaced 1.2mm in the X direction and 1.8mm in the Y direction to get an average representative of the whole specimen. An average was then calculated from all 25 hardness measurements.

3.11 Error analysis

An error analysis procedure has been performed on all average microstructure measurements taken during this study. By using the average value ($\bar{x}$), the standard deviation (SD), and the sample size (n) for each value, the error of the mean value can be calculated. This gives a range of values within which the true mean value could possibly fall, known as a confidence interval. This error value gives an estimation of whether any subsequent microstructural changes are statistically significant or if they are instead a product of natural variance. When the confidence intervals of two average values do not overlap, there is a statistically significant difference between the two. However, the opposite is not necessarily true, as two average values with overlapping confidence intervals can still have a statistically significant difference between them. Therefore, a statistical test must be applied to judge whether the difference in the two average values is significant or not, e.g. a t-test.

The two tail t-test and the two tail t-distribution were used as the basis of this error analysis. The equations used in this error analysis method are given in Table 8 and the method used to conduct this error analysis is detailed in the following pages.

Standard error of mean	**Variance**
$\frac{SD}{\sqrt{n}}$	SD^2
Two sample t-test **Null hypothesis = means are equal**	**Confidence interval for the difference of two means**
$t_{difference.} = \frac{\bar{x}_1 - \bar{x}_2 - 0}{\sqrt{\frac{SD_1^2}{n_1} + \frac{SD_2^2}{n_2}}}$	$(a, b) = \bar{x}_1 - \bar{x}_2 \pm t_{\alpha,df} \cdot \sqrt{\frac{SD_1^2}{n_1} + \frac{SD_2^2}{n_2}}$

Table 8 – List of equations associated with t-test used to conduct error analysis.

The t-test is a parametric test and therefore the t-test approach assumes the distribution of the data being compared is approximately normal. To find out if a set of data is approximately normally distributed, you can assess some of the descriptive statistics of the distributions, namely the skewness and the kurtosis. The skewness assesses the symmetry of the distribution while the kurtosis assesses the shape of the tails of the distribution. The data used to calculate the average values in the present research were assessed using Microsoft Excel's SKEW and KURT functions to calculate the skewness and kurtosis. For a distribution to be considered normal using these functions, both the skewness and the kurtosis should fall between -2 and +2.

All the data distributions fell within the commonly accepted -2 to +2 limits for skewness, with skewness ranging from -1.98 to + 1.94. Most of the distributions fell within the commonly accepted limits for kurtosis also, with kurtosis ranging from -1.96 to +1.95. The only distributions that did not fall between the -2 to +2 limits for kurtosis were the hardness distributions of four of the FG specimens. These hardness distributions belonged to the following FG specimens: 1160°C at 25°Cs^{-1} 1s hold time, 1160°C at 25°Cs^{-1} 45s hold time, 1200°C at 25°Cs^{-1} 1s hold time, and 1160°C at 12.5°Cs^{-1} 1s hold time. The kurtosis values for these specimens were above the +2 limit with the highest being +4.37. A study has been conducted by E. Schmider et al [126] on the robustness of parametric testing when the assumption of normally distributed data is violated. The authors found that the kurtosis values of the distributions being compared could fall between -9 and +9 and the parametric testing would remain robust.

The t-test approach was considered a valid method for the error analysis in this research because: all the distributions fell within the commonly accepted limits of skewness, the majority fell within the commonly accepted limits for kurtosis and the four exceptions were well within the potentially acceptable -9 to +9 limits for kurtosis. As a precautionary measure, the four FG specimens that exhibited larger kurtosis are highlighted in the results and discussion section if a significant difference was indicated by the t-test involving these specimen's average hardness measurements. This was done so that the possibility of a false significant difference indicated by the t-test due to the greater kurtosis could be taken into consideration when discussing the findings.

The semi-solid testing facility used to conduct the tests in this study has been proven to heat specimens evenly, so that they are free from temperature gradients. Therefore,

it would be expected that the microstructural changes throughout the specimen are also even. Despite this, there may still have been some slight thermal gradients within the specimen. The potential variation in microstructural changes is inherently accounted for in the confidence intervals calculated using the chosen conservative method of error analysis. As an extra precaution, the t-tests used to judge significant differences in average values were also conducted as conservatively as possible, details of which are given in the subsequent section. This ensured that any significant differences indicated by the t-tests were reliable.

A 95% confidence interval above and below the mean has been calculated for each average value, using the two tailed t-distribution to factor in the small sample sizes used to calculate the average microstructure measurements. The sample size is incorporated into the confidence interval by multiplying the standard error of the mean by a t-value given in the two tail t-distribution table (Table 9).

A confidence interval of 95% precision was selected, corresponding to an alpha number (α) of 0.05 in the t-distribution table. Using an α of 0.05 means that it can be stated with 95% confidence that the true mean value falls within the confidence interval calculated for the sampled mean value. To select the appropriate t-distribution value, the degrees of freedom (df) must be calculated, with df being equal to n-1 for the sample.

The appropriate t-value is then selected by entering the t-distribution table (Table 9) at the calculated df value and reading across to the column titled $\alpha = 0.05$. The 95% confidence interval for an average value is then calculated by multiplying the standard error of the average value by the appropriate t-value. The sample size n, df and appropriate t-value for each average microstructural measurement calculated in this study is given in Table 10.

In the results section the 95% confidence interval is given in brackets following the stated average value e.g. an average grain size of 10μm (+/- 2). In the graphical data the error bars of each average value indicate the 95% confidence interval.

	α						
df	0.2	0.1	0.05	0.02	0.01	0.002	0.001
∞	1.282	1.645	1.96	2.326	2.576	3.091	3.291
1	3.078	6.314	12.706	31.821	63.656	318.289	636.578
2	1.886	2.92	4.303	6.965	9.925	22.328	31.6
3	1.638	2.353	3.182	4.541	5.841	10.214	12.924
4	1.533	2.132	2.776	3.747	4.604	7.173	8.61
5	1.476	2.015	2.571	3.365	4.032	5.894	6.869
6	1.44	1.943	2.447	3.143	3.707	5.208	5.959
7	1.415	1.895	2.365	2.998	3.499	4.785	5.408
8	1.397	1.86	2.306	2.896	3.355	4.501	5.041
9	1.383	1.833	2.262	2.821	3.25	4.297	4.781
10	1.372	1.812	2.228	2.764	3.169	4.144	4.587
11	1.363	1.796	2.201	2.718	3.106	4.025	4.437
12	1.356	1.782	2.179	2.681	3.055	3.93	4.318
13	1.35	1.771	2.16	2.65	3.012	3.852	4.221
14	1.345	1.761	2.145	2.624	2.977	3.787	4.14
15	1.341	1.753	2.131	2.602	2.947	3.733	4.073
16	1.337	1.746	2.12	2.583	2.921	3.686	4.015
17	1.333	1.74	2.11	2.567	2.898	3.646	3.965
18	1.33	1.734	2.101	2.552	2.878	3.61	3.922
19	1.328	1.729	2.093	2.539	2.861	3.579	3.883
20	1.325	1.725	2.086	2.528	2.845	3.552	3.85
21	1.323	1.721	2.08	2.518	2.831	3.527	3.819
22	1.321	1.717	2.074	2.508	2.819	3.505	3.792
23	1.319	1.714	2.069	2.5	2.807	3.485	3.768
24	1.318	1.711	2.064	2.492	2.797	3.467	3.745
25	1.316	1.708	2.06	2.485	2.787	3.45	3.725
26	1.315	1.706	2.056	2.479	2.779	3.435	3.707
27	1.314	1.703	2.052	2.473	2.771	3.421	3.689
28	1.313	1.701	2.048	2.467	2.763	3.408	3.674
29	1.311	1.699	2.045	2.462	2.756	3.396	3.66
30	1.31	1.697	2.042	2.457	2.75	3.385	3.646
60	1.296	1.671	2	2.39	2.66	3.232	3.46
120	1.289	1.658	1.98	2.358	2.617	3.16	3.373

Table 9 – T-distribution table (two tailed). Critical t-values for given df and α.

Microstructural measurement	Sample size (n)	df	Critical t-value ($t_{crit.}$)
Grain size via MLI	5 micrographs	4	2.776
Grain size via EBSD	3 EBSD scans	2	4.303
γ' size	> 120 precipitates	>120	1.96
γ' volume fraction	3 micrographs	2	4.303
Σ3 twin boundaries	3 EBSD scans	2	4.303
Liquid fraction	13 micrographs	12	2.179
Vickers Hardness	25 hardness indents	24	2.064

Table 10 – Critical t-values for average microstructural measurements calculated.

The 95% confidence interval gives an indication of whether the difference between two average values is likely to be statistically significant. A two tailed two sample t-test was used to confirm whether any differences in average values, were in fact statistically significant.

The equation used to conduct the t-test is given in Table 8. This t-test equation is based on the null hypothesis of the mean values are the same. The average values being compared ($\bar{x}_1$, $\bar{x}_2$), their corresponding standard deviations (SD_1, SD_2) and sample sizes (n_1, n_2) were put into the t-test equation giving a t-difference value ($t_{diff.}$). This t-difference value was then compared to a critical t-value ($t_{crit.}$) for the microstructure measurements being compared.

The critical t-value for the comparison is based on the degrees of freedom of each average value and the alpha level chosen (α of 0.05). To be cautious, the most conservative critical t-value possible was selected for the comparison (i.e. the greatest critical t-value). This conservative selection is the critical t-value associated with the smaller of the two degrees of freedom, therefore, the smaller of n_1-1 or n_2-1. This ensured that any significant changes indicated by the t-test were reliable. The critical t-values for each microstructure measurement are given in Table 10 and are the same values used in the 95% confidence interval calculation. I.e. if measurements obtained via two different methods with different critical t-values were being compared, e.g. grain size via MLI and grain size via EBSD, the greatest critical t-value of the two, associated with the lowest df was used in the $t_{diff.}$ to $t_{crit.}$ comparison (4.303 in this example). Only if the magnitude of the t-difference value calculated was greater than the critical t-value ($t_{diff.} > t_{crit.}$), could the null hypothesis be rejected and the difference between the average values being compared be classed as statistically significant.

When a statistically significant difference in average values was found via the t-test method, a 95% confidence interval was also calculated for the difference between the two average values. This confidence interval was calculated by inputting the average values being compared ($\bar{x}_1$, $\bar{x}_2$), their corresponding standard deviations (SD_1, SD_2) and sample sizes (n_1, n_2) along with the critical t-value associated with the lowest df of the two measurements being compared ($t_{\alpha,df} = t_{crit}$) into the confidence interval between two means equation in Table 8.

In the results section any significant changes in average microstructure measurements are highlighted, with the results of the t-test given in brackets following the magnitude of the change. The brackets contain the 95% confidence interval for the magnitude of

the change, as well as the t-difference calculated for the comparison illustrating it is higher than the critical t-value confirming its significance. For example, an increase in average grain size of 5μm (+/- 2, $t_{diff.}$ 6.324 > $t_{crit.}$ 4.303) [127]–[130].

4 RESULTS AND DISCUSSION

4.1 Microstructural evolution of RR1000 during rapid heating

Specimens were subject to heat and quench only tests as detailed in section 3.8 of the experimental procedures. The microstructural changes were investigated to evaluate the dynamic evolution of the microstructure during rapid heating, paying particular attention to the γ' precipitates as they contribute to much of RR1000's strength and are the cause of the sub-solidus liquation mechanisms in both RR1000 variants.

4.1.1 Heating to above the liquidus temperature

As part of the induction heater trials conducted early in the project, two FG specimens were heated to 1300°C which is in the region of the alloys' liquidus temperature. These tests were conducted to assess whether induction heating was a suitable heat source for the semi-solid testing facility. These tests simultaneously provided information on how the FG RR1000 microstructure changes when subject to such extreme temperature as well as tested the induction heaters capability. The specimens were heated to 1300°C at approximately 48°Cs^{-1}, one specimen was air cooled and the other was water quenched. On inspection of the microstructure it was clear that the specimen had completely liquated and had only retained its shape due to the formation of a thick oxide scale on the specimen surface. The air-cooled specimen re-solidified in a similar fashion to an ingot casting with large columnar γ grains growing towards the centre of the specimen from the outer surface, with some smaller more equiaxed grains at the centre as can be seen in the EBSD orientation map in Figure 103.

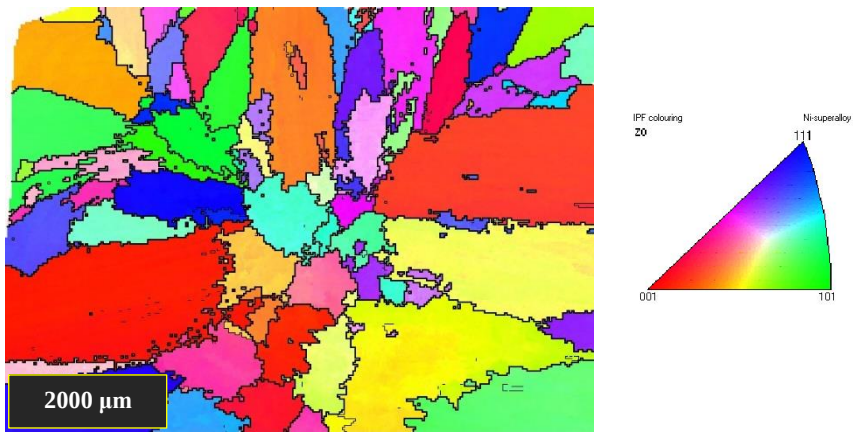

Figure 103 - EBSD IPF map showing the γ columnar grains growing in from the surface of the specimen.

Each of these γ grains contained long chain like γ' phases that grew in the direction of the columnar grains on re-solidification as can be seen in Figure 104.

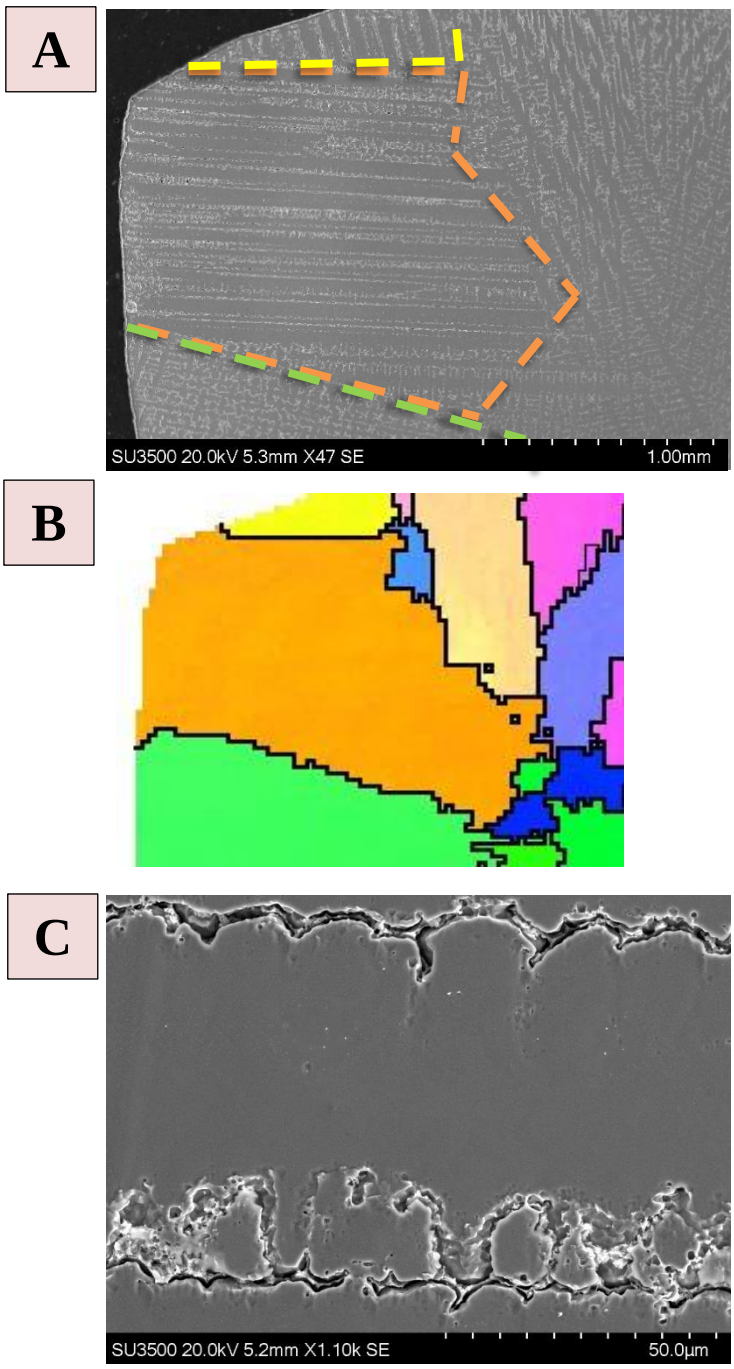

Figure 104 - A) SEM micrograph illustrating the γ' phase growing in the direction of the columnar grains. B) Corresponding grains from the EBSD IPF map. C) Higher magnification SEM image of the chain like γ' phase growing in the direction of the γ grain.

The second specimen had a slightly different resultant microstructure due to the water quenching. The columnar grains on the perimeter of the specimen were still present but the centre of the specimen contained a higher number of equiaxed grains, see in Figure 105. This is to be expected as the water quenching would create increased undercooling in the liquid phase leading to more nucleation of grains. The quenched specimen also exhibited a lot of shrinkage porosity due to the rapid cooling rate. This shrinkage revealed partially formed dendrites that did not have enough time to form completed grains, these dendrites can be seen in Figure 106.

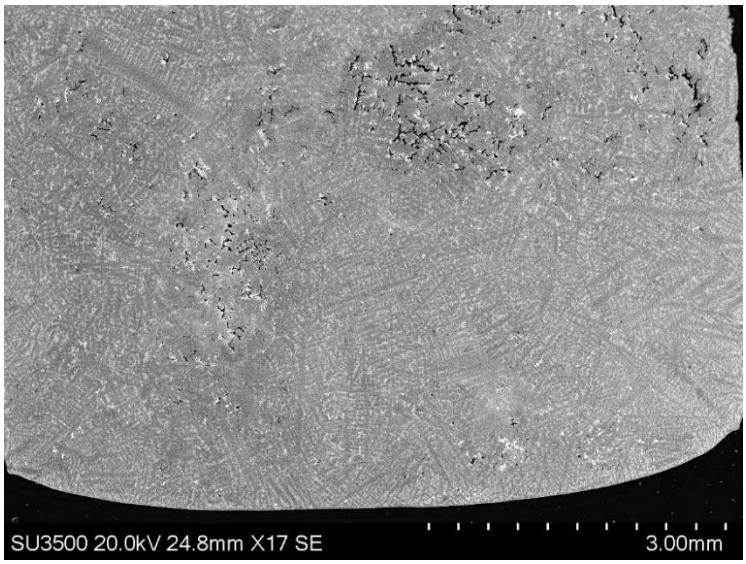

Figure 105 - SEM micrograph of the FG specimen water quenched from 1300 exhibiting more equiaxed grains along with shrinkage porosity.

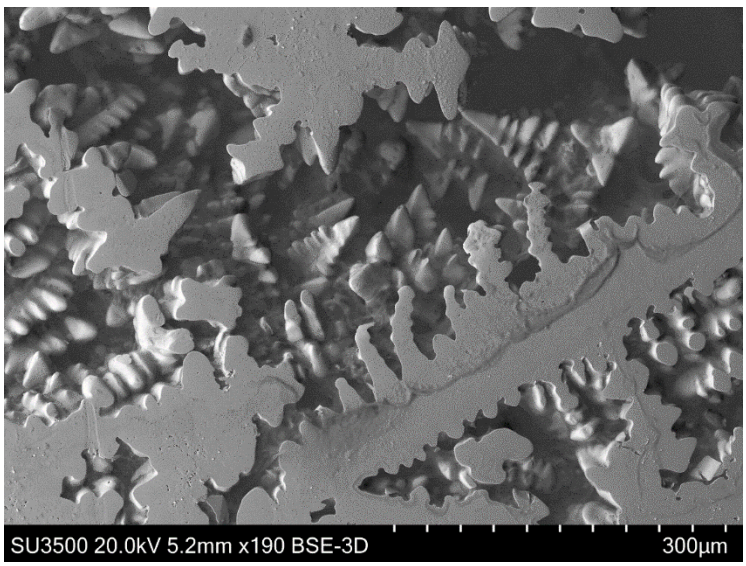

Figure 106 - High magnification SEM image of the partially formed dendrites revealed by the shrinkage porosity.

4.1.2 Microstructural analysis of a FG specimen with temperature gradient

During the development of the semi-solid testing facility a standard sized FG RR1000 specimen was heated to 1160°C at 5°Cs^{-1} using coil 9 followed by water quenching. During heating, the specimen was placed onto the lower tungsten platen, resulting in a large amount of heat soak from the specimen into the platen. As a result, the specimen exhibited a large temperature gradient from top to bottom throughout the test. The microstructure of this specimen was subsequently examined via SEM to investigate the microstructural changes that had occurred paying particular attention to the γ' precipitates.

SEM Micrographs taken from cooled base to correct temperature at the top of the specimen

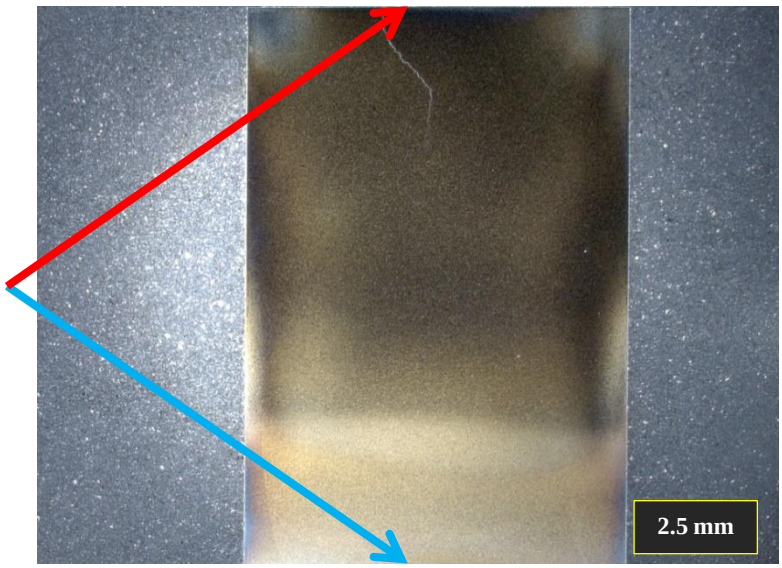

Figure 107 - Optical image of an FG specimen heated to 1160°C at 5°Cs^{-1} followed by water quenching. Specimen experienced large temperature gradients.

Even on a macro scale the effects of the temperature gradient could be seen due to the difference in etch response. The material that reached higher temperatures turned a darker colour when etched, see Figure 107. A closer inspection of the bottom of the specimen which was at the lowest temperature is shown in Figure 108. The SEM micrographs revealed that the primary γ' precipitates were largely unchanged, with only the secondary and tertiary γ' being affected. The tertiary γ' had completely diffused into the γ matrix while the secondaries were still present but had undergone severe spheroidization. These microstructural changes in FG RR1000 are associated with temperature exposures of between 900-1000°C.

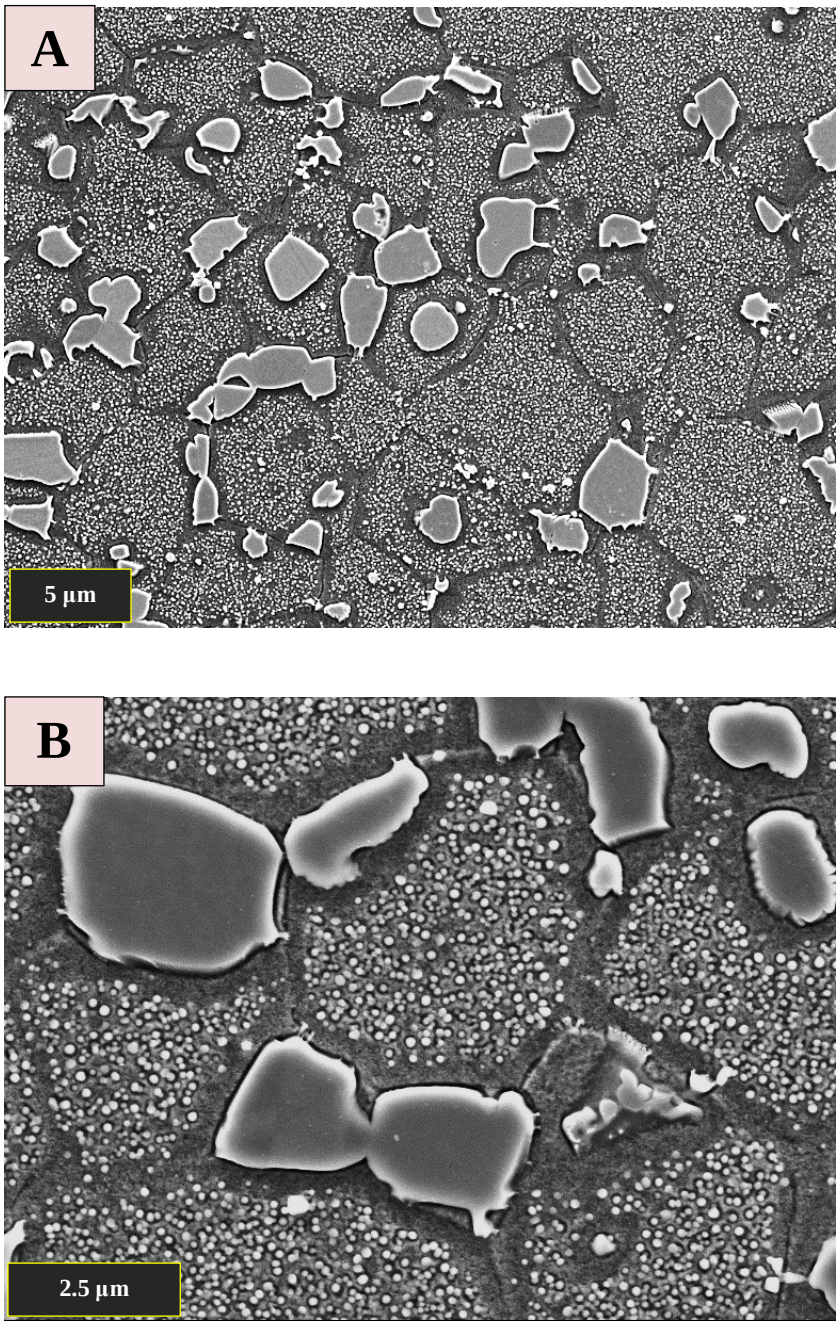

Figure 108 - SEM micrographs of the bottom of the specimen which experienced the lowest temperature. A) Low magnification, B) High magnification.

Moving further up the specimen, therefore increasing the peak temperature experienced by the region of inspection, the number of secondary γ' precipitates decreases. This is accompanied by the beginning of spheroidization of the primary γ' precipitates as illustrated in Figure 109. The areas where depletion of secondary γ' has occurred are now re-populated with a very fine re-precipitated γ' similar to that found at an RR100 inertia friction weld line [54].

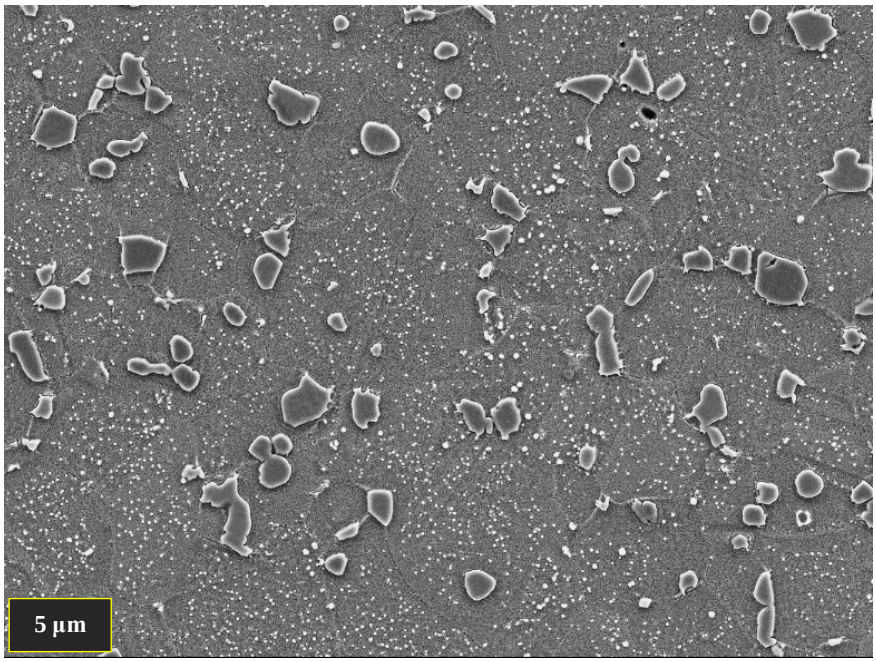

Figure 109 - SEM micrograph illustrating the depletion of secondary γ' and the onset of primary γ' spheroidization.

Moving further up the length of the specimen, to even higher peak temperature exposure, the secondaries have now completely diffused into the γ matrix and some of the sole remaining primary γ' is now featuring severe spheroidization, as can be seen in Figure 110. A microstructure of this nature in FG RR1000 would later be found to correlate with a temperature exposure of between 1000-1100°C.

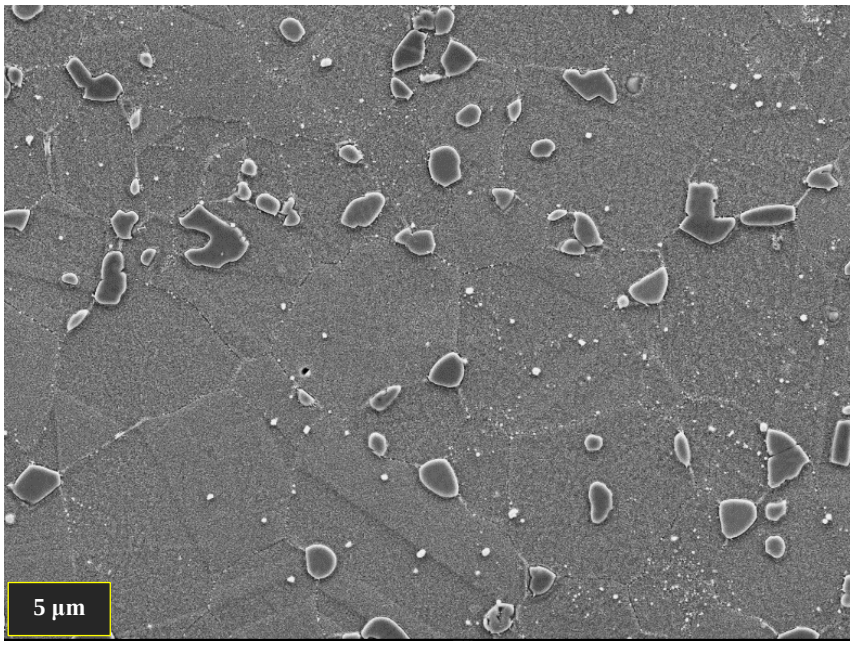

Figure 110 - SEM micrograph illustrating the complete dissolution of secondary γ'.

With the tungsten platen absorbing heat from the specimen and limiting the peak temperature the bottom of the specimen could reach, the heating rate that these regions had been exposed to was not known. It could be assumed that the heating rate would have been slower at the bottom of the specimen increasing gradually to the requested heating rate of $5°Cs^{-1}$ at the centre of the specimen where the pyrometer was recording the specimen temperature. The microstructure confirmed this, as moving further up the specimen in line with the colour change shown in the macro image, Figure 107, the spheroidization of the primary γ' is now accompanied by mottling of the γ grains. This was due to the γ' forming elements Al and Ti not having sufficient enough time to diffuse away and homogenise in the γ matrix leaving some areas of the γ matrix with more re-precipitated γ' than others as illustrated in Figure 111.

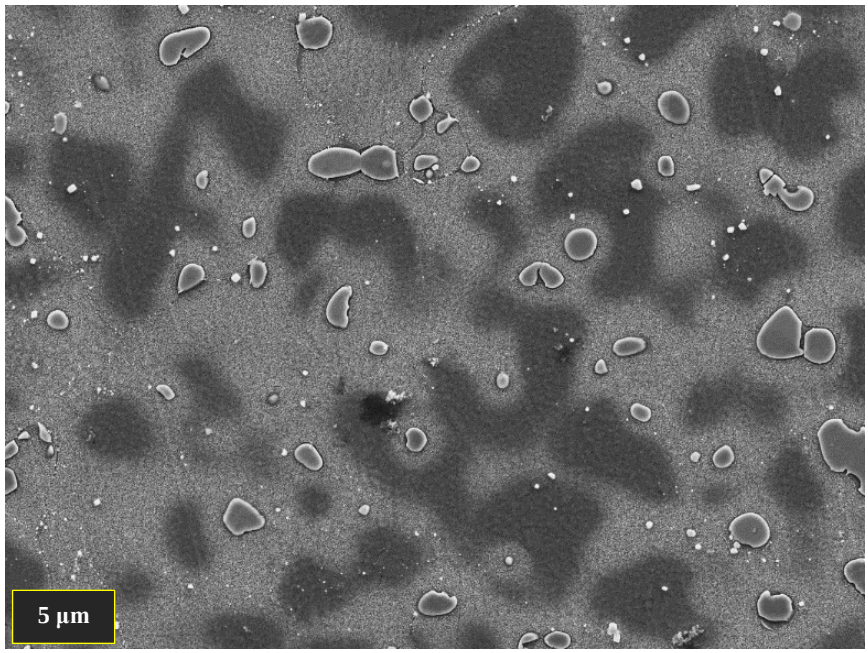

Figure 111 - SEM micrograph illustrating the mottled γ grains due to insufficient time for the diffusion of the γ' forming elements.

Figure 112 shows EDS analysis of these mottled regions that confirmed this, showing increased levels of Al and Ti and depleted levels of Mo, Cr and Co in the mottled regions which are characteristics of primary γ'.

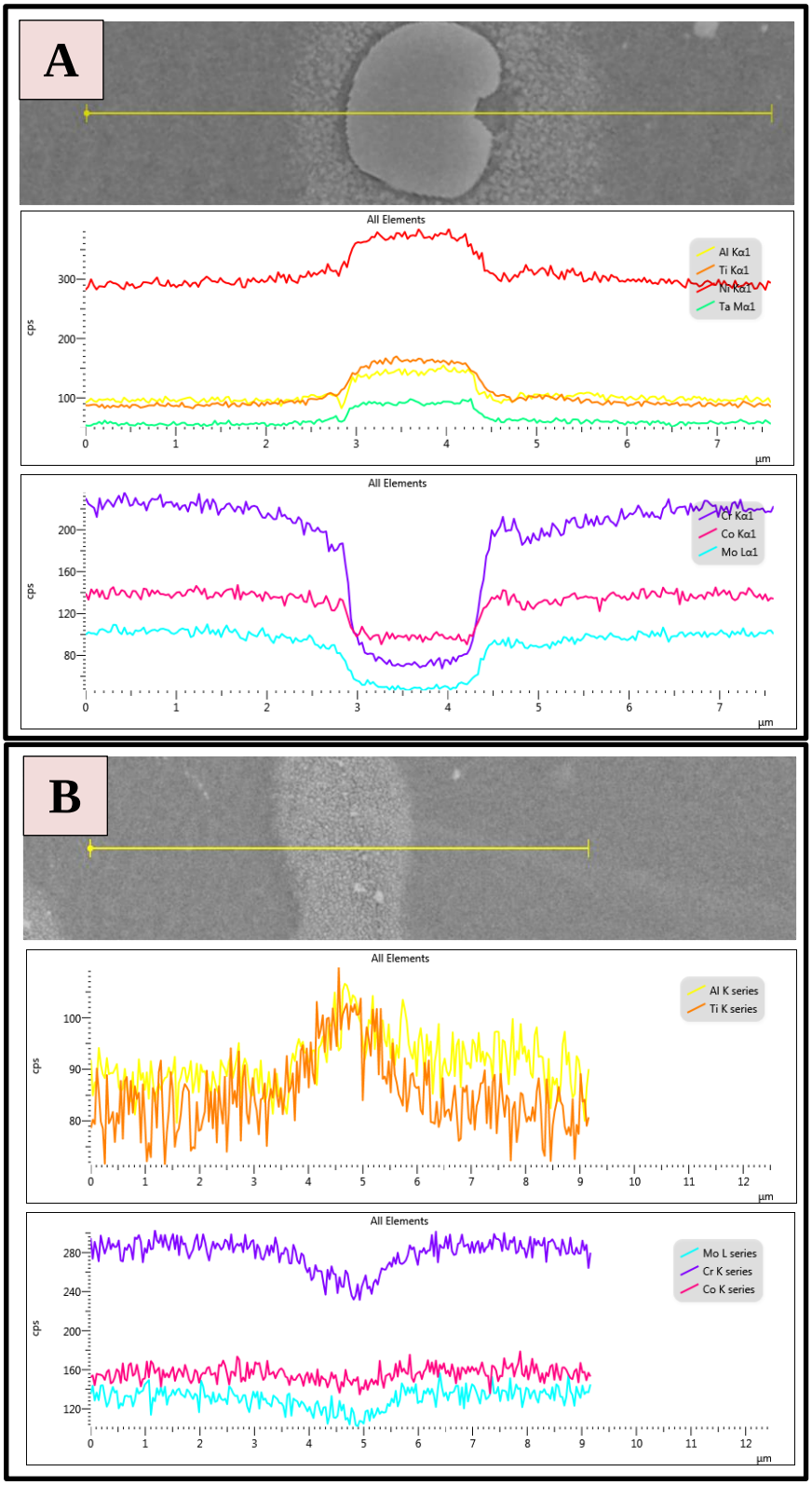

Figure 112 - EDS line scans showing the composition of A) A spheroidized γ' surrounded by enriched γ matrix. B) A section of mottled γ matrix enriched in γ' forming elements.

The specimen was then inspected at the centre of the specimen at the location of the pyrometer. This region is the only area where the temperature and heating rate could be guaranteed.

Figure 113 shows the microstructure found in this region. Here the heating rate was enough to allow some of the intergranular primary γ' to survive past its equilibrium solvus temperature of 1140°C where constitutional liquation can occur, liquating the γ' and a portion of the γ matrix surrounding it in a eutectic type reaction. Constitutional liquation of primary γ' in RR1000 is discussed in depth in sections 2.5.1 Constitutional liquation and 4.1.4.1 Liquation mechanisms. The evidence for a liquation event is given in the form of a γ-γ' eutectic phase found at the grain boundaries that is formed on rapid cooling of the liquid phase. This was in alignment with the findings of M. Attallah et al [4], in their study of constitutional liquation of primary γ' in fine grain RR1000. These eutectic microstructural features will be discussed in detail in section 4.5 Liquation products.

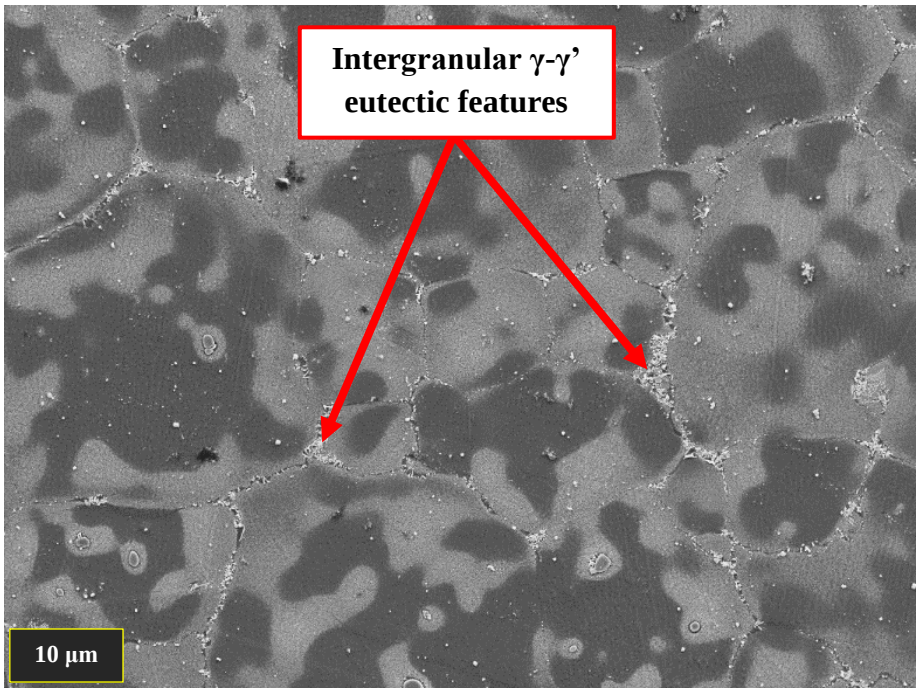

Figure 113 - SEM micrograph at taken at the centre of the specimen where evidence of liquation was found in the form of γ-γ' eutectic features.

From a test development standpoint this microstructural examination and proof of a temperature gradient was not a good result as the exact temperatures throughout the specimen were unknown.

In terms of microstructural evolution, the results of this test were very valuable indeed. This test had shown that FG RR1000's microstructural evolution is complex and is very sensitive to changes in both heating rate and peak temperature. These complex microstructural changes in both FG and CG RR1000 would need full characterisation in order to develop a better understanding of the conditions needed to produce sub-solidus liquation in both variants. Thus, a number of heat and quench only tests were undertaken.

4.1.3 Microstructural evolution of RR1000 during rapid heating to below the γ' solvus temperature

Specimens of both FG and CG RR1000 were heated at 25°Cs^{-1} to a range of temperatures below the γ' solvus temperature of 1140°C. Each specimen was water quenched on reaching the target temperature, in order to "freeze" the resultant microstructure at a rate that was comparable to IFW. Each specimen was then metallographically prepared and analysed to observe and quantify any changes compared to the parent material.

In each specimen the following microstructural characteristics were analysed:

1. Grain characteristics – Size, boundary types, texture & local misorientation.
2. γ' characteristics – Volume fraction, size & morphology.

Each specimen was also subject to Vickers hardness testing to give an indicator of strength and to assess the affect the microstructural changes had on the materials resistance to deformation. The results of this characterisation are summarised in Table 11 below. The grain orientation and local misorientation of each specimen was measured but is not included in the table or the subsequent sections, as the random texture and low local misorientation of the parent material was retained in both RR1000 pedigrees throughout all tests. This was evident as all MUD values fell between 0.52-1.84 and all average KAM values between 0.05° to 0.35°.

Details of the changes experienced by each specimen are described in the following sections. Each section indicates the heating rate and peak temperature that each specimen was subject to. All heat and quench only tests were performed on FG 431 and CG variants, FG443 was not used in this area of the study. All microstructural measurements have been subject to an error analysis as described in section 3.11 Error analysis. The 95% confidence interval calculated for each average measurement in the error analysis is given in brackets to illustrate the scatter in the average value. A t-test has also been conducted on all microstructural changes to judge their significance. If a change was found to be significant via the t-test method then the results are shown, stating the $t_{diff.}$ value calculated along with the $t_{crit.}$ value for the comparison. Significant changes have been highlighted and a 95% confidence interval given for the magnitude of the change if stated.

Test temperature	Variant	Grain Size (μm)	Primary γ' Volume Fraction (%) / size (μm)	Secondary γ' Volume Fraction (%) / size (nm)	Σ3 twin boundaries (%)	Hardness (Hv1)
Parent material	FG	6.4 (+/- 0.8)	10.2% / 1.71 (+/- 0.7% / 0.02)	33.4% / 137 (+/- 5.0% / 2)	22.1 (+/- 1.8)	423 (+/- 1)
	CG	48 (+/- 5.5)	N/A	31.9% / 147 (+/- 6.1% / 4)	46.2 (+/- 1.6)	410 (+/- 3)
900°C	FG	6.4 (+/- 0.9)	10.1% / 1.7 (+/- 3.8% / 0.02)	27.2% / 166 (+/- 1.4% / 6)	23.1 (+/- 3.3)	368 (+/- 2)
	CG	43.8 (+/- 5.4)	N/A	28.8% / 136 (+/- 4.2% / 3)	44.3 (+/- 1.6)	375 (+/- 4)
1000°C	FG	6.3 (+/- 1.1)	9.8% / 1.62 (+/- 1.8% / 0.02)	21.8% / 77 (+/- 6.4% / 3)	20.2 (+/- 2.4)	379 (+/- 3)
	CG	45.1 (+/- 4.5)	N/A	25.9% / 218 (+/- 0.6% / 4)	45.6 (+/- 2.0)	332 (+/- 4)
1050°C	FG	7.1 (+/- 1.2)	7.6% / 1.24 (+/- 1% / 0.02)	N/A	22.7 (+/- 2.4)	394 (+/- 4)
	CG	42.8 (+/- 4.6)	N/A	14.0% / 186 (+/- 1.0% / 4)	44.5 (+/- 1.4)	372 (+/- 6)
1100°C	FG	14.2 (+/- 2.0)	4.6% / 0.93 (+/- 0.8% / 0.02)	N/A	37.1 (+/- 3.2)	395 (+/- 5)
	CG	44.4 (+/- 5.6)	N/A	N/A	44.7 (+/- 2.4)	395 (+/- 5)

Table 11 - Sub-solvus "heat only" tests summary (95% confidence intervals given in brackets).

4.1.3.1 Resultant microstructure after 25°Cs^{-1} to 900°C heat exposure

Fine grain

Figure 114 illustrates the changes experienced by the γ' after reaching a peak temperature of 900°C. The size and distribution of the γ' experienced some minor changes at this temperature with the microstructure initially resembling the parent material. Closer inspection revealed that some of the smaller tertiary γ' usually located between the primary and secondary γ' have diffused into the γ matrix as can be seen in Figure 114 B.

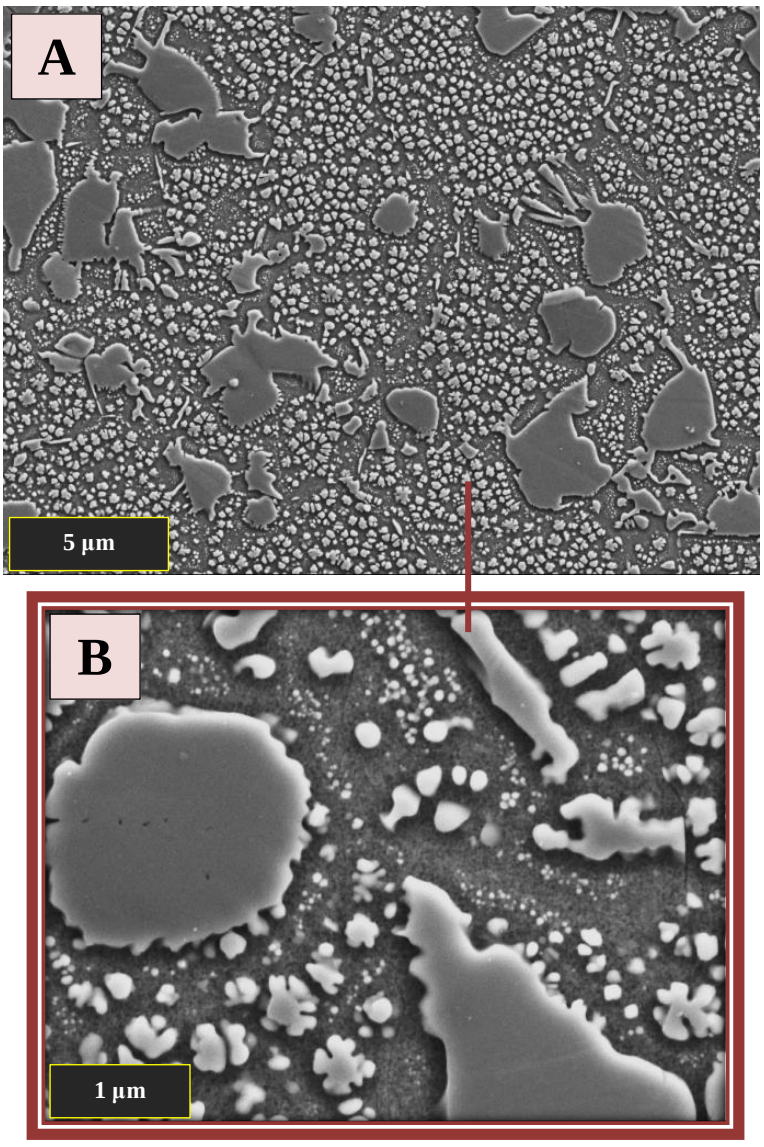

Figure 114 - SEM micrographs of a FG specimen heated to 900°C at 25°Cs^{-1}. A) Low magnification. B) High magnification.

Measurement of the γ' revealed that the primary γ' remained unchanged at 10.1% (+/- 3.8%) volume fraction and an average size of 1.7μm (+/- 0.02). The secondary γ' experienced some significant changes, with volume fraction decreasing to 27.2% (+/- 1.4%) a difference of -6.2% (+/- 5.2%, $t_{diff.}$ 5.102 > $t_{crit.}$ 4.303) and average size increasing from 137nm (+/- 2) in the parent material to 166nm (+/- 6) a difference of 29nm (+/- 6, $t_{diff.}$ 8.944 > $t_{crit.}$ 1.96). This increase in average size was due to the loss of some of the smaller secondary γ' that had diffused into the γ matrix. This smaller secondary γ' would have reduced the average size measurement in the parent material. Overall, the morphology of both the primary and secondary γ' was mostly unchanged, although some secondaries exhibited spheroidization.

As the primary γ' were still present at this temperature, providing grain boundary pinning, the grain size of this specimen was unchanged at 6.4μm (+/- 0.9). The grain boundary types were also similar with a large number of Σ3 twin grain boundaries present. There was no significant change in the quantity of these Σ3 boundaries, forming 23.1% (+/- 3.3%) of the total grain boundaries measured and are highlighted red in Figure 115. Other special boundaries are also coloured.

Figure 115 - EBSD map of a FG specimen heated to 900°C at 25°Cs^{-1}. Critical grain boundaries are marked in black with twin boundaries marked in red.

Vickers hardness testing revealed a significant drop in average hardness from the parent material value of 423 Hv (+/- 1) down to 368 Hv (+/- 2), a difference of -55 Hv (+/- 2, $t_{diff.}$ 55.022 > $t_{crit.}$ 2.064). The drop in hardness can be attributed to the diffusion of the tertiary and smaller secondary γ' into the γ matrix decreasing the number of γ' precipitates present to impede dislocation movement.

Coarse grain

The parent microstructure of the CG variant is vastly different to the FG variant and consequently behaves in a different manner. The secondary γ' have experienced some change with some of the smaller secondaries undergoing spheroidization this is accompanied by some of the tertiary γ' diffusing into the γ matrix. As a result, there has been a reduction in the average size of the secondaries from 147nm (+/- 4) in the parent CG to 136nm (+/- 3), a change of 11nm (+/- 5, $t_{diff.}$ 4.424 > $t_{crit.}$ 1.96). Despite this change in size the volume fraction of secondary γ' experienced no significant change being recorded at 28.8% (+/- 4.2%). These observations are illustrated in Figure 116.

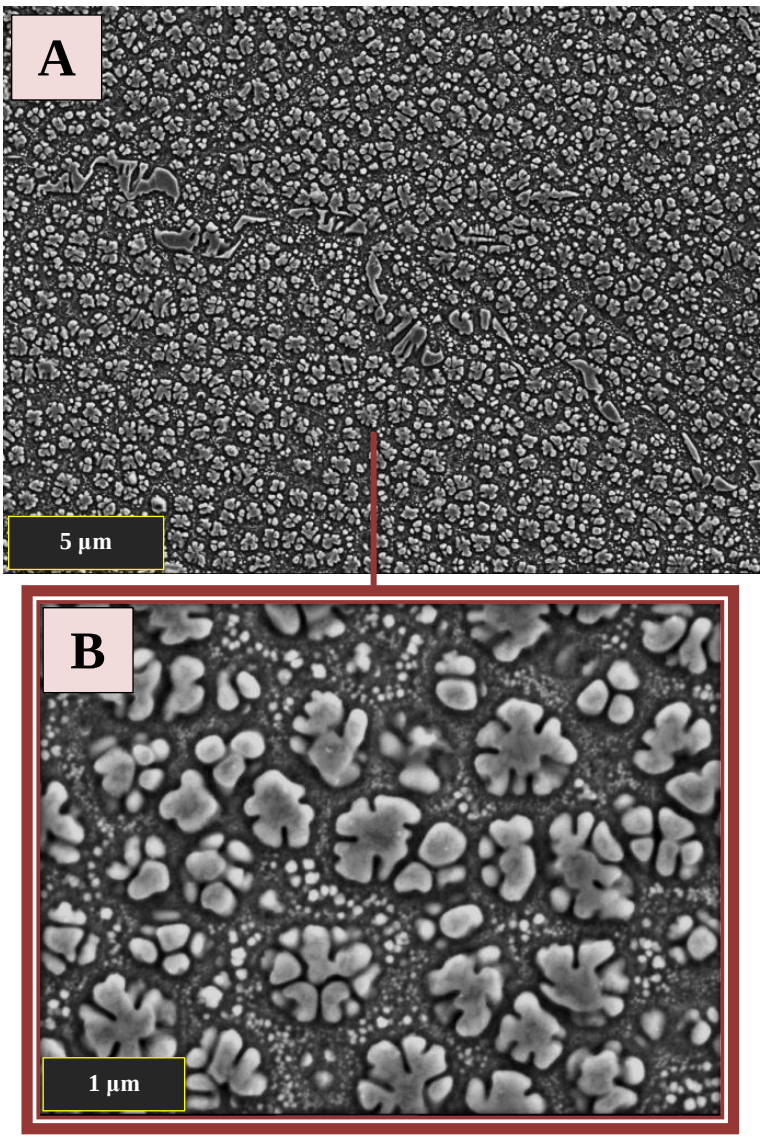

Figure 116 - SEM micrographs of a CG specimen heated to 900°C at 25°Cs^{-1}. A) Low magnification. B) Higher magnification.

The discrepancy in significance between the change in average volume fraction and change in average size is due to the measurement method of each. The average volume fraction is calculated by averaging the volume fraction of γ' in three images therefore a sample size of n=3, whereas the average size calculations are calculated from the average size of each γ' in those images giving a much larger sample size, n>1000. Therefore, during the error analysis, the smaller sample size used in the volume fraction calculation leads to a larger error and greater 95% confidence interval.

The grain size remained stable during this temperature exposure, experiencing no significant change, being measured at 43.8μm (+/- 5.4). The fraction of Σ3 twin grain boundaries also remained unchanged at 44.3% (+/- 1.6%) of the total grain boundaries measured. The EBSD map in Figure 117 illustrates the general size and shape of the grains in this specimen along with the Σ3 twin boundaries marked in red. Other special boundaries are also coloured.

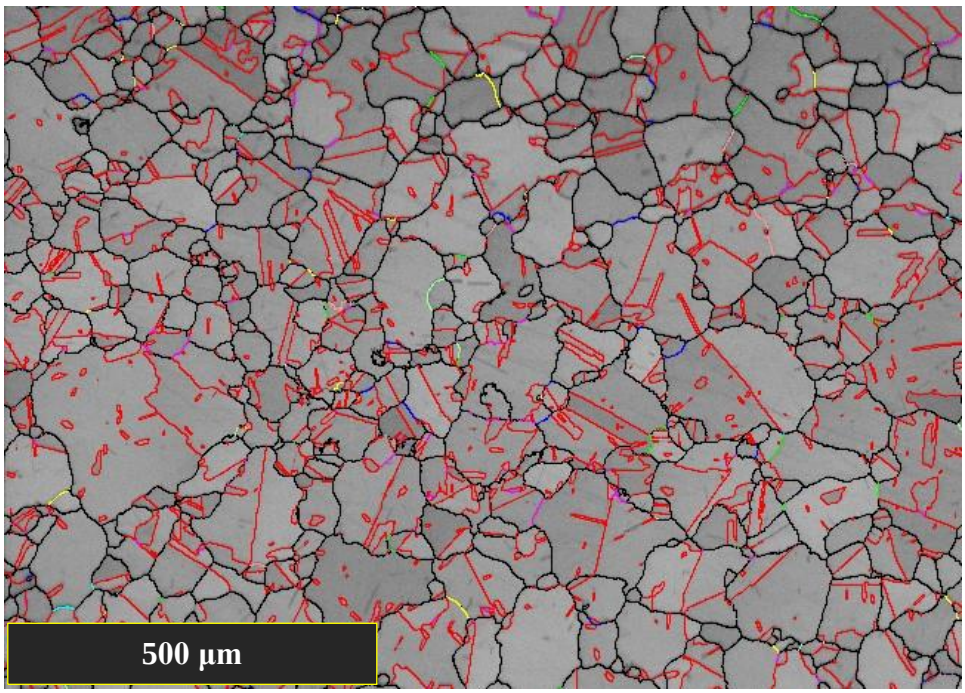

Figure 117 - EBSD map of a CG specimen heated to 900°C at 25°Cs^{-1}. Critical grain boundaries are marked in black with twin boundaries marked in red.

The average Vickers hardness for this specimen was calculated at 375 Hv (+/- 4) a significant drop from the parent material hardness of 410 Hv (+/- 3), a difference of -35 Hv (+/- 5, $t_{diff.}$ 14.033 > $t_{crit.}$ 2.064). Again, this can be attributed to the reduction of γ' volume fraction and the strengthening mechanisms they provide.

4.1.3.2 Resultant microstructure after 25°Cs^{-1} to 1000°C heat exposure

Fine grain

Increasing the peak temperature to 1000°C brings about more drastic microstructural changes in the FG variant. The primary γ' have begun to spheroidize slightly and are starting to lose their angular features. The secondary γ' have experienced the greatest change with almost all of the original secondaries diffusing into the γ matrix. Some of the larger secondaries still remain in the severely spheroidized form. This can be seen in Figure 118 A & B.

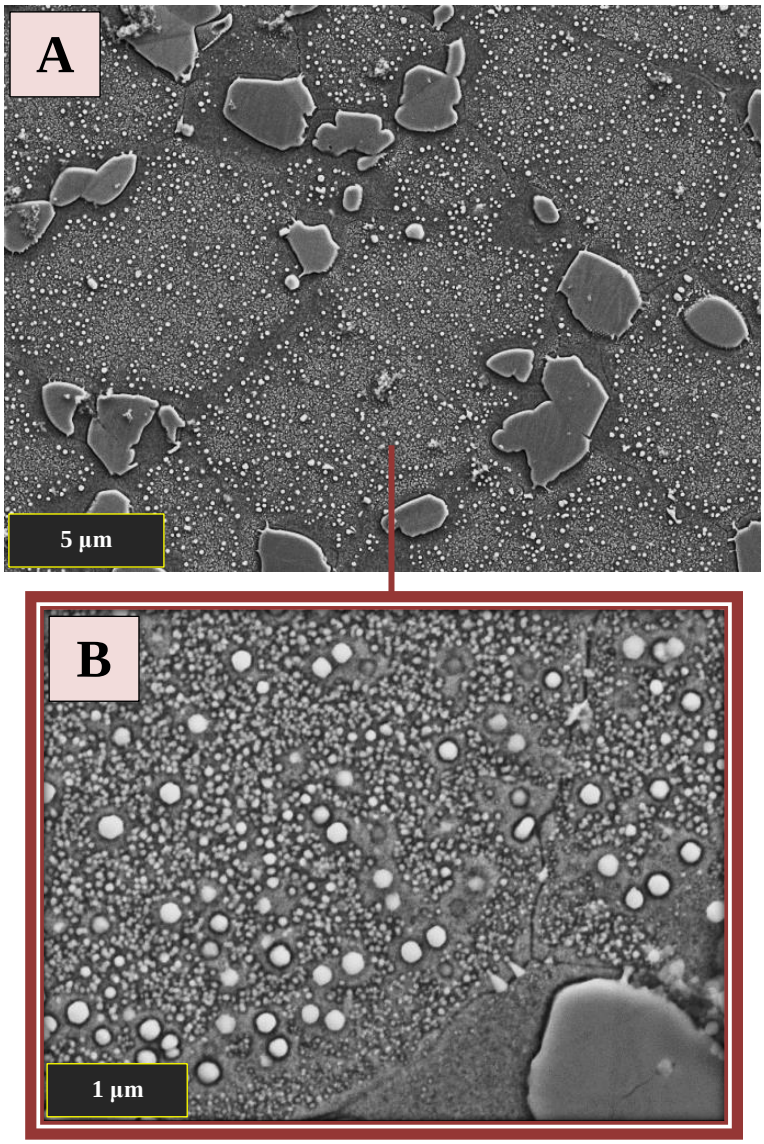

Figure 118 - SEM micrographs of a FG specimen heated to 1000°C at 25°Cs^{-1}. A) Multiple grains. B) inside the grains.

Measurement of the γ' revealed that the volume fraction of primary γ' experienced no significant change at 9.8% (+/- 1.8%), but with a slight reduction in average ECD to 1.62μm (+/- 0.02) when compared to the 900°C FG specimen's 1.7μm (+/- 0.02), a change of -0.08 μm (+/- 0.03, $t_{diff.}$ 5.508 > $t_{crit.}$ 1.96). This was due to the slight rounding of the edges as can be seen in Figure 118 A.

Analysis of the secondary γ' exhibited their drastic changes in both size and morphology with average size reducing to 77nm (+/- 3) from the 166nm (+/- 6) in the 900°C FG specimen, a change of -89nm (+/- 7, $t_{diff.}$ 26.136 > $t_{crit.}$ 1.96). However, no significant change in volume fraction was measured being calculated at 21.8% (+/- 6.4%). Again, this was likely due to the difference in sample sizes of the two measurements. As can be seen in Figure 118 B, the surviving secondary γ' were accompanied by a coarse re-precipitated tertiary γ' which would have contributed to the large reduction in measured average size of the secondary γ'.

At 1000°C the grain size was still stable due to the retained primary γ' measuring no considerable change at 6.3µm (+/- 1.1). The percentage of Σ3 twin grain boundaries was also consistent with the parent FG material and the FG specimen exposed to 900°C recorded at 20.2% (+/- 2.4%) of total boundaries measured. The EBSD map in Figure 119 illustrates the formation of the grains, with the Σ3 twin boundaries highlighted in red, as before. Other special boundaries are also coloured.

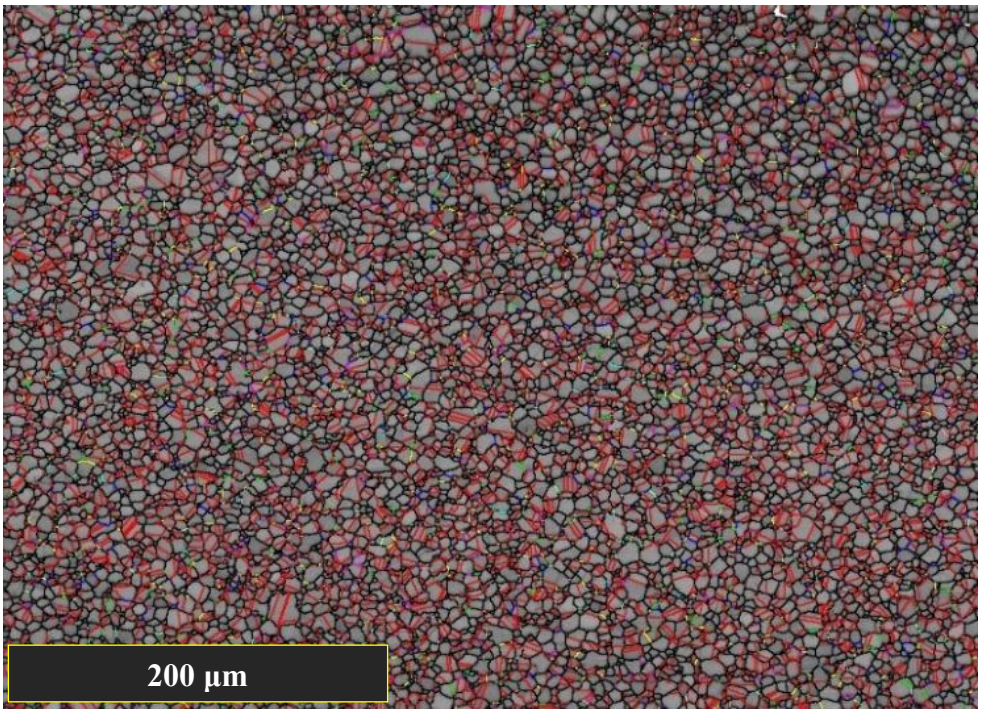

Figure 119 - EBSD map of a FG specimen heated to 1000°C at 25°Cs^{-1}. Critical grain boundaries are marked in black with twin boundaries marked in red.

The average hardness produced by the resultant microstructure in this specimen was 379 Hv (+/- 3). A significant increase in hardness of 11 Hv (+/- 4, $t_{diff.}$ 6.189 > $t_{crit.}$ 2.064), compared to the FG specimen used in the 900°C test (368 Hv +/- 2). This slight increase is likely due to re-precipitation of the coarse tertiary γ' between the surviving secondary γ', increasing the total number of γ' compared to the 900°C specimen, impeding dislocation movement.

Coarse grain

On raising the test temperature to 1000°C the CG variant now begins to undergo some slight changes in the size and morphology of the γ' phase, as can be seen in Figure 120. The tertiary γ' have all diffused into the γ matrix leaving only the secondary γ', which have begun to undergo spheroidization.

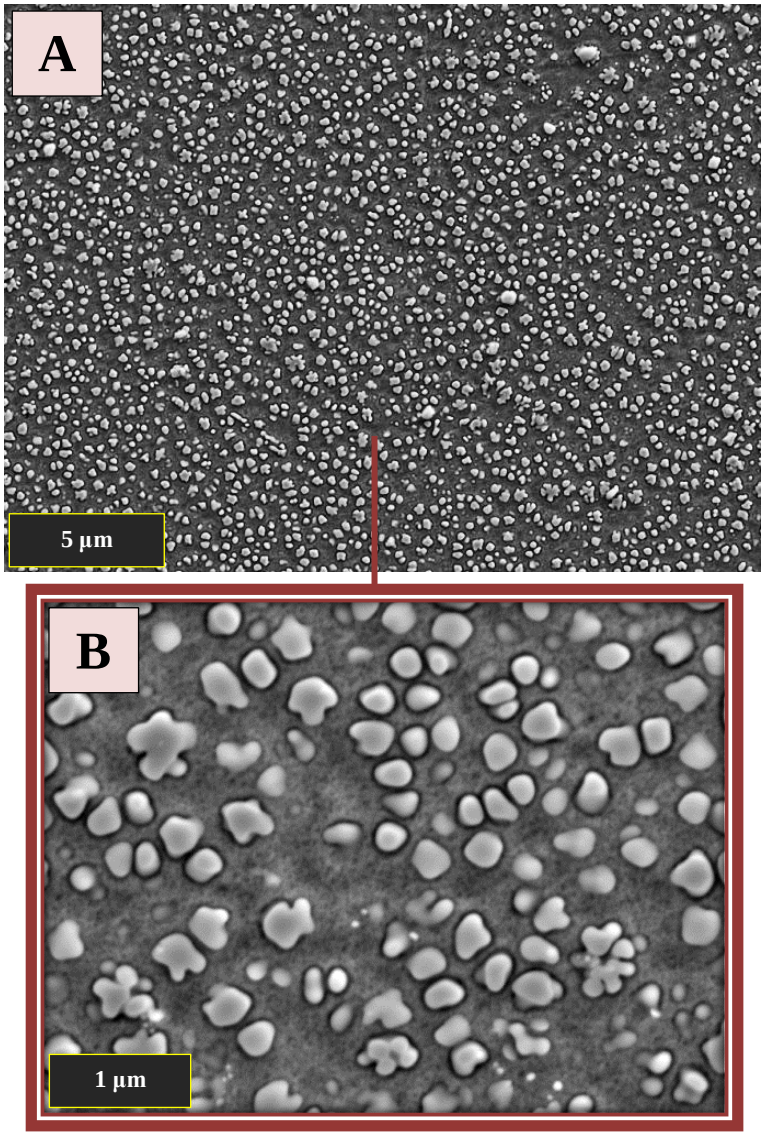

Figure 120 - SEM micrographs of a CG specimen heated to 1000°C at 25°Cs^{-1}. A) Low magnification. B) High magnification.

Despite the changes in morphology evident in the micrographs, the volume fraction of the sole remaining secondary γ' was measured at 25.9% (+/- 0.6%), showing no statistically significant change from the CG specimen tested at 900°C (28.8% +/- 4.2%). Again, this is due to the sample size used during the volume fraction calculations. Interestingly, the average size of the secondary γ' in this specimen had increased compared to the 900°C specimen from 136nm (+/- 3) to 218nm (+/- 4), a change of +82nm (+/- 5, $t_{diff.}$ 30.674 > $t_{crit.}$ 1.96). This is due to the loss of the smaller secondary γ' by diffusion into the γ matrix, see Figure 120 B. With the disappearance of the smaller secondary γ' only the large secondaries have survived, which increases the average particle size to a higher value.

The average grain size in this specimen remained comparably unchanged to the parent CG material and the 900°C CG specimen measuring at 45.1µm (+/- 4.5). Figure 121 shows that the overall grain characteristics of this specimen were very similar to the parent CG material, as well as the 900°C exposure specimen, with the percentage of Σ3 twin grain boundaries experiencing no change at 45.6% (+/- 2.0%).

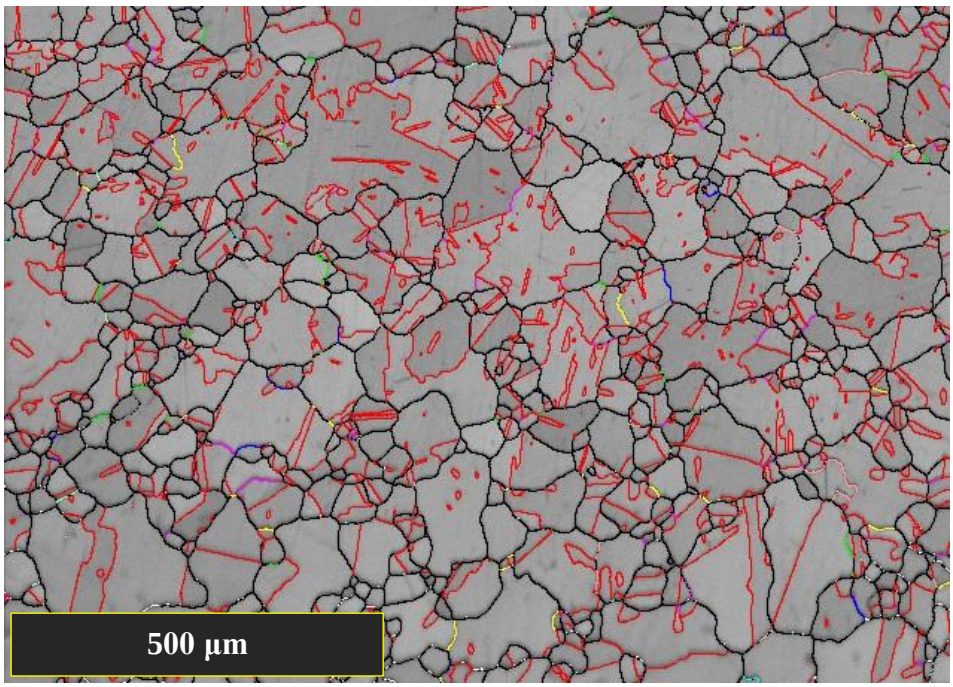

Figure 121 - EBSD map of a CG specimen heated to 1000°C at 25°Cs^{-1}. Critical grain boundaries are marked in black with twin boundaries marked in red.

The Vickers hardness tests revealed that this specimen's average hardness had decreased further from the hardness exhibited by the CG specimen tested at 900°C (375 Hv +/- 4). Decreasing by 43 Hv (+/- 6, $t_{diff.}$ 14.760 > $t_{crit.}$ 2.064), with an average of 332 Hv (+/- 4). This hardness drop was to be expected with the tertiary γ' now missing due to no re-precipitation of fine γ' occurring when quenching from this temperature, as shown in Figure 120 B.

4.1.3.3 Resultant microstructure after 25°Cs^{-1} to 1050°C heat exposure

Fine Grain

At a peak temperature of 1050°C, the sole remaining primary γ' begin to display significant changes in both size and morphology. The primary γ' volume fraction decreases from the 9.8% (+/- 1.8%) in the 900°C FG specimen to 7.6% (+/- 1.0%), a decrease of 2.2% (+/- 2.0%, $t_{diff.}$ 4.697 > $t_{crit.}$ 4.303). This was accompanied by a fall in average size to 1.24µm (+/- 0.02), a difference of -0.38µm (+/- 0.03, $t_{diff.}$ 27.657 > $t_{crit.}$ 1.96). Figure 122 illustrates the changes in γ' morphology.

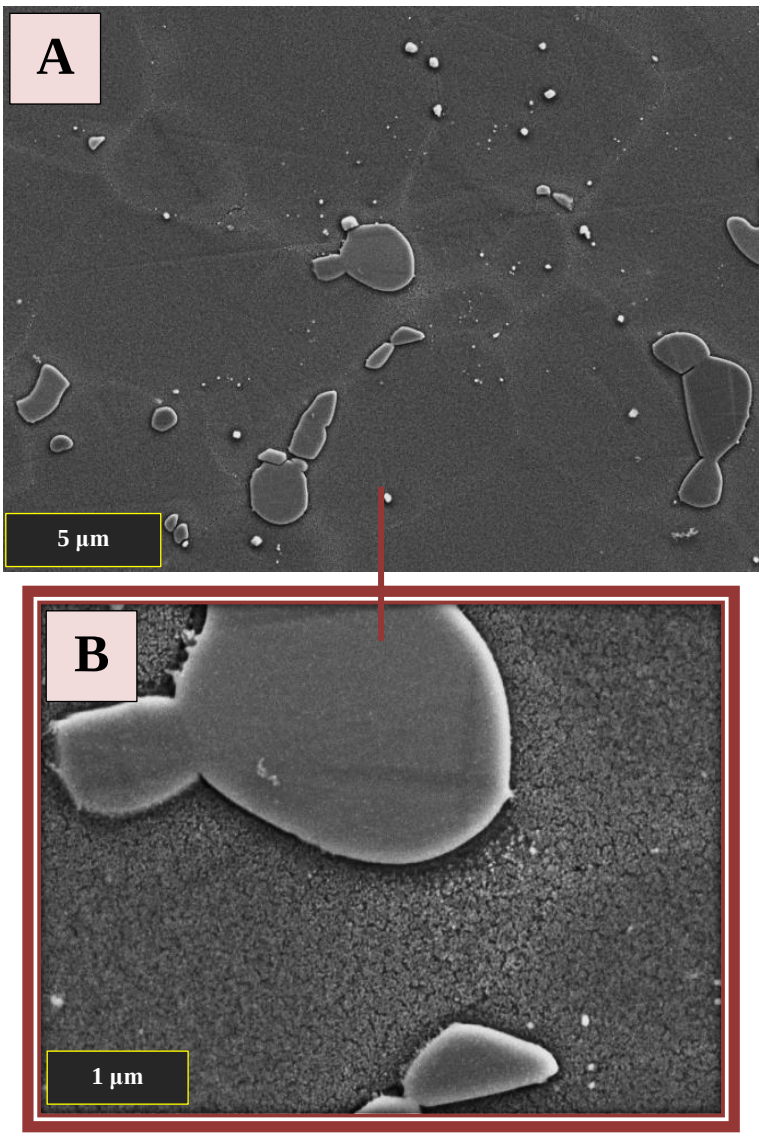

Figure 122 - SEM micrographs of a FG specimen heated to 1050°C at 25°Cs^{-1}. A) Multiple grains. B) Very fine tertiary γ' within the grains.

Figure 122 B shows an enlarged view of the γ matrix between the surviving primary γ'. Here an extremely fine re-precipitated γ' now lays, due to the large driving force for re-precipitation created by the diffusion of all the secondary and tertiary γ' as well as some primary γ' into the γ matrix during heating to 1050°C. This mass diffusion into the γ matrix resulted in it becoming super saturated, therefore it could no longer retain the gamma prime forming elements down to room temperature even under water quenching [56].

Some of the smaller intergranular primary γ' have now fully diffused into the γ matrix and the surviving primary γ' are showing severe spheroidization, therefore a slight reduction in grain boundary pinning would be expected. Despite this, the grain size experienced no significant change at this temperature being recorded at 7.1μm (+/- 1.2) for this specimen. There was also no meaningful change in the percentage of Σ3 twin boundaries being measured at 22.7% (+/- 2.4%). The EBSD map in Figure 123 illustrates the size and shape of the grains found in this specimen, with Σ3 twin boundaries highlighted red.

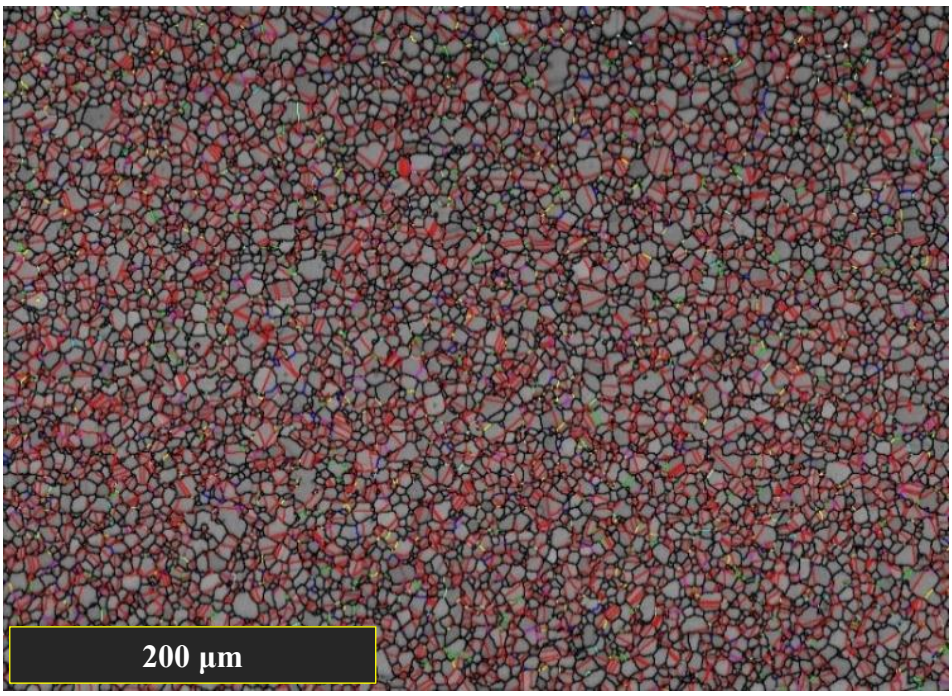

Figure 123 - EBSD map of a FG specimen heated to 1050°C at 25°Cs^{-1}. Critical grain boundaries are marked in black with twin boundaries marked in red.

Vickers hardness testing of this specimen revealed an average hardness value of 394 Hv (+/- 4) a significant increase of 15 Hv (+/- 5, $t_{diff.}$ 5.746 > $t_{crit.}$ 2.064), from the hardness exhibited by the FG specimen heated to 1000°C (379 Hv +/- 3). The very fine re-precipitated γ' is now having a powerful strengthening effect, much like the increase in strength due to a fine re-precipitated γ' found at the weld line of RR1000 inertia friction welds [58].

Coarse grain

Figure 124 shows the microstructural changes experienced by a CG specimen heated to 1050°C. Spheroidization of the secondary γ' is now well in process with a drop in volume fraction to 14% (+/- 1.0%) being recorded. This is a significant drop of 11.9% (+/- 1.2%, $t_{diff.}$ 43.874 > $t_{crit.}$ 4.303) from the previous CG specimen tested at 1000°C (25.9% +/- 0.6%) and a loss of over half the volume fraction of secondary γ' in the parent CG material. This can be seen in Figure 124.

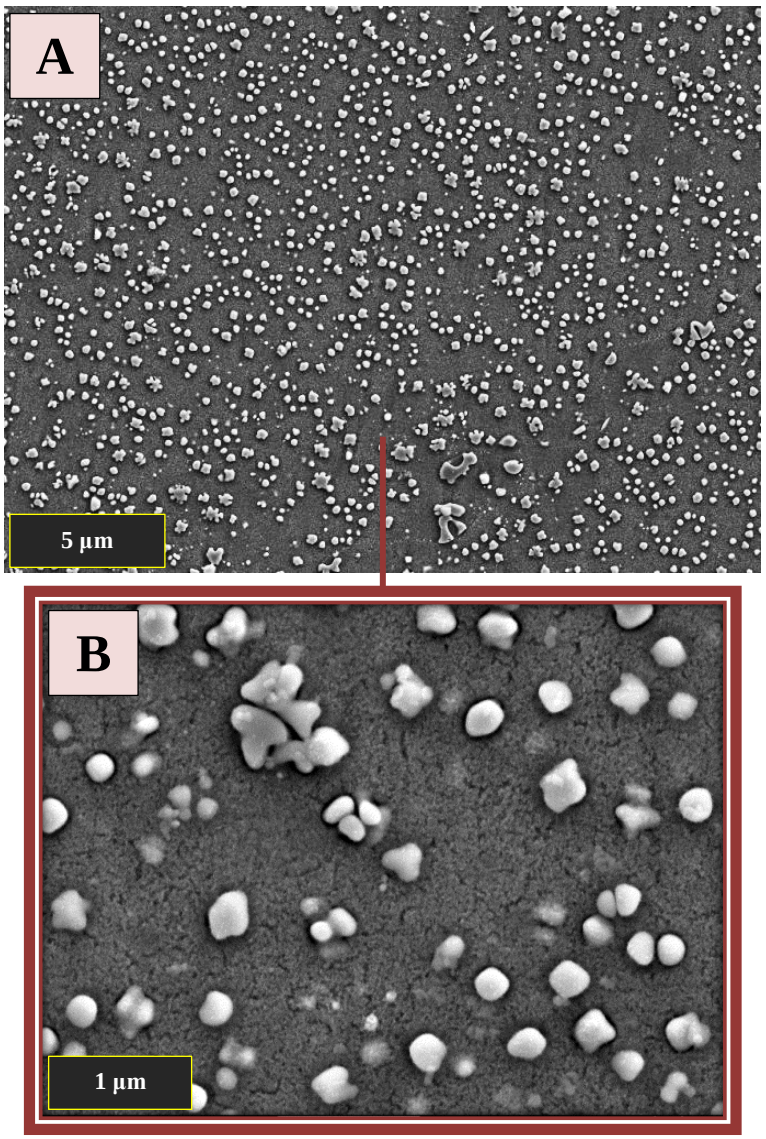

Figure 124 - SEM micrographs of a CG specimen heated to 1050°C at 25°Cs^{-1}. A) Low magnification. B) Very fine re-precipitated γ'.

The extent of the spheroidization at this temperature is sufficient enough that the average precipitate size has decreased to 186nm (+/- 4), a decrease of 32nm (+/- 5, $t_{diff.}$ 11.516 > $t_{crit.}$ 1.96) from the specimen tested at 1000°C (218nm +/- 4). At this peak temperature exposure, sufficient volume of the γ' precipitates have diffused into the γ matrix during heating to create a high enough concentration of γ' forming elements to cause a strong enough driving force for re-precipitation during water quenching. Consequently, the surviving secondary γ' are now surrounded by an evenly dispersed re-precipitated tertiary γ' which is very fine. The higher magnification SEM image in Figure 124 B illustrates this.

After exposure to 1050°C the grain size in the CG variant remained unchanged measuring at 42.8μm (+/- 4.6). The fraction of Σ3 twin grain boundaries recorded also remained unchanged being measured at 44.5% (+/- 1.4%) of grain boundaries measured. This is shown in the EBSD map in Figure 125.

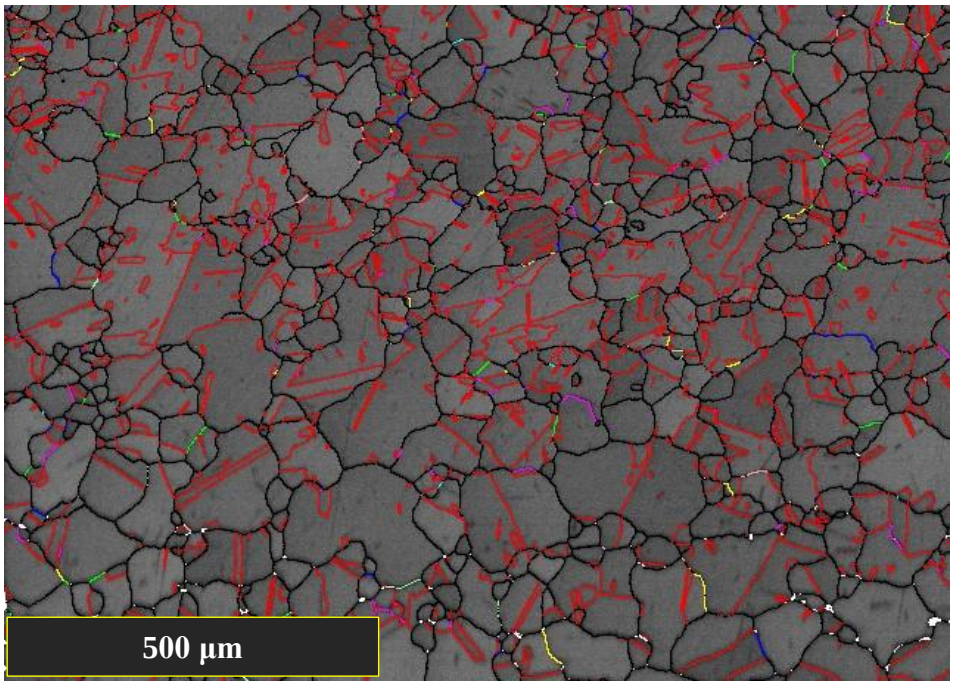

Figure 125 - EBSD map of a CG specimen heated to 1050°C at 25°Cs^{-1}. Critical grain boundaries are marked in black with twin boundaries marked in red.

As expected, the reintroduction of fine tertiary γ' via re-precipitation has brought with it an increase in hardness value, with this specimen producing an average hardness value of 372 Hv (+/- 6). This is an increase of 40 Hv (+/- 7, $t_{diff.}$ 11.077 > $t_{crit.}$ 2.064) over the previous CG specimen heated to 1000°C (332 Hv +/- 4), where no tertiary γ' was re-precipitated.

4.1.3.4 Resultant microstructure after 25°Cs^{-1} to 1100°C heat exposure

Fine grain

Increasing the thermal exposure to 1100°C has a distinct effect on the remaining primary γ'. At this temperature, the outer perimeter of the primary γ' begin to rapidly diffuse into the γ matrix. This results in only the largest primary γ' surviving albeit in a very spheroidized state. The γ matrix surrounding these surviving γ' is therefore enriched in γ' forming elements due to not having enough time at temperature to fully homogenise these elements throughout the rest of the matrix. In turn this creates an even stronger driving force for re-precipitation of γ', resulting in the re-precipitated 'islands' of coarsened tertiary around the surviving primary γ' that can be seen in Figure 126.

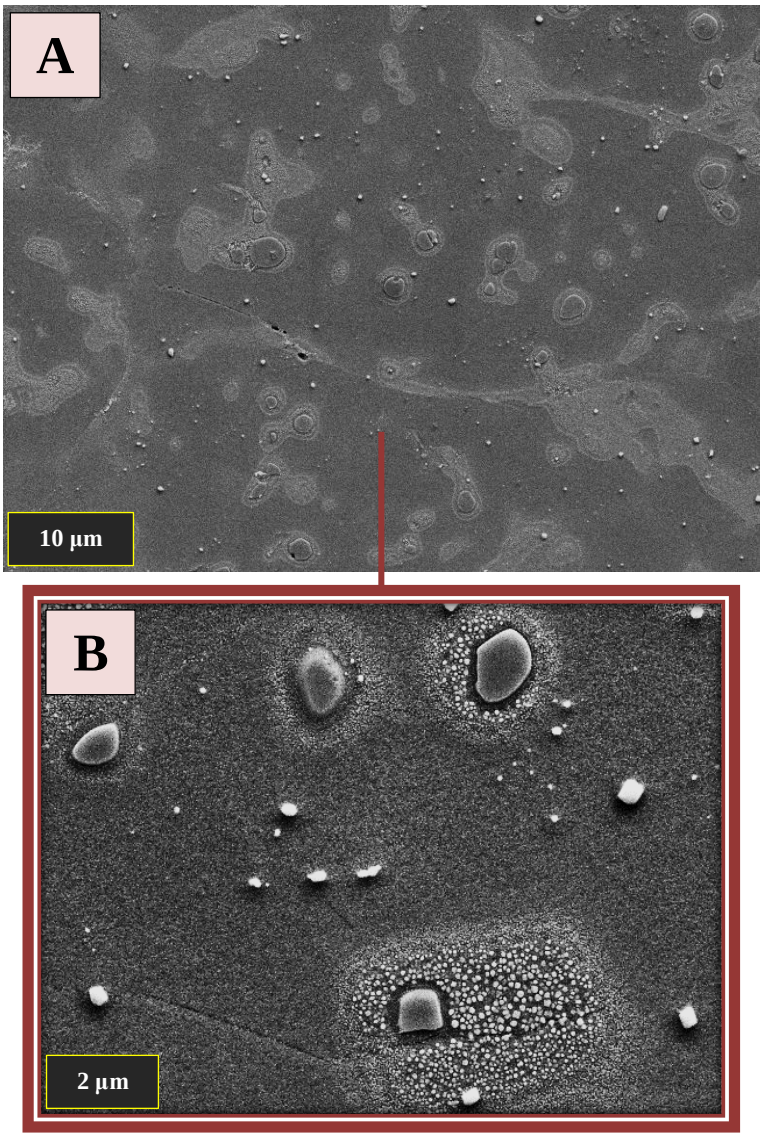

Figure 126 - SEM micrographs of a FG specimen heated to 1100°C at 25°Cs^{-1}. A) Low magnification. B) Higher magnification.

These ‘islands’ of coarsened tertiary γ’ can also be seen in areas where no surviving primary γ’ is present, these would have been the areas where a primary γ’ once was but its size was not sufficient enough for it to survive to this temperature at this heating rate.

Measurement of the primary γ’ revealed that only 4.6% (+/- 0.8%) volume fraction remained, a decrease of 3.0% (+/- 1.2%, $t_{diff.}$ 10.362 > $t_{crit.}$ 4.303) from the FG specimen tested at 1050°C (7.6% +/- 1%). The surviving primary γ’ were measured to have an average size of 0.93μm (+/- 0.02), a difference of -0.31μm (+/- 0.02, $t_{diff.}$ 24.910 > $t_{crit.}$ 1.96) when compared to the FG specimen tested at 1050°C (1.24 μm +/- 0.02).

As expected, with the loss of over half the volume fraction of the intergranular primary γ' precipitates, the grain boundary pinning they provided has been severely reduced, allowing grain growth. This specimen's grain size measured at 14.2µm (+/- 2.0), approximately double the 6.4µm (+/- 0.8) of the parent FG material and a significant increase of 7.1µm (+/- 2.3, $t_{diff.}$ 8.548 > $t_{crit.}$ 2.776) compared to the FG specimen tested at 1050°C (7.1µm +/- 1.2). The loss of primary γ' has also caused an increase in percentage of grain boundaries measured registering as Σ3 twin grain boundaries. This is partly due to there being less primary γ' to be recorded as small grains during EBSD. This specimen exhibited 37.1% (+/- 3.2%) Σ3 boundaries, an increase of 14.4% (+/- 4.0%, $t_{diff.}$ 15.677 > $t_{crit.}$ 4.303) over the FG specimen exposed to 1050°C (22.7% +/- 2.4%). The EBSD map in Figure 127 illustrates the large amount of grain growth exhibited by this specimen.

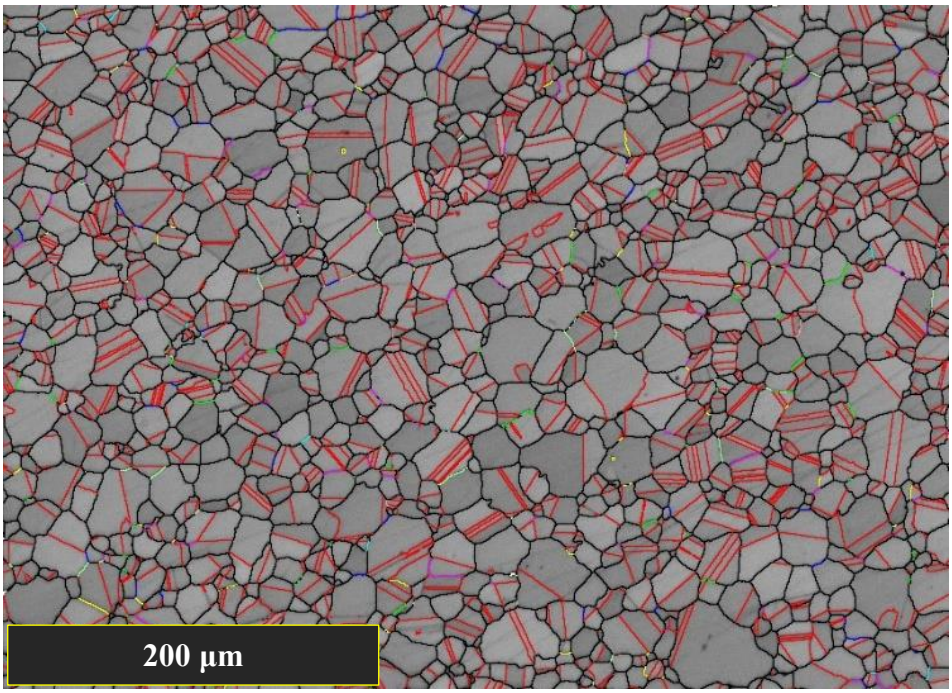

Figure 127 - EBSD map of a FG specimen heated to 1100°C at 25°Cs^{-1}. Critical grain boundaries are marked in black with twin boundaries marked in red.

The average hardness value for this specimen was 395 Hv (+/- 5), meaning there was no change in average hardness when compared to the FG specimen heated to 1050°C (394 Hv +/- 4). This suggests that the 'islands' of coarse re-precipitated tertiary γ' and change in grain size have made little difference on the resistance to deformation.

Coarse grain

Increasing the peak temperature to 1100°C has a drastic effect on the microstructure of the CG variant, producing a resultant microstructure that has no resemblance to the parent CG microstructure, see Figure 128. At this temperature all of the secondary γ' has diffused into the γ matrix. On water quenching the γ' forming elements have re-precipitated as a uniformly dispersed very fine tertiary γ' as shown in Figure 128 B.

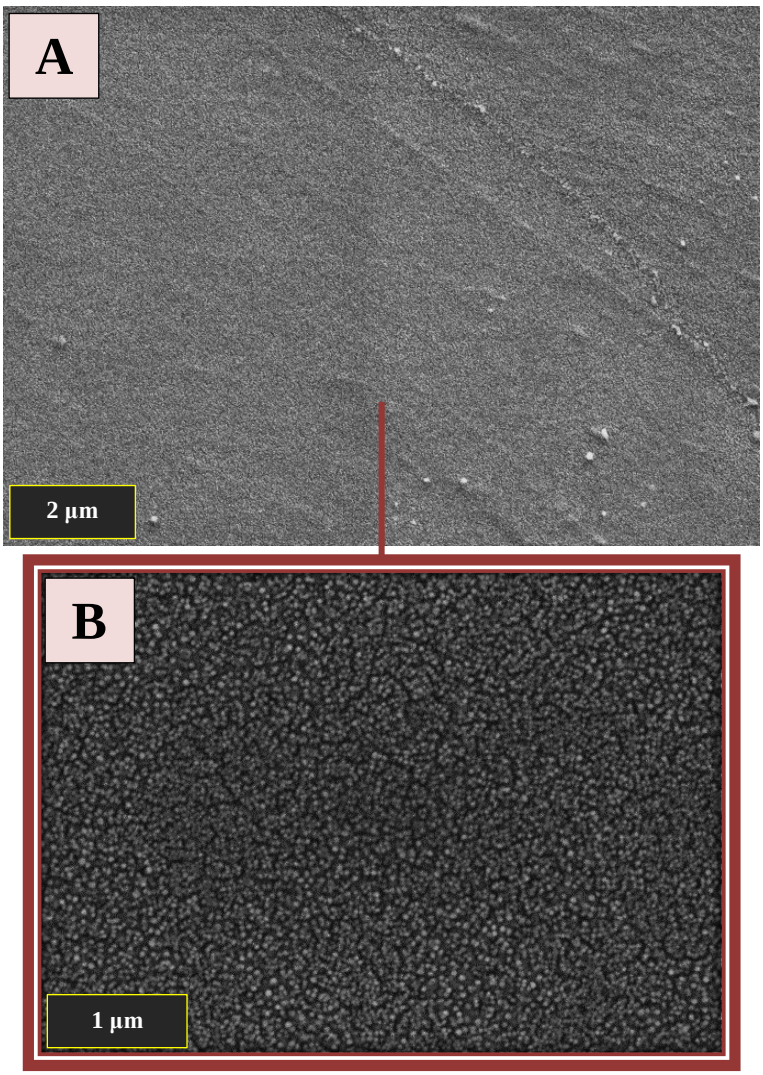

Figure 128 - SEM micrographs of a CG specimen heated to 1100°C at 25°Cs^{-1}. A) Low magnification. B) Higher magnification.

Despite the eradication of all of the original γ' precipitates the grain size remained unchanged at 44.4μm (+/- 5.6). This was expected as the CG variant grows to a stable grain size during the solution heat treatment applied to it during its manufacture, therefore does not have the driving force to grow further. Increasing the exposure temperature made no change to the fraction of Σ3 twin grain boundaries, with 44.7% (+/- 2.4%) of the total grain boundaries recorded being Σ3, as illustrated in Figure 129.

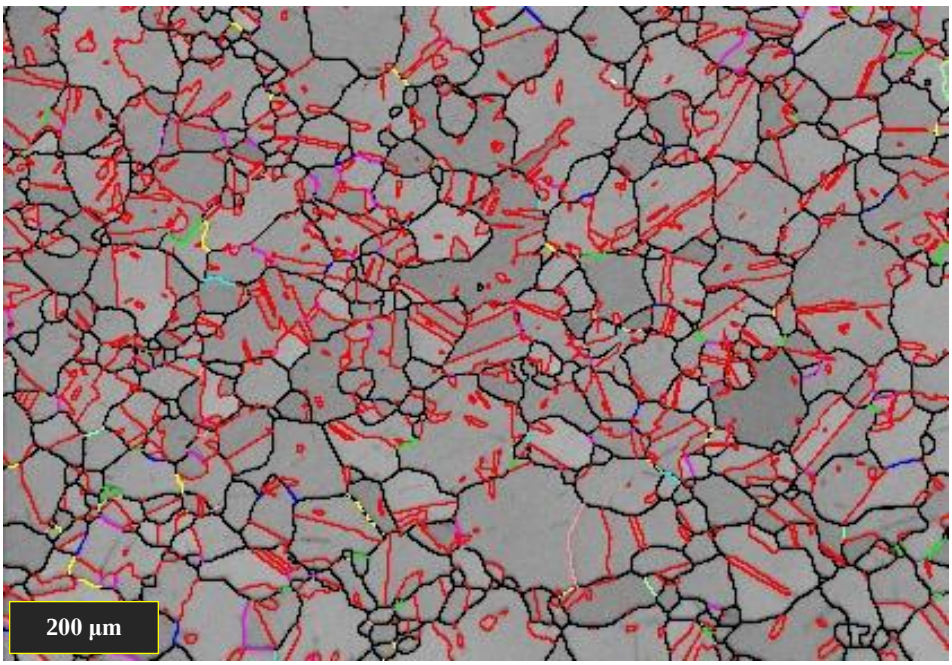

Figure 129 - EBSD map of a CG specimen heated to 1100°C at 25°Cs^{-1}. Critical grain boundaries are marked in black with twin boundaries marked in red.

The evenly distributed re-precipitated fine γ' had a marked improvement on the average hardness of this specimen with an average hardness value of 395 Hv (+/- 5). An increase of 23 Hv (+/- 8, $t_{diff.}$ 6.232 > $t_{crit.}$ 2.064) when compared to the CG specimen heated to 1050°C (372 Hv +/- 6). This specimen had regained much of its original hardness with only a slight deficit from the parent CG material. This is due to the fact all of the original γ' have been redistributed as a very fine re-precipitated γ', which is now having a powerful strengthening effect. This is comparable with the increase in strength due to a fine re-precipitated γ' found at the weld line of some nickel superalloy inertia friction welds, including RR1000 [58].

4.1.4 Microstructural evolution of RR1000 during rapid heating to above the gamma prime solvus temperature

Heating both RR1000 variants at 25°Cs^{-1} to just below the gamma prime solvus temperature of 1140°C produced two very different microstructures, as shown in Figure 130. Both variants have undergone drastic microstructural changes which have set up the foundations for two sub-solidus liquation mechanisms to occur in each variant, respectively.

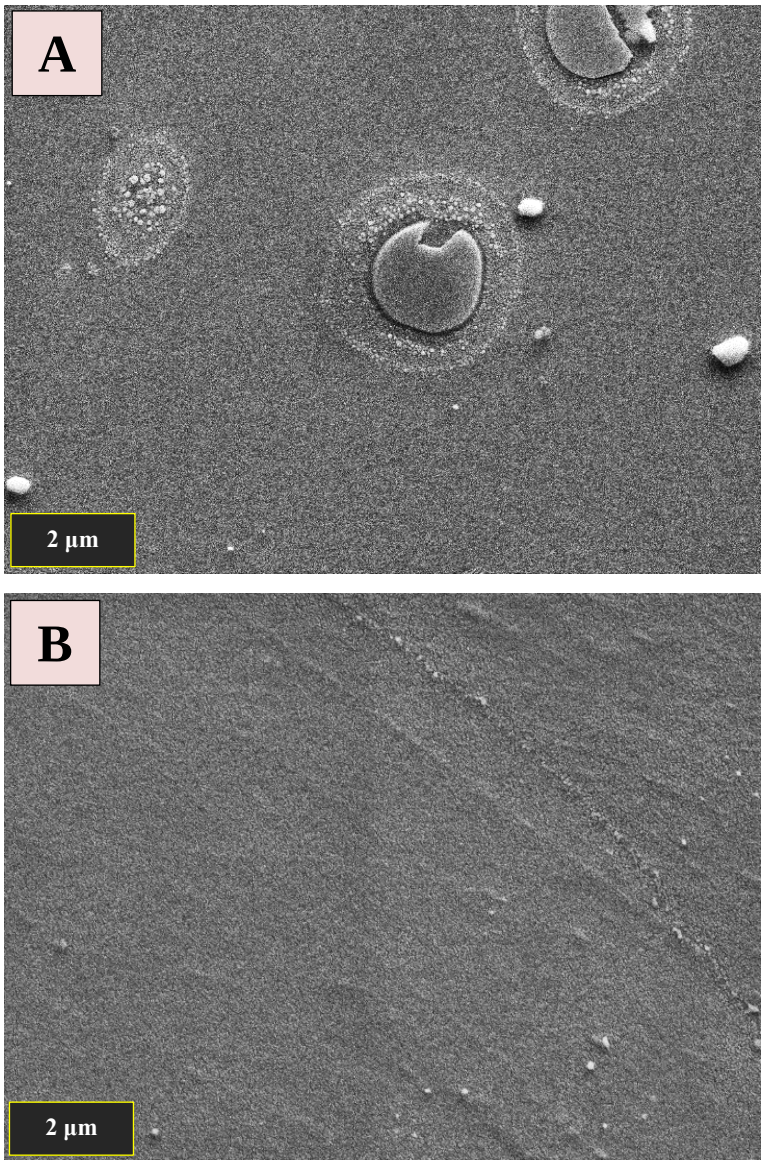

Figure 130 - SEM micrographs of both RR1000 variants heated to 1100°C at 25°Cs^{-1} A) FG variant. B) CG variant

Each specimen used in the super-solvus heat and quench only tests were also fully characterised. The results of this characterisation are summarised in the table below. Details of the changes experienced by each specimen are described in the following sections. The grain orientation and local misorientation of each specimen was measured but is not included in the table or the subsequent sections, as the random texture and low local misorientation of the parent material was retained in both RR1000 pedigrees throughout all tests. This was evident as all MUD values fell between 0.57-1.53 and all average KAM values between 0.25° to 0.35°.

Each section indicates the heating rate and peak temperature that each specimen was subject to. All heat and quench only tests were performed on FG 431 and CG variants, FG443 was not used in this area of the study. All microstructural measurements have been subject to an error analysis as described in section 3.11 Error analysis. The 95% confidence interval calculated for each measurement in the error analysis is given in brackets to illustrate the scatter in the average value calculated. A t-test has been conducted on all microstructural changes to judge their significance. If a change was found to be significant via the t-test method then the results are shown, stating the $t_{diff.}$ value calculated along with the $t_{crit.}$ value for the comparison. Significant changes have been highlighted and a 95% confidence interval given for the magnitude of the change if stated.

Test temperature	Variant	Grain Size (μm)	Primary γ' Vol.F. (%) / size (μm)	Secondary γ' Vol.F. (%) / size (nm)	Σ3 twin boundaries (%)	Hardness (Hv1)
Parent material	FG	6.4 (+/- 0.8)	10.2% / 1.71 (+/- 0.7% / 0.02)	33.4% / 137 (+/- 5.0% / 2)	22.1 (+/- 1.8)	423 (+/- 1)
	CG	48 (+/- 5.5)	N/A	31.9% / 147 (+/- 6.1% / 4)	46.2 (+/- 1.6)	410 (+/- 3)
1160°C	FG	14.8 (+/- 2.2)	N/A	N/A	31.7 (+/- 2.7)	392 (+/- 8)
	CG	45.9 (+/- 6.1)	N/A	N/A	42.6 (+/- 3.0)	397 (+/- 5)
1200°C	FG	13 (+/- 1.9)	N/A	N/A	25.4 (+/- 2.7)	373 (+/- 11)
	CG	35.9 (+/- 10.8)	N/A	N/A	34.6 (+/- 3.4)	393 (+/- 4)

Table 12 - Super-solvus "heat only" tests results summary (95% confidence intervals given in brackets).

4.1.4.1 RR1000 Liquation mechanisms

Sub-solidus liquation mechanisms have been discussed in detail in section 2.5. Each liquation mechanism has been taken into consideration for a potential cause of sub-solidus liquation during the rapid heating of both the FG and CG variants of RR1000. The following section gives a brief overview of the sub-solidus liquation mechanism that has been shown to occur in FG RR1000 during rapid heating to above its γ' solvus temperature, as reported by M. Attallah et al [4]. This is followed by a proposal of another sub-solidus liquation mechanism, which is most likely occurring in CG RR1000 during rapid heating to above its γ' solvus temperature. The occurrence of which, has not been reported in this alloy until the current study.

Fine grain – Constitutional liquation of primary γ'

Constitutional liquation of second phase particles was first proposed by J. Pepe and W. Savage, in 18Ni maraging steels, where the constitutional liquation of titanium sulphide particles was responsible for the creation of a liquid film at the grain boundaries[50]. Constitutional liquation of γ' precipitates was first reported by Ojo et al in Inconel 738 superalloy[63]. The mechanism in which constitutional liquation of γ' precipitates and the conditions needed for it to occur was discussed in detail in section 2.5.1. The main requirements for constitutional liquation of γ' to occur are summarised as:

1. Large γ' precipitates.
2. Rapid heating rates.
3. Heating to temperatures above the γ' equilibrium solvus temperature.

The particles susceptible to constitutional liquation in FG RR1000 are the primary γ' due to their large size. The heating rate experienced at the weld line during an inertia friction weld is more than sufficient to cause constitutional liquation of the primary γ' in FG RR1000. Furthermore, the heating rates in the TMAZ can be in the range of 25-50°Cs^{-1}, which can be replicated in the semi-solid testing facility. Primary γ' in FG RR1000 has been shown to persist to just below the γ' equilibrium solvus temperature of 1140°C when heated at 25°Cs^{-1}, therefore allowing it to constitutionally liquate on further heating via a eutectic type reaction with the surrounding γ matrix. Evidence of the occurrence of this mechanism in FG RR1000 has previously been reported by M. Attallah et al [4], when heating FG RR1000 specimens at 5°Cs^{-1} and 50°Cs^{-1} to above the γ' equilibrium solvus temperature. They provided evidence in the form of in situ

observations from the HT-CLSM tests as well as SEM micrographs illustrating the presence of dendritic γ-γ' eutectic structures within the liquated regions. Replicating the findings of this study with the novel semi-solid testing facility acted as a way of validating the testing facility and the testing method.

The present study has identified constitutional liquation of primary γ' in bulk FG RR1000 specimens, when heating to above the γ' equilibrium solvus temperature at heating rates between $5°Cs^{-1}$ and $25°Cs^{-1}$. This finding agrees with that of M. Attallah et al [4], and has therefore been used to validate the current novel semi-solid testing facility, fit for purpose.

<u>Coarse grain</u> – Insipient melting of the γ matrix

Incipient melting is the liquation of areas of material that have a high proportion of alloying elements in comparison to the bulk material. This can cause localised melting, due to the reduction in melting point, in these highly alloyed regions. Incipient melting in nickel superalloys is usually associated with the presence of low melting point phases at grain boundaries such as Ni_5Hf, although other intermetallics such as ZrS and NiZr are also susceptible to incipient melting [77]–[80].

During the present investigation sub-solidus liquation was identified both intergranularly and intragranularly in coarse grain RR1000. The liquation was evenly distributed throughout the specimens and was unlikely to be the result of low melting point phases.

The CG RR1000 material used in this study was created by applying a 2 hour solution heat treatment at 1170°C to as forged RR1000 material, followed by an aging heat treatment of 16 hours at 760°C. A study has been conducted by I.M.D. Parr et al [38] on the grain coarsening behaviour of RR1000 during super-solvus heat treating. Their work, investigating solution heat treatment hold times, reported that solution heat treatments of longer than 1 hour at 1170°C did not cause any significant variation in microstructure. This implies that RR1000 is most likely fully homogenised after a 1 hour solution heat treatment at 1170°C. The CG material used in the present research was subject to a solution heat treatment of 2 hours at 1170°C during its manufacture therefore, is almost certainly fully homogenised. Because of this, it is very unlikely that the incipient melting observed in CG RR1000 in this study was the result of pre-existing elemental inhomogeneity.

Instead, another incipient melting mechanism was proposed. The proposed mechanism was based on the possibility of incipient melting of the γ matrix in nickel superalloys reported by F. Tancret [5], which was discussed previously. The mass diffusion of γ' forming elements into the γ matrix during the dissolution of γ', when CG RR1000 is heated to temperatures above the γ' solvus temperature, could create enough chemical inhomogeneity in localised areas to cause a momentary drop in melting point, leading to localised melting. This mechanism would explain why such an evenly spread liquation pattern was exhibited by the CG specimens, as will be shown in the subsequent sections. The fact that the main γ' constituents Al and Ti are melting point depressants, further supports this mechanism[5], [63]. The slow diffusivity of Ti

through the γ matrix would also compound this effect by increasing the time needed for the Ti from the γ' to homogenise throughout the γ matrix. EDS analysis of liquated CG RR1000 specimens in this study supported this proposal and is shown in section 4.1.4.3, later. The occurrence of this mechanism in RR1000 has not been reported until the present study.

4.1.4.2 Resultant microstructure after 25°Cs^{-1} to 1160°C heat exposure

Fine grain

As expected, sustaining a rapid heating rate of 25°Cs^{-1} through the γ' solvus temperature to a peak temperature of 1160°C, resulted in the constitutional liquation of the surviving γ' precipitates at the grain boundaries. The presence of eutectic structures at the grain boundaries are evidence of this, as they are formed when two solidifying liquid fronts meet, and the solute rich liquid cools to a temperature where eutectics are favourable. The intergranular liquated regions can be seen in Figure 131. A higher magnification micrograph of the lamella γ-γ' eutectic structures, found at the grain boundaries, is shown in Figure 131 B. This result and the eutectic structures found were in alignment with the findings of M. Attallah et al [4] and therefore the novel semi-solid testing facility was deemed fit for purpose.

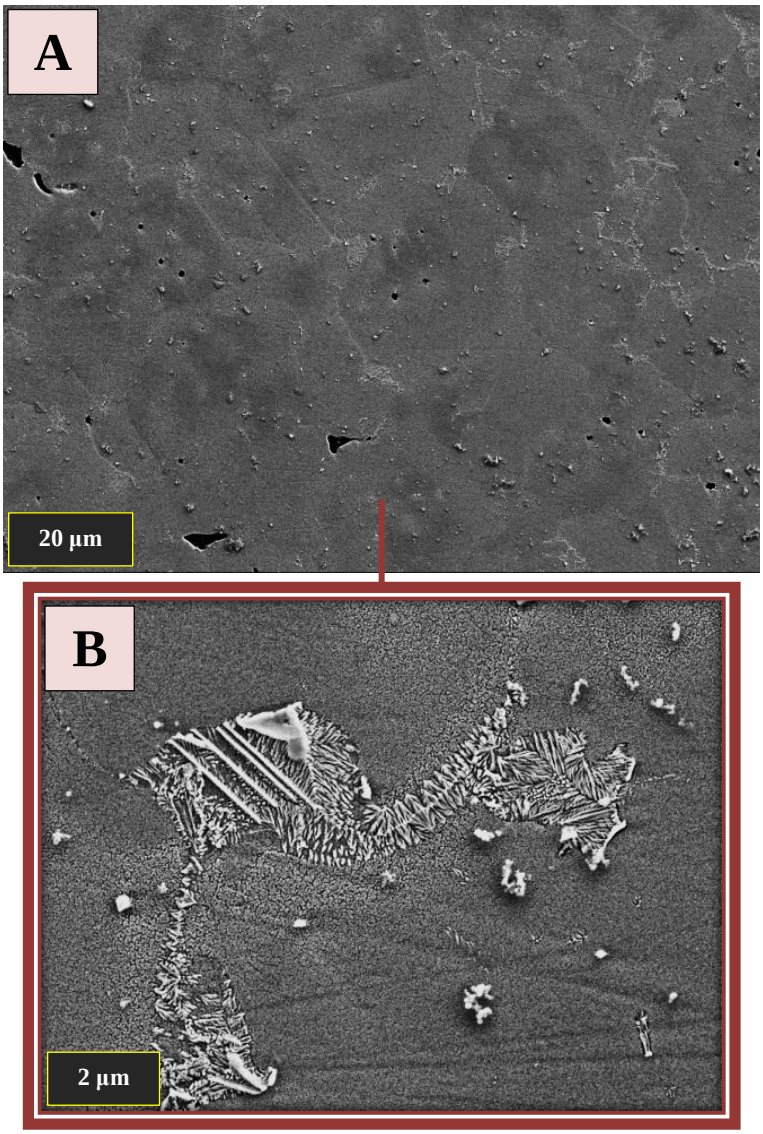

Figure 131 - SEM micrographs of a FG specimen heated to 1160°C at 25°Cs^{-1}. A) Multiple grains. B) Higher magnification image of the eutectic features.

Electro-etching the specimen via the procedure detailed in section 3.2.2, distinguished the liquated material from the surviving γ grains by differentially etching the liquated material as blue and white globular structures. An optical micrograph of this specimen is shown in Figure 132, where the intergranular liquated material can be clearly seen. The fraction of liquid for this specimen was quantified using the method described in section 3.2.3.1.3 via optical microscopy. The estimated fraction of liquid for this specimen was calculated to be 22.6% (+/- 2.0%).

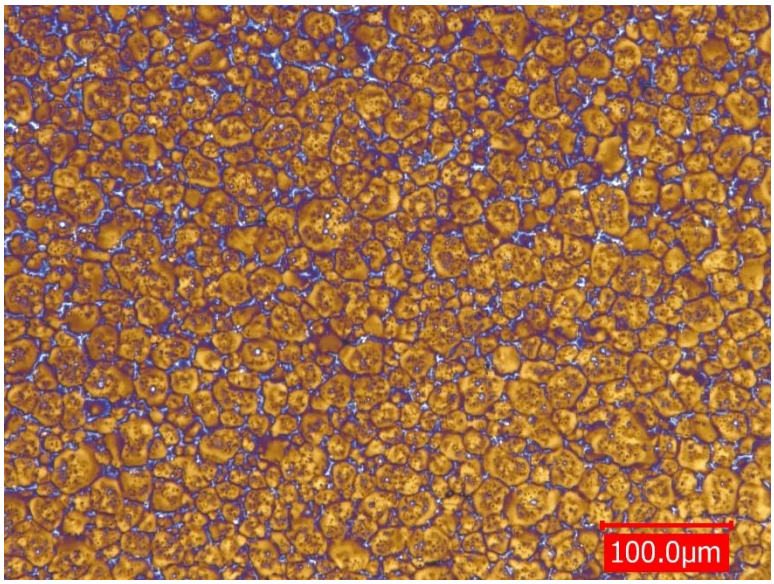

Figure 132 - Optical micrograph of a FG specimen heated to 1160°C at 25°Cs^{-1}.

At this temperature all the primary γ' are now either diffused into the γ matrix or have liquated, therefore further grain growth would be expected. Conversely, the grain size recorded for this specimen was 14.8µm (+/- 2.2), meaning no significant change in grain size had occurred compared to the FG specimen heated to 1100°C (14.2µm +/- 2.0) which had some primary γ' still pinning its grain boundaries. The lack of grain growth is caused by grain boundary pinning due to the presence of intergranular liquid films which have propagated from the constitutionally liquated primary γ'. This phenomenon has been reported in other alloy systems such as 18Ni maraging steel [50]. The EBSD map in Figure 133, illustrates the grain structure of this specimen. Interestingly, at this temperature the number of Σ3 twin grain boundaries has decreased to 31.7% (+/- 2.7%) of total boundaries measured, a difference of -5.4% (+/- 4.1%, $t_{diff.}$ 5.628 > $t_{crit.}$ 4.303) from the 37.1% (+/- 3.2%) measured in the FG specimen heated to 1100°C.

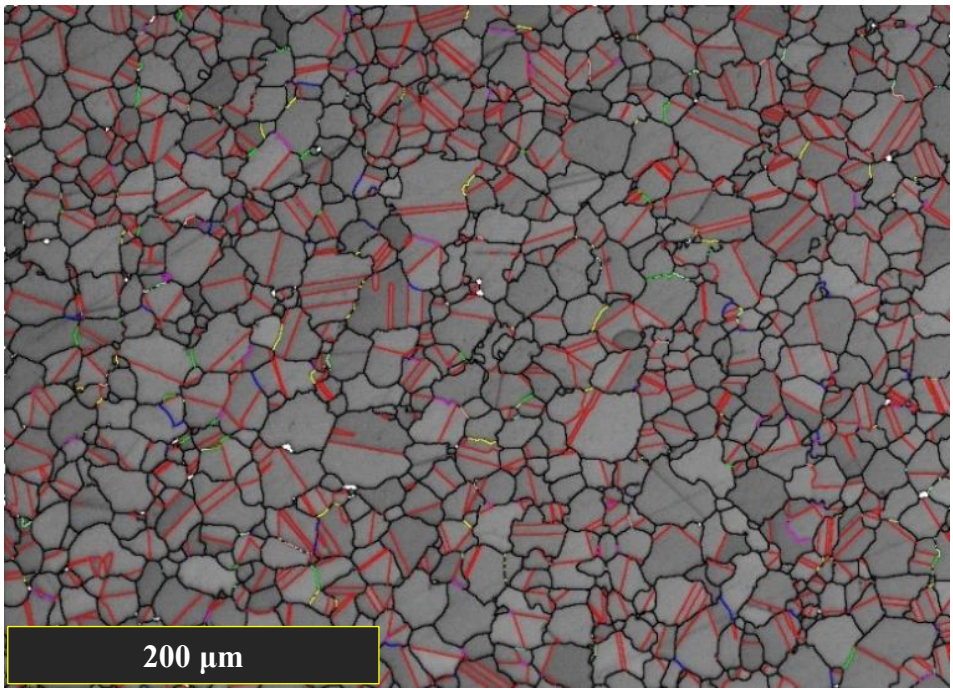

Figure 133 - EBSD map of a FG specimen heated to 1160°C at 25°Cs^{-1}. Critical grain boundaries are marked in black with twin boundaries marked in red.

Despite the presence of re-solidified material at the grain boundaries, the average hardness was unaffected with an average hardness value for this specimen being measured at 392 Hv (+/- 8). This represents no change over the FG specimen tested at 1100°C (395 Hv +/- 5), which displayed a similar microstructure of fine re-precipitated tertiary γ' throughout the γ matrix but without the presence of liquation products.

Coarse grain

Increasing the peak temperature exposure from 1100 °C to 1160°C had very little effect on the microstructure of the CG variant. At 1160°C, the CG variant exhibited much less liquation than the FG variant, with only a small amount of liquation occurring at the grain boundaries. This was due to the lack of primary γ' for constitutional liquation to occur. The small areas of liquated material were identified and quantified via optical microscopy. An example optical micrograph of this specimen is shown in Figure 134. The fraction of liquid measurement for this specimen was approximately 1.8% (+/- 0.4%).

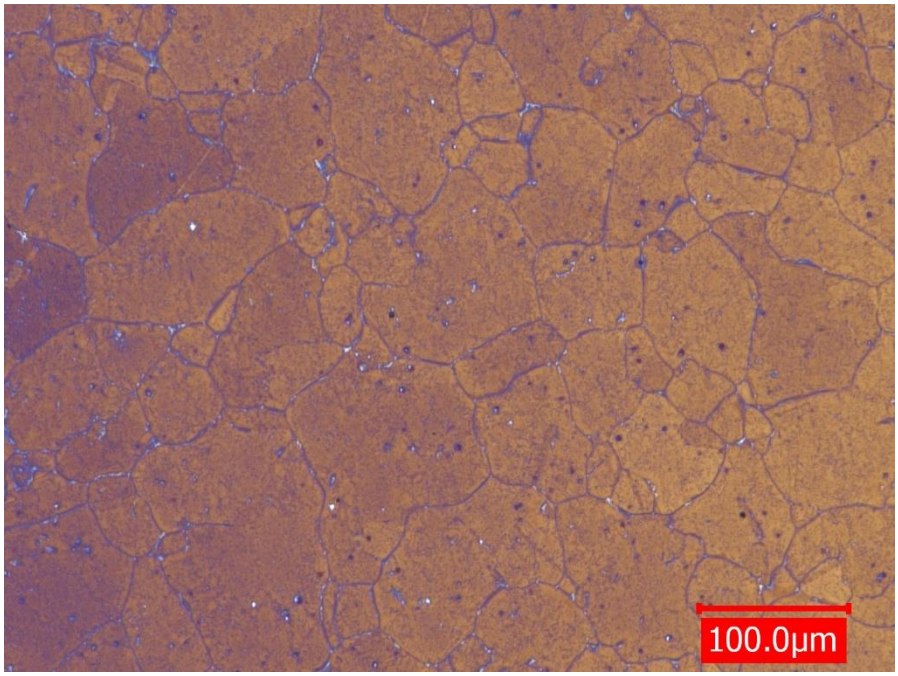

Figure 134 - Optical micrograph of a CG specimen heated to 1160°C at 25°Cs^{-1}.

The liquated regions on the grain boundaries were inspected via SEM to confirm liquation with the presence of eutectic features. The intragranular eutectic features found were much smaller due to the lack of liquated material at this temperature and are illustrated in Figure 135. As there was very little liquation at this temperature, it was assumed that the critical temperature for mass liquation via the proposed incipient melting of γ mechanism must be higher than 1160°C.

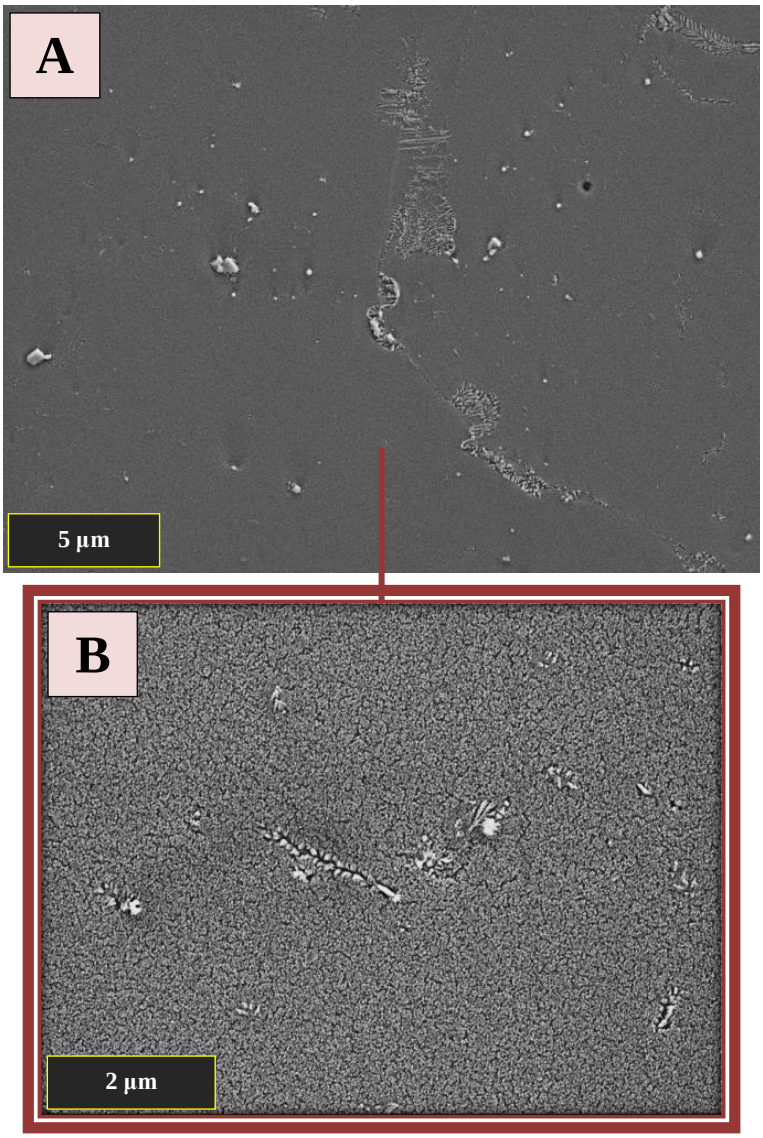

Figure 135 - SEM micrographs of a CG specimen heated to 1160°C at 25°Cs^{-1}. A) Larger eutectic feature. B) Smaller eutectic features.

With such little liquated material, the grain size was unchanged and measured at an average size of 45.9µm (+/- 6.1). The grain boundary characteristics were again analysed, revealing that the percentage of grain boundaries measured registering as Σ3 twin boundaries had experienced no significant change at 42.6% (+/- 3.0%). The EBSD map in Figure 136 illustrates an example of the grain structure found in this specimen.

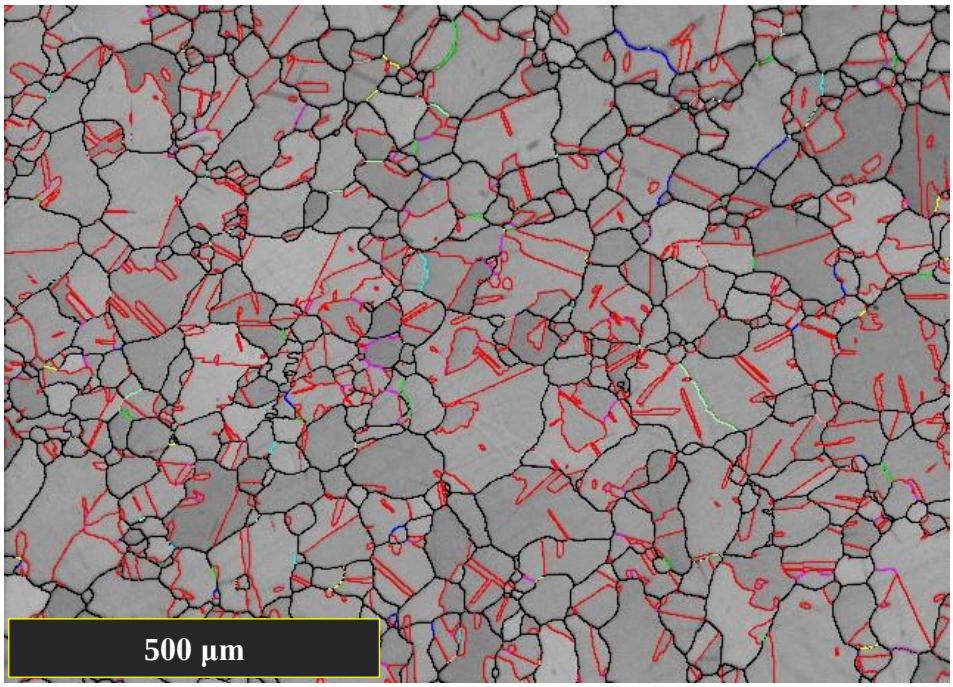

Figure 136 - EBSD map of a CG specimen heated to 1160°C at 25°Cs^{-1}. Critical grain boundaries are marked in black with twin boundaries marked in red.

As this specimen had a very similar microstructure to the previous CG specimen tested at 1100°C, it exhibited a comparable average hardness value of 397 Hv (+/- 5).

4.1.4.3 Resultant microstructure after 25°Cs^{-1} to 1200°C heat exposure

Fine grain

Increasing the peak temperature exposure to 1200°C had a significant effect on the amount of liquation produced in the FG variant. The bulk of the liquation was still located at the grain boundaries but now it was accompanied by some intragranular liquation caused by the incipient melting mechanism. This implies that the critical temperature for the incipient melting mechanism is between 1160°C and 1200°C. Figure 137 shows the microstructure of this specimen. The average liquid fraction was calculated to be approximately 31.8% (+/- 3.9%), an increase of 9.2% (+/- 4.4%, $t_{diff.}$ 4.539 > $t_{crit.}$ 2.179) over the FG specimen heated to 1160°C (22.6% +/- 2.0%).

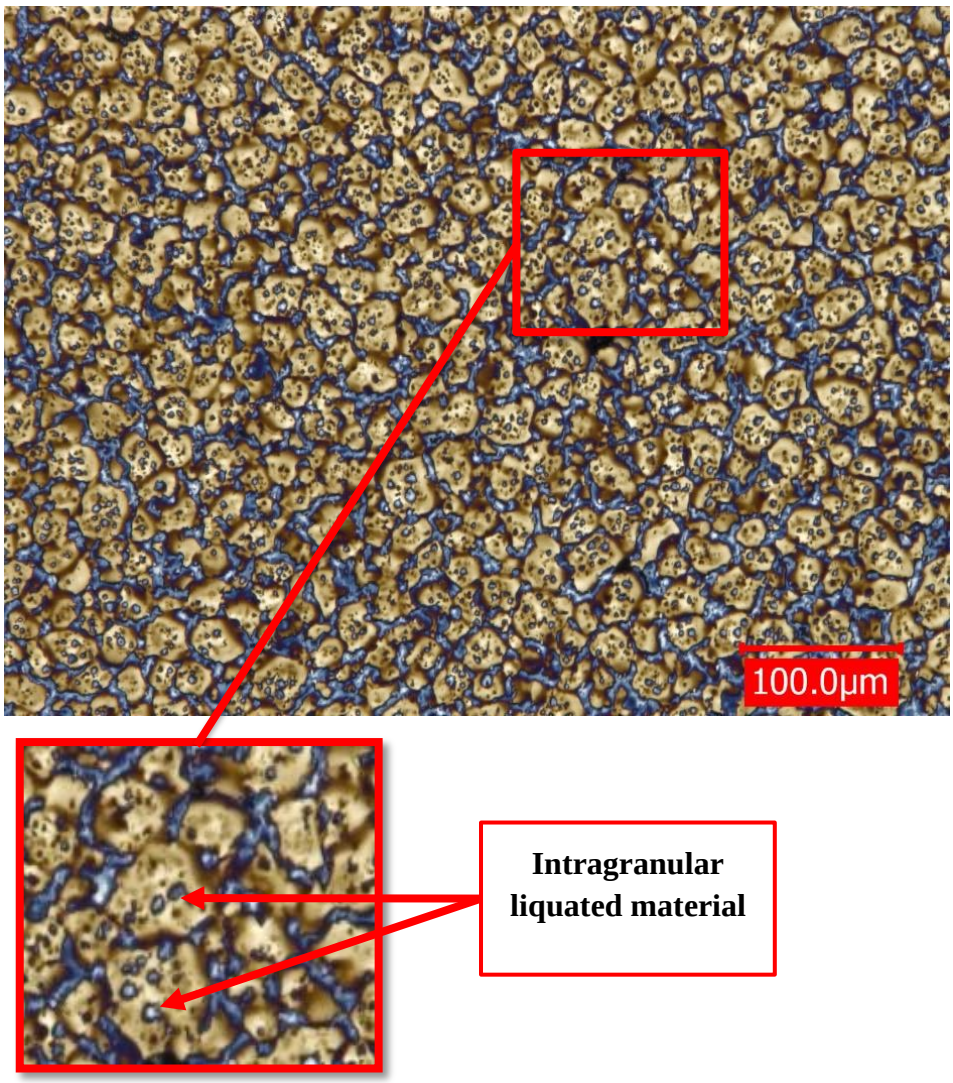

Figure 137 - Optical micrograph of a FG specimen heated to 1200°C at 25°Cs^{-1}.

Inspection of this specimen via SEM, revealed intergranular eutectic features as expected. Some intragranular eutectics were also found due to the pockets of liquation caused by the incipient melting. These eutectic features are illustrated in Figure 138.

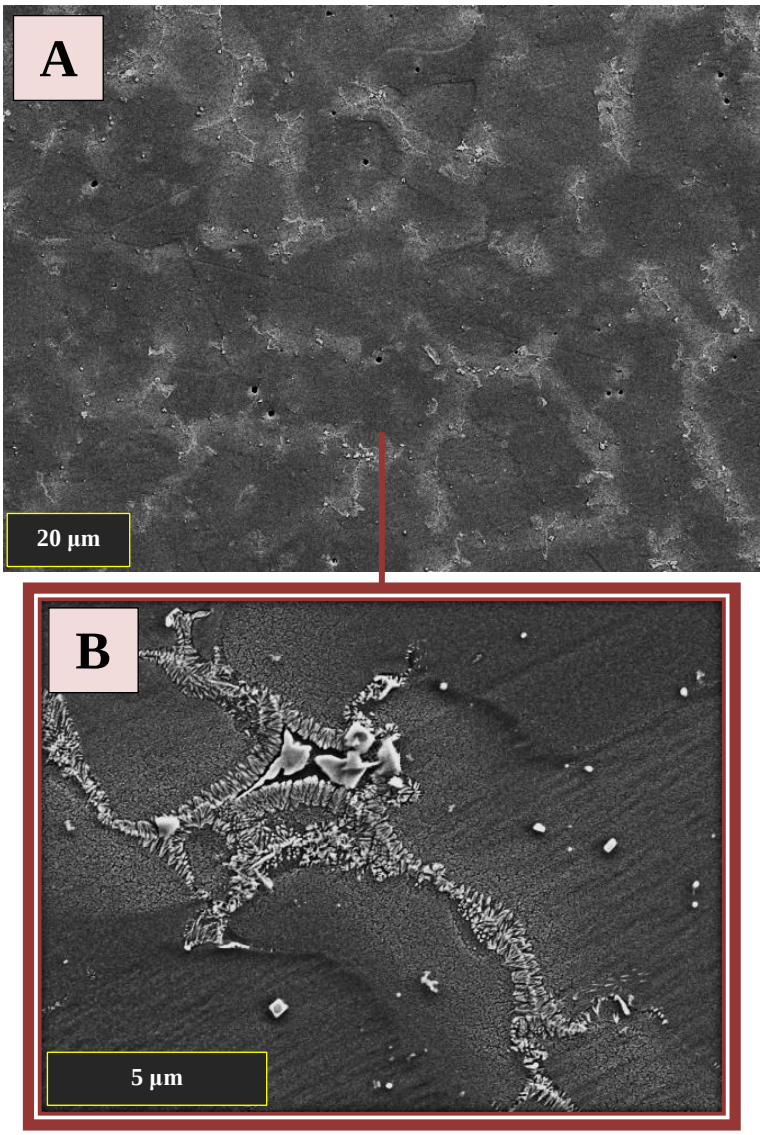

Figure 138 - SEM micrographs of a FG specimen heated to 1200°C at 25°Cs^{-1}. A) Multiple grains. B) Solidification feature at a grain boundary.

The presence of the intergranular liquid film again provided grain boundary pinning at this temperature, halting grain growth, as the average grain size was measured at 13.0µm (+/- 1.9). As a result, the grain size in this specimen experienced no significant change when compared to the FG specimens heated to 1100°C (14.2 µm +/- 2.0) and 1160°C (14.8µm +/- 2.2).

Grain boundary analysis found the average percentage of Σ3 twin grain boundaries in this specimen to be 25.4% (+/- 2.7%). A reduction of 6.3% (+/- 3.8%, $t_{diff.}$ 7.181 > $t_{crit.}$ 4.303) from the previous FG specimen tested at 1160°C (31.7% +/- 2.7%). Figure 139 illustrates an example of the grain structure found in this specimen.

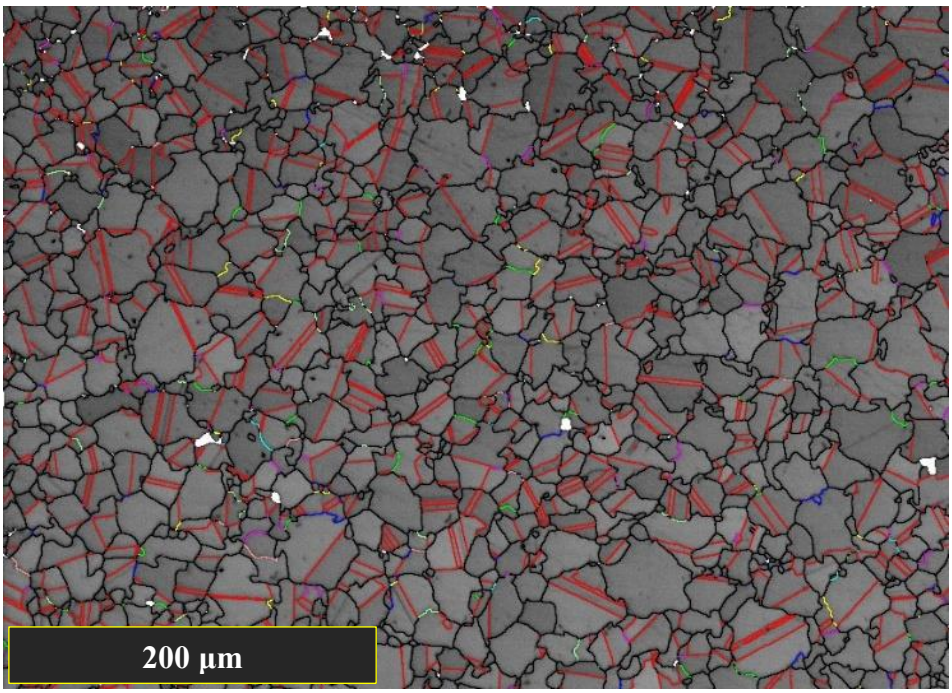

Figure 139 - EBSD map of a FG specimen heated to 1200°C at 25°C^{-1}. Critical grain boundaries are marked in black with twin boundaries marked in red.

The average hardness exhibited by this specimen was 373 Hv (+/- 11), a reduction of 19 Hv (+/- 14, $t_{diff.}$ 2.840 > $t_{crit.}$ 2.064) compared to the previous FG specimen tested at 1160°C (392 Hv +/- 7.8). It must be noted that the two average hardness measurements used in this t-test comparison were two of the FG specimens that exhibited hardness distributions with elevated kurtosis values therefore, this significant difference could be a false positive. However, evaluation of the microstructure found evidence to support the fact this drop in average hardness was in fact significant. This reduction in hardness was thought to be due to the specimen's susceptibility to quench cracking along the interface between re-solidified intergranular material and the surviving γ grains, as shown in Figure 140.

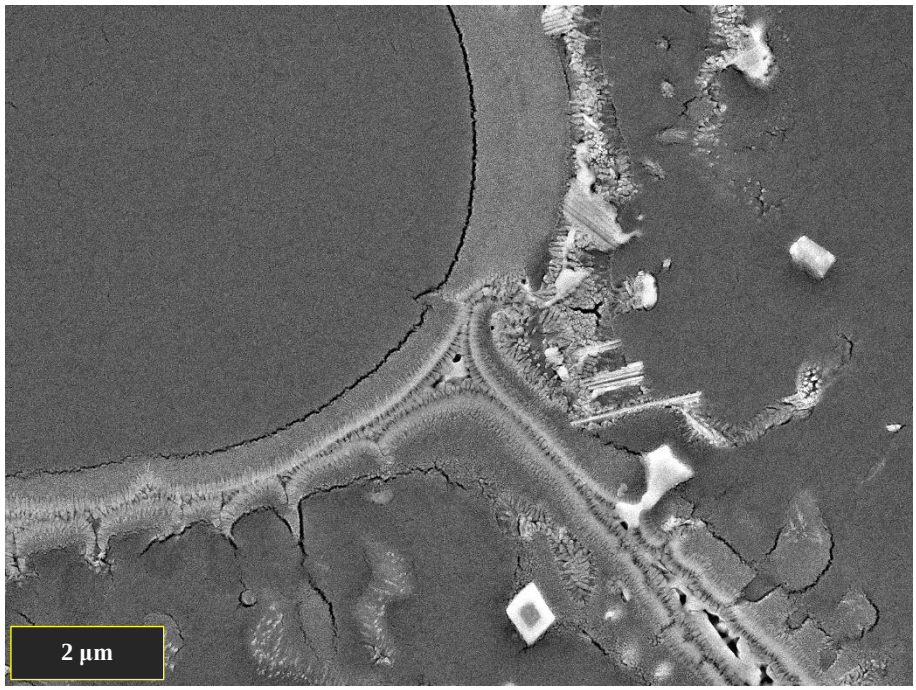

Figure 140 - SEM micrograph illustrating the cracking along the solid-re-solidified interface caused by water quenching.

This cracking is caused by the rapid re-precipitation of γ' in the re-solidified solute rich liquated regions which causes large shrinkage stresses[131]. In some cases, these liquation cracks would link up and propagate from the surface of the specimen into the centre. Hardness indents interacting with a quench crack exhibited a lower hardness value to the uncracked area.

Coarse grain

Significant liquation of the CG variant was only achieved when the peak temperature exposure was raised to 1200°C. This suggested that the CG variant was more resistant to temperature than the FG variant due to its lack of primary γ' and their constitutional liquation mechanism. This is likely to be a contributing factor to the difference in observed upset rate between the two variants during IFW. Inspection of the specimen via optical microscopy revealed that widespread intergranular and intragranular liquation had occurred as can be seen in Figure 141. The average fraction of liquid for this specimen was calculated at 37.3% (+/- 2.3%), a dramatic increase of 35.5% (+/- 2.3%, $t_{diff.}$ 33.821 > $t_{crit.}$ 2.179) over the liquid produced in the CG specimen heated to 1160°C (1.8% +/- 0.4%).

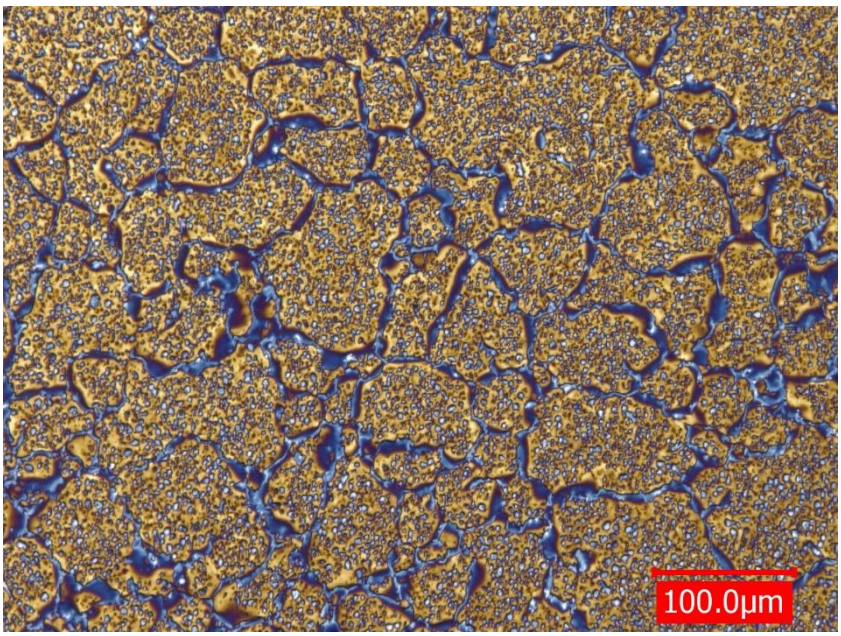

Figure 141 - Optical micrograph of a CG specimen heated to 1200°C at 25°Cs^{-1}.

The eutectic features, produced by the re-solidification of the liquated material, were found in abundance at the grain boundaries and in the pockets of liquation within the grains as shown in Figure 142, with Figure 142 B illustrating the eutectic features formed within the grains.

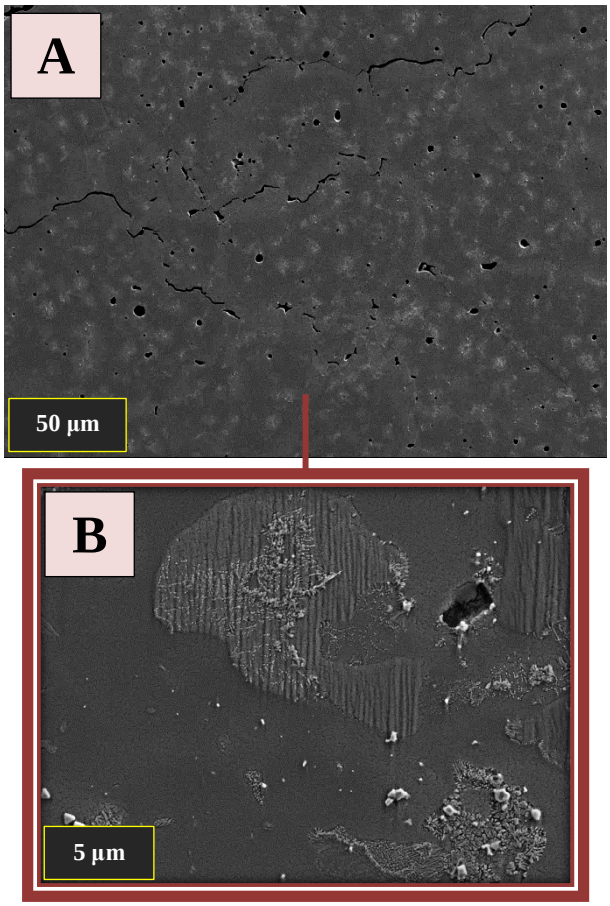

Figure 142 - - SEM micrographs of a FG specimen heated to 1200°C at 25°Cs^{-1}. A) Multiple grains. B) Liquation pockets within the grains.

EDS analysis of the intergranular liquid film and the intragranular pockets of liquation was conducted to assess their chemical composition. The three positions at which EDS analysis was conducted, are marked out in Figure 143 with the elemental composition of each location given in wt.% in Table 13.

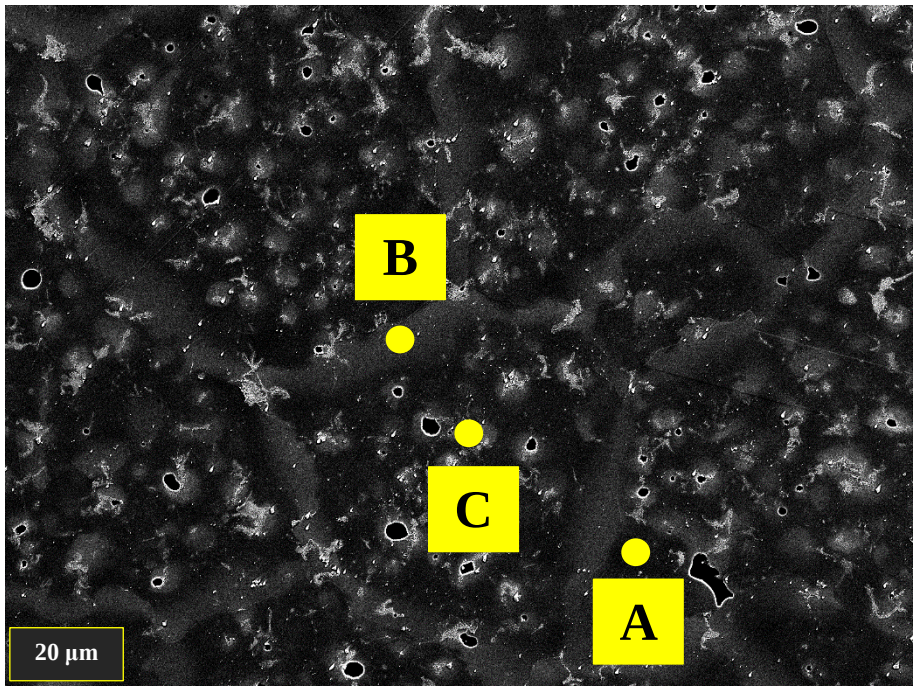

Figure 143 - SEM micrograph illustrating the position of the EDS analysis conducted on a liquated CG specimen.

	Al	Ti	Cr	Co	Ni	Zr	Mo	Hf	Ta
A) Surviving grain	2.96	3.49	9.07	20.14	57.09	0.33	4.81	0	2.1
B) Liquated grain boundary	3.16	4.28	8.68	18.86	57.37	0.15	4.78	0.06	2.65
C) liquid pocket inside surviving grain	3.08	5.58	5.5	16.97	60.22	0.23	3.84	1.51	3.07

Table 13 - Elemental composition of each site of the liquated CG specimen inspected via EDS in wt.%

The EDS analysis revealed that both the liquated areas at the grain boundaries and the intragranular pockets of liquation, contained elevated levels of γ' forming elements, especially Ti. This further supports the notion that the insipient melting, during the rapid heating of CG RR1000, is caused by the slow diffusivity of the γ' forming elements through the γ matrix, leading to localised regions with lower melting point compositions. This was in alignment with the chemical inhomogeneity required for the incipient melting of the γ matrix mechanism, that was reported to be possible in nickel superalloys by F. Tancret [5]. It is believed that the present research is the first study to provide evidence suggesting the occurrence of this mechanism in RR1000.

Heating the CG variant to 1200°C produced no meaningful change in grain size despite producing a substantial amount of liquation. The measured grain size for this specimen was 35.9µm (+/- 10.8). Although this appears to be a drop in average grain size compared to the other CG specimens initially, the large 95% confidence interval meant that this reduction could not be deemed statistically significant via a t-test. The percentage of Σ3 twin boundaries also decreased to 34.6% (+/- 3.4%), a decrease of 8.0% (+/- 4.5%, $t_{diff.}$ 7.703 > $t_{crit.}$ 4.303) from the CG specimen tested at 1160°C (42.6% +/- 3.0%). This decrease could be partly due to fact the intergranular liquated material did not solidify to form smooth grain boundaries. Instead, very serrated grain boundaries were formed as the re-solidifying material fronts grew towards each other, thus increasing their length. These serrated grain boundaries can be seen in the EBSD map in Figure 144. The increased length of the serrated grain boundaries would have reduced the percentage of boundaries recorded as Σ3 twin boundaries.

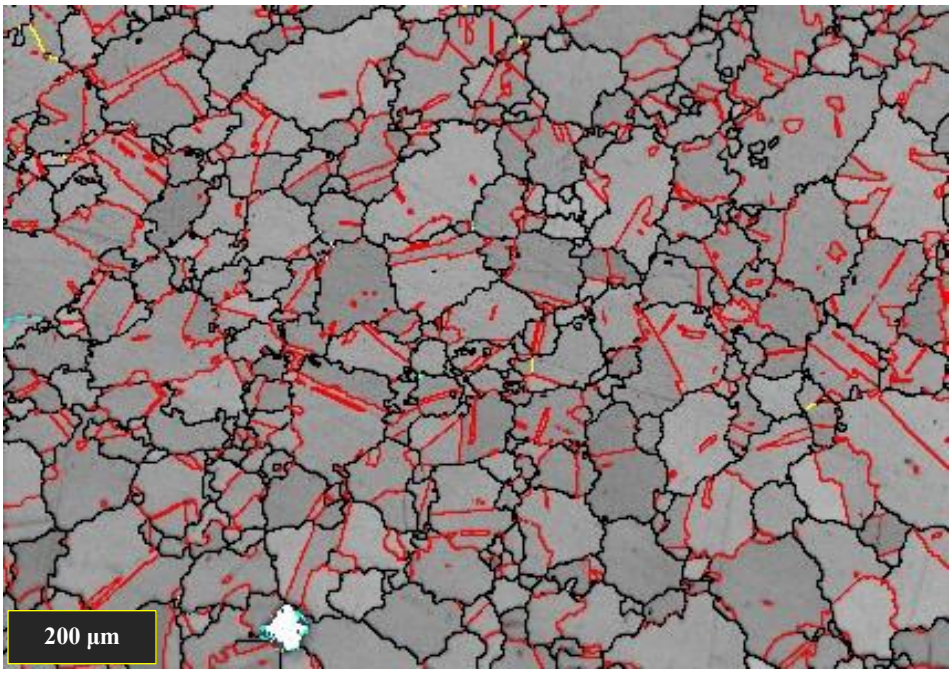

Figure 144 - EBSD map of a CG specimen heated to 1200°C at 25°C^{-1}. Critical grain boundaries are marked in black with twin boundaries marked in red.

The liquated CG specimen also had the tendency to form intergranular cracks on quenching. Despite this, there was no significant change in average hardness value recorded for this specimen at 393 Hv (+/- 4), when compared to the specimen heated to 1160°C (397 Hv +/- 5), which featured very little liquation and no quench cracks. The average hardness of the CG variant was thought to be less affected by the presence of intergranular quench cracks than the FG variant, simply because of the reduced number of grain boundaries for the cracks to propagate along, therefore there was less probability of a hardness measurement being taken in the vicinity of a crack.

4.1.4.4 Validation of liquid characterisation method

Now that liquation in both variants of RR1000 had been achieved, a validation was needed to confirm that the blue and white globular structures in the optical micrographs did indeed correspond to liquated material, by confirming the presence of eutectic features in these areas.

To do this, the fine grain specimen heated to 1200°C at 25°Cs^{-1} was metallographically re-prepped and electro-etched after the hardness measurements had been taken. The indents were used to locate exact liquated regions, so that images could be taken both optically and via SEM for comparison. Figure 145 shows the optical and SEM micrographs taken of this specimen at the same hardness indent. A pore in the material, next to the hardness indent, was also used as an alignment reference point. The area marked by the oval in the images highlights the region next to the pore showing that the eutectic features in the SEM micrograph align with the blue and white globular structures that represent the liquated material in the optical micrograph.

Figure 145 C is another optical micrograph taken in the same region but this time imaged under polarised light. The polarised light enhances the brightness of the eutectic features within the re-solidified liquated material, again confirming their location in the blue and white globular structures.

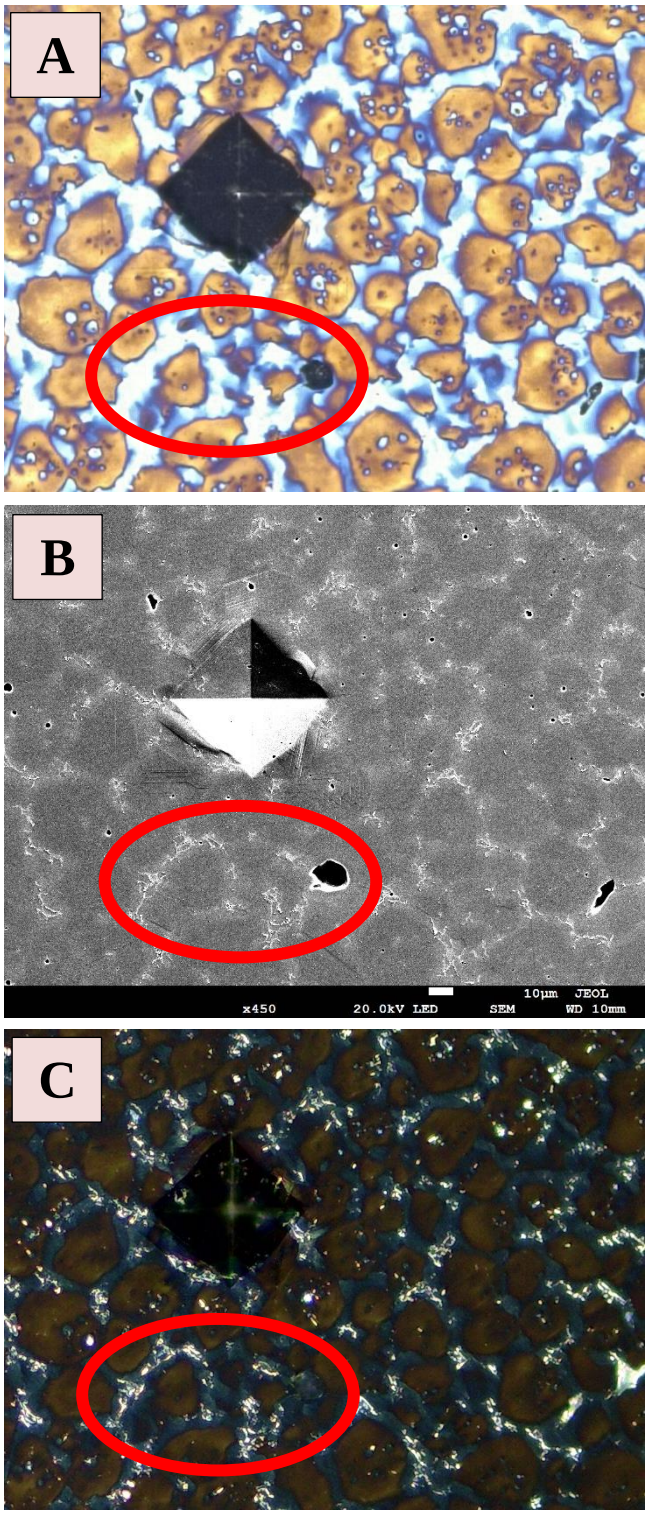

Figure 145 - Micrographs used to clarify that the blue and white globular structures in optical microscopy referred to liquated material. A) optical micrograph. B) SEM micrograph. C) Polarised light optical micrograph.

EDS analysis was also conducted on the liquated regions, to assess their composition. It was expected that as the intergranular liquid had originated from constitutionally liquated primary γ', that they would have compositional similarities. The EDS analysis was conducted in the same region highlighted by the oval in Figure 145. The positions the EDS analysis was conducted at are marked out in Figure 146.

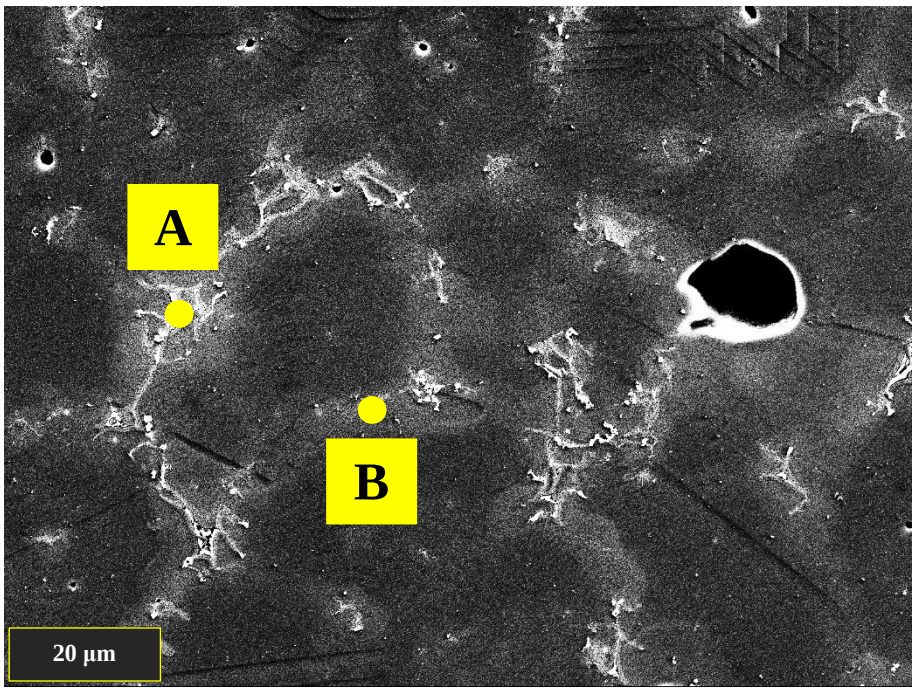

Figure 146 - SEM micrograph illustrating the position of the EDS analysis conducted on a liquated FG specimen.

	Al	Ti	Cr	Co	Ni	Zr	Mo	Hf	Ta
Reference γ matrix composition	2.47	2.74	17.89	21.02	47.89	0.1	5.89	0	2.01
Reference Primary γ' composition	4.82	7.33	5.44	12.64	61.85	0	1.53	1.4	4.99
Liquated grain boundary (A)	1.92	4.36	12.98	16.58	42.93	1.88	5.66	10.54	3.16
Liquated grain boundary (B)	3.15	4.81	14.35	17.38	51.53	0.08	5.12	0.43	3.14

Table 14 - Elemental composition of each site of the liquated FG specimen inspected via EDS in wt.%

Table 14 shows the results of the EDS chemical analysis. The intergranular liquid films have a similar composition to the parent γ matrix but contain elevated levels of the γ' forming elements Ti, Al and Hf. This would be expected as constitutional liquation of the primary γ' happens via a eutectic type reaction at the γ- γ' interface, resulting in a liquid comprised of a mix of elements from the two phases. This intermediate composition was in alignment with the findings of A.P.I. Popoolaa et al [86] during their research on the effects of rapid heating on astroloy, where they witnessed constitutional liquation of primary γ' precipitates when heating specimens at $20°Cs^{-1}$.

4.1.5 Microstructural evolution to 1200°C at 25°Cs^{-1}

Both the FG and CG variant experience dramatic microstructural changes when heated rapidly to above the γ' solvus temperature. These microstructural changes and the resultant effect on the hardness are summarised in Figure 147 to Figure 150. Each plot has the relevant parent microstructure value starred on the Y axis for reference.

γ' evolution.

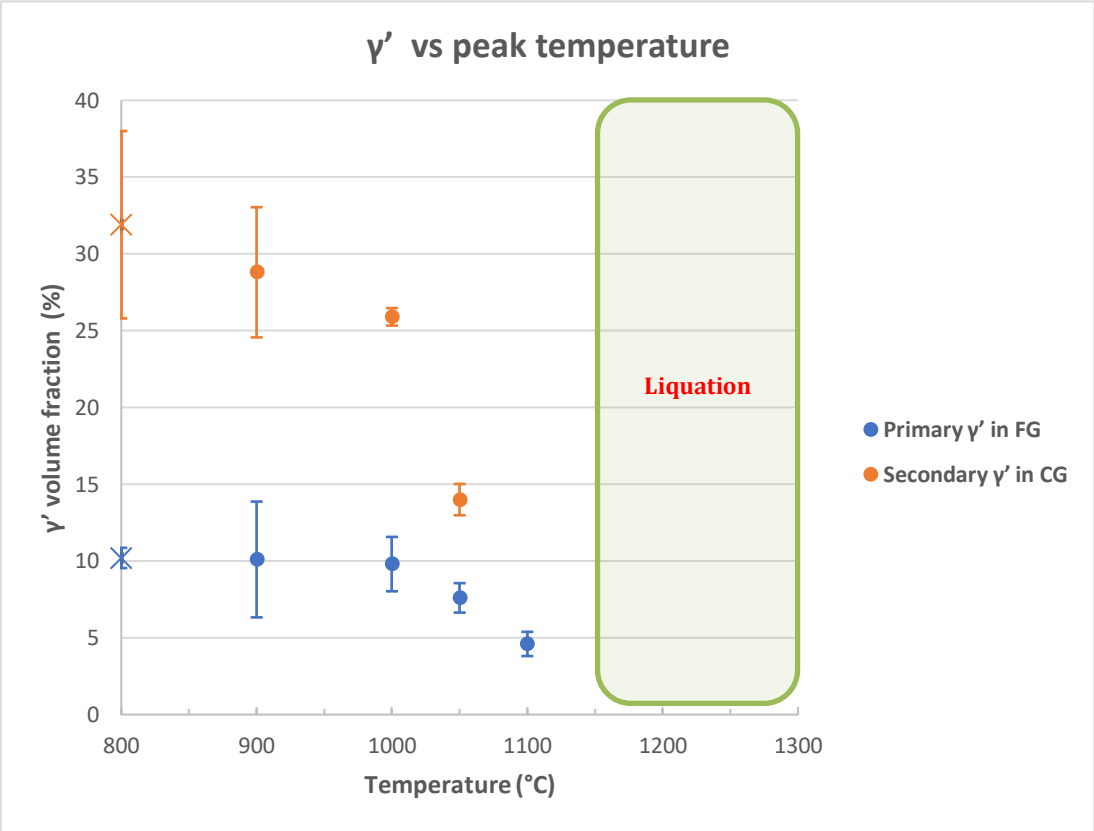

Figure 147 - Plot of γ' volume fraction vs peak temperature exposure for FG & CG specimens heated at 25°Cs^{-1} (Error bars indicate 95% confidence intervals).

Figure 147 illustrates the change in volume fraction of primary γ' in the FG variant and volume fraction of secondary γ', in the CG variant when heating at 25°Cs^{-1} to 1200°C. The primary γ' in the FG variant experienced no significant changes in volume fraction up to 1000°C, undergoing only slight spheroidization. The secondary γ' in the CG variant also behaved similarly, showing no statistically significant change in volume fraction to this temperature, although displaying more severe spheroidization. The FG variant was shown to lose its tertiary γ' by diffusion into the γ matrix at 900°C, whereas the CG variant retained its tertiary to a higher temperature, losing them at 1000°C instead.

Significant changes were experienced by both the primary γ' in FG and the secondary γ' in CG when the temperature was increased from 1000°C, both exhibited a decrease in volume fraction from this point, with the secondary γ' in the CG undergoing a sharper reduction rate due to their smaller initial size. On reaching 1160°C the FG variant exhibited widespread intergranular liquation caused by constitutional liquation of the surviving primary γ'. The CG variant exhibited very small pockets of intergranular liquation at this temperature with the onset of incipient melting. At 1200°C liquation was prevalent in both RR1000 variants. The FG variant now exhibited both intergranular liquid from constitutional liquation as well as intragranular liquation from incipient melting of the γ matrix. The CG variant featured extensive liquation at both the grain boundaries and within the grains, as a result of the incipient melting mechanism proposed for CG RR1000 in this study. The presence of significant amounts of intragranular incipient melting of the γ matrix in both variants at 1200°C, suggests that the critical temperature for mass liquation via this mechanism in RR1000 lies between 1160°C and 1200°C.

Grain size

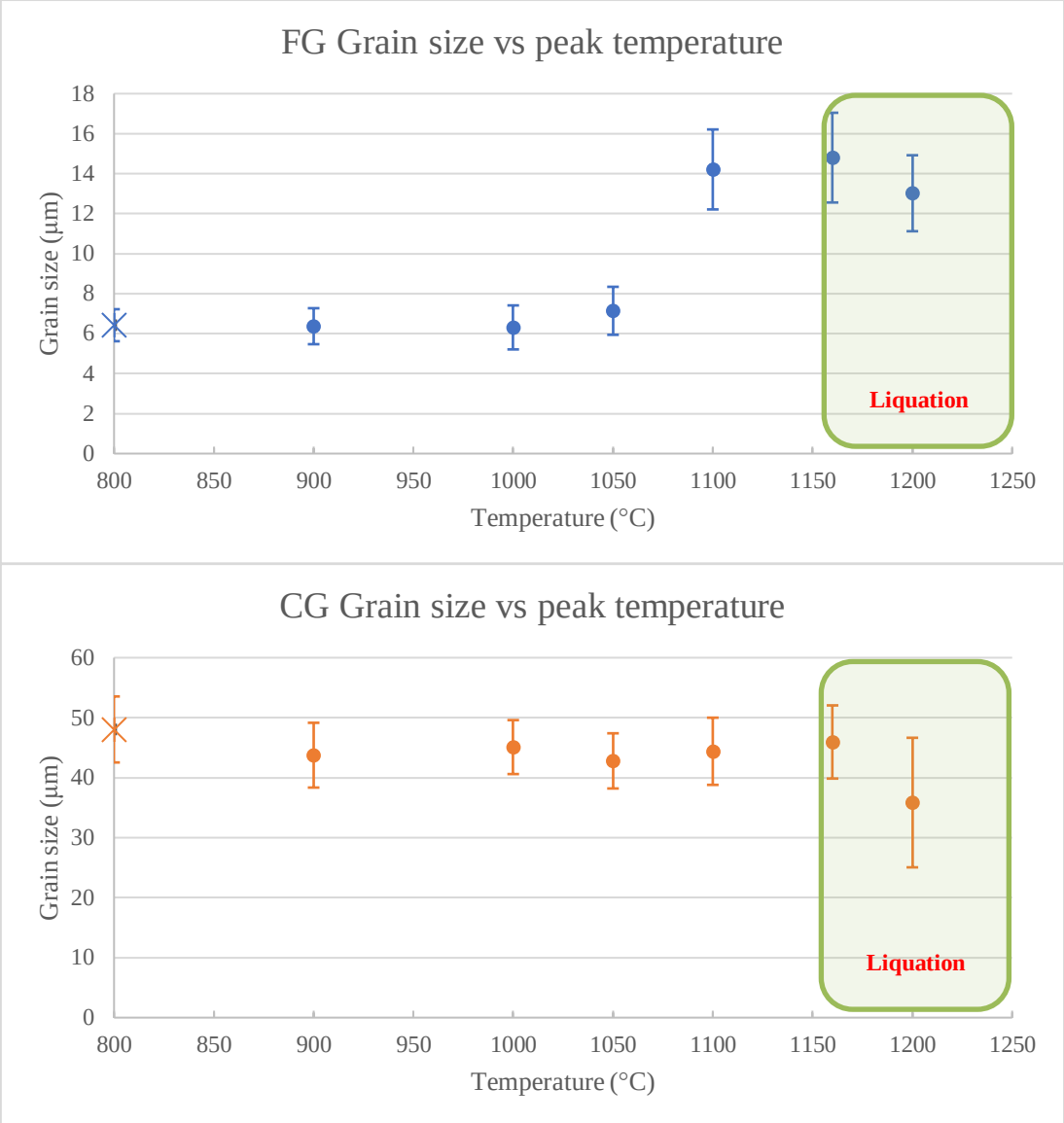

Figure 148 - Plot of grain size vs peak temperature exposure for FG & CG specimens heated at 25°Cs^{-1} (Error bars indicate 95% confidence intervals).

The evolution of grain size with peak temperature exposure when heating at 25°Cs^{-1} is illustrated in Figure 148. The FG variant initially experiences some grain growth on heating to temperatures over 1050°C. This growth can be associated with the loss of some primary γ' via diffusion into the γ matrix, reducing the grain boundary pinning effect they provide. The CG does not display any grain growth, even when all the secondary γ' has diffused into the γ matrix at 1100°C. The CG variant does not have the same driving force for grain growth as the FG because it has already coarsened to a stable grain size during the solution heat treatment its subject to in its manufacture. The grain size in both variants then remained stable up to 1200°C, showing no changes

that could be deemed significant via t-testing. The lack of continued grain growth in the FG was because of grain boundary pinning due to the presence of intergranular liquid films, which had propagated from the constitutionally liquated primary γ'. This phenomenon has been reported in other alloy systems such as 18Ni maraging steel by J. Pepe and W. Savage [50].

Σ3 twin grain boundaries

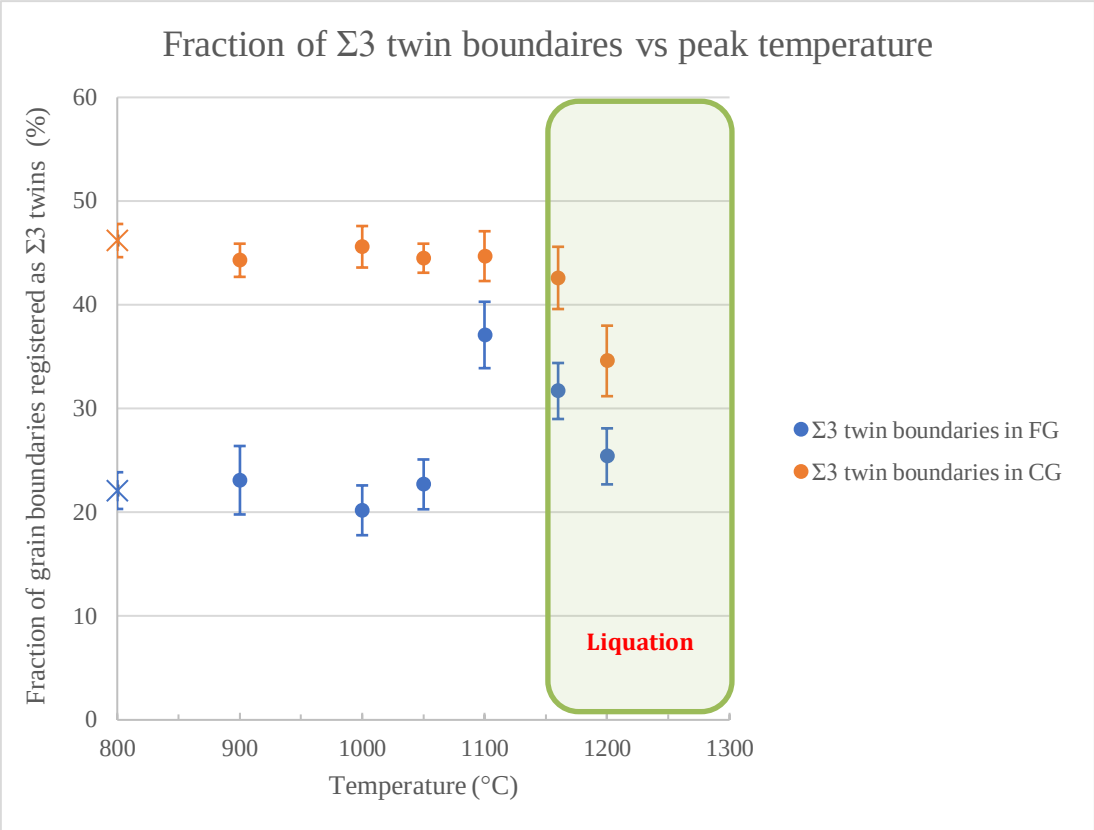

Figure 149 - Plot of the fraction of grain boundaries measured as Σ3 twin boundaries vs peak temperature exposure for FG & CG specimens heated at 25°Cs^{-1} (Error bars indicate 95% confidence intervals).

The Σ3 twin boundaries behaviour in response to the rapid heating was slightly different in each variant initially, but followed the same trend at higher temperatures, see Figure 149. The fraction of Σ3 twin boundaries remained stable in both variants up to 1050°C. On increasing the temperature to 1100°C, an increase in Σ3 boundaries in the FG variant was observed. Research conducted by Yuan Jin et al[132], on the evolution of annealing twin density during super-solvus grain growth of Inconel 718, has shown that this increase in Σ3 grain boundaries is not likely to be from the creation of new Σ3 boundaries. Rather it is a result of the density of Σ3 boundaries in the largest grains in the parent material which have now grown, elongating the twin boundaries' lengths.

Still, this increase in fraction of Σ3 twin boundaries is most likely grain growth driven. The grain growth exhibited in the FG variant would also involve the elimination of smaller grains further reducing the fraction of critical grain boundaries, therefore increasing the percentage of Σ3 twin boundaries recorded. The grain growth in the FG variant is also due to the loss of a lot of the primary γ'. The primary γ' would have

been recorded as small grains during the EBSD as they are incoherent with the γ matrix, so losing a large amount of the primary γ' would further reduce the fraction of critical grain boundaries, therefore increasing the percentage of Σ3 twin boundaries recorded further. Increasing the test temperature to 1160°C significantly reduced the percentage of Σ3 twin boundaries recorded in the FG variant. The reduction in Σ3 twin boundaries in the CG variant from 1100°C to 1160°C could not be confirmed to be statistically significant via t-test, although there was a significant reduction at 1160°C when compared to the parent CG material of -3.6% (+/- 3.4%, $t_{diff.}$ 4.583 > $t_{crit.}$ 4.303). Increasing the temperature to 1200°C resulted in significant reductions in the percentage of Σ3 twin boundaries recorded in both variants. Yuan Jin et al[132], also reported that a decrease in Σ3 twin density could occur through the migration of incoherent twin boundary segments, which may be a reason for these reductions at the higher temperatures. Although reductions in the percentage of Σ3 twin boundaries were evident in both RR1000 variants when heating to temperatures of 1160°C and above, these changes were found to have very little effect on the resultant hardness of the specimens. This is shown in the subsequent section and a later section (section 4.4) which compares the effects of heating rate on microstructural evolution and resultant hardness.

Hardness

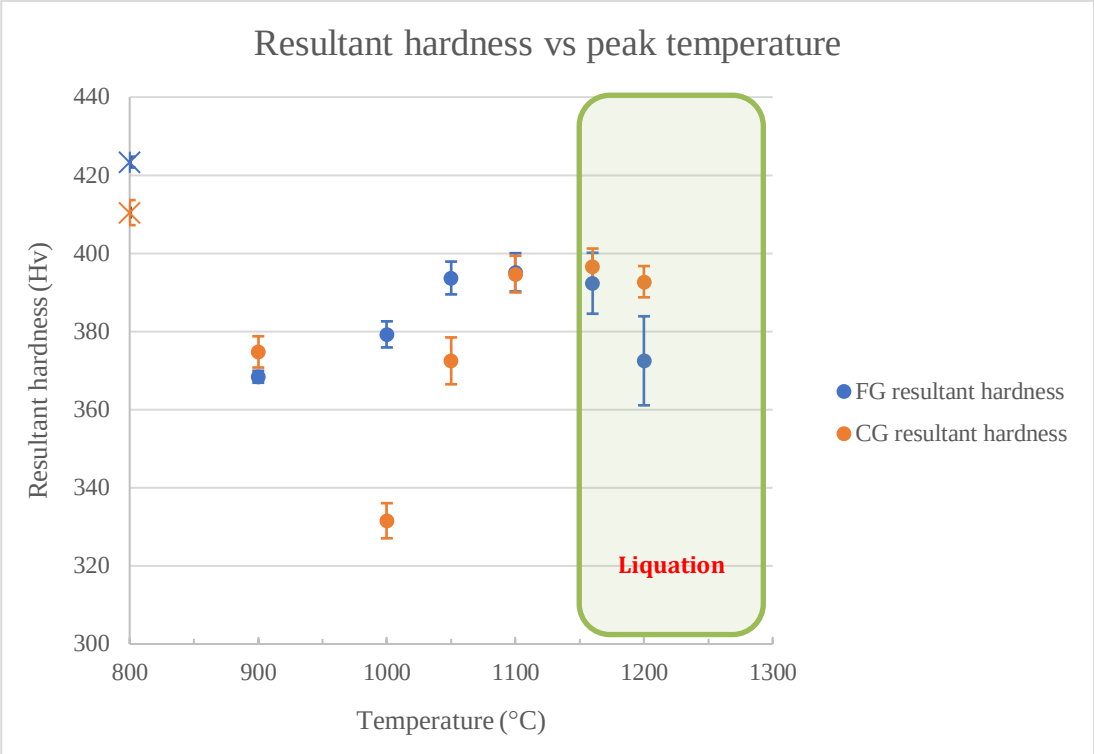

Figure 150 - Plot of specimen average hardness vs peak temperature exposure for FG & CG specimens heated at 25°Cs^{-1} (Error bars indicate 95% confidence intervals).

The resultant average hardness for each temperature exposure fluctuates a lot due to the complex interactions of each microstructural change. All specimens tested exhibited a reduction in average hardness over the parent material. A peak temperature exposure of 900°C produced a significant drop in hardness in both variants and can be attributed to the loss of some of the tertiary γ' at this temperature.

Increasing the test temperature to 1000°C had markedly different effects on each variant. The CG variant experienced a large drop in hardness compared to the FG variant, whereas the FG variant increased in strength slightly. This disparity in hardness can be attributed to the amount of secondary γ' that has diffused into the γ matrix at this temperature and the effect that has, on re-precipitation of γ'. The secondary γ' in the FG variant has almost completely diffused into the γ matrix creating a great enough driving force for re-precipitation of a very fine γ' on quenching. Whereas the secondary γ' in the CG variant has only just begun to spheroidize at 1000°C therefore, the γ matrix is not rich enough in γ' forming elements to provide a sufficient driving force for re-precipitation during water quenching resulting in no re-precipitated tertiary γ' in this specimen. The volume fraction of tertiary γ' was found to have a major influence on the hardness of RR1000 in a study

conducted by M. Preuss et al [58]. The study showed that higher volume fractions of tertiary γ' resulted in higher hardness. This explains the large drop in hardness experienced by the CG variant at this temperature.

At 1050°C enough γ' has diffused into the γ matrix in both variants to induce re-precipitation of a very fine γ' between the surviving γ' during water quenching resulting in an increase in hardness for both variants. This hardness increase is repeated at 1100°C as almost all the γ' has now diffused into the γ matrix except for some of the larger primary γ' in the FG variant. This resulted in the majority of both microstructures consisting of γ containing a very fine re-precipitated tertiary γ'. This would have provided a strengthening effect as the optimum γ' size for strength benefits is 23-40nm [36]. The two variants have very similar microstructures at this temperature with only the smaller grain size and presence of some primary γ' in the FG variant differentiating them. Consequently, the two variants exhibited a very similar average hardness value after being heated to 1100°C.

Increasing the peak exposure temperature to 1160°C induced liquation in both variants of RR1000, although in very different quantities, with the fine grain exhibiting much more. A reduction in Σ3 twin boundaries was also occurred at this temperature. This should have a negative effect on strength, because of the dislocation pile up and resistance to slip they cause, contributes to an FCC materials strength[27], [28]. Despite this, no significant reduction in hardness was evident in both variants. This suggests that the Σ3 twin boundaries contribution to the hardness of RR1000 is not that influential.

At 1200°C widespread liquation was prevalent in both variants. The presence of liquation and the intergranular quench cracking that accompanies it, had a pronounced effect on the average hardness of the FG variant, experiencing a significant decrease in average hardness. Unlike the FG variant the CG variant showed no meaningful change in average hardness after a peak temperature exposure at 1200°C. This disparity in hardness reduction is likely caused by the increased number of grain boundaries in the FG variant. As there are more grain boundaries present for the propagation of quench cracking, therefore a higher chance of the hardness indents interacting with a quench crack. The exposure at 1160°C and 1200°C coincides with a reduction of Σ3 twin boundaries, but again, the fact the CG retained its harness suggests they are not having a significant influence on the resultant hardness.

The FG variant recovers its strength via re-precipitation of fine γ' at lower temperature exposures than the CG variant. This is likely due to the smaller size of the secondary and tertiary γ' in the FG variant, resulting in their diffusion into the γ matrix at lower temperatures, therefore, creating a strong enough driving force for reprecipitation at these temperatures. Huang et al [55], reported in their study, that in the as welded state, the CG variant experienced a larger hardness trough alongside the hardened weld line when compared to the FG variant. It is likely, that the ability of the FG variant to recover its strength at lower peak temperature exposures, as shown in this study, is contributing to this difference in hardness response.

Grain texture & local miss-orientation

All specimens of both FG and CG variants retained their random grain texture no matter what peak temperature they were subject to, with all MUD values falling between 0.52 and 1.84. Each specimen also retained low levels of local misorientation with no average KAM recorded larger than 0.35°.

4.2 Liquid propagation

In order to assess the microstructural changes after the onset of liquation several tests were carried out where the specimen was again heated at 25°Cs^{-1} to 1160°C and 1200°C but held at this temperature for either 15 or 45 seconds. Doing this allowed the liquid propagation to be quantified along with any microstructural changes caused by the growth of the liquid. Table 15 shows optical micrographs illustrating the resultant microstructure after 1 second at temperature and after 45 seconds at temperature for comparison. Included in the table is the average fraction of liquid calculated for that specimen. The fraction of liquid produced in each test was then plotted against the approximate time that specimen had spent at a temperature above the γ' solvus temperature 1140°C, as shown in Figure 151.

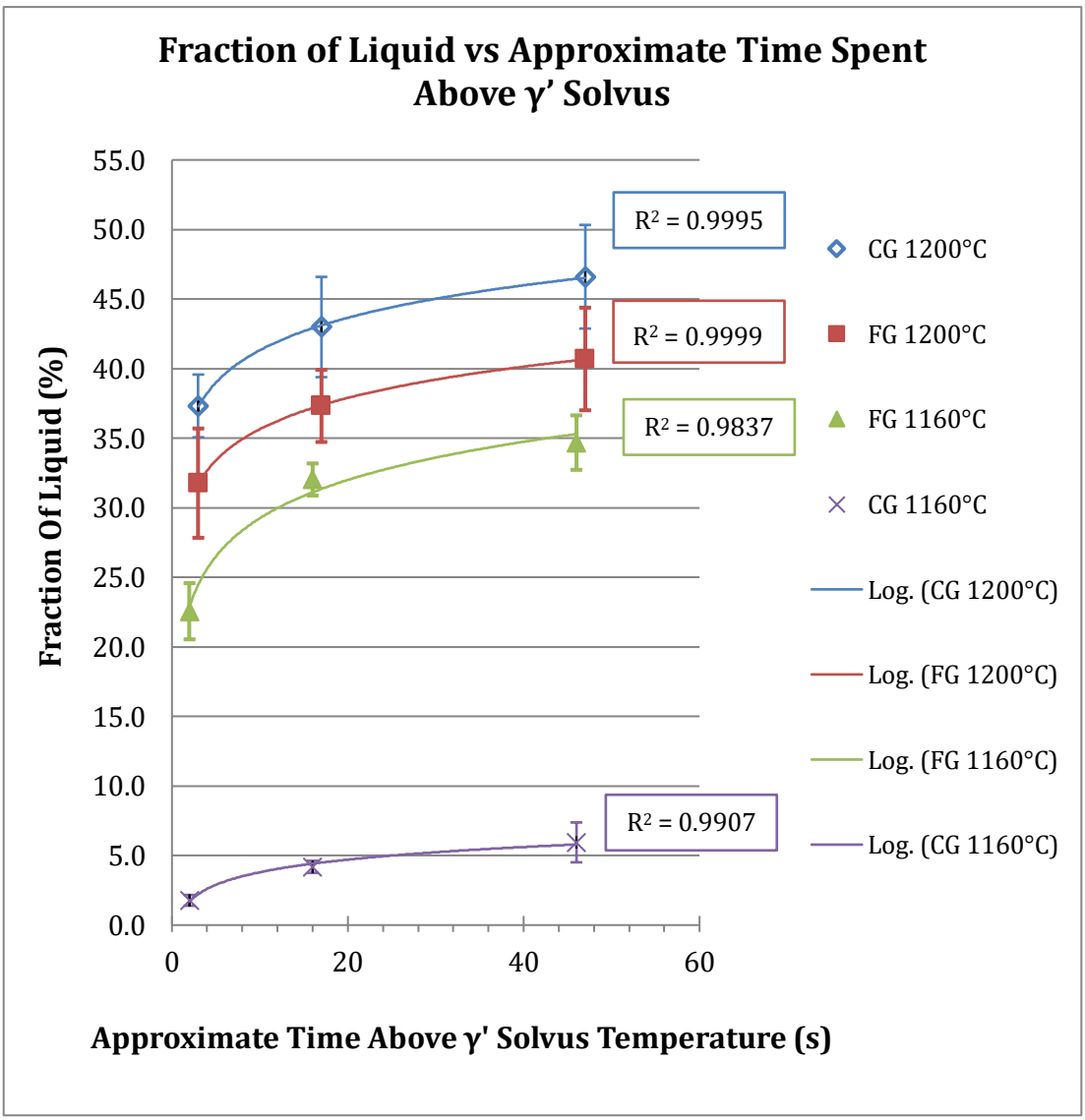

Figure 151 - Plot of fraction of liquid produced vs the time the specimen spent at a temperature above the γ' solvus temperature 1140°C (Error bars indicate 95% confidence intervals) (Solid shapes = FG, hollow/line shapes = CG).

	Hold time	
	1 second	45 seconds
FG at 1160°C	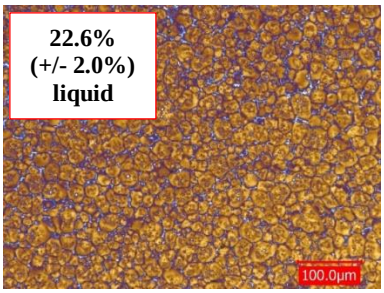	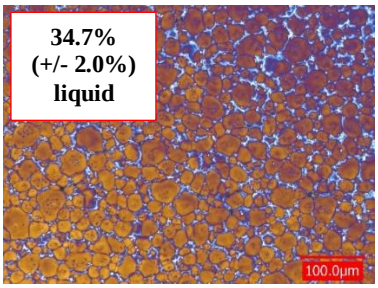
CG at 1160°C	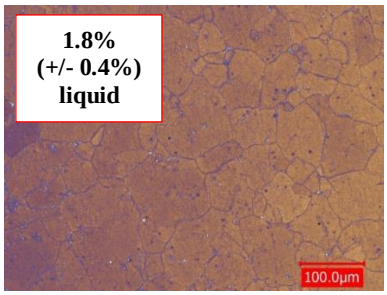	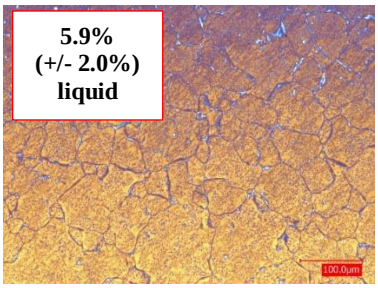
FG at 1200°C	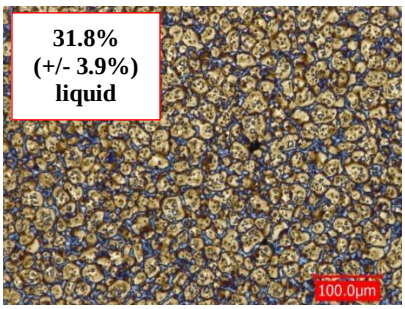	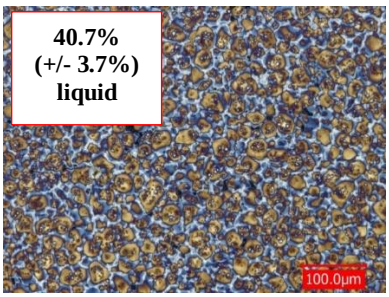
CG at 1200°C	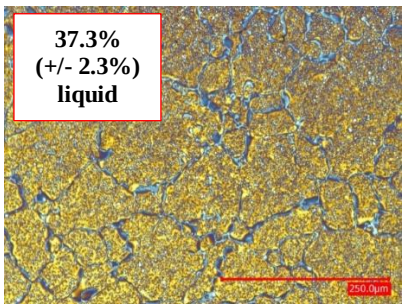	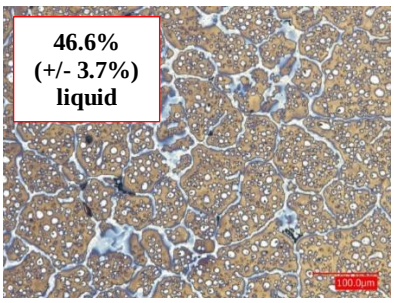

Table 15 - Optical micrographs of both variants of RR1000 held at both liquation temperatures for 1 second and 45 seconds. All micrographs were taken at x500 magnification.

Logarithmic trend lines fitted the data well, as indicated by the r^2 values nearing 1. This suggests that after the initial liquation event the volume of liquid propagates in a logarithmic manner. The propagation rate appears to be largely independent of temperature, whereas the initial fraction of liquid produced is temperature dependent especially in the case of the CG variant.

At 1160°C, the FG specimens experienced much more liquation than the CG specimens throughout the hold times, again suggesting that the CG variant is more resistant to temperature than the FG due to its lack of primary γ' and constitutional liquation. At 1200°C the amount of liquation in the two variants was more comparable, but with the CG variant featuring slightly more liquation than the FG variant at each hold time. These differences were confirmed via t-tests with the following results. At 1s hold time the CG variant exhibited 5.5% more liquation (+/- 4.5%, $t_{diff.}$ 2.646 > $t_{crit.}$ 2.179). at 15s hold time the CG variant exhibited 5.7% more liquation (+/- 4.4%, $t_{diff.}$ 2.799 > $t_{crit.}$ 2.179). At 45s hold time the CG variant exhibited 5.9% more liquation (+/- 5.2%, $t_{diff.}$ 2.454 > $t_{crit.}$ 2.179).

The sudden change in the amount of liquated material in the CG variant from 1160°C to 1200°C, may be a contributing factor to the discontinuous upset rate experienced by this variant during IFW. Sub-solidus liquid propagation in both RR1000 variants had not been characterised until this study.

These liquid propagation graphs can now be used to aid future semi-solid compression testing by using them as calibration curves to estimate the fraction of liquid in RR1000 specimens.

Each of the liquated specimens was analysed via EBSD, to assess the impact the different liquation levels have made on grain size, grain boundary characteristics, texture and local misorientation. All liquated specimens were then subject to Vickers hardness testing to determine if the presence of more re-solidified material is detrimental to strength. The results of this analysis are represented in the plots in Figure 152 to Figure 163. Each plot includes the relevant parent material data plotted at a hold time of 0 seconds for comparison.

Holding fine grain specimens at 1160°C

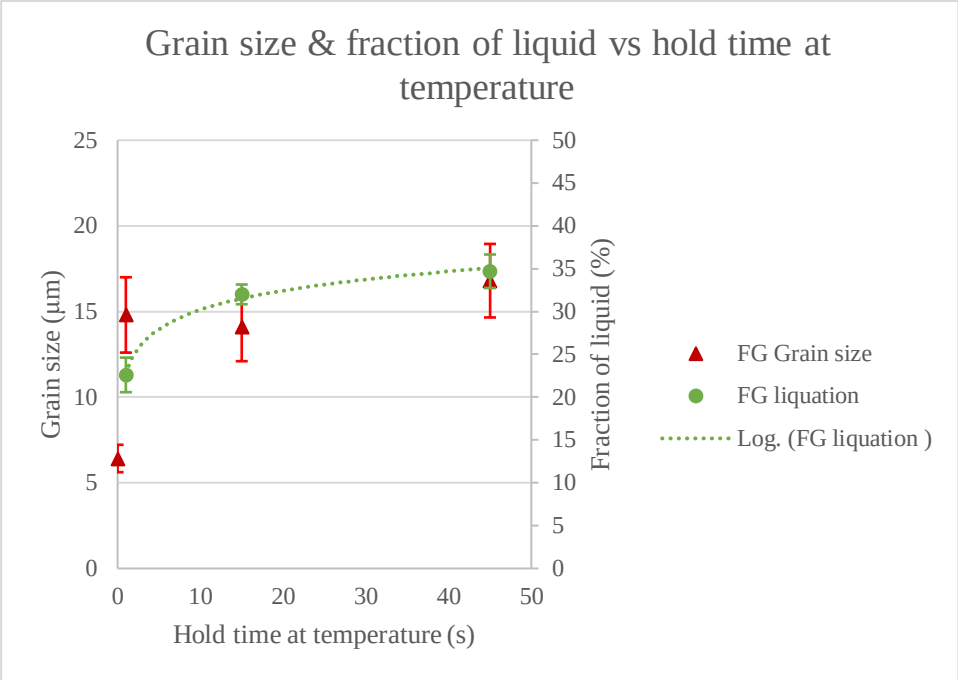

Figure 152 - Plot of grain size & fraction of liquid vs hold time for FG specimens held at 1160°C (Error bars indicate 95% confidence intervals).

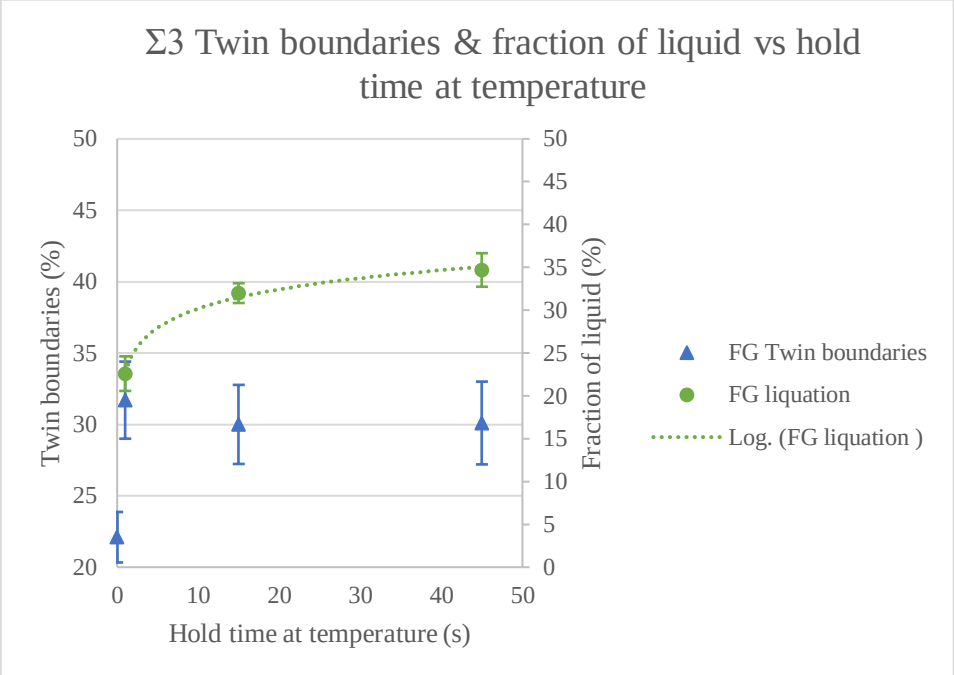

Figure 153 – Plot of Σ3 twin boundaries & fraction of liquid vs hold time for FG specimens held at 1160°C (Error bars indicate 95% confidence intervals).

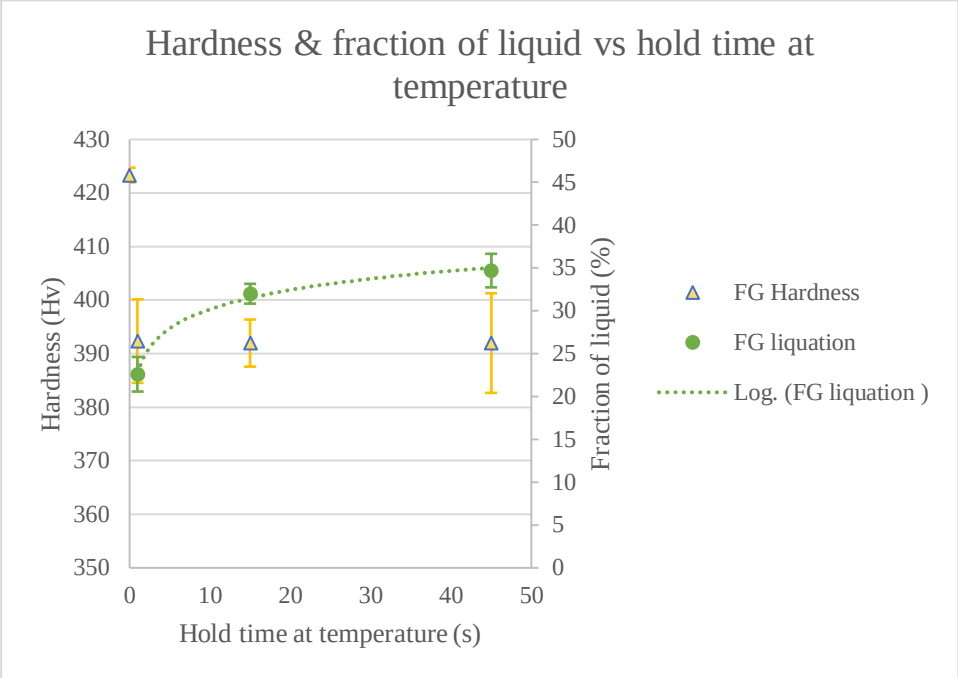

Figure 154 - Plot of hardness & fraction of liquid vs hold time for FG specimens held at 1160°C (Error bars indicate 95% confidence intervals).

The graphs in Figure 152 to Figure 154 show the average grain size, average percentage of Σ3 twin boundaries and the resultant average hardness, after holding FG specimens at 1160°C, where liquation propagated from 22.6% (+/- 2.0%) to 34.7% (+/- 2.0%). In all three cases, the microstructural characteristics experience no significant change after the initial liquation event, remaining comparable throughout the hold times. This suggests that hold time and the ensuing increase in liquid fraction have little effect and that the majority of microstructural changes happen on the lead up to and during the initial liquation. Therefore, the average hardness for each of the specimens was consistent.

Holding coarse grain specimens at 1160°C

Holding the CG variant at 1160°C yielded the same results. There were no significant changes in microstructural characteristics or hardness with increasing hold time, even with such a difference in fraction of liquid being produced compared to the FG. Consequently, the average hardness of each specimen was comparable. All three CG specimens heated to 1160°C experienced a significant drop in the percentage of Σ3 twin boundaries when compared to the parent CG material. Again, this suggests that exposing the CG variant to this temperature is influencing the amount of Σ3 grain boundaries. These results are summarised graphically in Figure 155 to Figure 157.

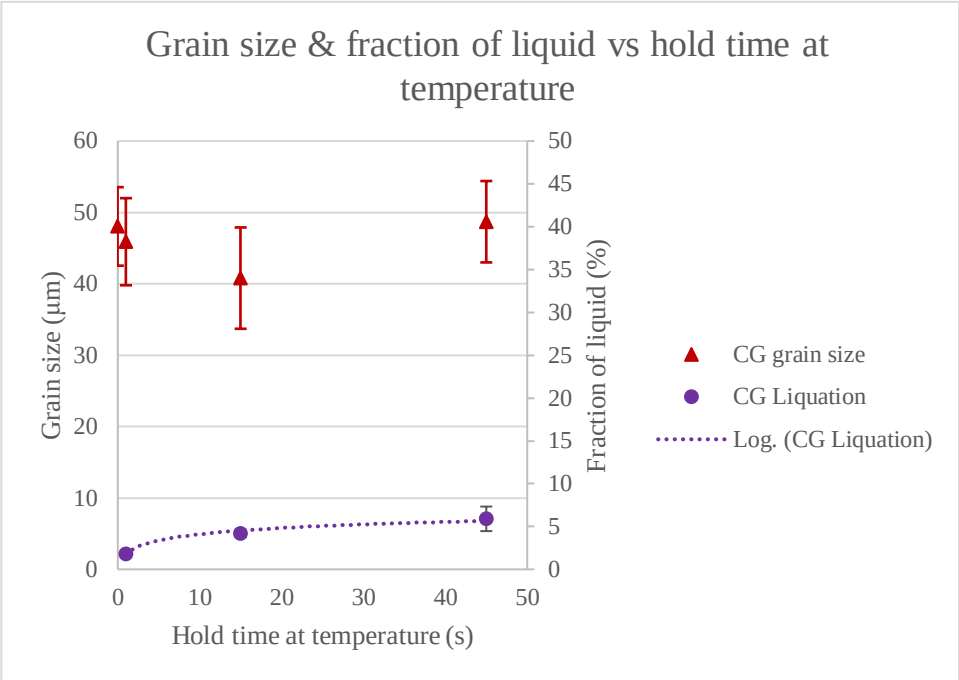

Figure 155 - Plot of grain size & fraction of liquid vs hold time for CG specimens held at 1160°C (Error bars indicate 95% confidence intervals).

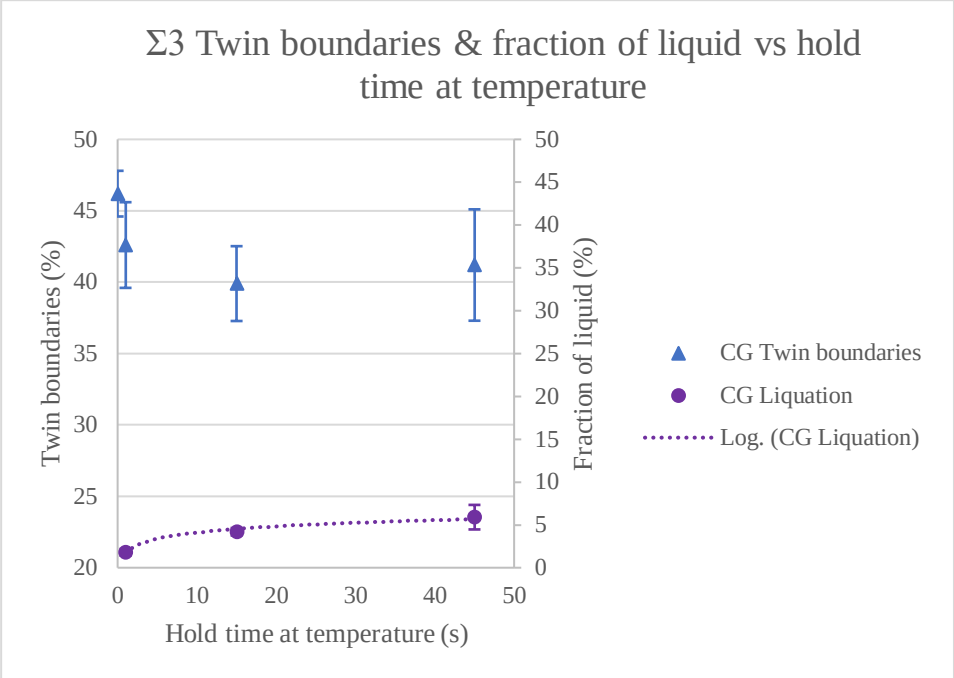

Figure 156 - Plot of Σ3 twin boundaries & fraction of liquid vs hold time for CG specimens held at 1160°C (Error bars indicate 95% confidence intervals).

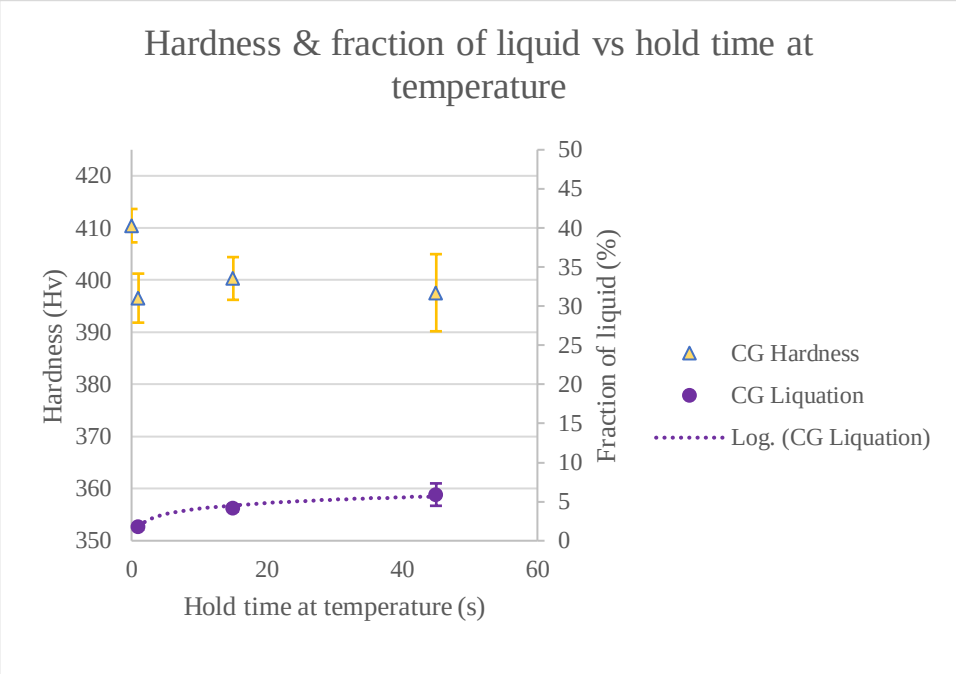

Figure 157 - Plot of hardness & fraction of liquid vs hold time for CG specimens held at 1160°C (Error bars indicate 95% confidence intervals).

Holding fine grain specimens at 1200°C

Increasing the hold temperature to 1200°C yielded a similar result to the 1160°C hold tests, with no significant changes in the three measured parameters with increasing hold time. Again, this implies that most of the microstructural changes happen on the lead up to and during the initial liquation.

Increasing the hold temperature had no effect on the resultant grain size in the FG specimens, as shown in Figure 158. Although, the temperature increase did slightly reduce the percentage of Σ3 twin boundaries compared to the percentage of Σ3 boundaries found in the FG specimens in the 1160°C hold tests. The differences from 1160°C to 1200°C found at 1s, 15s and 45s hold times were -6.3% (+/- 3.8%, $t_{diff.}$ 7.181 > $t_{crit.}$ 4.303), -4.4% (+/- 3.2%, $t_{diff.}$ 5.911 > $t_{crit.}$ 4.303) and -5.4% (+/- 4.1%, $t_{diff.}$ 5.634 > $t_{crit.}$ 4.303) respectively. The percentage of Σ3 boundaries with increasing hold time at 1200°C is illustrated in Figure 159.

A reduction in average hardness was also recorded at each hold time when the hold temperature was increased from 1160°C to 1200°C. The differences from 1160°C to 1200°C found at 1s, 15s and 45s hold times were -19 Hv (+/- 14, $t_{diff.}$ 2.840 > $t_{crit.}$ 2.064), -29 Hv (+/- 16, $t_{diff.}$ 3.789 > $t_{crit.}$ 2.064) and -15 Hv (+/- 11, $t_{diff.}$ 2.774 > $t_{crit.}$ 2.064) respectively. The average hardness of the FG specimens held at 1200°C is shown in Figure 160. It must be noted that three of the specimens in these comparisons were the FG specimens that exhibited hardness distributions with higher kurtosis. These specimens were: 1160°C at 25°Cs^{-1} 1s hold time, 1160°C at 25°Cs^{-1} 45s hold time and 1200°C at 25°Cs^{-1} 1s hold time. There is a possibility that the positive t-test results associated with these specimens may not be reliable. However, this decrease in hardness was likely a real decrease, as the FG has been shown to be susceptible to quench cracking when quenched from 1200°C, increasing the likelihood of hardness indents interacting with quench cracks. This is further supported by the fact that the t-test comparison for the difference in hardness from 1160°C to 1200°C at 15s hold time above, yielded the most significant difference when both hardness distributions exhibited normal kurtosis values.

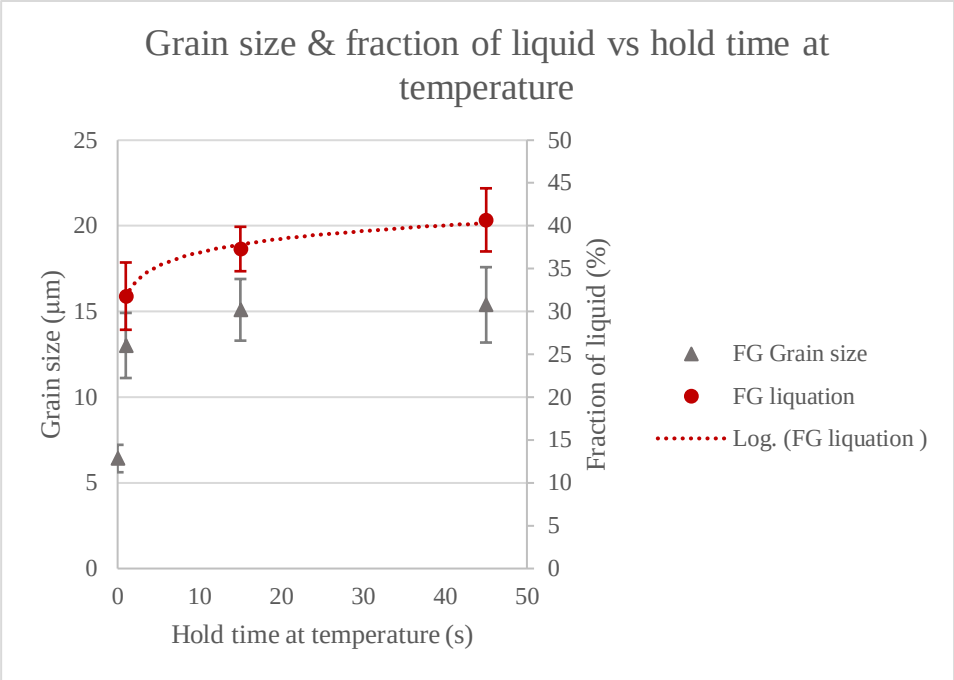

Figure 158 - Plot of grain size & fraction of liquid vs hold time for FG specimens held at 1200°C (Error bars indicate 95% confidence intervals).

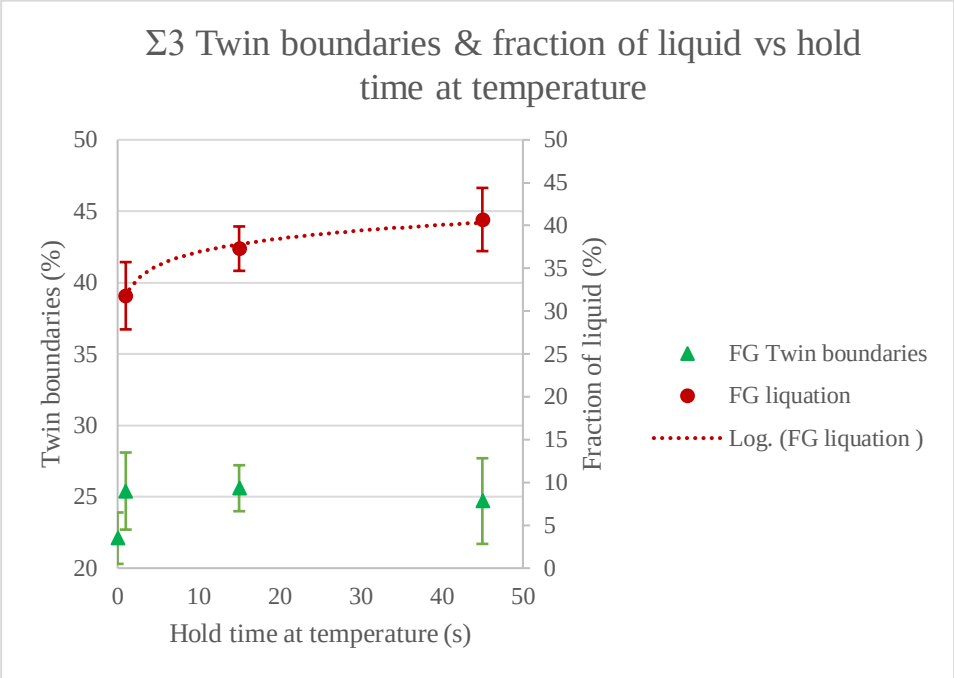

Figure 159 - Plot of Σ3 twin boundaries & fraction of liquid vs hold time for FG specimens held at 1200°C (Error bars indicate 95% confidence intervals).

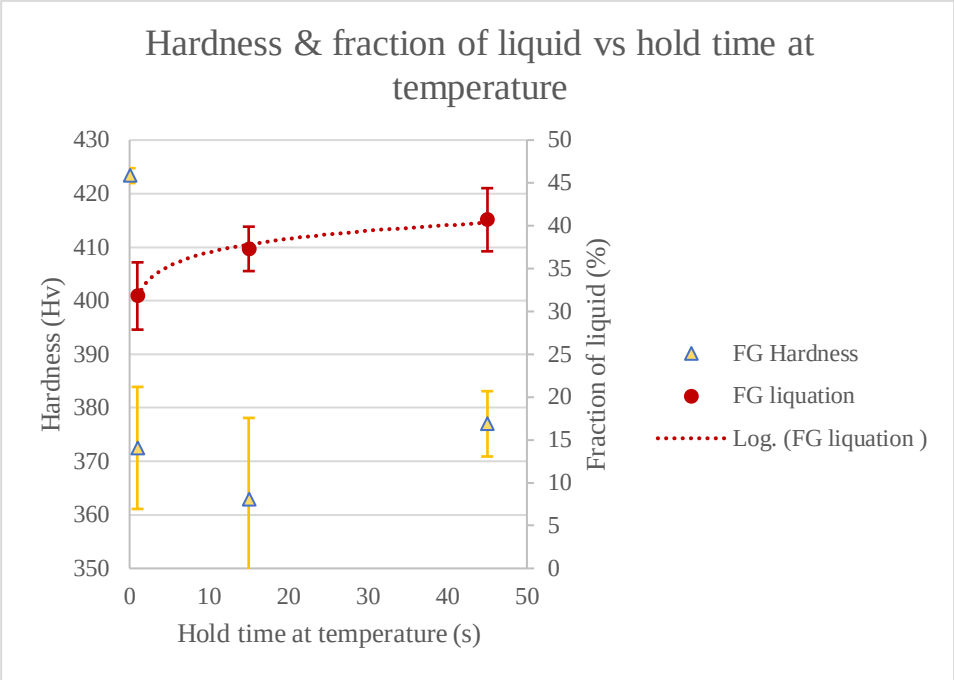

Figure 160 - Plot of hardness & fraction of liquid vs hold time for FG specimens held at 1200°C (Error bars indicate 95% confidence intervals).

Holding coarse grain specimens at 1200°C

The CG variant also produced the same outcome when held at 1200 °C, with no significant changes in the three parameters with increasing hold time at temperature. Increasing the holding temperature to 1200°C also had no influence on the resultant grain size of the CG specimens, see Figure 161. The CG variant did however exhibit a reduction in the amount of Σ3 twin boundaries when increasing the hold temperature to 1200°C, when compared to the CG specimens held at 1160°C. The differences in Σ3 twin boundaries from 1160°C to 1200°C found at 1s, 15s and 45s hold times were -8.0% (+/- 4.5%, $t_{diff.}$ 7.303 > $t_{crit.}$ 4.303), -8.5% (+/- 2.9%, $t_{diff.}$ 12.512 > $t_{crit.}$ 4.303) and -7.7% (+/- 5.0%, $t_{diff.}$ 6.676 > $t_{crit.}$ 4.303) respectively. Again, the drop was thought to be associated with being exposed to the test temperature and was unaffected by the hold times applied and the increase in liquid fraction, as illustrated in Figure 162. Figure 163 shows the average hardness exhibited by the CG specimens held at 1200°C. T-testing found that there was no significant change in hardness when compared to the CG specimens held at 1160°C, unlike the FG variant. This discrepancy between variants is likely due to the larger grains and therefore fewer grain boundaries found in the CG variant. The fewer grain boundaries mean there are less liquated grain boundaries for the quench cracks to propagate along. Therefore, there is less chance of the hardness indents interacting with quench cracks in the CG variant. The fact the resultant hardness did not change significantly when the percentage of Σ3 twin boundaries reduced significantly also suggests the reduction in Σ3 twin boundaries is having little effect on the resultant hardness.

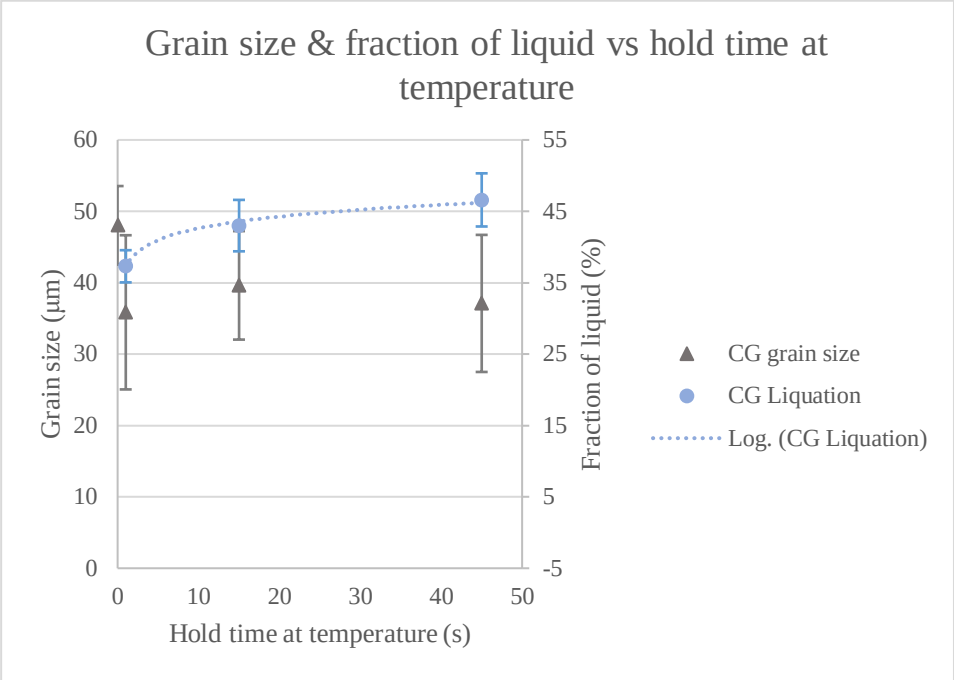

Figure 161 - Plot of grain size & fraction of liquid vs hold time for CG specimens held at 1200°C (Error bars indicate 95% confidence intervals).

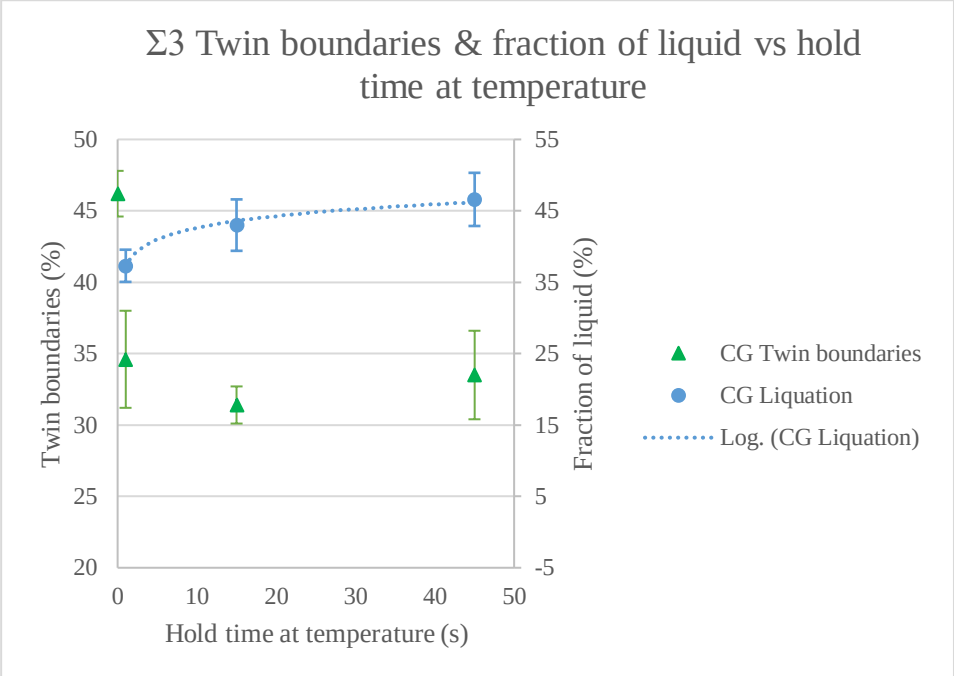

Figure 162 - Plot of Σ3 twin boundaries & fraction of liquid vs hold time for CG specimens held at 1200°C (Error bars indicate 95% confidence intervals).

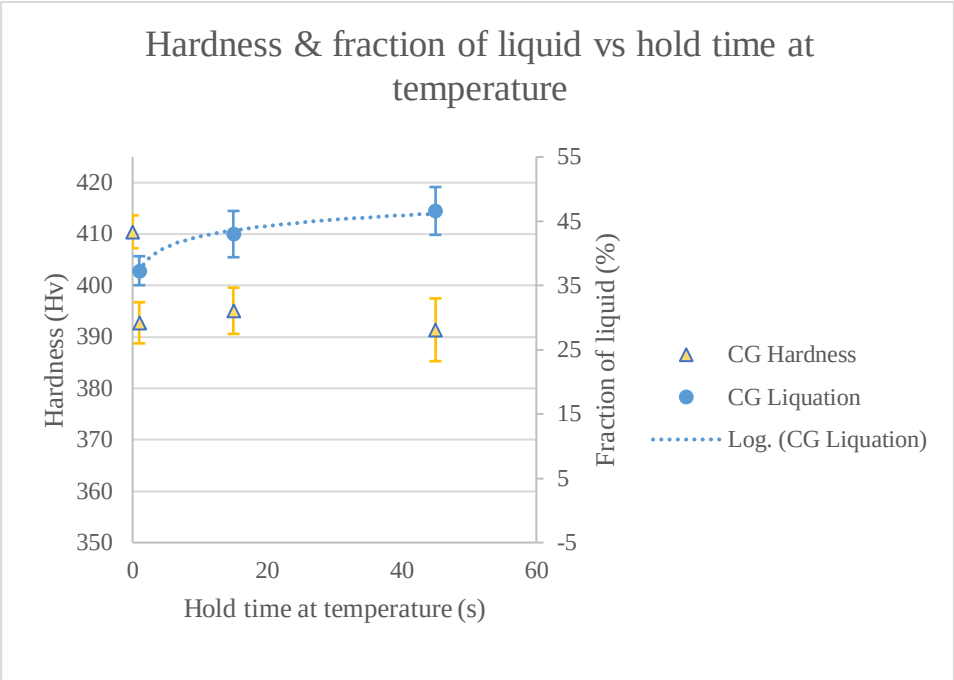

Figure 163 - Plot of hardness & fraction of liquid vs hold time for CG specimens held at 1200°C (Error bars indicate 95% confidence intervals).

4.2.1 Intermediate heating rates to above the gamma prime solvus

Most of the heat and quench only tests conducted above 1160°C at 25°Cs^{-1} produced a significant fraction of liquid during the initial liquation event, yielding between 22.6% (+/- 2.0%) and 37.3% (+/- 2.3%) from the initial liquation at 1s hold time. The exception was the test conducted on the CG variant at 1160°C. In order to proceed with any future semi-solid compression testing at a range of liquid fractions, a way of producing lower fractions of liquid was needed.

In an attempt to produce lower initial liquid fractions, several heat and hold tests were conducted using a slower 12.5°Cs^{-1} heating rate. Again, the specimens were held at temperature for either 1, 15 or 45 seconds. The lower heating rate meant that less of the primary γ' in the FG variant would be of sufficient size to survive to their eutectic melting temperature on passing the γ' solvus temperature. This would create fewer initial liquation sites via constitutional liquation. The lower heating rate would also help to reduce the amount of liquation in the CG variant by allowing more time for homogenisation of the γ' forming elements throughout the γ matrix. This would result in fewer areas of highly alloyed material, with temporarily lowered melting points, as per the liquation mechanism for CG RR1000 proposed in this work.

The fraction of liquid for each specimen was measured and has been plotted against the approximate time the specimen spent above the γ' solvus temperature as shown in Figure 164. The liquid fraction data from the 25°Cs^{-1} tests has also been added to the plot for comparison.

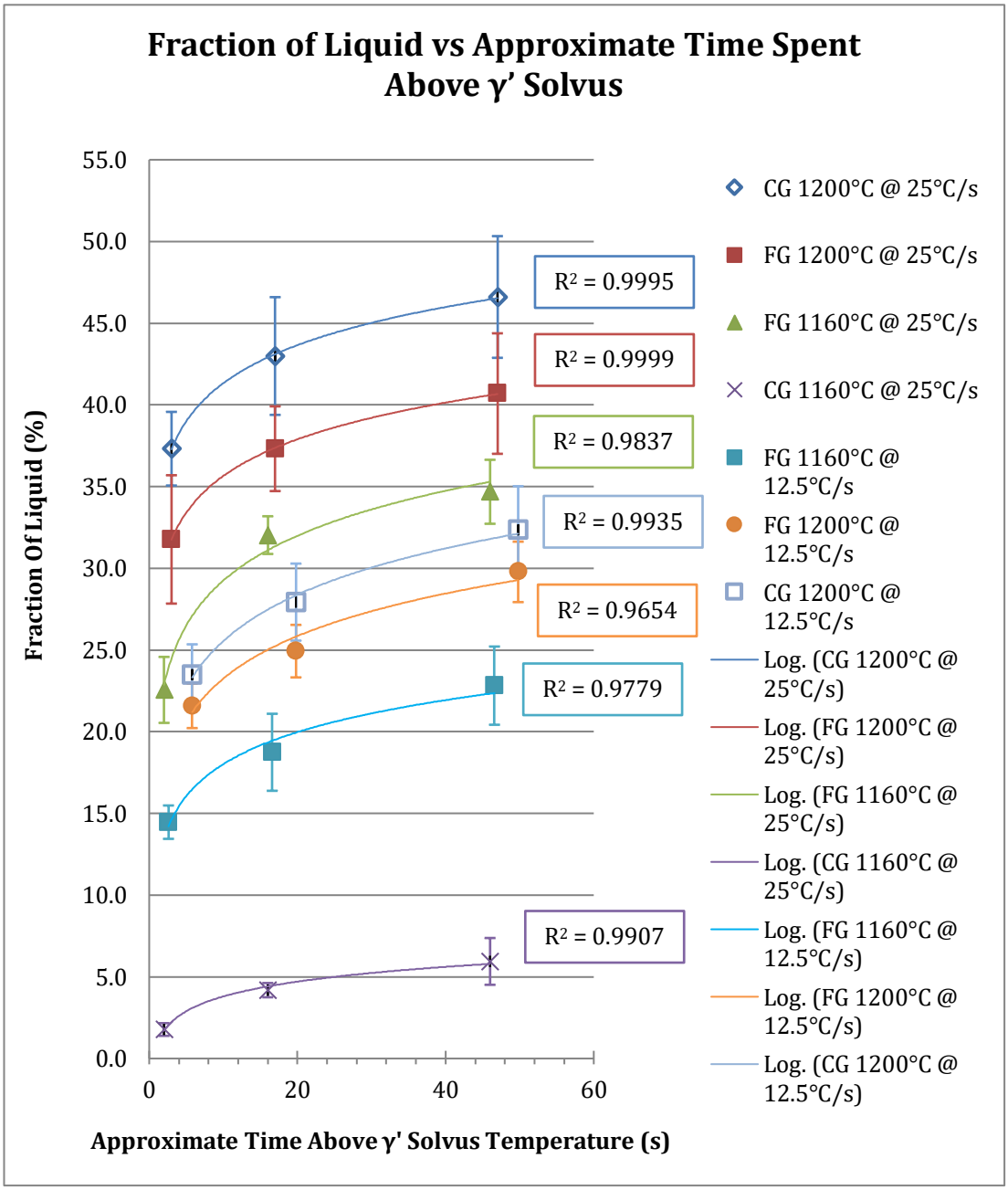

Figure 164 - Plot of fraction of liquid produced vs the time the specimen spent at a temperature above the γ' solvus temperature 1140°C (Error bars indicate 95% confidence intervals) (Solid shapes = FG, hollow/line shapes = CG).

As can be seen in Figure 164 all three 12.5°Cs^{-1} yielded lower fractions of liquid on initial liquation when compared to the same tests, conducted at 25°Cs^{-1}. The liquation curves have also all shifted to the right due to the extra time needed to reach the target temperature at the slower heating rate.

These tests confirmed that lower initial fractions of liquid are possible by reducing the heating rate, allowing future semi-solid compression testing of RR1000 at a much wider range of liquid fractions. They also open the possibility of finding the critical

heating rate for both liquation mechanisms of RR1000 in future work, by performing tests at incrementally lower heating rates until no liquation occurs.

From the 25°Cs^{-1} heat and hold tests discussed earlier, it was found that when heating and holding at 1200°C, the CG variant exhibited significantly more liquation than the FG variant at each hold time. When the heating rate was reduced to 12.5°Cs^{-1} in these tests, the difference in liquid fraction between the FG and CG variants at 1200°C was more comparable. Performing t-tests revealed that the differences at this heating rate could not be deemed significant.

The specimens used in the 12.5°Cs^{-1} heating rate tests were also analysed via EBSD and then subject to hardness testing for comparison with the specimens in the 25°Cs^{-1} tests. The same trend was exhibited by the 12.5°Cs^{-1} specimens as the 25°Cs^{-1}, with very little change to grain size and Σ3 twin boundary density and therefore very little change to the average hardness value of each specimen with increased hold time at temperature.

The only differences in trend between the 12.5°Cs^{-1} heat and hold tests and the 25°Cs^{-1} heat and hold tests were that the drop in hardness and the reduction in Σ3 twin boundaries experienced by the FG specimens when the test temperature was increased to 1200°C were not as prominent and couldn't be confirmed to be statistically significant via t-test. The graphs illustrating these results can be seen in appendix A.

These results further reinforced the notion that most of the microstructural changes occur on the lead up to and during the initial liquation event with little or no changes occurring in the liquid propagation phase.

Grain orientation texture & Local miss-orientation.

EBSD analysis of the grain orientation and local misorientation was also conducted on all the specimens from the heat, hold and quench tests. As with all the previous heat and quench only tests, the grain texture and local misorientation were unaffected by the initiation and propagation of liquid in both variants of RR100. No specimen in these tests exhibited more than 0.35° average KAM and all MUD values ranged between 0.41 and 1.53.

4.3 Slow heating rates to above the gamma prime solvus

In order to differentiate the liquation experienced during the rapid heating rate tests from any that may be produced by simply heating to the target temperature of 1200°C, FG and CG specimens were heated slowly at a rate of $1°Cs^{-1}$ to 1200°C, followed by water quenching. The aim of this experiment was to confirm whether a rapid heating rate was required for sub-solidus liquation. The resultant microstructures were inspected for any signs of liquation.

Fine grain

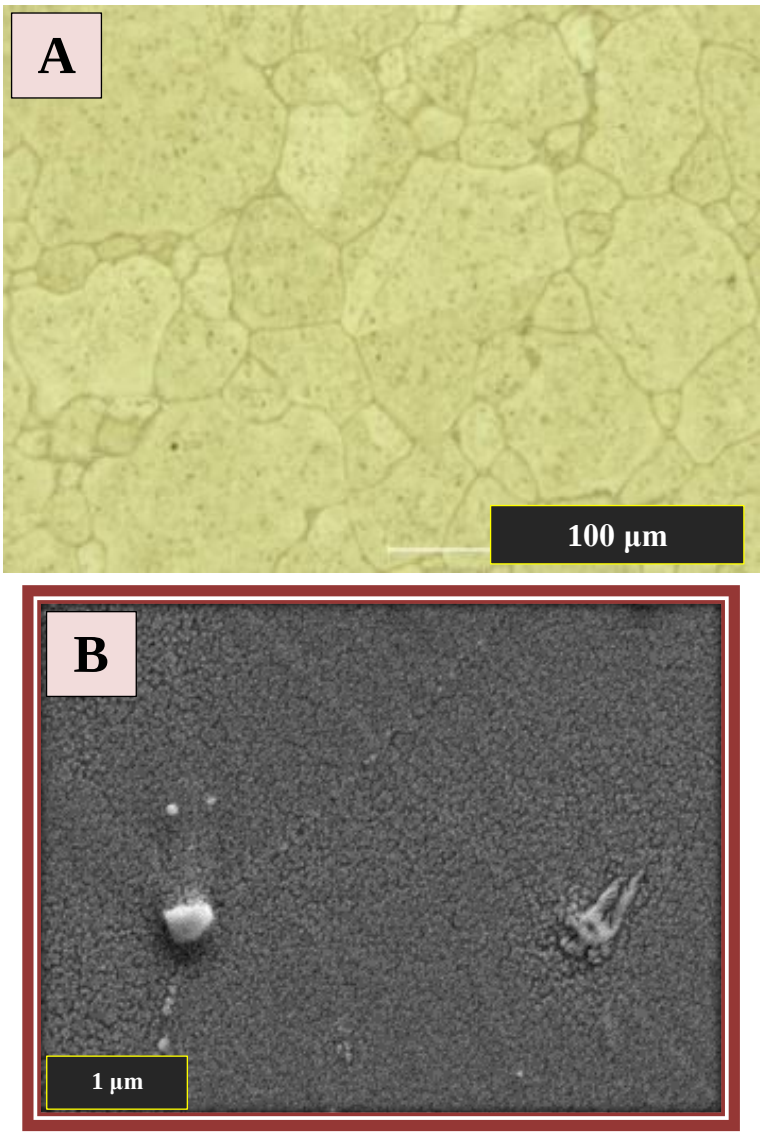

Figure 165 - Micrographs illustrating the microstructure of a FG specimen heated to 1200°C at 1°Cs^{-1}. A) Optical micrograph. B) SEM micrograph.

The FG variant exhibited almost no liquation, with only very small eutectic features appearing on some grain boundaries (Figure 165). These features were thought to be the result of the traditional form of incipient melting involving the liquation of low melting point phases. As expected, all the γ' precipitates had diffused into the γ matrix leading to an even re-precipitation of a fine γ' throughout the specimen.

EBSD analysis of this specimen revealed that the grain size had increased dramatically, from the original 6.4µm (+/- 0.8) to 22.9µm (+/- 3.3). This large grain growth when little to no liquid is present, reaffirms the concept of intragranular liquid providing grain boundary pinning.

The percentage of grain boundaries registered as Σ3 twin boundaries had also increased significantly from 22.1% (+/- 1.8%) in the parent FG material to 33.3% (+/- 2.9%) in this specimen. Again, this increase was likely a result of the loss of small grains during grain growth, and the loss of the primary γ', reducing the ratio of critical grain boundaries to Σ3 twin boundaries.

The increase in grain size and re-distribution of γ' led to a 16 Hv (+/- 4, $t_{diff.}$ 9.161 > $t_{crit.}$ 2.064) reduction in average hardness to 407 Hv (+/- 3), from the hardness of the parent FG material (423 Hv +/- 1).

Coarse grain

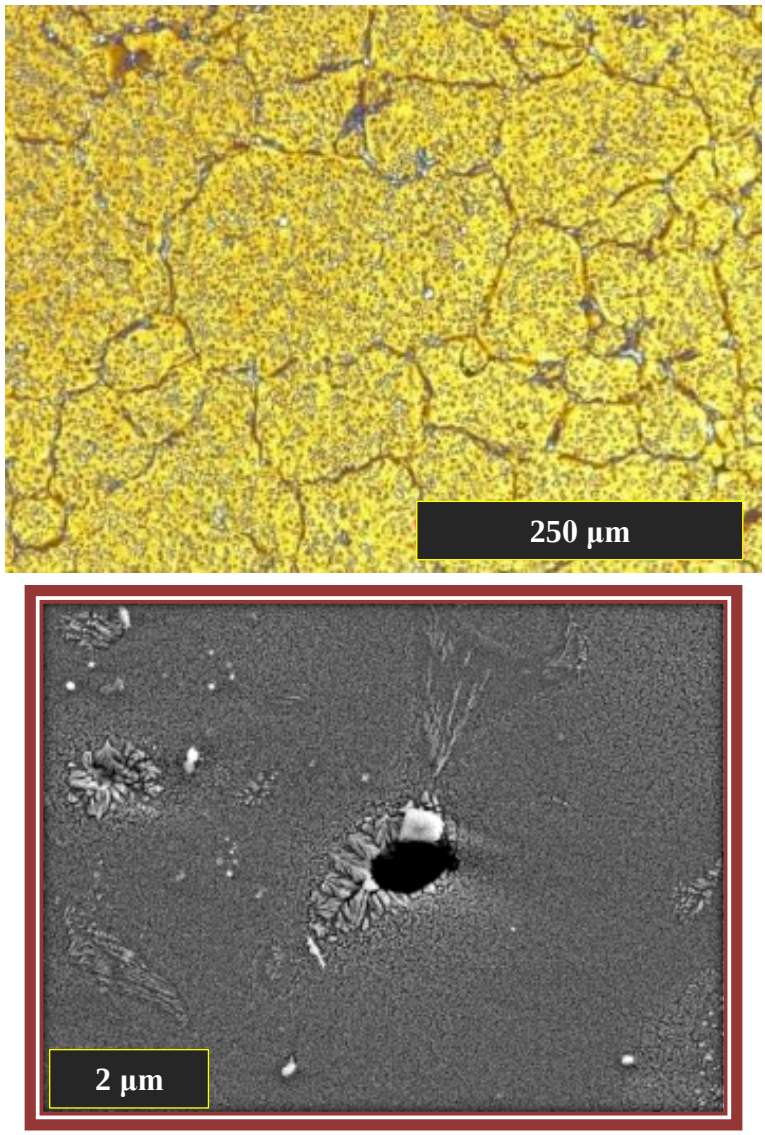

Figure 166 - Micrographs illustrating the microstructure of a CG specimen heated to 1200°C at 1°Cs-1. A) Optical micrograph. B) SEM micrograph.

The CG variant featured more liquated material after being heated to 1200°C at 1°Cs^{-1}, with small pockets of liquated regions spread evenly throughout the grains with some additional minor grain boundary liquation. Figure 166 shows an example SEM micrograph of these small intragranular liquated regions featuring γ-γ' eutectic structures. The grain size in this specimen remained stable showing no change from the parent CG material, being recorded at 45.6µm (+/- 2.0).

This CG specimen was analysed via EBSD in the usual fashion. The fraction of Σ3 twin boundaries had decreased due to the exposure at 1200°C to 33.1% (+/- 1.9%), from the 46.2% (+/- 1.6%) in the parent CG material, just like the specimens heated at $25°Cs^{-1}$.

As there was very little liquation present in this specimen, this result further suggests that the reduction in Σ3 twin boundaries is due to the exposure to such an extreme temperature and not because of the liquation.

After being heated to 1200°C at this slow heating rate, the CG variants resultant average hardness was recorded as 405 Hv (+/- 6). This was comparable with the hardness of the parent CG material (410 Hv +/- 3). The minimal liquation at the grain boundaries of this specimen has reduced the tendency to quench crack. Therefore, the interactions between quench cracks and hardness indents that usually reduce hardness are unlikely. This has allowed the hardness to be regained by the redistribution of the original γ' as a very fine re-precipitated tertiary γ'.

In both the FG and CG variants the amount of liquation produced was significantly reduced by decreasing the heating rate down to a moderate $1°Cs^{-1}$. The FG variant showed the greatest difference with almost no liquation occurring. The CG variant still exhibited some melting although significantly less than in the rapid heating rate tests, suggesting that its critical heating rate to induce liquation in the CG variant is lower than $1°Cs^{-1}$ if a peak temperature of 1200°C is reached.

Grain orientation texture & Local miss-orientation.

EBSD analysis of the grain orientation and local misorientation was also conducted on both the specimens from the $1°Cs^{-1}$ tests. As with all the previous heat and quench only tests, the grain texture and local misorientation were unaffected. Both MUD values ranged between 0.61 and 1.5 and neither specimen exhibiting more than 0.25° average KAM.

4.4 Heating rate comparison

Heat and quench only tests have been conducted to 1200°C at three different heating rates: 1°Cs^{-1}, 12.5°Cs^{-1}and 25°Cs^{-1}. This has allowed the resultant microstructure and the consequent hardness produced by each heating rate to be compared. The results of this comparison are shown in Figure 167 to Figure 170. Each plot includes the relevant parent material data plotted at a hold time of 0 seconds for comparison.

Fine grain

As has been shown in the previous heat and quench tests, increasing the heating rate results in a higher fraction of liquid created when heating FG specimens to 1200°C. This introduction of liquated material has led to a reduction in hardness, as illustrated in Figure 167. The resultant hardness appears to have an inverse relationship to the fraction of liquid, although the reduction in hardness from the 12.5°Cs^{-1} test to the 25°Cs^{-1} test could not be confirmed to be statistically significant via t-testing. This relationship is due to the susceptibility of the FG specimens to quench cracking when they contained significant fractions of liquid. As there are a lot of grain boundaries in the FG material, there are more pathways for the quench cracks to propagate along. This resulted in a high probability of hardness indents interacting with the quench cracks.

At 1°Cs^{-1} there was almost no liquation in the FG at 1200°C. As a result, the grain size grew considerably due to the lack of the grain boundary pinning effect of intergranular liquation. This can be seen in Figure 168. This increase in grain size has again increased the percentage of Σ3 twin grain boundaries, due to the loss of the smaller grains during the grain growth. It appears that this increase in Σ3 twin boundaries was even greater than that experienced in the 25°Cs^{-1} heat and quench tests. This is because in those tests, the percentage of Σ3 twin boundaries initially increased when heating to 1100°C, to 37.1% (+/- 3.2%), but then decreased when temperature was increased further. The specimen heated at 1°Cs^{-1} has likely also experienced a decrease in Σ3 twin boundaries as it was heated to 1200°C, yet its final Σ3 content was comparable with the 25°Cs^{-1} to 1100°C test, being recorded at 33.3% (+/- 2.9%). Increasing the heating rate to 12.5°Cs^{-1} and 25°Cs^{-1} and therefore introducing greater quantities of liquated material, reduced the amount of grain growth due to the grain boundary pinning effect of intergranular liquation. As can be seen in Figure 168, this resulted in the grain size and Σ3 twin boundary content at these heating rates being comparable.

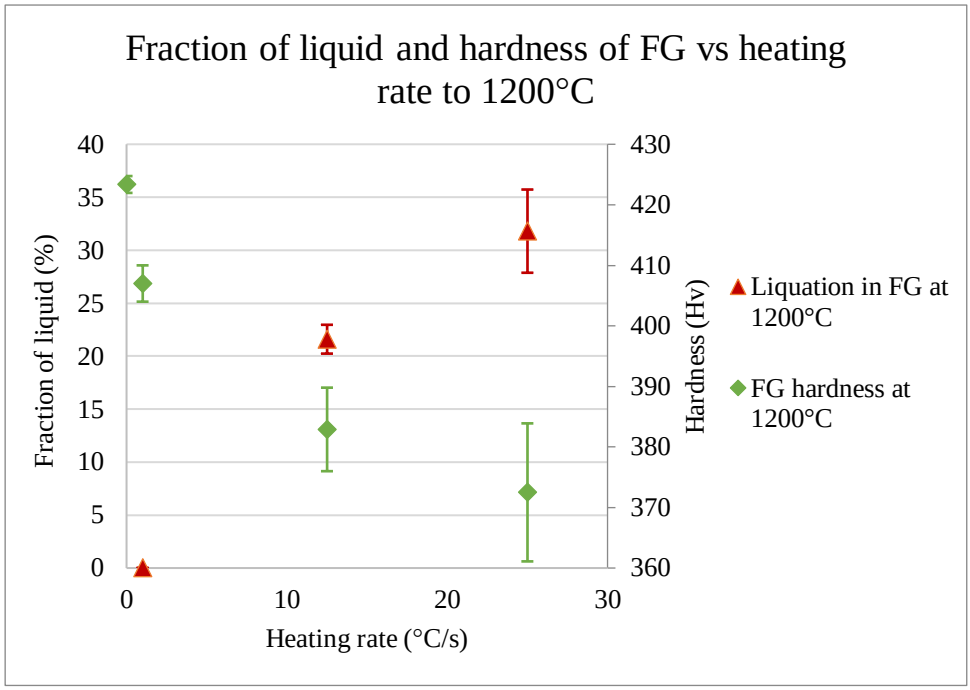

Figure 167 - Plot of hardness & fraction of liquid vs heating rate for FG specimens heated to 1200°C (Error bars indicate 95% confidence intervals).

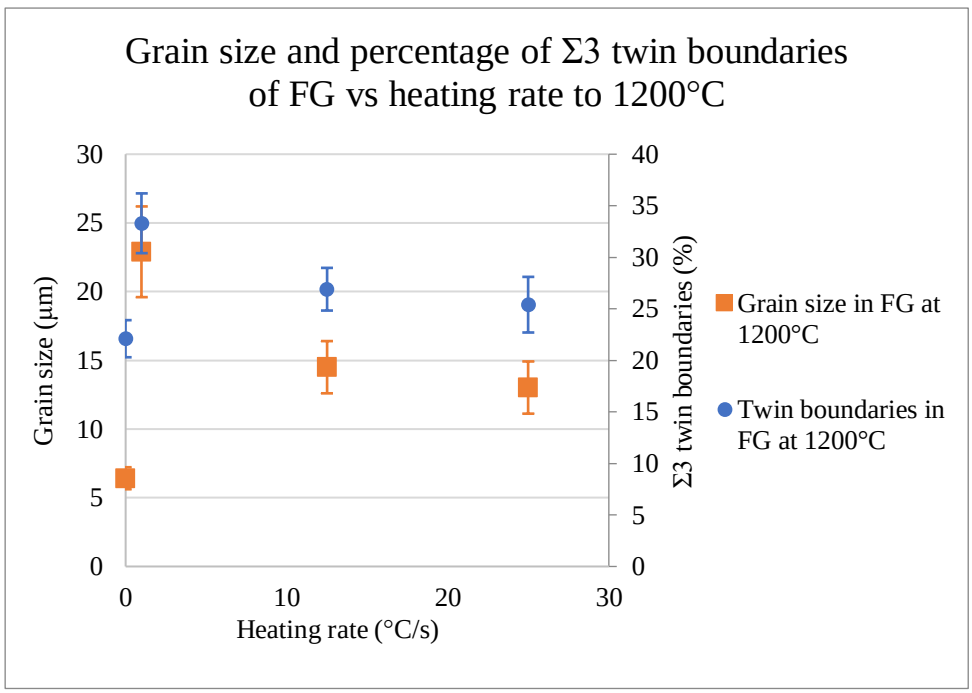

Figure 168 - Plot of grain size & percentage of twin boundaries vs heating rate for FG specimens heated to 1200°C (Error bars indicate 95% confidence intervals).

Coarse grain

The coarse grain behaved similarly, with hardness appearing to reduce with increasing liquid fraction. Even though the individual reductions in hardness between the $1°Cs^{-1}$ and $12.5°Cs^{-1}$ tests and between the $12.5°Cs^{-1}$ and $25°Cs^{-1}$ tests could not be confirmed to be statistically significant via t-testing, overall there is a clear trend. This can be seen in Figure 169. The reduction in hardness with increasing liquid fraction is not as severe in the CG variant when compared to the FG. This is due to fewer grain boundaries for quench crack propagation.

Figure 170 illustrates that increasing the heating rate and consequently the fraction of liquated material had no meaningful effect on the resultant grain size or the percentage of Σ3 twin boundaries in the CG variant. This implies that the reduction in hardness is likely the result of quench cracking as suspected and not a result of the drop in percentage of Σ3 twin boundaries. This reinforced the notion that although significant reductions in Σ3 twin boundaries were occurring in RR1000 after exposure at temperatures of 1160°C and above, ultimately this was not having a significant effect on the resultant hardness. This is further supported by the disparity in hardness drop with increasing heating rate between the two variants, as the lesser reduction experienced by the CG variant is thought to be due to the fewer grain boundaries for quench crack propagation. Therefore, there is less chance of hardness indents interacting with quench cracks.

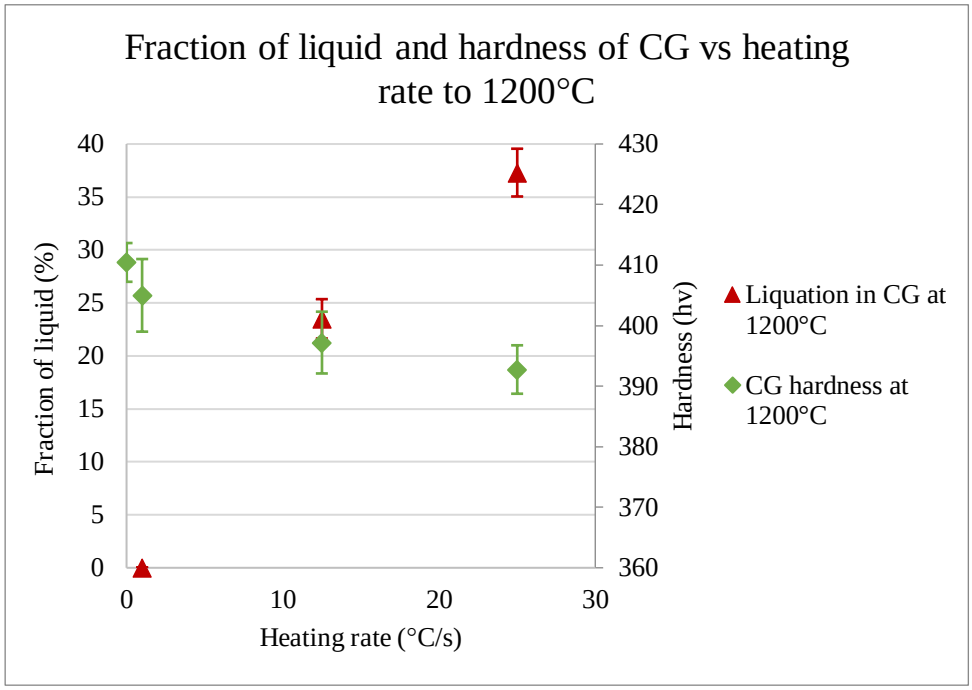

Figure 169 - Plot of hardness & fraction of liquid vs heating rate for CG specimens heated to 1200°C (Error bars indicate 95% confidence intervals).

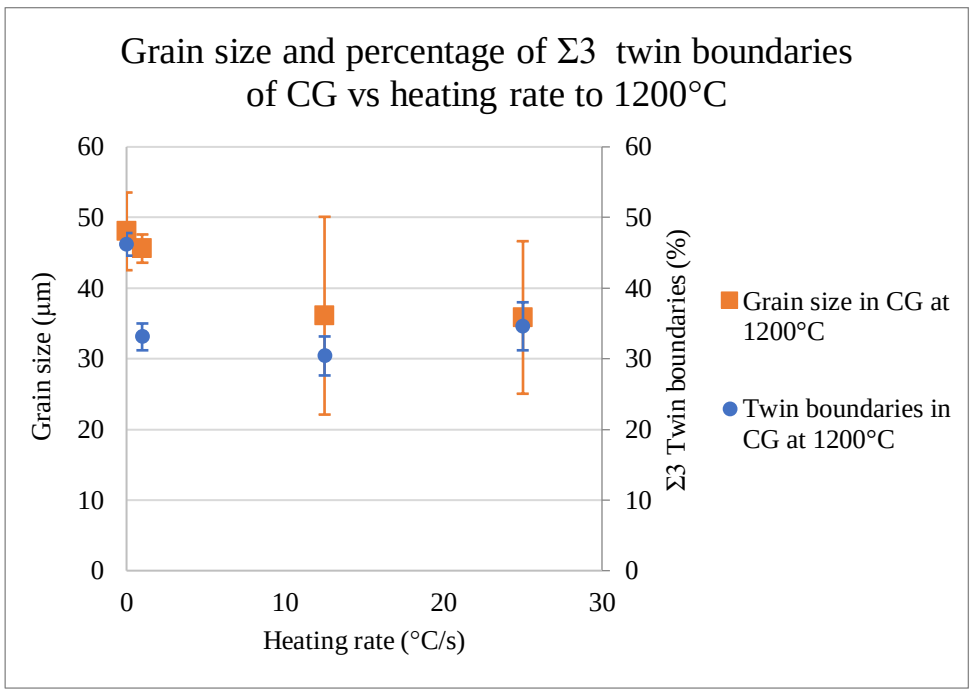

Figure 170 - Plot of grain size & percentage of twin boundaries vs heating rate for CG specimens heated to 1200°C (Error bars indicate 95% confidence intervals).

4.5 Liquation products formed on re-solidification

The liquated material in both the FG and CG variant of RR1000 solidified in the same manner producing the same eutectic features and intermetallic structures. These liquation products would exhibit the same morphology and are formed when two (or more) re-solidifying fronts meet during cooling. Figure 171 illustrates an example of these liquation products. The liquation features have been analysed via SEM and EDS to characterise their composition and gain an insight into their formation mechanics.

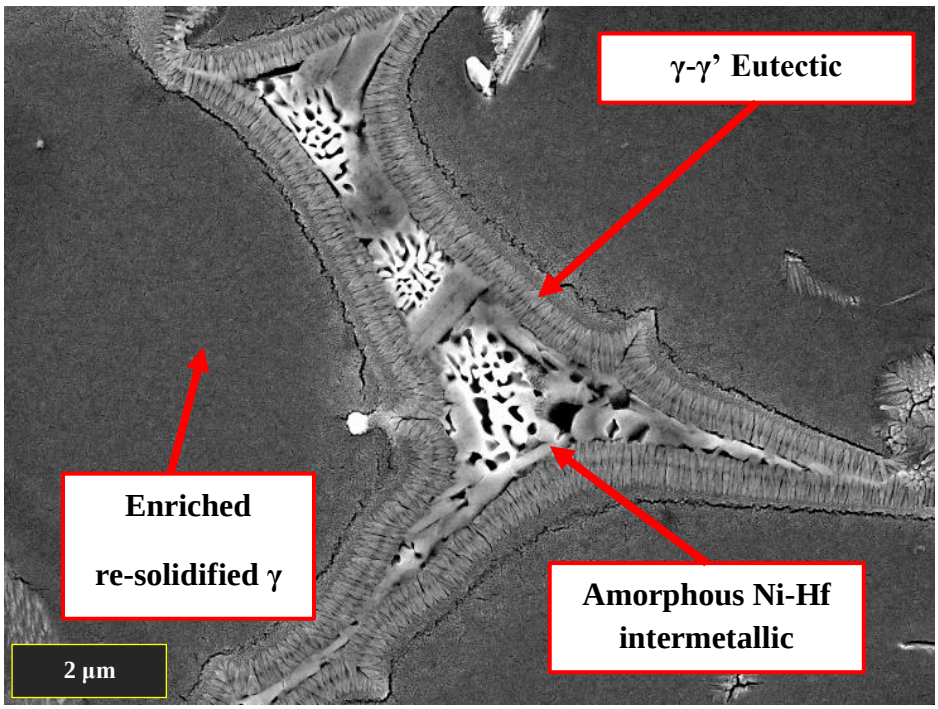

Figure 171 - SEM micrograph of a eutectic feature formed on re-solidification of liquated material.

Most of the re-solidification products contain a central amorphous material. Yi-Hsin Cheng et al [87], reported on their research into HAZ liquation cracking of a similar nickel based super alloy Mar-M004, where they found an identical amorphous material as a result of re-solidification after welding. Their research concluded, via an array of analytical techniques, that these amorphous regions were Ni-Hf intermetallics. The composition of Mar-M004 is very similar to that of RR1000 and therefore, it is highly likely that the amorphous material found in these specimens are also Ni-Hf intermetallics.

This amorphous region is always encapsulated in a lamella structure, which literature suggests is a lamella γ- γ' eutectic feature [63], [88]. Surrounding the lamella γ-γ' is the re-solidified γ, which has a higher density of re-precipitated γ' than the neighbouring γ grains that survived the liquation.

More evidence was needed to confirm the identity of these features therefore, the re-solidification features found in RR1000 were analysed via SEM, backscatter electron SEM (BSE SEM) and EDS.

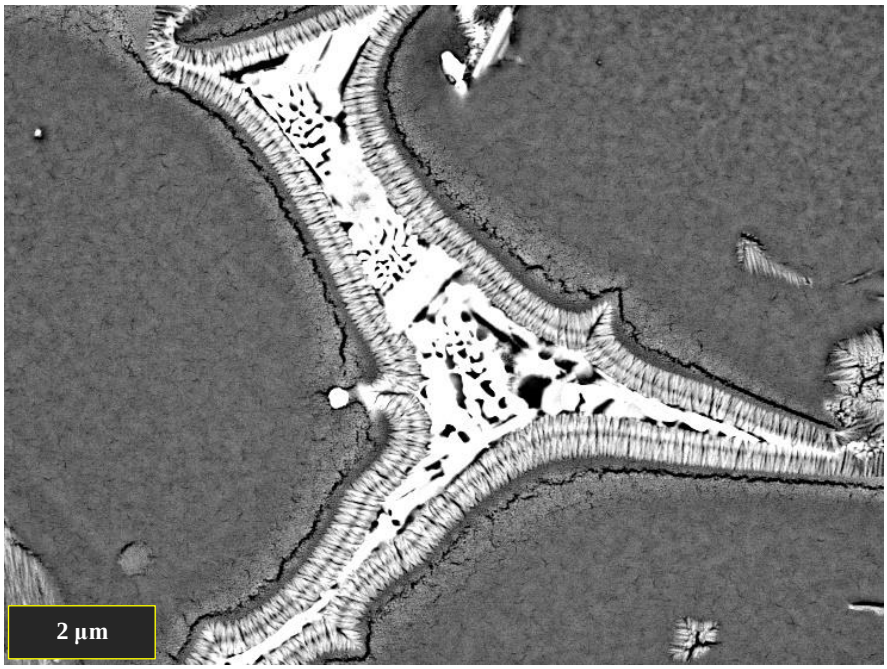

Figure 172 – BSE SEM micrograph of a eutectic feature formed on re-solidification of liquated material.

Imaging the re-solidification product under BSE SEM, see Figure 172, revealed that the suspected lamella γ-γ' eutectic structures and Ni-Hf intermetallic contained considerably more heavy elements than the re-solidified enriched γ surrounding them. They appeared much brighter, further supporting the notion that they may both contain high quantities of Hf.

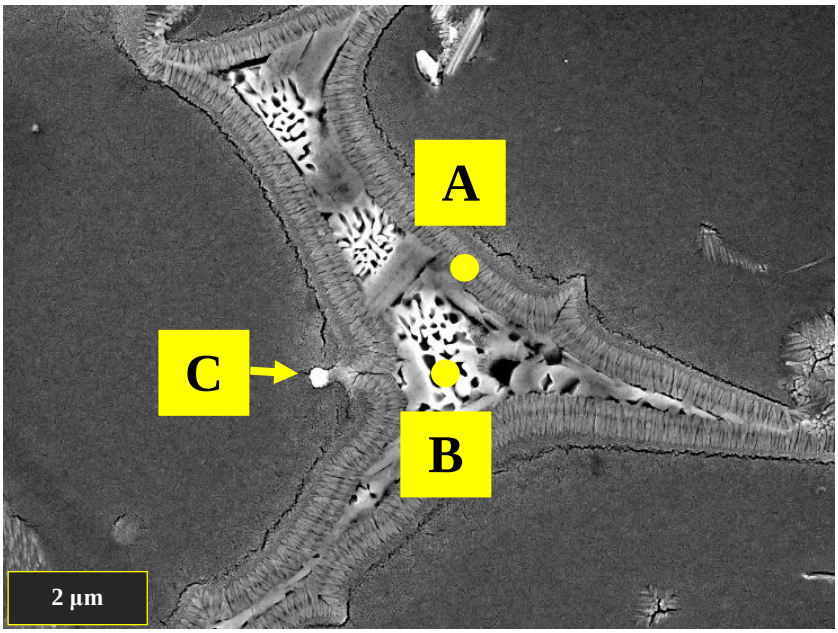

Figure 173 - SEM micrograph illustrating the position of the EDS analysis conducted on a common re-solidification product.

	C	O	Al	Ti	Cr	Co	Ni	Zr	Mo	Hf	Ta
A) suspected lamella γ-γ'	0.0	0.0	3.7	8.1	0.0	14.8	63.2	0.6	2.1	2.7	4.8
B) Suspected Ni-Hf intermetallic	5.5	0.0	0.8	2.0	2.8	13.8	42.9	4.0	4.2	20.1	4.0
C) Hafnia	6.6	12.8	0.8	2.0	0.0	3.8	17.3	1.6	1.0	49.3	4.7

Table 16 - Chemical composition of each site analysed via EDS given in wt.%.

EDS analysis of the three main components found in the re-solidification products was conducted. Although a small spot size and low accelerating voltage was used to minimise the interaction volume, it cannot be guaranteed that the interaction volume was not also encompassing some of the surrounding features. Therefore, this EDS analysis composition data should only be used for a basic comparison and not treated as an exact composition. This analysis revealed that site A in Figure 173, the lamella structure surrounding the amorphous material had significant amounts of Ti, Al, Hf and Ta much like the composition of primary γ'. This further supported that this structure was very likely a lamella γ-γ' formed via a eutectic reaction.

Analysis of the amorphous material at the centre of the re-solidification products (Figure 173, site B) indicated that it contained large amounts of Hf as expected. The composition of the amorphous material found in this study was comparable to that found in Mar-M004 by Yi-Hsin Cheng et al[87]. Often small circular particles would be found neighbouring the re-solidification products. The EDS analysis at Figure 173, site C indicated that these are hafnia particles that are distributed throughout RR1000. The morphology and arrangement of the re-solidification products seen in this study resemble those observed in a study on Mar-M002, conducted by V.R Ming. Where Ni-Hf intermetallics surrounded by γ-γ' eutectic features and accompanying hafnia particles were observed[88].

Figure 174 illustrates the elemental segregation in a typical re-solidification product. Hf, Cr and Mo are seen to segregate to the amorphous NiHf intermetallic region, whereas Ti is heavily concentrated in the lamella γ- γ' eutectic features. The EDS map also highlighted another common re-solidification product, Ti-Ta carbide which can be found in the vicinity of the amorphous Ni-Hf intermetallics and the γ-γ' lamella.

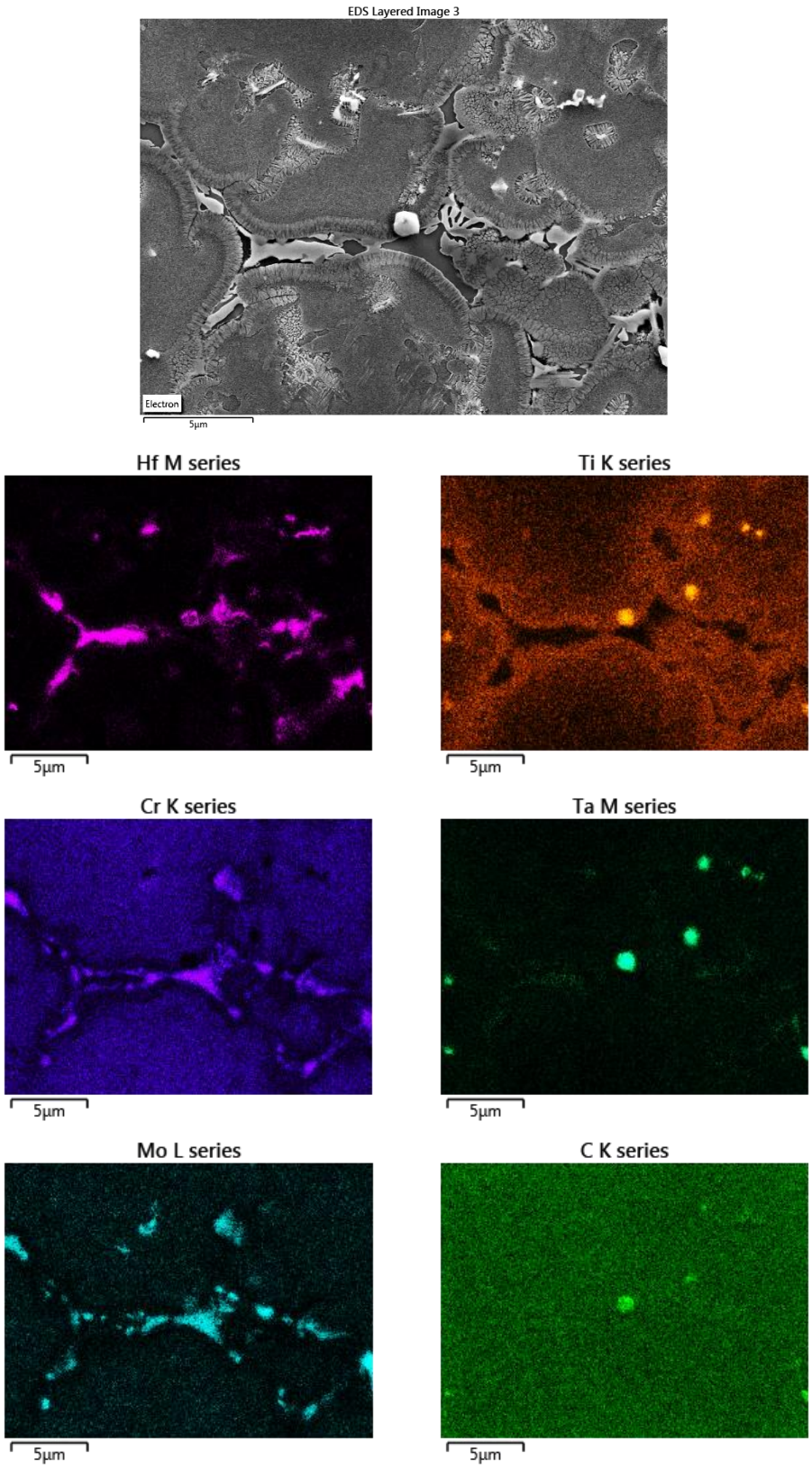

Figure 174 - EDS analysis map of a re-solidification product illustrating the composition.

One of the cuboidal Ti, Ta carbides was analysed via an EDS point scan to give a rough indication of its composition. Figure 175 illustrates the carbide that was analysed. The results of this analysis are given in Table 17 in wt.%.

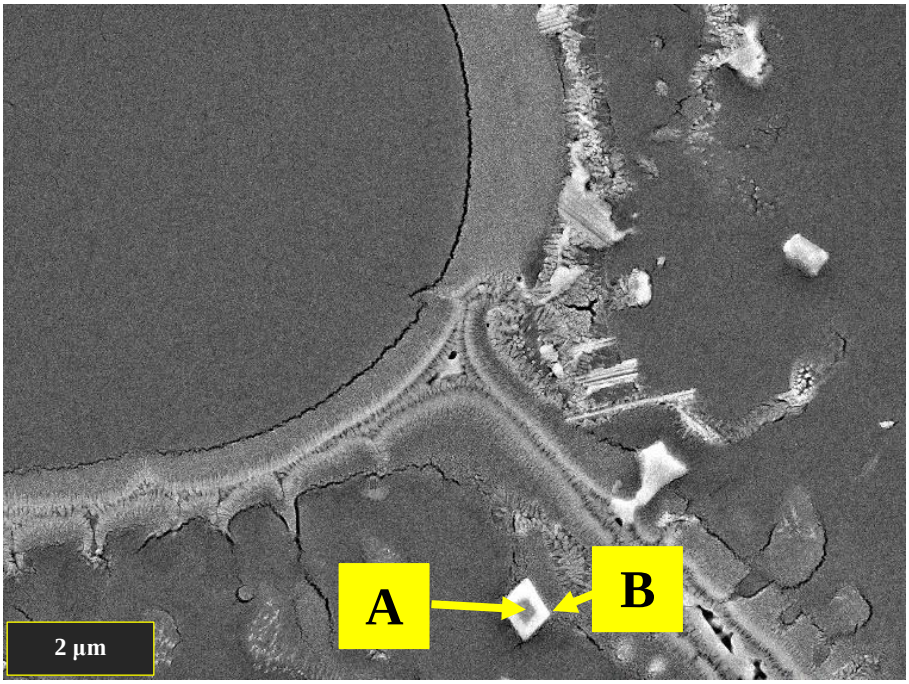

Figure 175 -SEM micrograph illustrating the position of the EDS analysis conducted on another common re-solidification product.

	C	Al	Ti	Cr	Co	Ni	Zr	Mo	Hf	Ta
A) Ti, Ta Carbide - centre	24.5	0.3	30.8	0.0	2.5	7.2	0.0	3.3	4.6	27.0
B) Ti, Ta Carbide - perimeter	17.2	0.8	16.8	0.0	5.0	17.4	0.4	5.9	4.8	31.7

Table 17 - Chemical composition of each site analysed via EDS given in wt.%.

The Ti-Ta carbide had two distinct regions, a bright, outer perimeter and a dark centre. The EDS analysis indicated that the centre had much more Ti and C than the perimeter, whereas the perimeter contained more Ni. Although, both regions of the cuboidal particle had elevated levels of all three elements as well as Hf in comparison with the γ matrix. This analysis can only confirm that the inner and outer regions of the particle likely have differing compositions, as the interaction volume of the EDS point analysis is likely picking up from both regions during each scan. To analyse the exact composition of each region, transmission electron microscopy is required but this was outside the scope of the current research.

4.5.1 Liquated material adopting the orientation of neighbouring grains

When an RR1000 specimen of either variant is heated in an appropriate manner to produce liquation, the liquid adopts the orientation of the surviving grains neighbouring it. Evidence of this is shown in Figure 176 and Figure 177.

Figure 176 is an SEM micrograph of an FG RR1000 specimen that has been heated to 1200°C at 25°Cs^{-1}, resulting in liquation at the grain boundaries and within the grains. Clearly shown is a Σ3 twin boundary in the surviving grain, that has grown back, though the liquated material within the grain and propagated right up to the γ-γ' eutectic feature within the re-solidified material at the grain boundary. This supports the notion that the liquated material is adopting the orientation of the surviving grain it resides by.

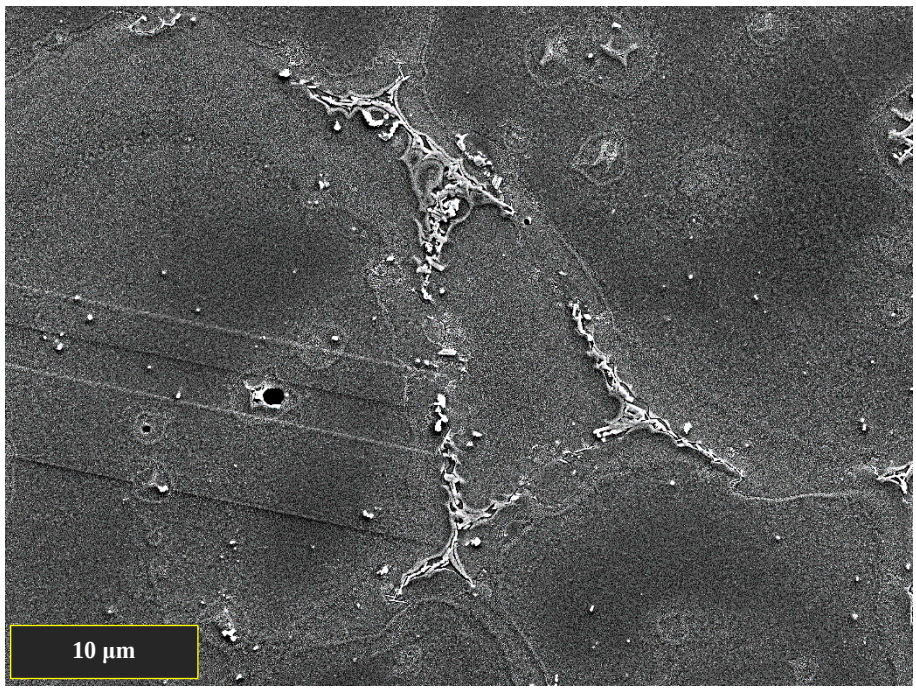

Figure 176 - SEM micrograph illustrating liquated material adopting the orientation of neighbouring grains on solidification.

The EBSD map shown in Figure 177 A shows an orientation map of a CG specimen that was heated to 1200°C at 25°Cs^{-1} resulting in liquation. Figure 177 B, shows an orientation map of the parent CG material. It has been shown that when CG RR1000 liquates, the liquid is widespread throughout the grains as well as at the grain boundaries. Despite this, the orientation map shows no evidence of any intragranular liquid solidifying as new smaller grains with both maps appearing very similar. The only difference between the parent CG orientation map and the liquated CG orientation map is the serrated grain boundaries in the liquated specimen. The serrated grain boundaries are caused by opposing liquid fronts solidifying towards each other and competing for growth. This must mean that the liquated material within the grains is adopting the orientation of the grain in which it resides.

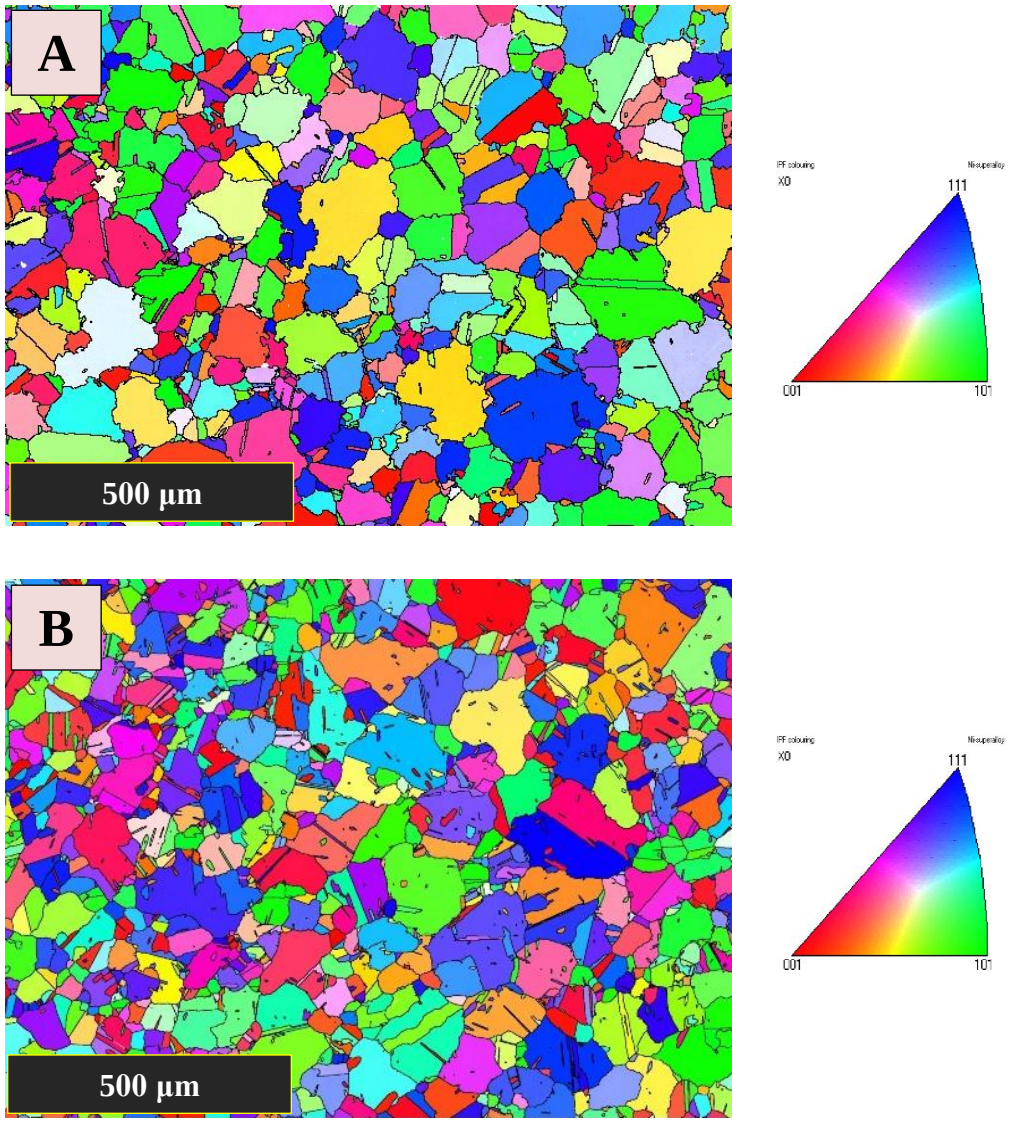

Figure 177 - EBSD IPF maps illustrating the grain orientation of A) A liquated CG specimen. B) The parent CG material.

4.6 Evidence of liquation in interrupted RR1000 inertia friction welds

In order to better understand the dynamic evolution of microstructure during inertia friction welding of both FG and CG RR1000, several interrupted inertia friction welds were conducted by technical staff, at Rolls-Royce Plc [6], [7].

A reduced scale inertia friction welding machine was modified so that one side of the parts to be welded could be released part way through the welding process via a clutch mechanism. This modification has allowed welds of both FG and CG RR1000 to be interrupted at different stages of upset. The graphs in Figure 178 and Figure 179 illustrate the amount of upset each interrupted weld progressed to in comparison to a baseline fully competed inertia friction weld.

Figure 178 shows each interrupted weld conducted with FG RR1000; Figure 179 shows the interrupted welds conducted with CG RR1000. Sections of these interrupted welds have been inspected in this study via optical microscopy and SEM to look for evidence of liquation occurring during the inertia friction welding process.

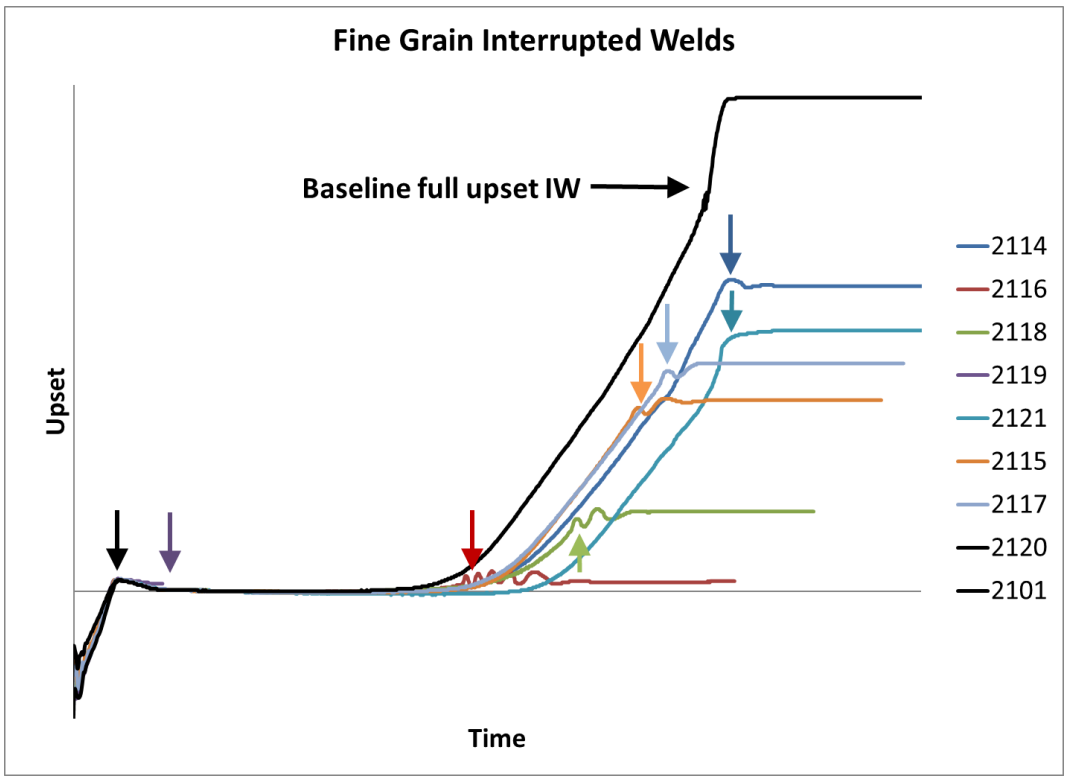

Figure 178 - Weld upset vs weld time curves for the interrupted inertia friction welds conducted with FG RR1000. Graph provided by S.Bray – Rolls-Royce Plc..

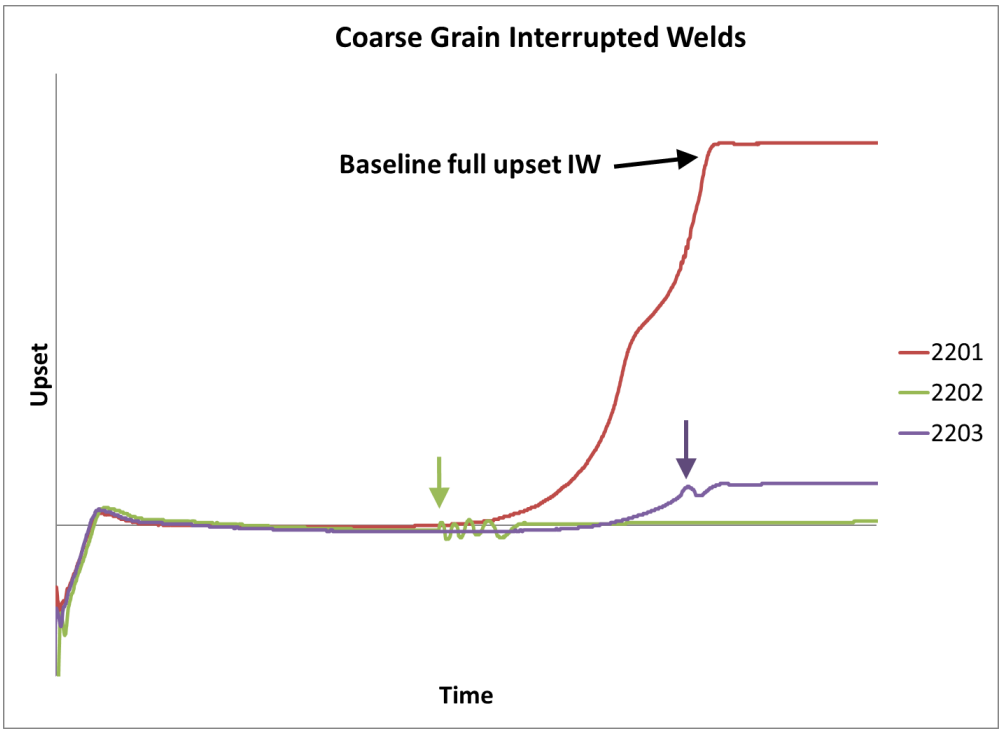

Figure 179 - Weld upset vs weld time curves for the interrupted inertia friction welds conducted with CG RR1000. Graph provided by S.Bray – Rolls-Royce Plc..

Each interrupted weld was inspected for the presence of eutectic features as evidence of liquation. The specimens were also examined optically to assess whether the liquid quantification method detailed in section 3.2.3.1.3 could be applied to calculate the fraction of liquid at the weld line during each stage of welding. The findings of these inspections are detailed below.

4.6.1 Fine grain interrupted welds

Early stages of welding - FG welds 2120 & 2119

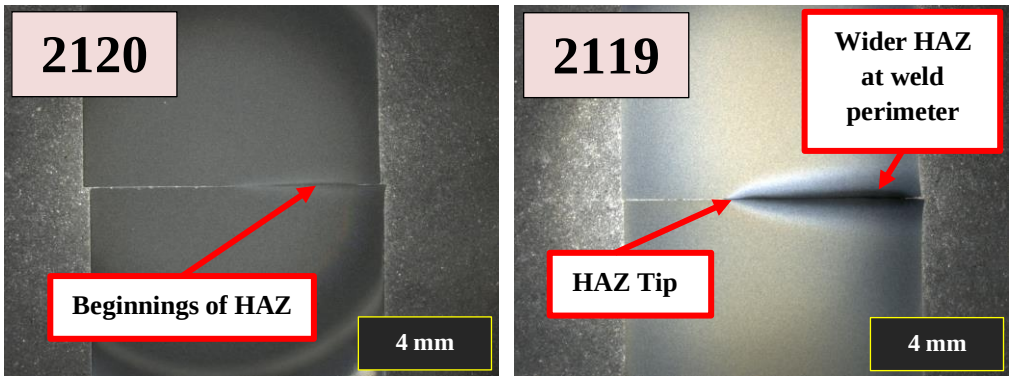

Figure 180 - Optical micrographs of interrupted FG welds 2120 and 2119 taken.

Fine grain welds 2120 and 2119 were interrupted very early on in the inertia friction welding process. As a result, very little microstructural changes were observed in the bulk of the material despite the rapid heating rate at the weld interface. The beginnings of a HAZ are seen in weld 2120; this HAZ has grown larger in weld 2119, both specimens are shown in Figure 180.

A higher magnification optical micrograph of the weld interface of weld 2119 is shown in Figure 181. The image was taken at the tip of the HAZ region where a thin layer of highly deformed material can be found propagating along the weld interface.

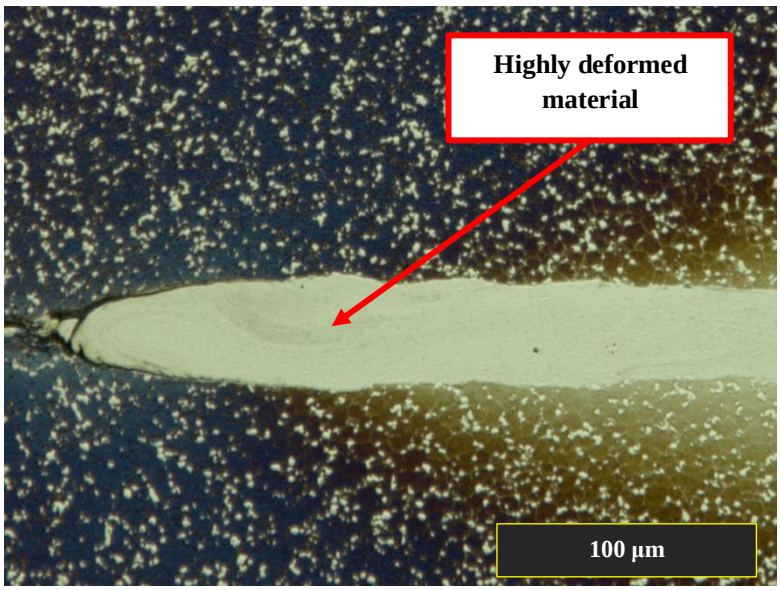

Figure 181 - Optical micrograph of the HAZ tip of interrupted FG weld 2119.

SEM images of this region are shown in Figure 182. The bulk material, adjacent to the highly deformed material, at the weld interface still contains a full distribution of γ' precipitates including tertiary γ'. This suggests that there must be an extreme temperature gradient between these two regions.

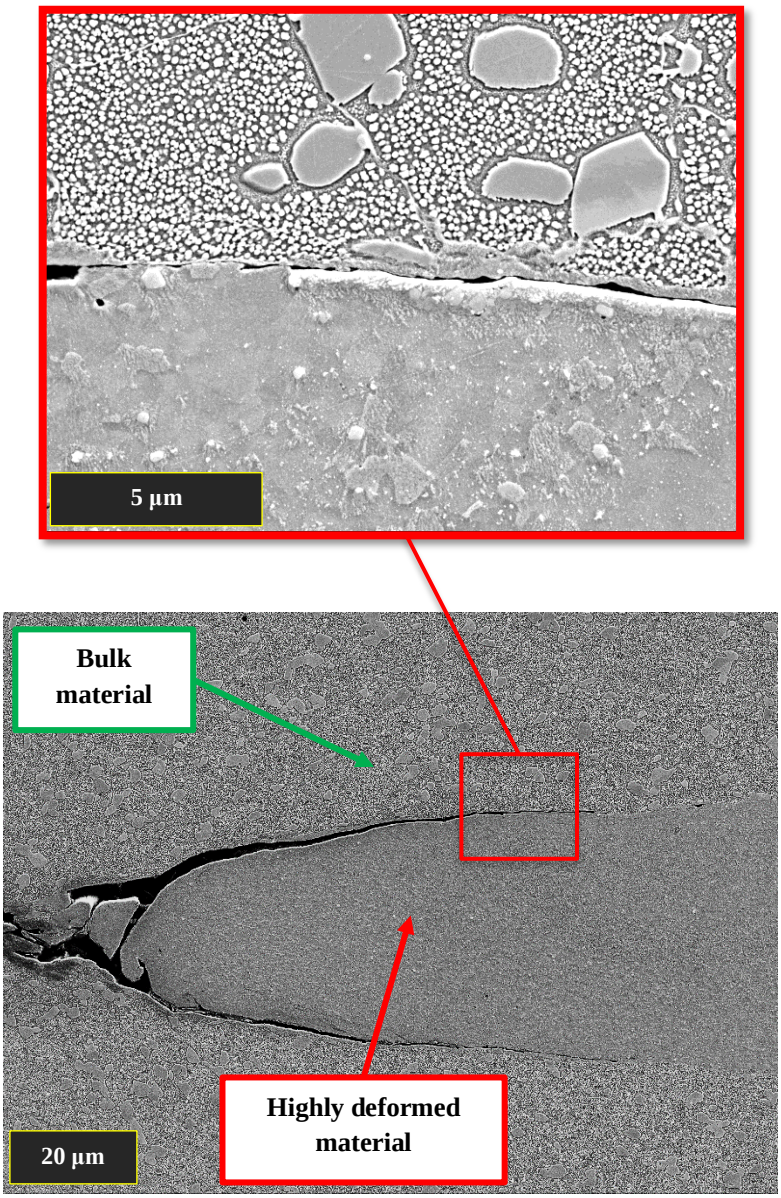

Figure 182 - SEM micrographs of the HAZ tip in interrupted FG weld 2119.

Moving further towards the perimeter of the weld, where the HAZ is largest, microstructural changes to the bulk material can be seen. The weld line still appears highly deformed and unrecognisable in comparison with the parent material. But temperatures in this region have risen enough for the diffusion of the γ' into the γ matrix in the bulk material as can be seen by the γ' gradient in Figure 183.

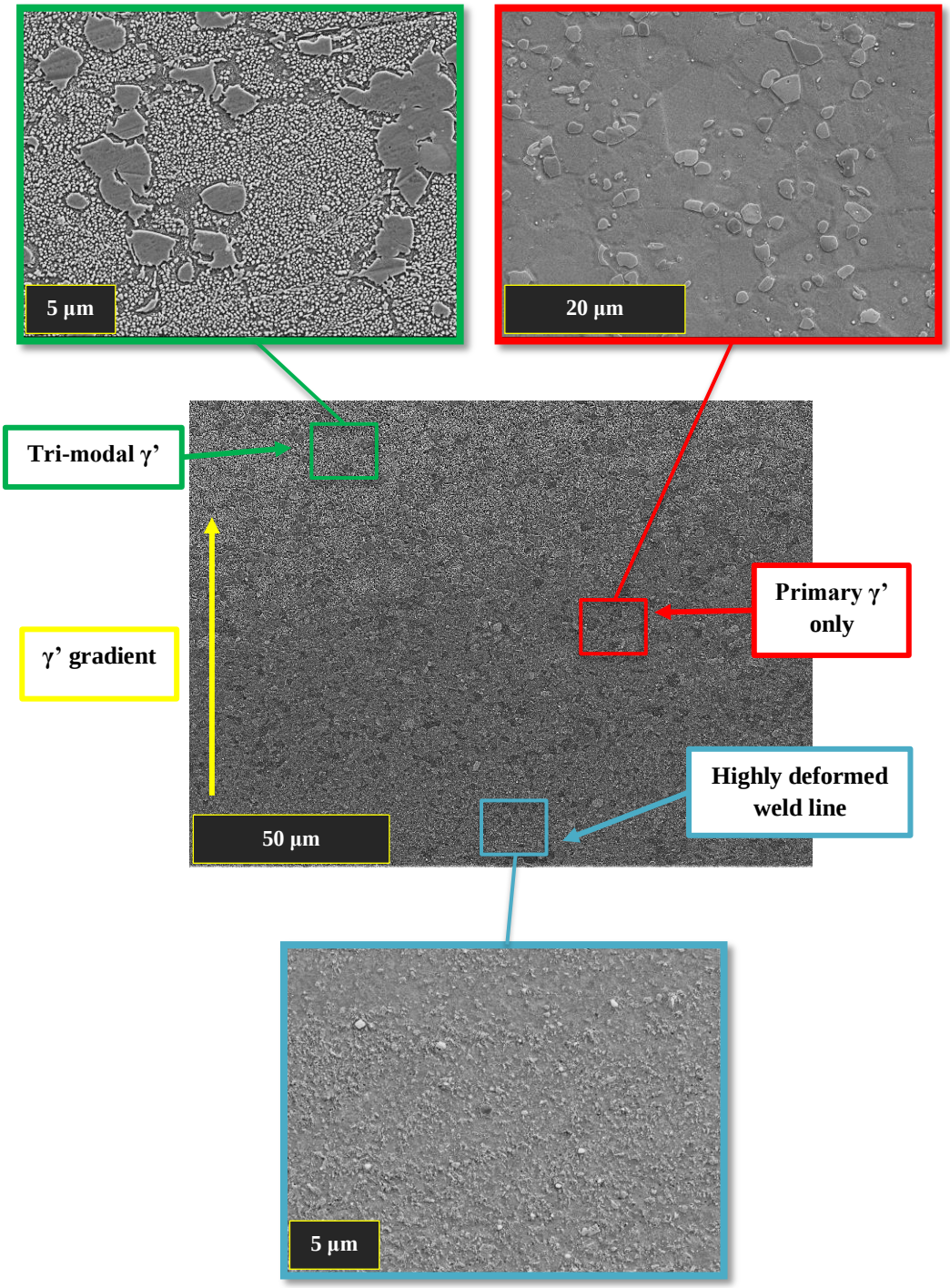

Figure 183 - SEM micrographs of interrupted FG weld 2119 taken in the widened HAZ region.

Although sufficient heat is being generated in this region to cause diffusion of the γ' and the heating rates experienced at the weld interface should be more than enough to cause constitutional liquation of the primary γ' precipitates, no eutectic products were found as proof of liquation.

The specimen was inspected via optical microscopy to see if any liquated regions could be identified via the method previously used on the specimens tested in the semi-solid testing facility. Figure 184 shows the etch response of the wide HAZ region of FG weld 2119. The HAZ region, where liquation would be expected, has had a completely different etch response to the rest of the specimen, possibly due to the extreme amount of strain within this area. As a result of the poor etch response in the HAZ, it could not be confirmed if eutectic products were present in this region to prove the presence of liquated material at this point in the weld.

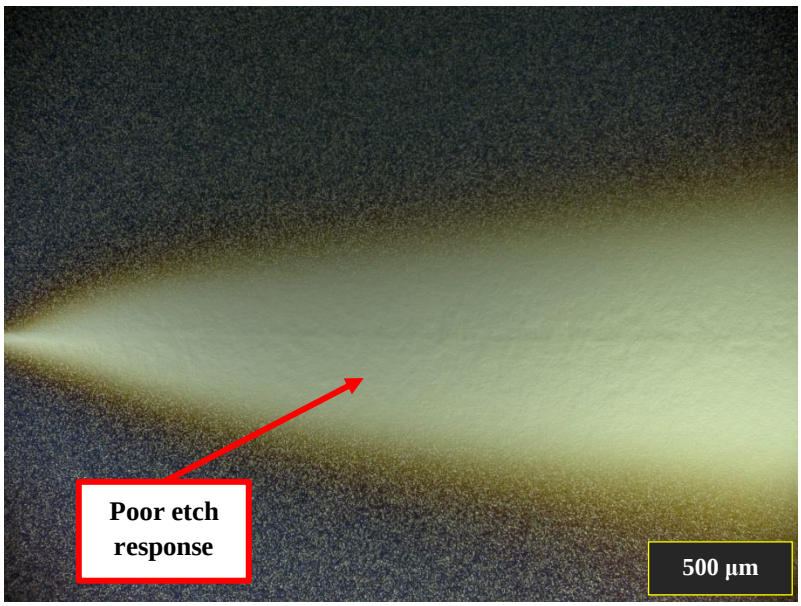

Figure 184 - Optical micrograph of the wide HAZ region in interrupted FG weld 2119.

Mid stage of welding – FG weld 2118

It is not until the bulk material begins to upset significantly, that the current specimens begin to show a similar etch response to the semi-solid specimens previously described. A reason for this could be that fresh material containing γ' is pushed into the weld line during the onset of upset. This material then undergoes rapid heating, which causes the constitutional liquation of primary γ', creating an intergranular liquid. The optical micrograph in Figure 185 illustrates the etch response near the weld line of FG weld 2118, which was interrupted just after significant upset had begun.

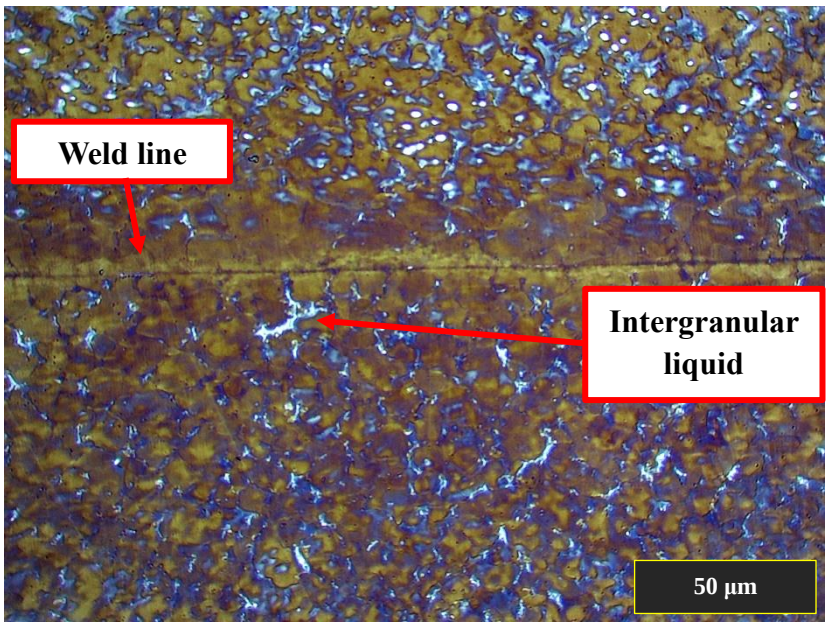

Figure 185 - Optical micrograph of the weld line of interrupted FG weld 2118.

The optical micrograph clearly shows the presence of intergranular liquid adjacent to the weld line, with liquated regions propagating into the bulk material. This area was inspected via SEM to confirm the presence of liquid by locating the intergranular eutectic features that would be formed on re-solidification.

An SEM image, Figure 186, taken at the weld line of FG weld 2118, shows an abundance of intergranular eutectic features. Figure 186 B shows a higher magnification SEM image of the eutectic features exhibiting their lamella γ-γ' structure.

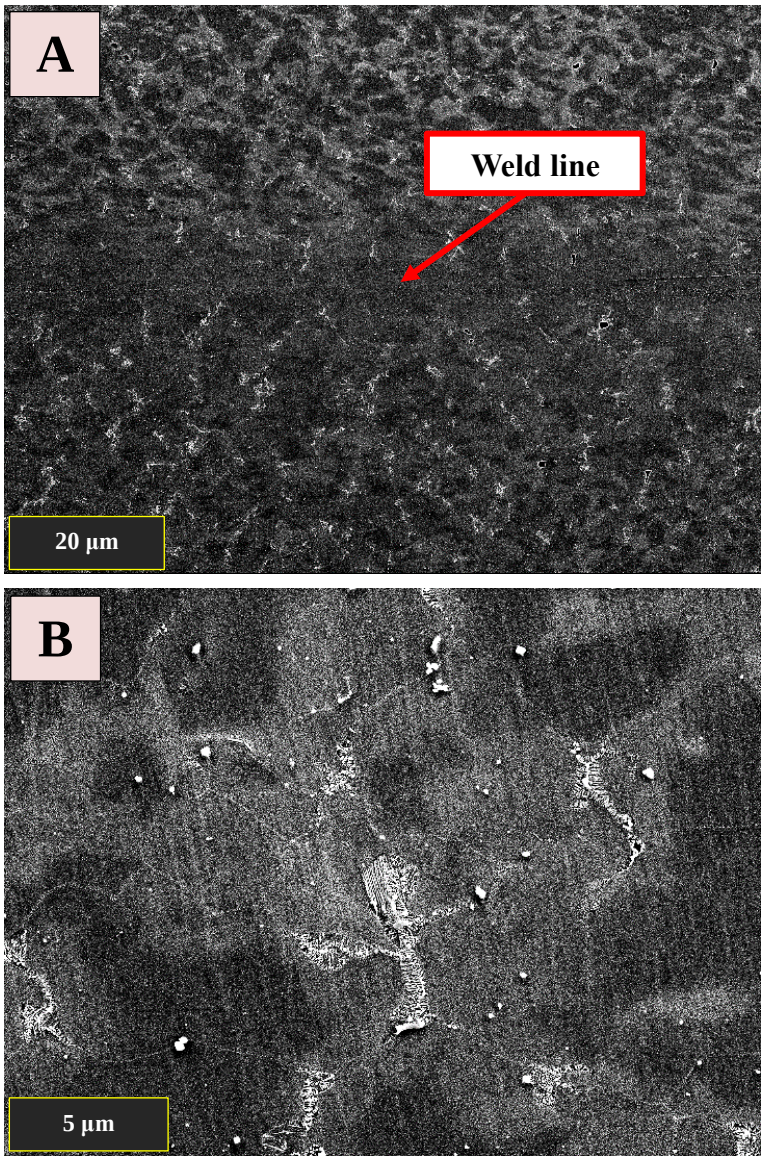

Figure 186 - SEM micrographs of the weld line zone of interrupted FG weld 2118. A) The weld line. B) Image of the eutectic features found at the weld line.

Moving further away from the weld line between the TMAZ and HAZ region the onset of constitutional liquation can be seen, as illustrated in Figure 187. Here you can see pockets of lamella γ-γ' neighbouring a primary γ' which was part way through constitutional liquation when the weld was interrupted.

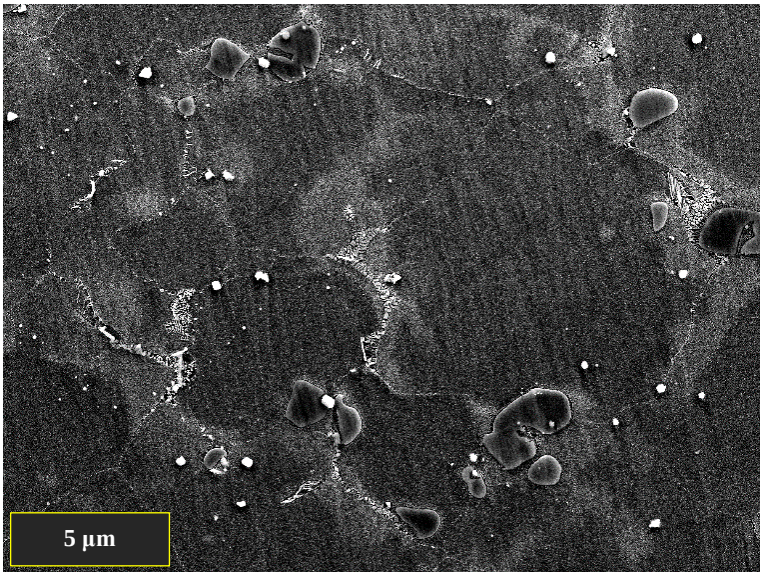

Figure 187 - SEM micrograph taken at the TMAZ-HAZ boundary of interrupted FG weld 2118.

Later stages of welding – FG welds 2114, 2115, 2117 and 2121.

As the weld progresses further and the upset is increased, the liquated material could no longer be distinguished from the bulk material due to the mixing caused by the severe strain experienced at the weld line. As a result, this highly deformed mixture of liquated and un-liquated material etched differently to the semi-solid specimens tested in the semi-solid testing facility. This is shown in the optical micrograph in Figure 188 which depicts the weld line and TMAZ sections of FG weld 2115.

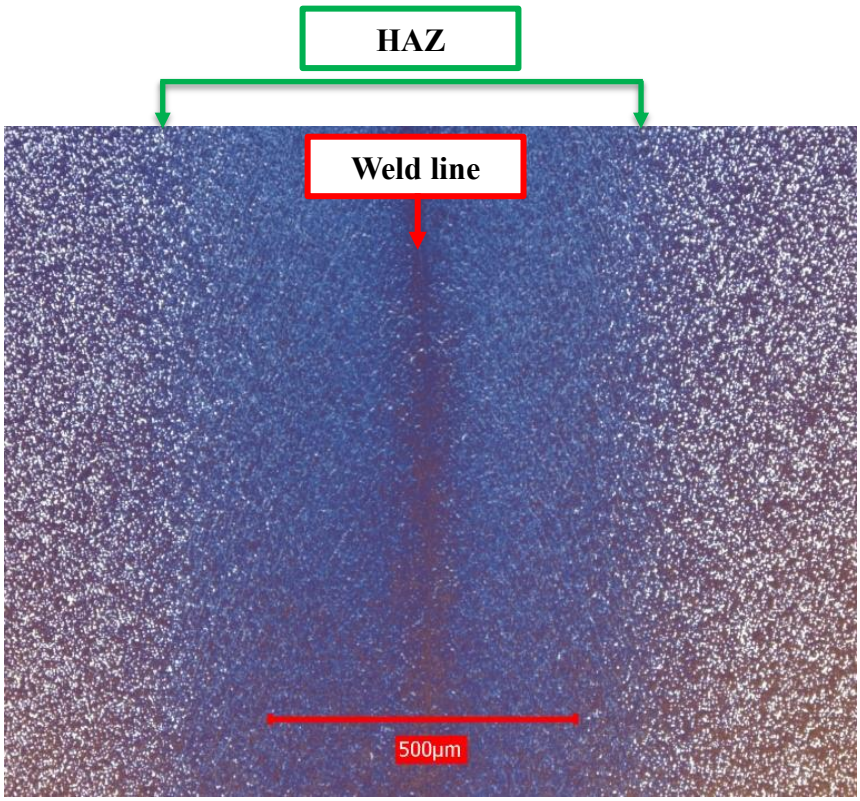

Figure 188 - Optical micrograph of the weld line, TMAZ and HAZ of interrupted FG weld 2115.

Although proof of the presence of liquid could not be obtained optically, inspection of these specimens via SEM revealed eutectic liquation products throughout the TMAZ region as shown in Figure 189. This suggests that heating rates are still high enough, at this late stage of the welding cycle, to initiate constitutional liquation away from the weld line.

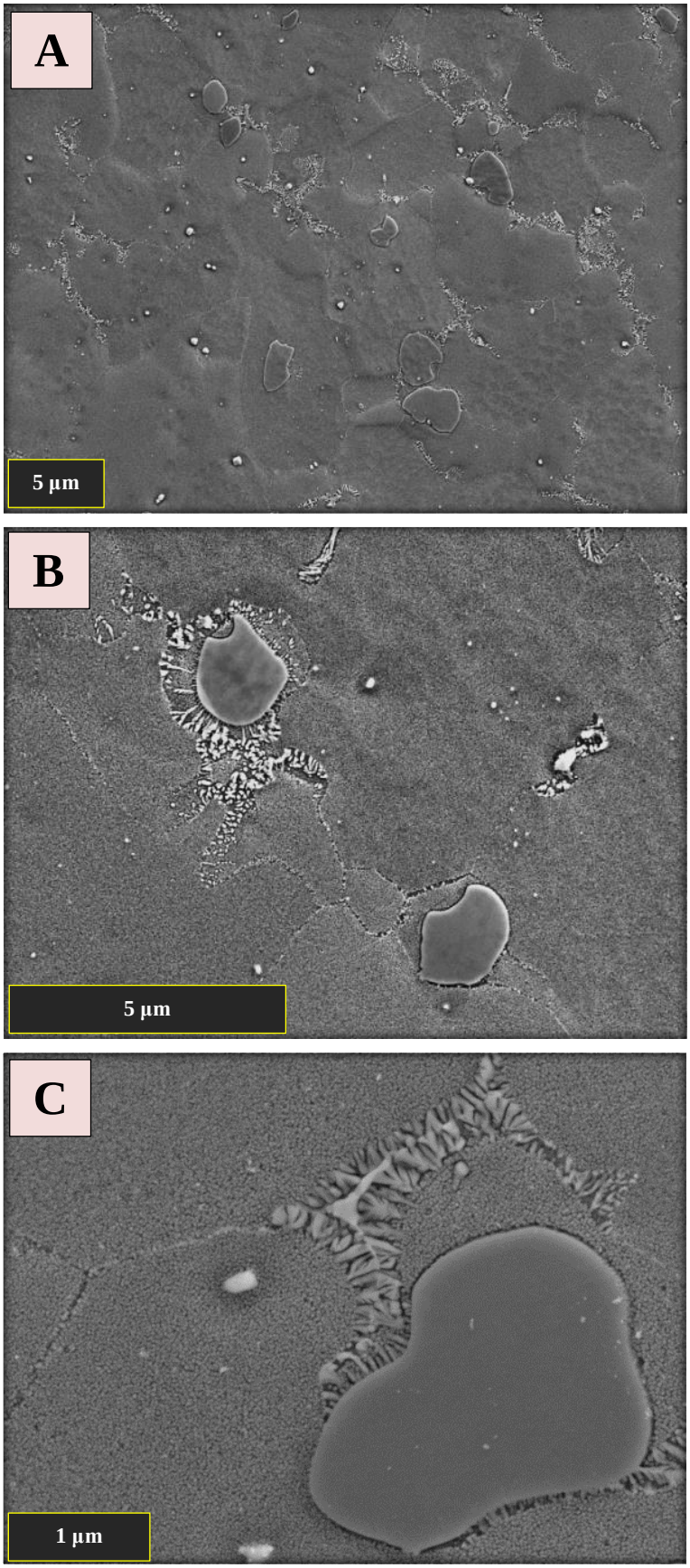

Figure 189 - SEM micrographs of eutectic liquation products found in the TMAZ of FG welds A) 2114 B) 2117 C) 2117.

4.6.2 Coarse grain interrupted welds

Early stage of welding – CG weld 2202

CG weld 2202 was interrupted at the end of the conditioning phase just before the onset of upset. The optical micrograph in Figure 190 shows the weld line and TMAZ of CG weld 2202. The beginnings of liquation are apparent at the grain boundaries as multiple long intergranular eutectic features reside there. The grains closest to the weld line have also started to show some intragranular liquation and begun to disintegrate from the intense strain experienced at the weld line.

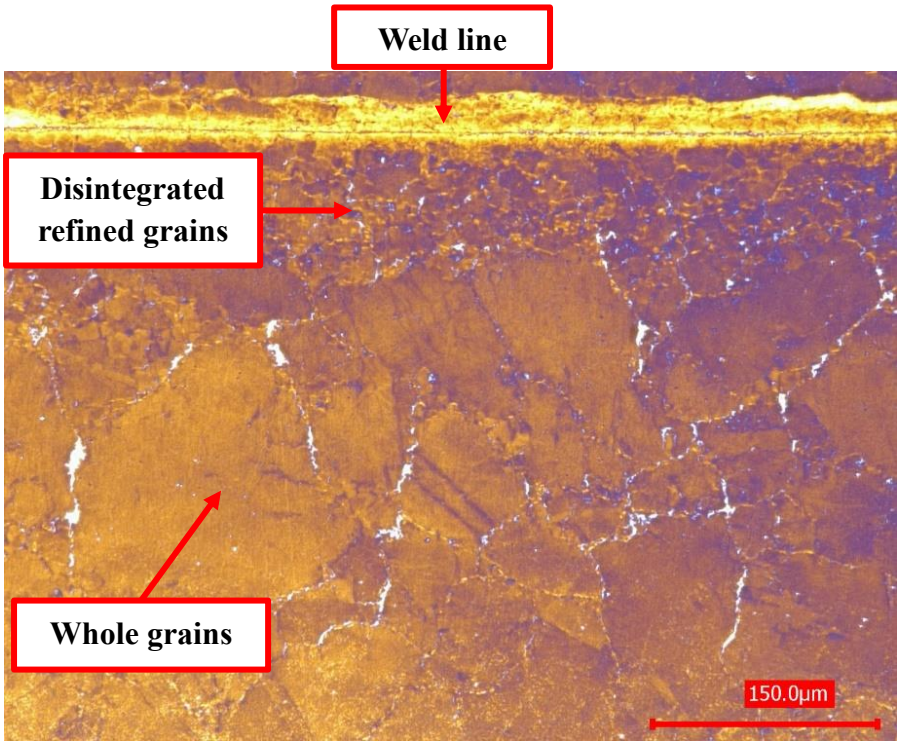

Figure 190 - Optical micrograph of interrupted CG weld 2202.

Interrupted CG weld 2202 was further investigated under SEM to confirm the presence of intergranular eutectic features. The SEM micrographs in Figure 191, illustrate the long features found at the grain boundaries near the weld line in CG weld 2202.

Eutectic features found here resembled those observed in the semi-solid specimens created in the semi-solid testing facility. The liquated material had again re-solidified firstly as a solute rich γ matrix then followed by a lamella γ-γ' eutectic feature, which surrounded a Hf rich centre at the grain boundary.

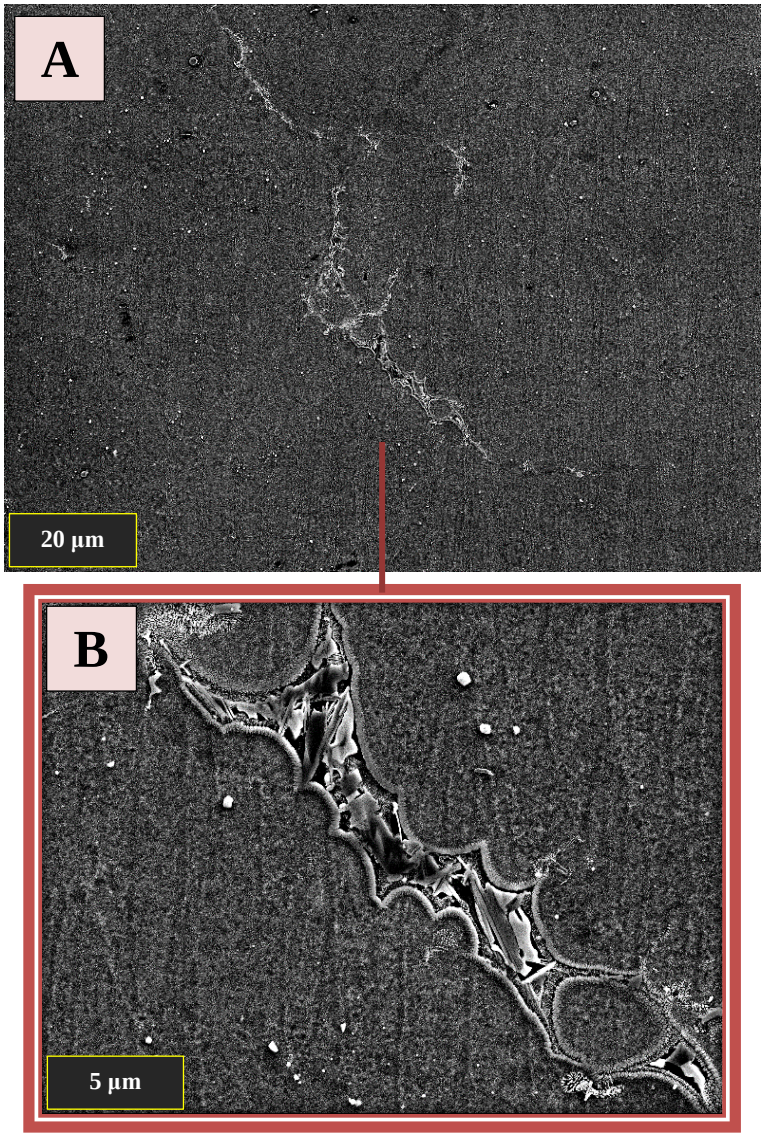

Figure 191 - SEM micrographs of the eutectic features found near the weld line of interrupted CG weld 2202. A) Low magnification. B) High magnification.

Mid stage of welding, the beginning of upset - CG weld 2203

CG weld 2203 was interrupted just after plastic flow had started, leading to a large increase in upset rate. The optical micrograph in Figure 192 depicts the microstructure found at the weld line and TMAZ region of CG weld 2203.

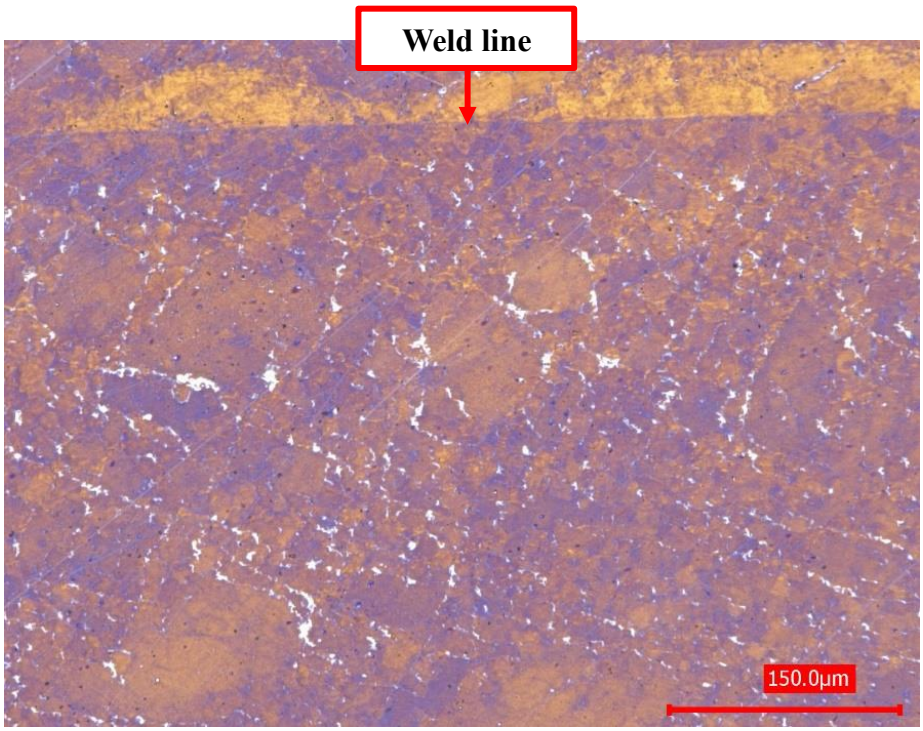

Figure 192 - Optical micrograph of interrupted CG weld 2203.

At this stage in the welding process, the number of grains near the weld line exhibiting intragranular liquation has increased dramatically. SEM analysis of this area confirmed the presence of both intergranular and intragranular eutectic re-solidification products as can be seen in Figure 193 A and Figure 193 B respectively.

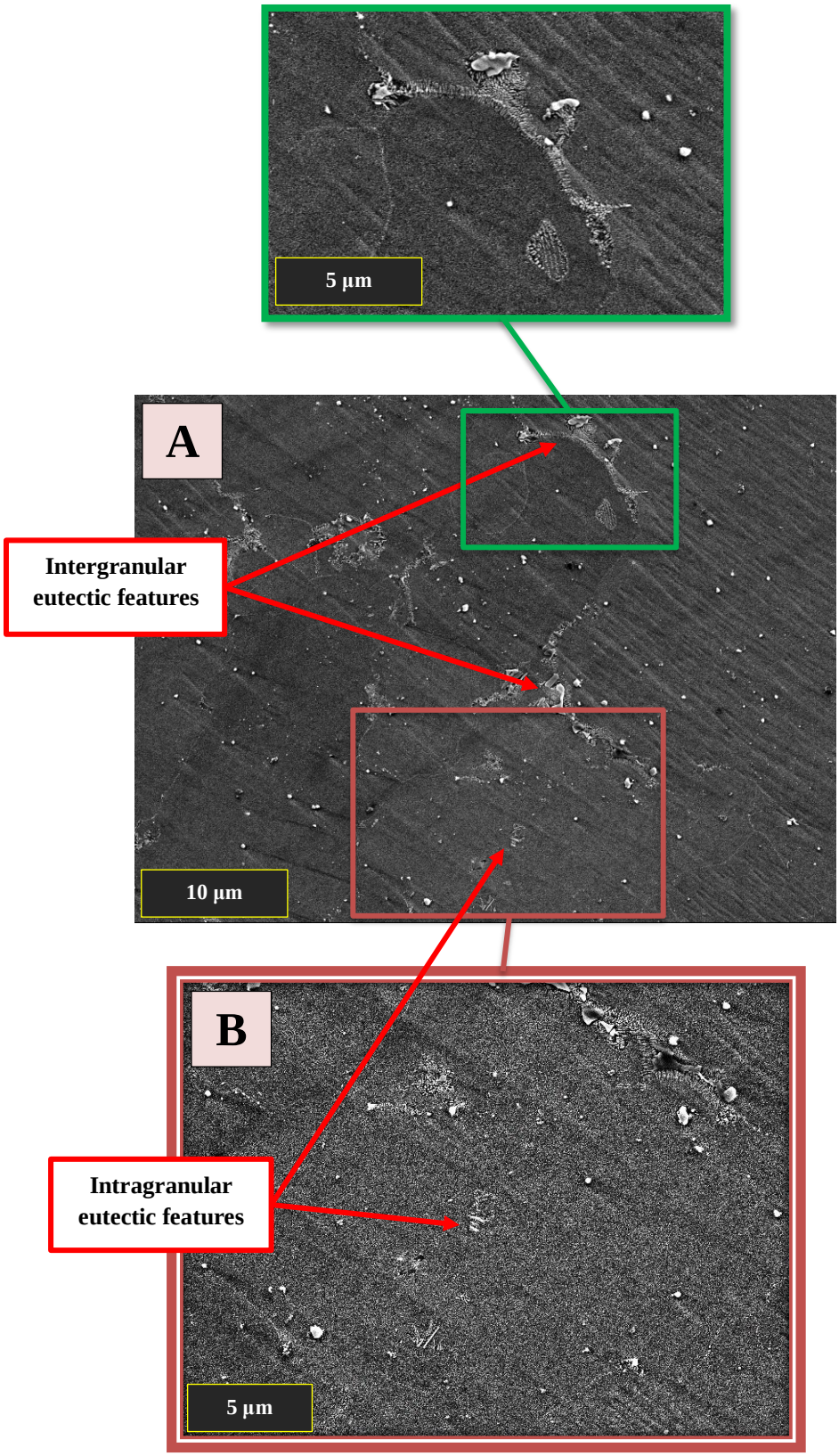

Figure 193 - SEM micrographs of the eutectic features found near the weld line of interrupted CG weld 2203. A) Intergranular features. B) Intragranular features.

Intragranular liquation at the weld line and within the TMAZ region was investigated further via EBSD analysis. The orientation map, Figure 194, shows that the grain structure near the weld line is very different to that of the parent microstructure. The onset of intragranular liquation has led to further refinement of the large grains into smaller grains. Usually it would be assumed that this grain refinement is the result of dynamic recrystallization, but as there is liquid present in this scenario both intergranularly and intragranularly, another mechanism of grain refinement could be at play.

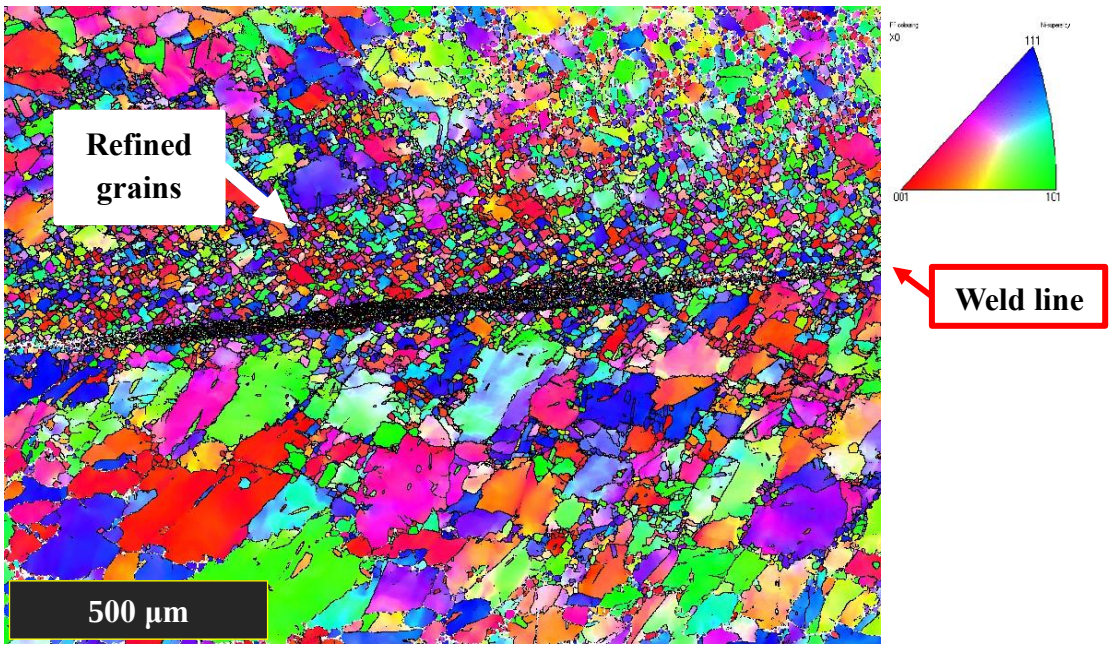

Figure 194 - EBSD IPF map of the weld line and TMAZ zone of interrupted CG weld 2203.

A mechanism for grain refinement via transgranular liquation cracking of semi-solid materials has been reported by S. Karagadde et al[133], during their research on indentation of semi-solid globular microstructures. Their work involved localised indentation of an Al-15wt.% Cu alloy in a semi-solid state with 26% fraction of liquid. The experiments were observed using quantitative in-situ synchrotron X-ray tomographic microscopy, allowing the grain interactions to be recorded in 3D. The mechanism for transgranular liquation cracking they observed is outlined in Figure 195.

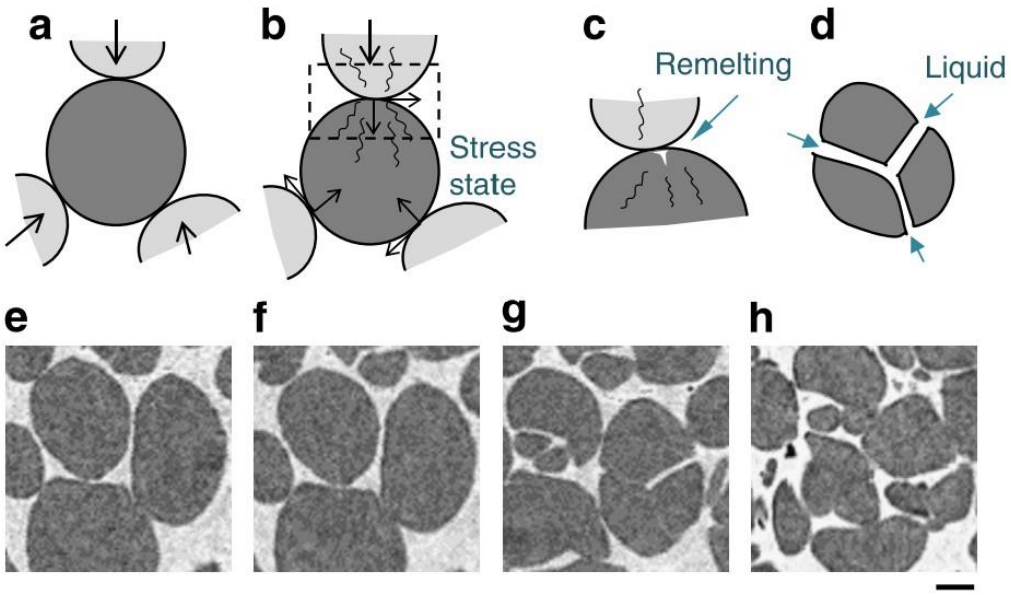

Figure 195 - A-D) Schematic diagram of the transgranular liquation cracking process. E-H) 2D image slices taken from the in-situ synchrotron X-ray tomographic microscopy data illustrating the transgranular liquation cracking happening during testing. Adapted from [133]

The authors reported that there were four stages to transgranular liquation cracking. The first is the motion and pinning of grains against one and other that results in compressive and shear loads (A). Secondly the loading on the grains now induces straining and dislocation movement (B). This can lead to surface re-melting (C), which then allows crack growth from the surface of the grain internally which is accelerated by liquid entrainment (D) [133].

This mechanism for grain refinement, via transgranular liquation cracking, is a very suitable explanation for the reduction of grain size during a CG RR1000 inertia friction weld. This mechanism would likely be more favourable with the presence of vast amounts of intragranular liquation, as exhibited in the CG variant in the heat and quench only semi-solid tests conducted in this study. Further analysis of the EBSD data gathered for the interrupted CG weld 2203, revealed that the surviving large grains near the weld line exhibited transgranular local misorientation. This suggests that they too are experiencing the same transgranular compressive and shear loads prior to their refinement into smaller grains. This transgranular local misorientation is shown in the local misorientation EBSD map in Figure 196.

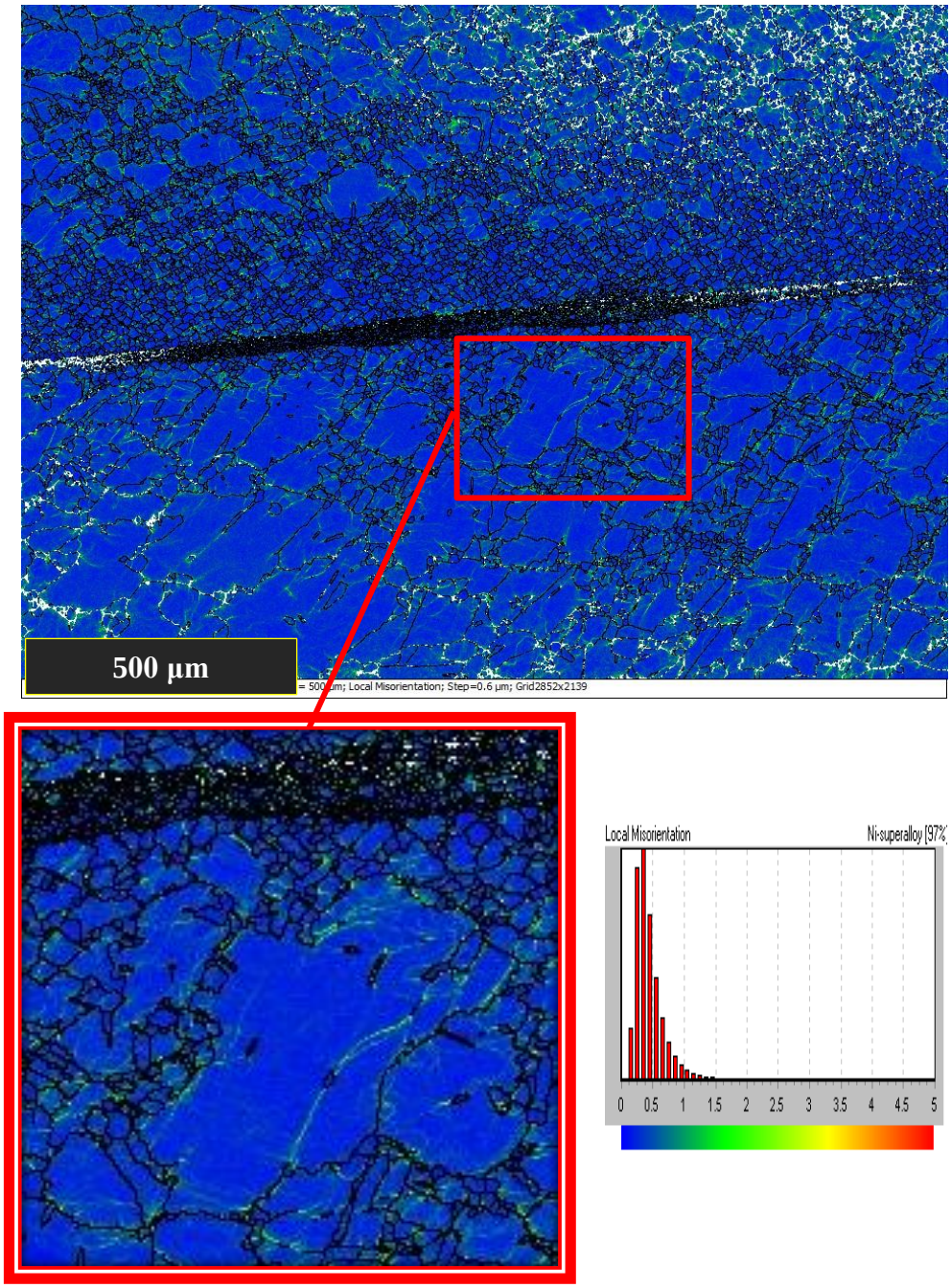

Figure 196 - EBSD local miss-orientation map of the weld line and TMAZ area of the interrupted CG weld 2203.

4.6.3 The role of microstructural evolution and liquation during inertia friction welding of RR1000

This work has detailed many microstructural changes that are experienced by both variants of RR1000 during rapid heating, much like the rapid heating experienced during an inertia friction weld.

Although some grain size and boundary characteristics are altered during rapid heating to temperatures above the γ' solvus temperature (1140°C), the overriding factor in microstructural evolution and the resultant strength is the dissolution of the γ' precipitates and the inherent liquation mechanisms that this brings with it.

It has been shown that the two variants of RR1000 liquate in different ways. The fine grain exhibited constitutional liquation of its primary γ' precipitates on rapid heating past the γ' solvus temperature and then some incipient melting of the γ matrix at 1200°C. The coarse grain exhibited incipient melting of localised areas on rapid heating to temperatures between 1160-1200°C, due to the lack of time for homogenisation of the γ' forming elements after their dissolution into the γ matrix. The difference in liquation mechanisms and the varying distribution of liquid that they produce means that at a given temperature and heating rate, the two variants can possess totally different fractions of liquid, with the FG appearing to be more sensitive to temperature. This would clearly have a dramatic effect on the mechanical properties, and is likely a contributing factor to the difference in upset rates during inertia friction welding of the two variants as shown in Figure 197.

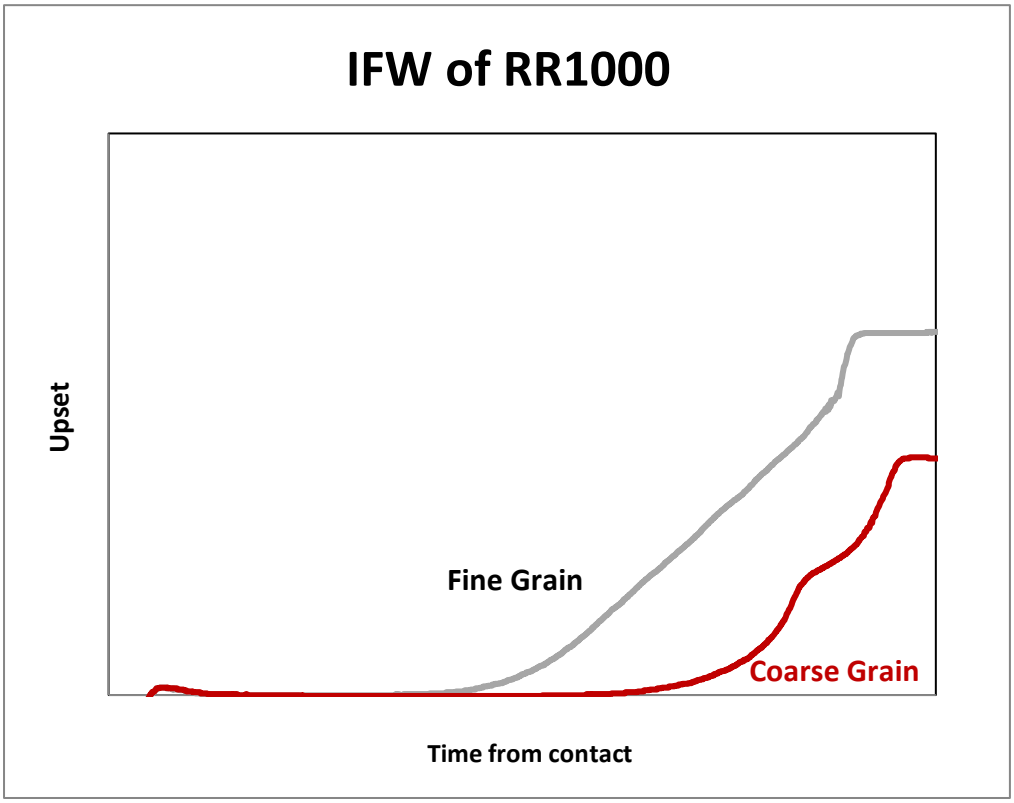

Figure 197 - Weld upset vs weld time plot for inertia friction welds of fine grain and coarse grain RR1000. Graph provided by S.Bray - Rolls-Royce Plc.

It has been shown that the CG variant is more resistant to peak temperature and does not show signs of significant liquation until 1200°C, whereas the FG variant shows substantial amounts of intergranular liquation at 1160°C. This temperature resistance demonstrated by the CG variant is the probable cause of the delay in upset in the CG weld, compared to the FG weld.

As Figure 197 illustrates, the FG material displays a steady upset rate after plastic deformation has been initiated. The CG has a discontinuous upset rate which is initially slower than the FG variant but increases rapidly, then stalls out to a more moderate upset rate before an increase in upset rate is seen again until the end of the weld.

The heat and quench only tests and inspection of the interrupted CG welds, showed that the CG material initially liquates in higher volumes at the grain boundaries. This intergranular liquation would aid grain mobility allowing for the onset of upset. CG weld 2203 was interrupted at the point at which the upset rate begins to increase rapidly. Evidence was found for a transgranular liquation cracking mechanism, which was causing the large grains to be refined into smaller grains. This grain refinement is presumably a contributing factor to the rapid increase in upset rate at this point. The CG variant has also been shown to produce a larger fraction of liquid when heated at $25°Cs^{-1}$ to 1200°C compared to the FG, which would exacerbate the increase in upset

rate further. The combination of these two CG characteristics would most likely cause most of the material at the weld line to be ejected into the flash of the weld after the liquation and ensuing grain refinement had occurred. This would result in fresh material being introduced to the weld interface for the process to start again and could explain the sudden increase, followed by a decrease, in upset for the CG variant.

The FG variant exhibits intergranular liquation on rapid heating past the γ' solvus temperature, as a result of constitutional liquation of the primary γ'. This liquation quickly leads to a microstructure that consists of fine grains that are fully wetted at the grain boundaries, again leading to improved grain mobility. This newly found grain mobility would allow the weld interface to upset at this point, like the CG variant, but at a faster rate due to the smaller grain size.

This liquated material would then be pushed into the flash of the weld at a steady rate while fresh material is pushed into the weld interface inducing more constitutional liquation. This cycle of liquation and removal of material would explain the constant upset rate exhibited by the FG variant.

A crude analogy that compares the physical process of welding the two variants would be to think of welding the FG variant as stirring wet sand, where the surviving grains are the sand particles and the liquated material is the water. Whereas welding the CG variant is initially like stirring wet gravel where the larger grains are the gravel and the liquated material at the grain boundaries is the water. The CG then undergoes the grain refinement as shown and becomes more like the stirring of wet sand like the FG variant.

5 CONCLUSIONS

5.1 Semi-solid testing facility

Much of the current project was spent on the design and commissioning of a new semi-solid testing facility. The new testing facility is capable of heating RR1000 compression specimens at 25°Cs^{-1} to 1200°C with no temperature gradients. This capability has allowed investigation into the evolution of microstructure and sub-solidus liquation mechanisms induced by rapid heating, and the liquid propagation rate to be characterised in both FG and CG RR1000. In order to get the testing facility to this point, many iterative modifications were needed, to improve the performance and functionality of the facility, after its installation. The outcomes of these alterations are summarised here.

- Optimisation of induction coil design - The best performing coils were manufactured from 4mm diameter copper tubing in a conventional helical style coil of 20mm diameter with 8 turns. Fluxtrol magnetic flux concentrator was also shown to be beneficial to coil performance.

- Temperature gradients across the specimen could only be removed by complete isolation from the platens during heating. This was achieved using either the 'floating' specimen method or fibrous insulating specimen holders.

- The emissivity of different specimen coatings was trialled, resulting in HE6 thermal paint being used to achieve accurate temperature readings.

- Conventional PID tuning methods could not be used in the semi-solid testing facility, due to the small thermal capacity of the specimen and the large power of the induction heater. Consequently, the PID controller was tuned via an iterative method. This tuning method produced allowed temperature to be controlled accurately between 900°C and 1200°C.

- The semi-solid testing facility was used to reproduce the observations of M. Attallah et al [4], showing evidence of constitutional liquation of primary γ' in FG RR1000. This validated the semi-solid testing facility, allowing the work of M. Attallah et al to be built on, by investigating the liquation mechanisms of CG RR1000 and the liquid propagation rates in bulk specimens of both variants.

- Although the complications with RF radiation prevented the semi-solid compression tests from being conducted, the two proof of capability tests illustrated that the platen temperature could be increased to the specimen temperature during testing. This shows that compression testing in the semi-solid facility is feasible with some further modifications.

5.2 The microstructural evolution and liquation mechanisms of RR1000 in response to rapid heating.

This research has demonstrated that when subject to rapid heating, both variants of RR1000 experienced drastic microstructural changes. The parent microstructure has a major influence on how each variants' microstructure evolves during heating and the effect on mechanical properties that these resultant changes lead to. The main findings are summarised here.

γ' distribution and its effects on hardness

Each of the microstructural changes has an impact on the resultant mechanical properties, but the size and distribution of the γ' precipitates were found to be the overriding factors governing resultant hardness.

- Rapidly heating both variants to 900°C resulted in a reduction in hardness in both variants due to the loss of some tertiary γ'.

- Strength was not regained until the re-precipitation of a very fine γ' occurred.

- Reprecipitation of fine γ' was only induced at temperatures where sufficient volume of the original γ' had diffused into the γ matrix to create a strong enough driving force for re-precipitation during rapid cooling.

- The temperature needed for reprecipitation was lower in FG than in CG, resulting in the FG variant regaining most of its hardness at lower temperature exposures compared to the CG.

- The ability of the FG variant to recover its strength at lower temperature exposures compared to the CG is a likely cause of the shallower hardness trough in the FG inertia friction weld that was reported by Huang et al[55].

Grain Characteristics

The change in grain characteristics of the two variants when rapidly heated had some similarities and some differences.

- The FG underwent grain growth when heated to temperatures above 1050°C due to the loss of some of the intergranular primary γ'. This grain growth was halted by the presence of intergranular liquation. Slow heating rate tests confirmed this by showing the grains would grow considerably more if no intergranular liquation were present.

- The CG variant's grain size was unaffected in any of the heat and quench tests, even when large quantities of liquation were created.

- The FG variant experienced an increase in the percentage of Σ3 twin boundaries when the grain size had grown.

- Both variants experienced reductions in the percentage of Σ3 twin boundaries when heated to 1160°C and above. This reduction in Σ3 twin boundaries was found to have no significant effect on the resultant hardness.

Liquation mechanisms

Two liquation mechanisms were found to occur in RR1000, namely: -

- Constitutional liquation of primary γ'.
- Incipient melting of the γ matrix.

❖ Constitutional liquation of the primary γ' in the FG variant was caused by rapid heating. Rapid heating rates cause a change in the dissolution kinetics of γ' precipitates allowing them to survive to temperatures where they would usually diffuse into the matrix under equilibrium conditions. If the heating rate was sufficient, then the primary γ' in FG RR1000 survived to a temperature above the γ' solvus (1140°C) where it liquated via a eutectic reaction with the surrounding γ matrix. The occurrence of this mechanism in FG RR1000 had been previously reported by M. Attallah et al [4]. The new semi-solid testing facility was deemed fit for the purpose of investigating liquation mechanisms in RR1000 after it was used to reproduce the findings of M. Attallah et al.

❖ Incipient melting was witnessed in both RR1000 variants but was most prevalent in CG. The incipient melting that occurred was not the conventional incipient melting of low melting point phases, but an incipient melting of the γ phase mechanism. This type of incipient melting was caused by the mass diffusion of γ' forming elements into the γ matrix, which led to localised areas of highly alloyed material with reduced melting points. This possibility of this incipient melting mechanism being able to occur in nickel superalloys was reported by F. Tancret [5]. The present study proposed that this mechanism was the likely cause of the mass liquation in CG RR1000. Evidence was found to support the occurrence of this mechanism in RR1000, which has not been reported until this study. This type of incipient melting was found to occur even at $1°Cs^{-1}$ in CG RR1000 but was exacerbated by increasing heating rate.

Volume of liquation and its propagation

- A method of quantifying the fraction of liquid via examination of optical micrographs has been developed. This method has been validated by corresponding the blue and white globular regions in optical micrographs to the eutectic γ-γ' re-solidification products in SEM micrographs.

- The FG variant was found to be more sensitive to peak temperature exposure, producing significant quantities of liquation when rapidly heated to 1160°C. In contrast the CG exhibited very little liquation at 1160°C but went on to surpass the FG in liquid fraction when peak temperatures were raised to 1200°C.

- The volume of liquid created during the initial liquation event was strongly dependent on heating rate in both variants, with faster heating rates resulting in higher initial fractions of liquid.

- The liquid propagation rate has been characterised and appeared to be largely unaffected by peak temperature or heating rate. The liquid fractions in all heat, hold and quench tests increased with hold time, in a similar manner. Logarithmic trend lines were found to fit the liquid propagation rate well. The liquid propagation rate in RR1000 had not been characterised until this study.

- The CG variant was found to exhibit more liquation then the FG variant when heated to 1200°C at 25°Cs^{-1}. This trend was consistent at all hold times. When the heating rate was reduced to 12.5°Cs^{-1} the fraction of liquid in each variant at 1200°C became comparable.

- The propagation of liquid with time held at temperature, had little to no effect on grain size, grain boundary characteristics or the resultant hardness, suggesting that most microstructural changes occur on the lead up to and during the initial liquation event.

- Only if the initial fraction of liquid was increased considerably was a reduction in hardness observed. This was most evident when increasing the heating rate to induce more liquation. The reduction in hardness was more prominent in the FG variant due to the increased number of grain boundaries for the quench crack mechanism to act upon.

- The presence of intergranular liquid acted to pin the grain boundaries in the FG variant, preventing any further grain growth.

Re-solidification products

- Most of the solidified liquated material adopts the orientation of the grain it resides in or, in the case of intergranular liquated material, the orientation of the grain neighbouring it. Re-solidified liquated material was also shown to adopt the orientation of Σ3 twin boundaries.

- Fronts of re-solidifying material grow from neighbouring grains towards each other competing for material. This resulted in serrated grain boundaries.

- Liquated material re-solidifies initially as γ enriched in γ' forming elements, followed by a γ-γ' lamella eutectic feature, which is also rich in γ' forming elements especially Ti. This lamella γ-γ' surrounds a Hf rich amorphous intermetallic, which is the last to solidify.

- Ti-Ta carbides and hafnia particles can often be found neighbouring the γ-γ' eutectic features.

- Liquated material was shown to have a composition that was an intermediate between γ and γ'. This supported the suspected liquation mechanisms in each variant.

5.3 The role of liquation in IFW of RR1000

- Evidence of liquation was found in both the FG and CG interrupted inertia friction welds.

- Evidence was found to suggest the grains were completely wetted at the onset of significant upset in both variants. Therefore, upset is likely controlled by grain mobility in liquid.

- The CG variant showed signs of grain refinement with evidence to suggest a transgranular liquation cracking mechanism as proposed by S. Karagadde et al[133].

- The grain refinement exhibited by the CG variant would lead to a change in grain mobility and is a likely cause of the discontinuous upset rate experienced in the CG welds.

6 Further Work

- **Semi-solid compression tests.** Development of the semi-solid testing facility during this project has shown that semi-solid compression testing via this method is feasible. The work in this thesis provides a strong base for the research in this project to be continued. In order to conduct these compression tests, some alterations would have to be made to achieve correct platen temperature. The cause of the RF radiation would need to be found and eliminated. The flow stress produced from these tests along with micrographs of the resultant specimens could be used to confirm whether the upset rate of RR1000 during IFW is governed largely by grain mobility after the onset of liquation.

- **Finding the critical heating rate for liquation.** The critical heating rate to induce liquation in the FG variant was found to be between $1°Cs^{-1}$ and $5°Cs^{-1}$. In the CG variant liquation was induced at $1°Cs^{-1}$. Conducting more heat and quench only tests at incrementally lower heating rates could allow the critical heating rate to be quantified. This information can then be applied to the temperatures experienced in an IFW to map out the areas where liquation can be expected.

- **Identification of liquation products.** The exact identity and composition of the re-solidification products, including the Hf rich intermetallics at the centre of the solidification products, could be found via the use of X-ray diffraction (XRD), EBSD and transmission electron microscopy.

7 Appendix A

The specimens used in the 12.5°Cs^{-1} heating rate heat, hold and quench tests were also fully characterised. The same trend was exhibited by the 12.5 °Cs^{-1} specimens as the 25°Cs^{-1}, with very little change to grain size, Σ3 twin boundary density and therefore, very little change to the average hardness value of each specimen. The plots illustrating these results are included below for reference.

FG specimens heated at 12.5°Cs^{-1} to 1160°C and held at temperature.

Grain size vs hold time.

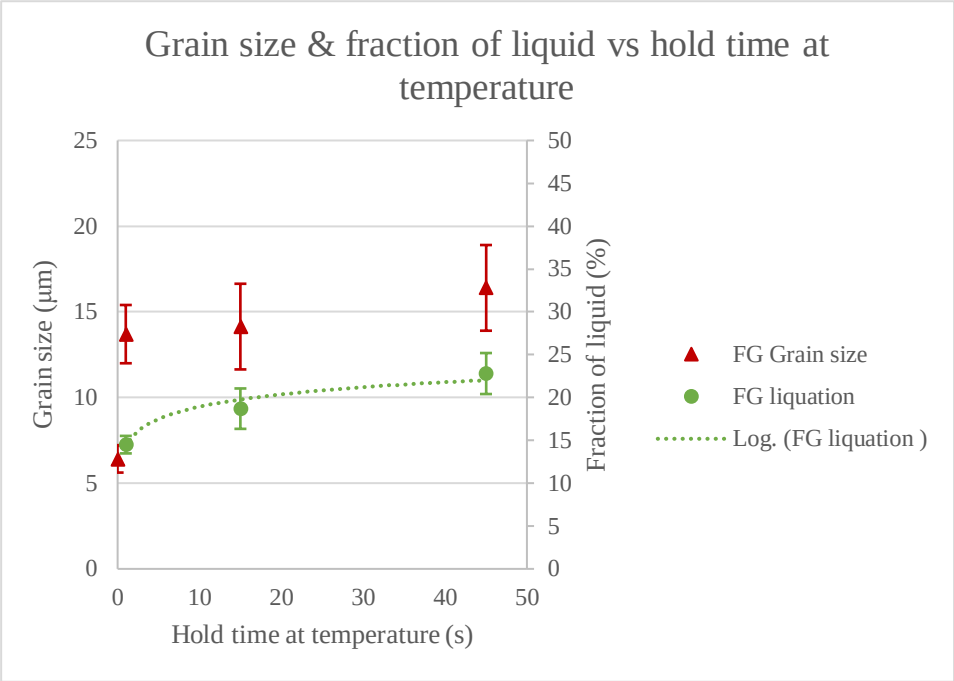

Figure 198 - Plot of grain size & fraction of liquid vs hold time for FG specimens heated at 12.5°Cs^{-1} and held at 1160°C.

Σ3 twin boundaries vs hold time.

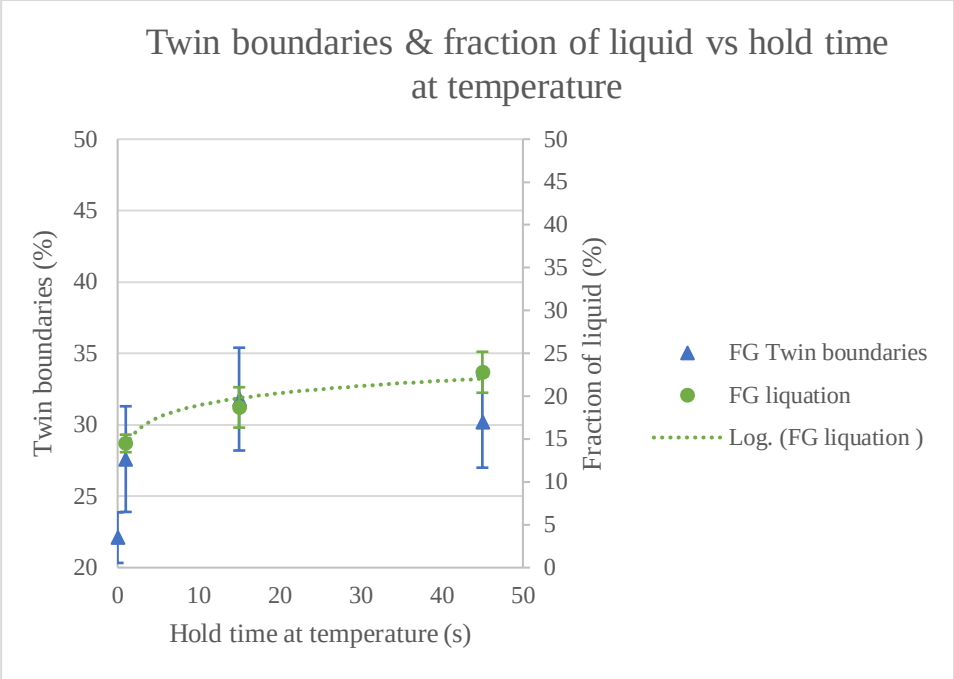

Figure 199 - Plot of Σ3 twin boundaries & fraction of liquid vs hold time for FG specimens heated at 12.5°Cs^{-1} and held at 1160°C.

Vickers hardness vs hold time.

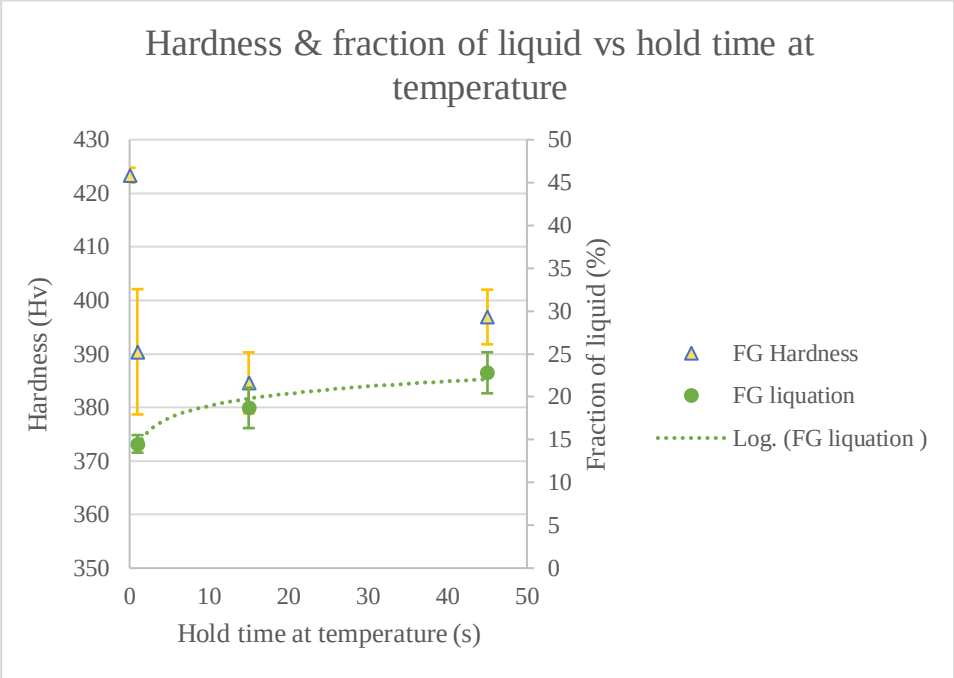

Figure 200 - Plot of hardness & fraction of liquid vs hold time for FG specimens heated at 12.5°Cs^{-1} and held at 1160°C.

FG specimens heated at 12.5°Cs^{-1} to 1200°C and held at temperature.

Grain size vs hold time.

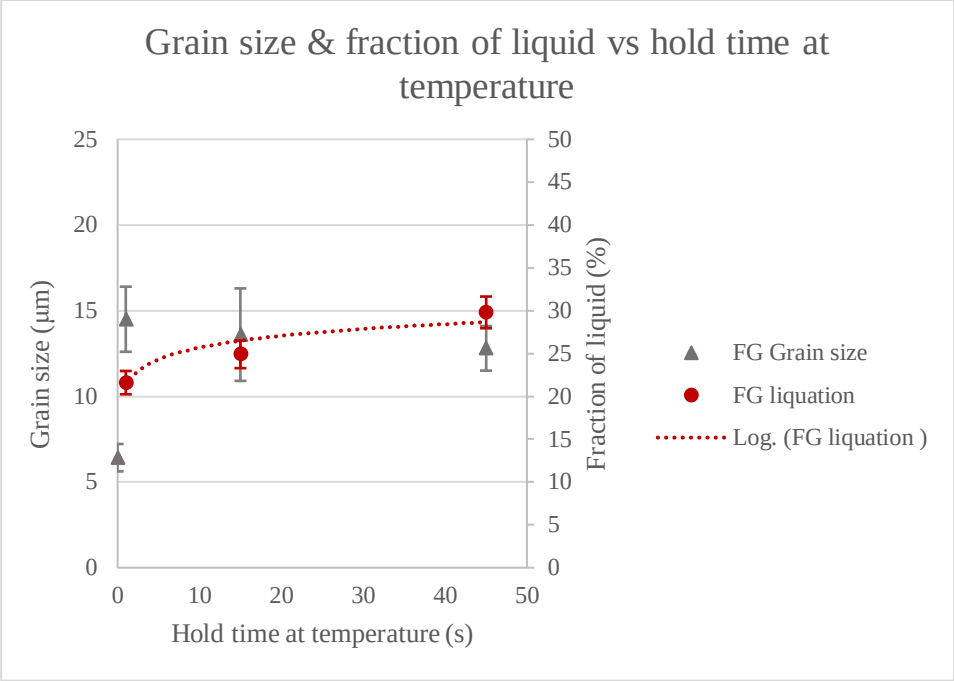

Figure 201 - Plot of grain size & fraction of liquid vs hold time for FG specimens heated at 12.5°Cs^{-1} and held at 1200°C.

Σ3 twin boundaries vs hold time.

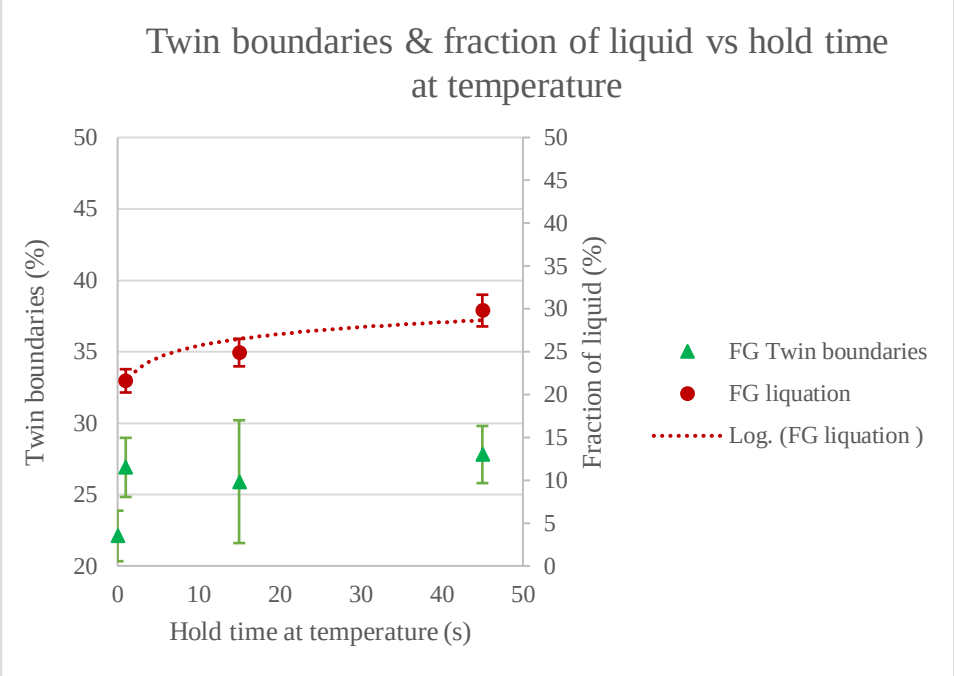

Figure 202 - Plot of Σ3 twin boundaries & fraction of liquid vs hold time for FG specimens heated at 12.5°Cs^{-1} and held at 1200°C.

Vickers hardness vs hold time.

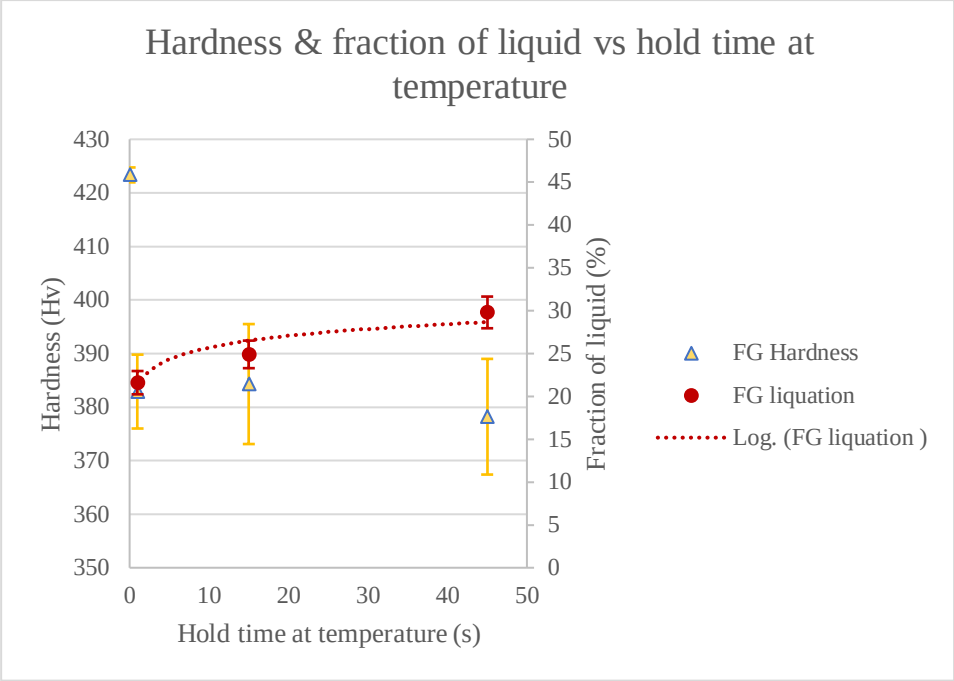

Figure 203 - Plot of hardness & fraction of liquid vs hold time for FG specimens heated at 12.5°Cs^{-1} and held at 1200°C.

CG specimens heated at 12.5°Cs^{-1} to 1200°C and held at temperature.

Grain size vs hold time.

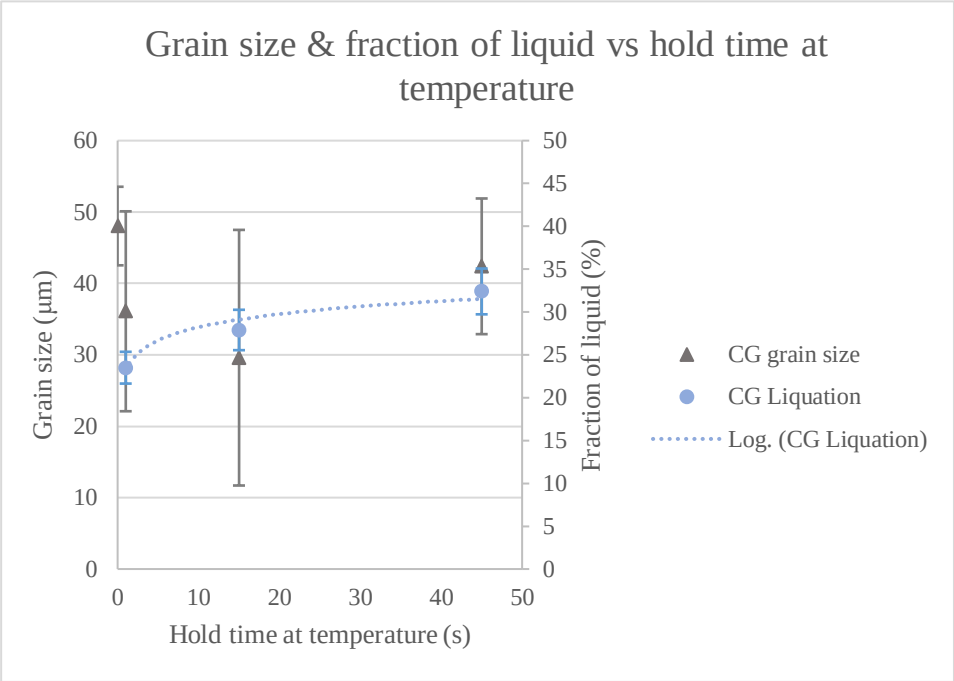

Figure 204 - Plot of grain size & fraction of liquid vs hold time for CG specimens heated at 12.5°Cs^{-1} and held at 1200°C.

Σ3 twin boundaries vs hold time.

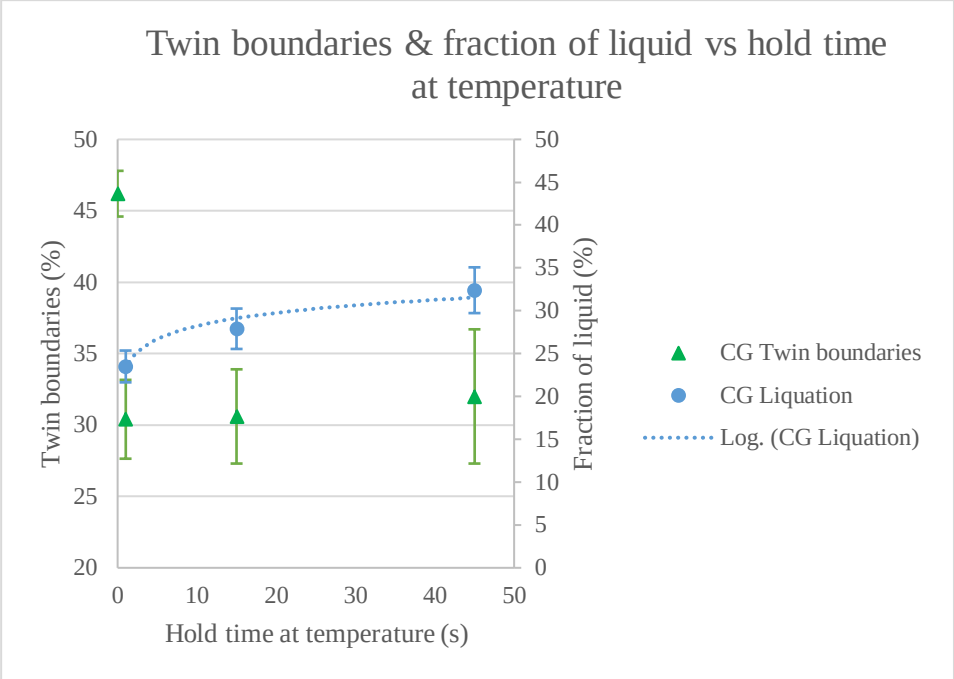

Figure 205 - Plot of Σ3 twin boundaries & fraction of liquid vs hold time for CG specimens heated at 12.5°Cs^{-1} and held at 1200°C.

Vickers hardness vs hold time.

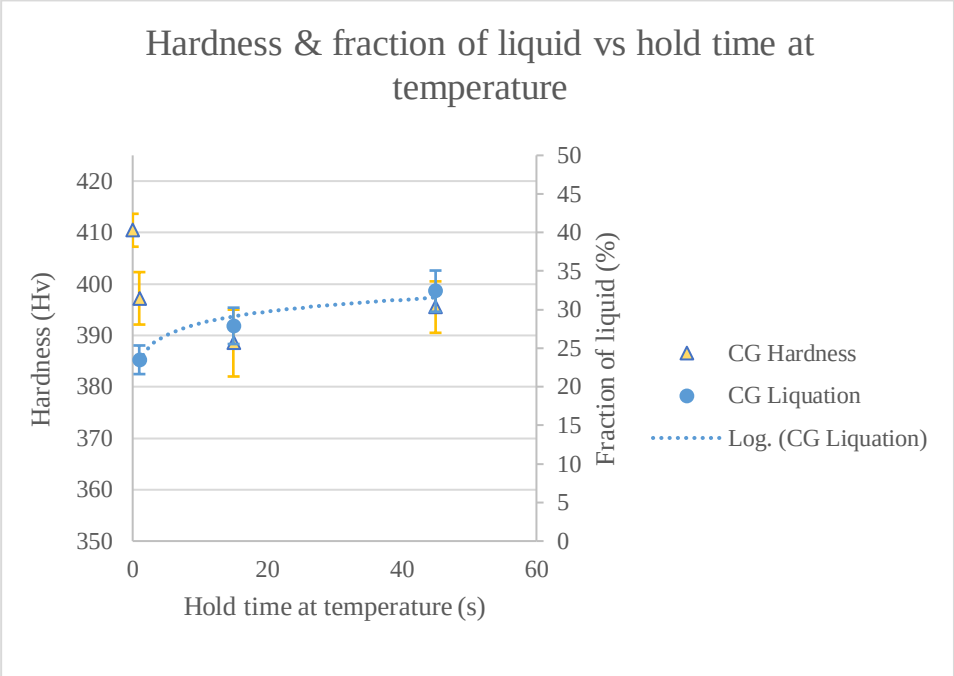

Figure 206 - Plot of hardness & fraction of liquid vs hold time for CG specimens heated at 12.5°Cs^{-1} and held at 1200°C.

8 References

[1] M. Soucail, A. Moal, L. Naze, E. Massoni, C. Levaillant, and Y. Bienvenu, "Microstructural Study and Numerical Simulation of Inertia Friction Welding of Astroloy," pp. 847–856, 2012.

[2] I. Bhamji, M. Preuss, P. L. Threadgill, R. J. Moat, A. C. Addison, and M. J. Peel, "Linear friction welding of AISI 316L stainless steel," *Mater. Sci. Eng. A*, vol. 528, no. 2, pp. 680–690, 2010.

[3] M. B. Henderson, D. Arrell, M. Heobel, R. Larsson, and G. Marchant, "Nickel-Based Superalloy Welding Practices for Industrial Gas Turbine Applications," *Sci. Technol. Weld. Join.*, vol. 9, pp. 1–14, 2004.

[4] M. M. Attallah, H. Terasaki, R. J. Moat, S. E. Bray, Y. Komizo, and M. Preuss, "In-Situ observation of primary γ′ melting in Ni-base superalloy using confocal laser scanning microscopy," *Mater. Charact.*, vol. 62, no. 8, pp. 760–767, 2011.

[5] F. Tancret, "Thermo-Calc and Dictra simulation of constitutional liquation of gamma prime (c0) during welding of Ni base superalloys F.," *Comput. Mater. Sci.*, vol. 45, no. 2, pp. 388–389, 2009.

[6] A. Vastano, S. Bray, and C. Magazzeni, "A Guide to the influence of microstructure on the inertia friction welding process characteristics of Nickel Superalloy RR1000 (Rolls-Royce Technical Report - EDNS01000845983)," 2019.

[7] S. Bray and C. Magazzeni, "A First Approximation of the Condition and Evolution of the Contact 'Shear Zone' During Inertia Friction Welding of Fine Grain Nickel superalloy RR1000 (Rolls-Royce Technical Report - EDNS01000884134)," 2020.

[8] Rolls-Royce, "The jet engine." p. 292, 1996.

[9] J. Wickerson, *Holistic Gas Turbine*. Rolls-Royce plc 2016, 2016.

[10] P. Spittle, "Gas turbine technology," *Phys. Educ.*, vol. 38, no. 6, pp. 504–511, 2003.

[11] "Aviation History," *2019 GE*, 2019. [Online]. Available: https://www.geaviation.com/company/aviation-history. [Accessed: 02-Jul-2020].

[12] "Trent multiple shafts diagram." [Online]. Available: http://www.roger-

wilco.net/wp-content/uploads/2010/11/Untitled-312.jpg. [Accessed: 18-Aug-2016].

[13] N. Wright and S. Thompson, *The Jet Engine*, 5th ed. London: Rolls-Royce technical publications, 2005.

[14] T. Sourmail, "Coatings for Turbine Blades." [Online]. Available: http://www.msm.cam.ac.uk/phase-trans/2003/Superalloys/coatings/.

[15] M. J. Donachie and S. J. Donachie, *Superalloys A Technical Guide*, 2nd ed. Ohio: ASM International, 2002.

[16] R. C. Reed and C. M. F. Rae, *Physical Metallurgy of the Nickel-Based Superalloys*, Fifth Edit., vol. 1. Elsevier B.V., 2014.

[17] R. C. Reed, *The Superalloys: Fundamentals and Applications.*, 1st ed. Cambridge, UK: cambridge university press, 2006.

[18] C. Tian, L. Xu, C. Cui, and X. Sun, "Creep Mechanisms of a Ni-Co-Based-Wrought Superalloy with Low Stacking Fault Energy," *Metall. Mater. Trans. A Phys. Metall. Mater. Sci.*, vol. 46, no. 10, pp. 4601–4609, 2015.

[19] T. M. Pollock and S. Tin, "Nickel-Based Superalloys for Advanced Turbine Engines: Chemistry, Microstructure and Properties," *J. Propuls. Power*, vol. 22, no. 2, pp. 361–374, 2006.

[20] S. J. Park, S. M. Seo, Y. S. Yoo, H. W. Jeong, and H. J. Jang, "Effects of Cr, W, and Mo on the high temperature oxidation of Ni-based superalloys," *Materials (Basel).*, vol. 12, no. 18, 2019.

[21] E. W. Ross, "Rene 100-A Sigma-Free Turbine Blade Alloy," *J. Met.*, vol. 19, no. 12, pp. 12–14, 1967.

[22] D. Nystrom, J, T. M. Pollock, W. H. Murphy, and A. Garg, "Dis-continuous Cellular Precipitation in a High-Refractory Nickel-Base Su-peralloy," *Metall. Mater. Trans.*, vol. 28A, pp. 1443–2452, 1997.

[23] S. . Wlodek, "The Structure of IN100," *Trans. ASM*, vol. 57, pp. 110–119, 1964.

[24] N. Hansen, "Hall-petch relation and boundary strengthening," *Scr. Mater.*, vol. 51, no. 8 SPEC. ISS., pp. 801–806, 2004.

[25] J. C. Williams and E. A. Starke, "Progress in structural materials for aerospace systems," *Acta Mater.*, vol. 51, no. 19, pp. 5775–5799, 2003.

[26] M. Detrois, J. Rotella, R. L. Goetz, R. C. Helmink, and S. Tin, "Grain boundary engineering of powder processed Ni-base superalloy RR1000: Influence of the

deformation parameters," *Mater. Sci. Eng. A*, vol. 627, pp. 95–105, 2015.

[27] C. A. Schuh, M. Kumar, and W. E. King, "Analysis of grain boundary networks and their evolution during grain boundary engineering," *Acta Mater.*, vol. 51, no. 3, pp. 687–700, 2003.

[28] M. Schneider *et al.*, "Analysis of strengthening due to grain boundaries and annealing twin boundaries in the CrCoNi medium-entropy alloy," *Int. J. Plast.*, 2019.

[29] S. L. Lee and N. L. Richards, "The effect of single-step low strain and annealing of nickel on grain boundary character," *Mater. Sci. Eng. A*, vol. 390, no. 1–2, pp. 81–87, 2005.

[30] M. Kumar, W. E. King, and A. J. Schwartz, "Modifications to the microstructural topology in f.c.c. materials through thermomechanical processing," *Acta Mater.*, vol. 48, no. 9, pp. 2081–2091, 2000.

[31] P. HAASEN†, "Mechanical Properties of Solid Solutions," *Phys. Metall.*, pp. 2009–2073, 1996.

[32] T. M. Pollock and A. S. Argon, "Creep resistance of CMSX-3 nickel base superalloy single crystals," *Acta Metall. Mater.*, vol. 40, no. 1, pp. 1–30, 1992.

[33] J. Zhang, T. Jin, Y. Xu, Z. Hu, and X. Wu, "Antiphase boundary strengthening in a single crystal nickel-base superalloy," *Journal of Materials Science and Technology*, vol. 18, no. 2. pp. 159–162, 2002.

[34] K. Alit and R. J. Stewart, "Precipitation in a nimonic PE 16 alloy," vol. 15, no. June 1984, pp. 487–505, 1985.

[35] B. Reppich, "Some new aspects concerning particle hardening mechanisms in γ' precipitating Ni-base alloys-I. Theoretical concept," *Acta Metall.*, vol. 30, no. 1, pp. 87–94, 1982.

[36] M. P. Jackson and R. C. Reed, "Heat treatment of UDIMET 720Li: the effect of microstructure on properties," *Mater. Sci. Eng. A259*, vol. 259, pp. 85–97, 1999.

[37] R. J. Mitchell, M. C. Hardy, M. Preuss, and S. Tin, "DEVELOPMENT OF y' MORPHOLOGY IN P/M ROTOR DISC ALLOYS DURING HEAT TREATMENT," *Superalloys 2004*, pp. 361–370, 2004.

[38] I. M. . Parr *et al.*, "INHOMOGENEOUS GRAIN COARSENING BEHAVIOR IN SUPERSOLVUS HEAT TREATED NICKEL-BASED SUPERALLOY RR1000," *Superalloys 2016 Proc. 13th Int. Symp. Superalloys*, vol. 1, pp. 447–456, 2016.

[39] J. . Davies, *ASM Specialty Handbook: Nickel, Cobalt, and Their Alloys*, 1st ed. Materials Park, Ohio: ASM International, 2000.

[40] F. . Campbell, "Superalloys," in *Manufacturing Technology for Aerospace Structural Materials*, 1st ed., F. . Campbell, Ed. London: Elsevier Ltd, 2006, pp. 211–272.

[41] R. E. Schafrik and R. Sprague, "Saga of gas turbine materials, part III," *Adv. Mater. Process.*, vol. 162, no. 5, pp. 29–33, 2004.

[42] M. HERNÁNDEZ, R. R. AMBRIZ, R. CORTÉS, C. M. GÓMORA, G. PLASCENCIA, and D. JARAMILLO, "Assessment of gas tungsten arc welding thermal cycles on Inconel 718 alloy," *Trans. Nonferrous Met. Soc. China (English Ed.*, vol. 29, no. 3, pp. 579–587, 2019.

[43] H. Naffakh Moosavy, M. R. Aboutalebi, S. H. Seyedein, and C. Mapelli, "Microstructural, mechanical and weldability assessments of the dissimilar welds between γ′- And γ″-strengthened nickel-base superalloys," *Mater. Charact.*, vol. 82, pp. 41–49, 2013.

[44] S. Venukumar, P. Sarkar, J. S. Sashank, P. Sampath, and K. Saikiran, "Microstructural and mechanical properties of Inconel 718 TIG weldments," *Mater. Today Proc.*, vol. 5, no. 2, pp. 8480–8485, 2018.

[45] K. Han, H. Wang, L. Shen, and B. Zhang, "Analysis of cracks in the electron beam welded joint of K465 nickel-base superalloy," *Vacuum*, vol. 157, no. July, pp. 21–30, 2018.

[46] M. Lachowicz, W. Dudziński, K. Haimann, and M. Podrez-Radziszewska, "Microstructure transformations and cracking in the matrix of γ-γ′ superalloy Inconel 713C melted with electron beam," *Mater. Sci. Eng. A*, vol. 479, no. 1–2, pp. 269–276, 2008.

[47] Y. Mei *et al.*, "Effect of base metal and welding speed on fusion zone microstructure and HAZ hot-cracking of electron-beam welded Inconel 718," *Mater. Des.*, vol. 89, pp. 964–977, 2016.

[48] D. R. K., D. Sidharth, P. P. Phani, R. Rajendran, G. M. K., and S. Narayanan, "Microstructure and properties of inconel 718 and AISI 416 laser welded joints," *J. Mater. Process. Technol.*, vol. 266, no. November 2018, pp. 52–62, 2019.

[49] M. Montazeri and F. M. Ghaini, "The liquation cracking behavior of IN738LC superalloy during low power Nd:YAG pulsed laser welding," *Mater. Charact.*,

vol. 67, pp. 65–73, 2012.

[50] J. Pepe and W. Savage, “The Weld Heat-Affected Zone of the 18Ni Maraging Steels,” *Weld. Journal, Res. Suppl.*, vol. 49, no. 12, pp. 545–553, 1970.

[51] S. Kou, “Solidification and liquation cracking issues in welding,” *Jom*, vol. 55, no. 6, pp. 37–42, 2003.

[52] W. Li, A. Vairis, M. Preuss, and T. Ma, “Linear and rotary friction welding review,” *Int. Mater. Rev.*, vol. 61, no. 2, pp. 71–100, 2016.

[53] Y. Ding, G. You, H. Wen, P. Li, X. Tong, and Y. Zhou, “Microstructure and mechanical properties of inertia friction welded joints between alloy steel 42CrMo and cast Ni-based superalloy K418,” *J. Alloys Compd.*, vol. 803, pp. 176–184, 2019.

[54] M. Preuss, P. J. Withers, and G. J. Baxter, “A comparison of inertia friction welds in three nickel base superalloys,” *Mater. Sci. Eng. A*, vol. 437, no. 1, pp. 38–45, 2006.

[55] Z. W. Huang, H. Y. Li, G. Baxter, S. Bray, and P. Bowen, “Electron microscopy characterization of the weld line zones of an inertia friction welded superalloy,” *J. Mater. Process. Technol.*, vol. 211, no. 12, pp. 1927–1936, 2011.

[56] J. P. Ferte, “Metallurgical joining of engine parts Inertia welding of nickel superalloy HP compressor disks.,” *J. Phys. 4*, vol. 3, pp. 1019-1027., 1993.

[57] F. Torster, G. Baumeister, J. Albrecht, G. Lütjering, D. Helm, and M. a. Daeubler, “Influence of grain size and heat treatment on the microstructure and mechanical properties of the nickel-base superalloy U 720 LI,” *Mater. Sci. Eng. A*, vol. 234–236, pp. 189–192, 1997.

[58] M. Preuss, P. J. Withers, J. W. L. Pang, and G. J. Baxter, “Inertia welding nickel-based superalloy: Part I. Metallurgical characterization,” *Metall. Mater. Trans. A Phys. Metall. Mater. Sci.*, vol. 33, no. 10, pp. 3215–3225, 2002.

[59] T. Ma and G. Den Ouden, “Liquation cracking susceptibility of Al-Zn-Mg alloys,” *Int. J. Join. Mater.*, vol. 11, no. 3, pp. 61–67, 1999.

[60] J. . Dudas and F. . Collins, “Preventing weld cracks in high strength aluminum alloys,” *Weld. J.*, vol. 45, p. 241, 1966.

[61] J. E. Steenbergen and H. R. Thornton, “A Quantitative Determination of the Conditions for Hot Cracking During Welding for Aluminum Alloys A combination of strain and susceptible microstructure causes failure which

occurs preferentially in the heat-affected," *J. Am. Weld. Soc.*, vol. 68, pp. 61s-68s, 1970.

[62] O. A. Ojo and N. L. Richards, *Welding and Joining of Aerospace Materials - 5 - Heat-affected zone cracking in welded nickel superalloys*. Woodhead Publishing Limited, 2012.

[63] O. A. Ojo, N. L. Richards, and M. C. Chaturvedi, "Contribution of constitutional liquation of gamma prime precipitate to weld HAZ cracking of cast Inconel 738 superalloy," *Scr. Mater.*, vol. 50, no. 5, pp. 641–646, 2004.

[64] M. R. Jahangiri, S. M. A. Boutorabi, and H. Arabi, "Study on incipient melting in cast Ni base IN939 superalloy during solution annealing and its effect on hot workability," *Mater. Sci. Technol. (United Kingdom)*, vol. 28, no. 12, pp. 1402–1413, 2012.

[65] B. Radhakrishnan and R. G. Thompson, "Kinetics of Grain Growth in the Weld HAZ of Alloy 718," *Metall. Trans. A*, vol. 24A, p. 1409, 1993.

[66] B. Weiss, G. . Grotke, and R. Stickler, "The Effect of Weld Heat-Affected Zone (HAZ) Liquation Kinetics on the Hot Cracking Susceptibility of Alloy 718," *Weld. J.*, vol. 49, p. 471, 1970.

[67] J. . Brooks, "Physical Metallurgy of Hot Ductility Testing," *Weld. J.*, vol. 53, p. 517, 1974.

[68] R. Nakkalil, N. L. Richards, and M. C. Chaturvedi, "Effect of Alloy Modifi ca- tions on HAZ Cracking of A-286 Stainless Steel," *Metall. Trans.*, vol. 24A, p. 1169, 1993.

[69] R. Nakkalil, N. L. Richards, and M. C. Chaturvedi, "Microstructural characterization of INCOLOY 903 weldments," *Metall. Trans. A*, vol. 24, no. 5, pp. 1169–1179, 1993.

[70] O. A. Ojo, N. L. Richards, and M. C. Chaturvedi, "Study of the fusion zone and heat-affected zone microstructures in tungsten inert gas-welded INCONEL 738LC superalloy," *Metall. Mater. Trans. A Phys. Metall. Mater. Sci.*, vol. 37, no. 2, pp. 421–433, 2006.

[71] O. A. Ojo, N. L. Richards, and M. C. Chaturvedi, "Microstructural study of weld fusion zone of TIG welded IN 738LC nickel-based superalloy," *Scr. Mater.*, vol. 51, no. 7, pp. 683–688, 2004.

[72] O. A. Ojo, N. . Richards, and M. C. Chaturvedi, "Liquation of various phases in HAZ during welding of cast Inconel 738LC," *Mater. Sci. Technol.*, vol. 20, no. 8, pp.

1027–1034, 2004.

[73] O. A. Ojo and M. C. Chaturvedi, “On the role of liquated γ′ precipitates in weld heat affected zone microfissuring of a nickel-based superalloy,” *Mater. Sci. Eng. A*, vol. 403, no. 1–2, pp. 77–86, 2005.

[74] P. Willemin and M. Durand-Charre, “The nickel-rich corner of the Ni-Al-Ti system,” *J. Mater. Sci.*, vol. 25, no. 1, pp. 168–174, 1990.

[75] M. Soucail and Y. Bienvenu, “Dissolution of gamma prime phase in a Nickel-base Superalloy at Equilibrium and under Rapid Heating,” *Mater. Sci. Eng. A*, vol. 220, no. 96, pp. 215–222, 1996.

[76] J. . DuPont, J. . Lippold, and S. . Kiser, *Welding Metallurgy And Weldability Of Nickel-Base Alloys*, 1st ed. New Jersey: John Wiley & Sons, Inc., 2009.

[77] M. Durand-Charre, *The Microstructure of Superalloys*, 1st ed. Amsterdam B.V: CRC PRess, 1997.

[78] S. Singh and J. Andersson, “Hot cracking in cast alloy 718,” *Sci. Technol. Weld. Join.*, vol. 23, no. 7, pp. 568–574, 2018.

[79] A. Baldan, “Electron microprobe investigation of lower melting regions in the as-cast structure of DS200 + Hf single crystal,” *J. Mater. Sci.*, vol. 25, no. 10, pp. 4341–4348, 1990.

[80] M. Mostafaei and S. M. Abbasi, “Influence of Zr content on the incipient melting behavior and stress-rupture life of CM247 LC nickel base superalloy,” *J. Alloys Compd.*, vol. 648, pp. 1031–1037, 2015.

[81] A. Lombardi, W. Mu, C. Ravindran, N. Dogan, and M. Barati, “Influence of Al2Cu morphology on the incipient melting characteristics in B206 Al alloy,” *J. Alloys Compd.*, vol. 747, pp. 131–139, 2018.

[82] A. Lombardi, W. Mu, C. Ravindran, N. Dogan, and M. Barati, “In-situ investigation of incipient melting in a 319 type Al alloy using laser scanning confocal microscopy,” *Mater. Charact.*, vol. 141, no. April, pp. 328–337, 2018.

[83] W. . Owczarski, D. . Duvall, and C. . Sullivan, “Model for Heat Affected Zone Cracking in Nicke-Base Superalloy,” *Weld J.*, vol. 45, pp. 145–155, 1966.

[84] B. Radhakrishnan and R. G. Thompson, “Liquid film migration (LFM) in the weld heat affected zone (HAZ) of a ni-base superalloy,” *Scr. Metall. Mater.*, vol. 24, no. 3, pp. 537–542, 1990.

[85] R. Nakkalil, N. L. Richards, and M. C. Chaturvedi, “The influence of solidification

mode on heat affected zone microfissuring in a nickel-iron base superalloy," *Acta Metall. Mater.*, vol. 41, no. 12, pp. 3381–3392, 1993.

[86] A. P. I. Popoolaa, K. M. Oluwasegun, O. E. Olorunniwo, P. O. Atanda, and V. S. Aigbodion, "Thermal and mechanical effect during rapid heating of astroloy for improving structural integrity," *J. Alloys Compd.*, vol. 666, pp. 482–492, 2016.

[87] Y. Cheng, J. Chen, R. Shiue, and L. Tsay, "Liquation Cracking of Mar-M004 Weld," no. c, pp. 22–24, 2018.

[88] V. R. Ming, "The Effect of Solution Heat Treatment on the Tensile and Creep Properties of MarM-002," University of Cape Town, 1995.

[89] D. Chatain, E. Rabkin, J. Derenne, and J. Bernardini, "Role of the solid/liquid interface faceting in rapid penetration of a liquid phase along grain boundaries," *Acta Mater.*, vol. 49, no. 7, pp. 1123–1128, 2001.

[90] I. A. Aksay, C. E. Hoge, and J. A. Pask, "Wetting under chemical equilibrium and nonequilibrium conditions," *J. Phys. Chem.*, vol. 78, no. 12, pp. 1178–1183, 1974.

[91] M. Kiuchi and R. Kopp, "Mushy/Semi-Solid Metal Forming Technology – Present and Future," *CIRP Ann. - Manuf. Technol.*, vol. 51, no. 2, pp. 653–670, 2002.

[92] G. Hirt and R. Kopp, *Thixoforming*, 1st ed. Weinheim: WILEY-VCH, 2009.

[93] M. . Lewandowski and R. . Overfelt, "High temperature deformation behavior of solid and semi-solid alloy 718," *Acta Mater.*, vol. 47, no. 18, pp. 4695–4710, 1999.

[94] H. Liao, Y. Wu, K. Zhou, and J. Yang, "Hot deformation behavior and processing map of Al–Si–Mg alloys containing different amount of silicon based on Gleebe-3500 hot compression simulation," *Mater. Des.*, vol. 65, pp. 1091–1099, 2015.

[95] "DSI GLEEBLE APPLICATION NOTES," *2020 Dynamic Systems Inc.* [Online]. Available: https://www.gleeble.com/resources/application-notes.html. [Accessed: 08-Feb-2016].

[96] A. A. Tseng, "Deformation behavior of steels in mushy state," *Mater. Des.*, vol. 22, pp. 83–92, 2001.

[97] P. K. Seo, S. W. Youn, and C. G. Kang, "The effect of test specimen size and strain-rate on liquid segregation in deformation behavior of mushy state material," *J. Mater. Process. Technol.*, vol. 130–131, pp. 551–557, 2002.

[98] J.-Y. Li, S. Sugiyama, and J. Yanagimoto, "Microstructural evolution and flow stress of semi-solid type 304 stainless steel," *Journal of Materials Processing*

Technology, vol. 161. pp. 396–406, 2005.

[99] E. Tzimas and a. Zavaliangos, "Mechanical behavior of alloys with equiaxed microstructure in the semisolid state at high solid content," *Acta Mater.*, vol. 47, no. 2, pp. 517–528, 1999.

[100] R. Kopp *et al.*, "Flow stress measuring by use of cylindrical compression test and special application to metal forming processes," *Steel Res.*, vol. 72, no. 10, pp. 394–401, 2001.

[101] Y. XU, L. Chen, D. Wang, and L. Jin, "Flow behaviour and evolution of microstructure during hot deformation for a high mo stainless steel," *Mater. Sci. Technol.*, vol. 16, no. 3, 2000.

[102] O. Lashkari and R. Ghomashchi, "A new machine to characterize microstructural evolution of semi-solid metal billets through viscometery," vol. 28, pp. 1321–1325, 2007.

[103] A. Bolouri, M. Shahmiri, and C. G. Kang, "Study on the effects of the compression ratio and mushy zone heating on the thixotropic microstructure of AA 7075 aluminum alloy via SIMA process," *J. Alloys Compd.*, vol. 509, no. 2, pp. 402–408, 2011.

[104] K. M. Kareh, P. D. Lee, R. C. Atwood, T. Connolley, and C. M. Gourlay, "Revealing the micromechanisms behind semi-solid metal deformation with time-resolved X-ray tomography," *Nat Commun*, vol. 5, p. 4464, 2014.

[105] K. M. Kareh, C. O'Sullivan, T. Nagira, H. Yasuda, and C. M. Gourlay, "Dilatancy in semi-solid steels at high solid fraction," *Acta Mater.*, vol. 125, pp. 187–195, 2017.

[106] A. Bolouri and C. G. Kang, "Correlation between solid fraction and tensile properties of semisolid RAP processed aluminum alloys," *J. Alloys Compd.*, vol. 516, pp. 192–200, 2012.

[107] S. Benke, S. Dziallach, G. Laschet, U. Prahl, and W. Bleck, "Modeling of the uniaxial tensile and compression behavior of semi-solid A356 alloys," *Comput. Mater. Sci.*, vol. 45, no. 3, pp. 633–637, 2009.

[108] O. Lashkari, F. Ajersch, A. Charette, and X. G. Chen, "Microstructure and rheological behavior of hypereutectic semi-solid Al-Si alloy under low shear rates compression test," *Mater. Sci. Eng. A*, vol. 492, no. 1–2, pp. 377–382, 2008.

[109] G. E. Dieter, H. A. Kuhn, and S. L. Semiatin, *Handbook of workability and process*

design, 1st ed. Ohio: ASM International, 2003.

[110] R. . Evans and P. . Scharning, "Axisymmetric compression test and hot working properties of alloys," *Mater. Sci. Technol.*, vol. 17, no. 8, pp. 995–1004, 2001.

[111] M. Kiuchi, S. Sugiyama, and K. Arai, "Study of Metal Forming in the Mashy State 1st Report: Flow Stress and Deformation Behaviour of Alloys in Mashy State," in *Proceedings of the Twentieth International Machine Tool Design and Research Conference*, 1980, pp. 71–78.

[112] J. G. Webster, R. Vilanova, and A. Visioli, "The Proportional-Integral-Derivative (PID) Controller," *Wiley Encycl. Electr. Electron. Eng.*, no. 3, pp. 1–15, 2017.

[113] J. Jones, S. P. Brookes, M. T. Whittaker, and R. J. Lancaster, "Non-invasive temperature measurement and control techniques under thermomechanical fatigue loading," *Mater. Sci. Technol. (United Kingdom)*, vol. 30, no. 15, pp. 1862–1876, 2014.

[114] H. Y. Li *et al.*, "Effects of microstructure on high temperature dwell fatigue crack growth in a coarse grain PM nickel based superalloy," *Acta Mater.*, vol. 90, pp. 355–369, 2015.

[115] Astm Standard, "E112-12:Standard Test Methods for Determining Average Grain Size," *ASTM Int.*, vol. E112-12, pp. 1–27, 2012.

[116] R. C. Buckingham, "Methodologies for the preparation and microstructural assessment of nickel-based metallographic samples. (Rolls-Royce Technical Report - EDNS01000657400)," 2018.

[117] A. Winkelmann, C. Trager-Cowan, F. Sweeney, A. P. Day, and P. Parbrook, "Many-beam dynamical simulation of electron backscatter diffraction patterns," *Ultramicroscopy*, vol. 107, no. 4–5, pp. 414–421, 2007.

[118] M. D. A. Pereira-da-silva and F. A. Ferri, "1 - Scanning Electron Microscopy," in *Nanocharacterization Techniques*, Elsevier Inc., 2017, pp. 1–35.

[119] L. E. Watt, P. A. Bland, D. J. Prior, and S. S. Russell, "Fabric analysis of Allende matrix using EBSD," *Meteorit. Planet. Sci.*, vol. 41, no. 7, pp. 989–1001, 2006.

[120] J. A. S. and J. D. J. B Roebuck†, M Brooks†, P N Quested†, R W Evans*, "Mechanical Tests Close to the Solidus," 2004.

[121] J. . Spittle, S. G. R. Brown, J. . James, and R. . Evans, "Mechanical properties of partially molten alloys," in *Physical simulation of casting, hot rolling and welding*, 1997, pp. 81–91.

[122] S. Louhenkilpi, “Continuous Casting of Steel,” in *Treatise on Process Metallurgy*, vol. 3, Elsevier Ltd., 2014, pp. 373–434.

[123] S. Bray, “Results of welding process trials, temperature data logging and metallurgical cut-up assessment of 50 mm and 143 mm diameter Inertia Friction Welded R1000 for the TSB ProMoTE Project (Rolls-Royce Technical Report - DHC311259/MPL27686),” 2008.

[124] R. Brandt, C. Bird, and G. Neuer, “Emissivity reference paints for high temperature applications,” *Meas. J. Int. Meas. Confed.*, vol. 41, no. 7, pp. 731–736, 2008.

[125] V. VanDoren, “Control Engineering | Understanding PID control and loop tuning fundamentals,” 2019. [Online]. Available: https://www.controleng.com/articles/understanding-pid-control-and-loop-tuning-fundamentals/. [Accessed: 23-Aug-2019].

[126] E. Schmider, M. Ziegler, E. Danay, L. Beyer, and M. Bühner, “Is It Really Robust?: Reinvestigating the robustness of ANOVA against violations of the normal distribution assumption,” *Methodology*, vol. 6, no. 4, pp. 147–151, 2010.

[127] N. R. Smalheiser, “Null Hypothesis Statistical Testing and the t-Test,” *Data Lit.*, pp. 127–136, 2017.

[128] “The t tests,” *2020 BMJ Publishing Group Ltd*, 2020. [Online]. Available: https://www.bmj.com/about-bmj/resources-readers/publications/statistics-square-one/7-t-tests. [Accessed: 02-Mar-2020].

[129] “Two Sample t test for Comparing Two Means,” *2020 Houghton Mifflin Harcourt.*, 2020. [Online]. Available: https://www.cliffsnotes.com/study-guides/statistics/univariate-inferential-tests/two-sample-t-test-for-comparing-two-means. [Accessed: 02-Mar-2020].

[130] A. Field, *Discovering Statistics Using SPSS*, 3rd ed. London: Sage Publications Ltd, 2009.

[131] M. . Haafkens and G. . Matthey, “No Title,” *Weld. J.*, vol. 61, pp. 25–30, 1982.

[132] Y. Jin *et al.*, “Evolution of the annealing twin density during δ-Supersolvus grain growth in the nickel-based superalloy Inconel™ 718,” *Metals (Basel).*, vol. 6, no. 1, pp. 1–13, 2015.

[133] S. Karagadde *et al.*, “Transgranular liquation cracking of grains in the semi-solid state.,” *Nat. Commun.*, vol. 6, p. 8300, 2015.